Technische Universität Graz

DISSERTATION

Buckling Analysis of Carbon Nanotubes:

Application of a Molecular Statics Approach and a Mixed Atomistic-Continuum Model

ausgeführt zum Zwecke der
Erlangung des akademischen Grades
eines

Doktors der technischen Wissenschaften

eingereicht an der
Technischen Universität Graz
Fakultät für Maschinenbau und Wirtschaftswissenschaften

von

Dipl.-Ing. Stefan Hollerer

Betreuer:
Prof. Dipl.-Ing. Dr.techn. Christian C. Celigoj

Gutachter:
Prof. Dipl.-Ing. Dr.techn. Alois Steindl

Institut für Festigkeitslehre der Technischen Universität Graz
Graz, April 2012

Deutsche Fassung:

Beschluss der Curricula-Kommission für Bachelor-, Master- und Diplomstudien vom 10.11.2008

Genehmigung des Senates am 1.12.2008

EIDESSTATTLICHE ERKLÄRUNG

Ich erkläre an Eides statt, dass ich die vorliegende Arbeit selbstständig verfasst, andere als die angegebenen Quellen/Hilfsmittel nicht benutzt, und die den benutzten Quellen wörtlich und inhaltlich entnommenen Stellen als solche kenntlich gemacht habe.

Graz, am ……………23.04.2012…………   ………………………………………………..

(Unterschrift)

Englische Fassung:

STATUTORY DECLARATION

I declare that I have authored this thesis independently, that I have not used other than the declared sources / resources, and that I have explicitly marked all material which has been quoted either literally or by content from the used sources.

……………………………   ………………………………………………..

date   (signature)

Abstract

This thesis applies a molecular statics and a continuum mechanics approach, independently of each other, in order to analyse the buckling behaviour of carbon nanotubes. The remarkable properties of carbon nanotubes are an immediate consequence of the interatomic interactions. These are considered in the internal potential of the atomistic structure, which models the bonded energy and the non-bonded energy by means of interatomic potentials. In combination with the energy of external contributions, the total potential of the loaded carbon nanotube can be stated for the discrete atomistic structure. The total potential of the continuous counterpart, which is represented by a surface, is defined by an application of the quasi-continuum method.

The molecular statics approach directly considers the interatomic potentials in a discrete setting. The search for equilibrium configurations of the atomistic structure leads to a non-linear system of equations, which is linearised and solved iteratively. Within this model, finite element equivalents are set up for the bonded and non-bonded interactions, enabling the use of non-linear finite element frameworks. With the molecular statics approach, in particular, the influence of the in-layer and the inter-layer non-bonded interactions is investigated.

In the continuum mechanics approach, the constitutive behaviour is derived from the underlying lattice structure. In particular, the quasi-continuum method is applied and a so-called mixed atomistic-continuum model is obtained. Thereby, the coupling between deformations on the atomistic level and the deformation of the continuum surface is done by an expanded Cauchy-Born rule. Furthermore, the continuum is discretised by means of finite elements and the derived non-linear system of equations is linearised and solved iteratively. Consequently, the continuum approach provides an alternative to the full atomistic calculations.

Applying both approaches, the buckling characteristics of carbon nanotubes in consequence of different loading conditions are studied and the results are compared. Instability points are detected by an accompanying eigenvalue analysis of the global stiffness matrix in combination with a bisection algorithm. By means of branch switching, investigations into the behaviour of carbon nanotubes in the postbuckling regime are enabled. With the help of this framework, numerical simulations are performed for various carbon nanotubes under torsion, axial compression and bending.

Kurzfassung

Diese Arbeit untersucht das Beulverhalten von Kohlenstoffnanoröhren unter Verwendung zweier unabhängiger Modellierungsansätze. Dabei kommen eine Formulierung der Molekularstatik und ein Modell auf der Grundlage der Kontinuumsmechanik zur Anwendung. Die außergewöhnlichen Eigenschaften von Kohlenstoffnanoröhren sind eine unmittelbare Konsequenz aus den Wechselwirkungen der Atome. Diese werden im inneren Potential der atomaren Struktur zusammengefasst, welches mittels interatomarer Potentiale die Energieanteile aus den gebundenen und ungebundenen Atomwechselwirkungen berücksichtigt. Durch die zusätzliche Modellierung der Energie aus externen Belastungen kann das Gesamtpotential der belasteten Kohlenstoffnanoröhre angegeben werden. Dies erfolgt für die diskrete Atomanordnung und unter Verwendung der Quasi-Kontinuumsmethode für eine Fläche als kontinuierliche Ersatzstruktur.

In der Molekularstatik werden die interatomaren Potentiale direkt in der diskreten Beschreibung modelliert. Zur Ermittlung von Gleichgewichtskonfigurationen der atomaren Struktur wird das beschreibende nichtlineare Gleichungssystem linearisiert und iterativ gelöst. In diesem Modell werden für die gebundenen und ungebundenen Interaktionen der Atome äquivalente finite Elemente definiert. Dadurch ist eine rechnerische Umsetzung auf Basis der nichtlinearen Methode der finiten Elemente möglich. Mit dem Verfahren der Molekularstatik wird insbesondere der Einfluss der lageninternen und lagenübergreifenden ungebundenen Wechselwirkungen untersucht.

Im Falle des kontinuumsmechanischen Modells wird das Werkstoffverhalten direkt von der zugrundeliegenden Gitterstruktur abgeleitet. Hierzu wird die Quasi-Kontinuumsmethode angewandt und das sogenannte gemischt atomistisch-kontinuierliche Modell erhalten. Zur Kopplung der Verformungen der atomaren Ebene und der kontinuierlichen Fläche wird eine erweiterte Cauchy-Born Regel verwendet. Die daraus erhaltene kontinuierliche Modellbeschreibung wird unter Einsatz von finiten Elementen diskretisiert. Das resultierende nichtlineare Gleichungssystem wird nach der entsprechenden Linearisierung auf iterative Weise gelöst. Dieses kontinuumsmechanische Modell stellt somit eine Alternative zur vollständig atomaren Simulation zur Verfügung.

Die Untersuchung des Beulverhaltens von Kohlenstoffnanoröhren behandelt unterschiedliche Belastungssituationen. In den Simulationen kommen beide Modellierungsvarianten zur Anwendung und die erhaltenen Resultate werden entsprechend verglichen. Die kritischen Punkte der Deformation werden mittels einer begleitenden Eigenwertanalyse der globalen Steifigkeitsmatrix und eines Bisektionsalgorithmus ermittelt. Eine Pfadwechselprozedur erlaubt die Beobachtung des Verhaltens von Kohlenstoffnanoröhren im Nachbeulbereich. Unter Anwendung dieser Vorgehensweise werden numerische Simulationen für verschiedene Kohlenstoffnanoröhren unter Torsion, axialer Kompression und Biegebelastung durchgeführt.

Acknowledgements

The work presented in this thesis was carried out in the years between 2009 and 2012. During that time I was employed as a scientific assistant at the Institute for Strength of Materials at Graz University of Technology. With the completion of my thesis I would like to thank the people who have supported and accompanied me in different ways.

I want to thank my thesis supervisor Professor Christian C. Celigoj for his scientific encouragement and for many valuable discussions.

Furthermore, I would like to thank Professor Alois Steindl for acting as the external examiner of this thesis and for his interest in my research.

My special thanks go to my colleagues, Michael Hammer and Manfred Ulz, who are responsible for the good collaboration and organisation at the institute. Their helpful suggestions and many scientific discussions contributed to the development of this thesis.

I am forever grateful to my parents, Johann and Gertrud Hollerer, for their everlasting support. Finally, I would like to take this opportunity to thank my brother Robert Hollerer.

Stefan Hollerer, Graz, April 2012

Contents

List of Figures

List of Tables

1 Introduction

1.1 Motivation

In the last decades, nanostructures captured the advertence of many researchers. In particular, carbon nanotubes became very popular, probably because of their predicted remarkable properties in distinct scopes. Among these, mechanical and electrical attributes are of special interest. Additionally, the remarkable chemical and thermal performance makes carbon nanotubes promising materials for the future. As a consequence, carbon nanotubes were brought up for discussion in various applications. For a better understanding of their assumed potentials, much work was performed in the experimental community as well as in the field of numerical simulations. In the course of this, the applied numerical approaches run up the different levels from quantum mechanics beyond molecular mechanics up to continuum mechanics. Of course, all of these methods own their special advantages and disadvantages.

The central idea of quantum mechanical simulations is the solution of the Schrödinger equation for atoms and molecules. This solution provides detailed informations related to the electronic structure of the involved atoms. However, analytical or exact solutions are ascertainable only for simple problems. Consequently, approximations and assumptions are made, leading to various numerical procedures like density functional theory, Hartree-Fock method and tight-binding method. More informations on quantum mechanical simulations can for instance be found in the books of Allen and Tildesley [1] and Leach [27] or in the overview papers of Qian *et al.* [41] and Liu *et al.* [32]. While the quantum mechanics offers the most accurate results, it is up to now only applicable in relative small systems for a short interval in time.

In the case of molecular mechanics, the complex electronic structure of each atom is not taken into account. In particular, the smallest unit to be modelled is the atom, which is represented as a soft sphere. Thus, nanostructures are represented as multi-particle systems of interacting atoms. The interactions among the individual atoms are commonly specified by empirically derived interatomic potentials. On the basis of these interatomic potentials, the total potential of the entire system and the forces between the atoms can be calculated. The related major methods are molecular dynamics and molecular statics. In the case of molecular dynamics, the atomistic configuration is allowed to vary in time and the associated evolution is obtained by Newton's equations of motion. In contrast, a molecular statics approach is characterised by the exclusion of the dynamic and thermal effects. In particular, the atomistic structure is considered at a temperature of $0\,\mathrm{K}$, where the kinetic energy terms are neglected. The desired static equilibrium configurations of the system are then obtained by a minimisation of the total potential. For a full treatment on this subject see for example Allen and Tildesley [1], Rappé and Casewit [42] and Leach [27]. The approaches of molecular mechanics allow to perform simulations of systems that contain a large amount of atoms at relatively high accuracy compared to the quantum mechanics procedures .

Finally, at the level of continuum mechanics, the discrete atomistic structure of materials is not taken into account and continuous bodies are considered. The constitutive behaviour of the body is generally described by phenomenological macroscopic strain energy densities. See classical text books on continuum mechanics for instance Bonet and Wood [9] or Marsden and Hughes [34] for a detailed treatment. But besides that, the microscopic atomistic structure can be considered by the application of homogenisation approaches. In this context, the quasi-continuum method developed by Tadmor *et al.* [52] and Tadmor *et al.* [53] is very popular. This approach derives the strain energy density function from the underlying lattice and the associated interatomic

potentials by linking the continuum deformation to that of the atomistic structure. In the case of continuum mechanics, the problem is often numerically handled on the basis of the finite element method. Thereby, various finite element types are applied in the studies of carbon nanotubes. As guidance for the concepts of the finite element method, classical text books for example Bathe [7], Zienkiewicz and Taylor [64, 65] and Wriggers [61] can be recommended. The main disadvantages of the continuum mechanics approaches is the fact that local effects at the level of atoms cannot be modelled. However, they allow the simulation of very large systems and offer remarkable agreement to molecular mechanics approaches for moderate local deformations.

In order to combine the advantages of these methods and to overcome their individual limitations, several multi-scale approaches were developed. These approaches for instance use a continuum mechanics model in all regions with smooth deformation and a molecular mechanics method or even a quantum mechanics procedure in a small subset where the behaviour at the atomistic level is essential. Consequently, the investigated systems can be quite large so that they would not be accessible for a isolated full atomistic simulation. An overview of multi-scale approaches can for instance be found in Liu *et al.* [32] with a focus on their application in nanotechnology.

Of special interest within the experimental and numerical studies is the structural stability of carbon nanotubes and consequently, their buckling behaviour under different loading scenarios. By collecting the works of several researchers, Wang *et al.* [59], Wang *et al.* [58] and Shima [46] provide a literature survey that gives a review of the progress in the buckling analysis of carbon nanotubes. To get insight into this interesting behaviour of carbon nanotubes simulations using different approaches based on various length scales were performed.

With the help of molecular dynamics, Yakobson *et al.* [62] investigated the buckling behaviour of single-walled carbon nanotubes. Iijima *et al.* [26] realised experimental studies on bent carbon nanotubes and performed comparative atomistic simulations. Using molecular mechanics, Cao and Chen [12] as well as Mylvaganam *et al.* [36] investigated single-walled carbon nanotubes upon bending. Simulations on the basis of molecular statics were performed by Guo *et al.* [23] for the buckling analysis of bent single-walled carbon nanotubes. The buckling of multi-walled carbon nanotubes under axial compression was studied by Sears and Batra [45] using molecular dynamics. Applying molecular statics, Liu *et al.* [30] and Leung *et al.* [29] investigated carbon nanotubes under axial compression. Wackerfuß [56] used a molecular statics approach for the buckling analysis of single-walled carbon nanotubes under axial compression and torsion. These molecular mechanics approaches consider the entire multi-particle system of the carbon nanotube and are therefore able to model local features at the atomic order of magnitude. However, as each atom has to be considered, the feasible size of the investigated carbon nanotubes is limited.

In addition to these molecular mechanics approaches, a good deal of work was spent in the development of continuum mechanics based simulation methods for nanotubes. These approaches mostly use different thin shell formulations. Based on phenomenological macroscopic constitutive models the buckling of carbon nanotubes was studied by Yakobson *et al.* [62] and Ru [44] using linear elasticity and by Pantano *et al.* [39] and Pantano *et al.* [40] applying non-linear elasticity. To avoid the parameter fitting for these models and the uncertain definition of a shell thickness other approaches based on the quasi-continuum method, given in Tadmor *et al.* [52] and Tadmor *et al.* [53], were introduced. These approaches use the Cauchy-Born rule to link the atomistic level to the deformation of the continuum. Arroyo [2] and Arroyo and Belytschko [3, 4, 5, 6] extended the classical Cauchy-Born rule for an application to single layer crystalline films and analysed the buckling behaviour of carbon nanotubes. A different extension, denoted as higher order Cauchy-Born rule, was proposed by Leamy *et al.* [28]. The concept of the higher order Cauchy-Born rule was applied by Guo *et al.* [24] and by Sun and Liew [49, 50] for analysing the buckling behaviour of carbon nanotubes. The simulation methods based on continuum mechanics use the standard finite element formulation and the framework behind. This allows the construction of a discrete

system of unknowns independent from the number of atoms in the analysed structure. Of course these approaches cannot capture all the local properties of the atomistic model but they are more efficient with respect to computational aspects in the simulation of large carbon nanotubes.

All these scientific observations on the buckling behaviour of carbon nanotubes provide enough motivation for an entrance into this astonishing subject. In particular, the interest lies on a numerical investigation into the structural stability analysis of carbon nanotubes under different loading conditions. Moreover, the direct comparison of independent simulations on the basis of molecular mechanics and continuum mechanics approaches is desirable.

1.2 Outline of the work

The thesis presents a study on the buckling analysis of carbon nanotubes. In particular, it applies a molecular statics approach and a mixed atomistic-continuum model. Both approaches are used side by side such that the obtained results can be compared. Furthermore, this allows the clarification of the associated advantages and limitations. With regard to molecular statics, a special formulation is applied that allows the integration of atomistic simulations into a framework on the basis of the finite element formalism. In doing so, the implementation utilises the design configuration proposed by Wackerfuß [56]. The mixed atomistic-continuum model stems from the quasi-continuum approach given in Tadmor *et al.* [52] and Tadmor *et al.* [53] and is mainly based on the thesis of Arroyo [2] and the related papers of Arroyo and Belytschko [3, 4, 5, 6]. The numerical treatment of this model is performed by means of the finite element method. Therefore, both approaches, the molecular statics approach and the mixed atomistic-continuum model, can be integrated into a single stand-alone computational framework. Consequently, the essential algorithms with regard to the entire structural stability analysis are shared among them.

- **Molecular statics approach**

  For the application of molecular statics, the definition of the total potential energy of the discrete carbon nanotube structure is crucial. This energy consists of the contributions of the bonded potential, the non-bonded potential and the potential of the external loads. In the course of this, the bonded energy is widely modelled by the interatomic Tersoff-Brenner potential proposed by Brenner [11] on the basis of the bond-order formalism of Tersoff [54]. However, this short-range interatomic potential does not take into consideration the van der Waals interactions. Therefore, these long-range interactions have to be considered independently by an additional non-bonded energy. For that purpose, the Lennard-Jones '6-12' interatomic potential, as inspected by Girifalco *et al.* [22], is applied in many studies on non-bonded interactions. Especially in the simulation of multi-walled carbon nanotubes, it is common to model non-bonded interactions across the distinct layers. Simulations related to this topic can for instance be found in Pantano *et al.* [39], Pantano *et al.* [40], Arroyo and Belytschko [5, 6] and Qian *et al.* [41] as well as the references therein. The inclusion of this type of non-bonded reaction is evident from the fact that these interactions are responsible for the relative alignment of the individual walls and, therefore, affect the behaviour of the loaded carbon nanotubes. In particular, in the case of buckled multi-walled carbon nanotubes, these so-called inter-layer non-bonded interactions prevent the tube from penetration of different walls. In addition, non-bonded interactions have to be considered also within one layer of multi-walled carbon nanotubes and in single-walled carbon nanotubes. The treatment of these in-layer non-bonded interactions is based on a usual convention of molecular mechanics. This convention implies that pairs of atoms, which are not linked directly by the short-range bonded interatomic potential, should be considered separately by long-range van der Waals interactions. Nonetheless, the in-layer non-bonded interactions are sparsely incorporated in the simulations of carbon nanotubes. In this context, Chen *et al.* [15] and Cheng *et al.* [16] investigated the influence of in-layer non-bonded interactions on the mechanical properties of single-walled carbon nanotubes. In another telling example, Arroyo and Belytschko

[4, 5, 6] considered the in-layer non-bonded interactions in the simulation of a twisted single-walled carbon nanotube that folded onto itself. Recapitulating, the in-layer non-bonded interactions are essential to prevent single-walled carbon nanotubes and individual layers of multi-walled carbon nanotubes from self-intersection. Particularly in the stability analysis of carbon nanotubes, the in-layer non-bonded interactions affect the behaviour of the buckled structure. In order to integrate the molecular statics into a computational framework, using the formalism of the finite element method, two different approaches have been developed. These notations consider the atomistic structure and the dedicated interatomic potentials for the definition of finite element equivalents. The first one is known as bond-related finite element and models the interactions of the bond-wise interatomic potential directly or by replacing the individual terms by different springs. Elements of this type can for instance be found in Nasdala and Ernst [37] or Zhang [63]. The second type is the atom-related finite element, which relies on a reference atom and the neighbourhood of atoms within the interaction range of the interatomic potential. Liu *et al.* [30] proposed the so-called atomic-scale finite element method (AFEM), which is valid for various interatomic potentials and applicable for multi-scale simulations. This method was successfully applied to the buckling analysis of carbon nanotubes in the papers of Liu *et al.* [30], Liu *et al.* [31] and Leung *et al.* [29]. Another finite element of this formulation was developed by Wackerfuß [56] in a universal manner and numerical simulations of carbon nanotubes with different interatomic potentials were performed. The use of the atom-related finite element methods ends up in the same equilibrium equations that are achieved by classical molecular statics approaches and are therefore exact in that sense. That is because the appendant equilibrium configurations of the atomistic structure are characterised by the state of minimal potential energy. Consequently, solution methods based on the first-order derivative of the total potential energy with respect to the degrees of freedom are commonly employed in molecular statics. For this reason, conjugate gradient methods, quasi-Newton methods as well as the steepest descent method are often applied in the numerical treatment of the direct minimisation problem. Alternatively, the non-linear equilibrium equations can be solved using the Newton-Raphson approach. A summary of these minimisation algorithms is for example given in Rappé and Casewit [42] and Leach [27]. In the case of the Newton-Raphson approach, the first-order and second-order derivatives of the total potential energy with respect to the degrees of freedom are essential. These expressions are related to the global residuum vector and the global stiffness matrix of the non-linear finite element method. The formulation of an atom-related finite element allows to assemble these global quantities in an efficient way directly from elemental contributions. Thus, the atom-related finite element permits to take advantage of assemblage algorithms and solution methods that are implemented in non-linear finite element frameworks. In particular, as examined by Liu *et al.* [30], the application of the Newton-Raphson procedure for solving the non-linear system of equilibrium equations is beneficial. Additionally, the availability of the global stiffness matrix enables the investigation of the structural stability of equilibrium states. Thus, the implementation of the atom-related finite element into the classical non-linear finite element framework provides an effective method for the buckling analysis of carbon nanotubes based on molecular statics. Following this thoughts, the thesis applies the atom-related finite element proposed by Wackerfuß [56] in the structural stability analysis of carbon nanotubes. In particular, the corresponding finite element patch is set up for the interatomic Tersoff-Brenner potential in order to model bonded interactions. In addition, the important influence of modelling non-bonded interactions is analysed. For this task, the distinction into in-layer and inter-layer non-bonded interactions is carried out. In doing so, particularly, the modelling of in-layer non-bonded interactions is discussed. For the implementation of both types of non-bonded interactions, an appendant non-linear finite spring element is used. Furthermore, a complete linearisation of the necessary atomistic kinematics and the interatomic potentials is given. The stability analysis is accomplished by means of an accompanying eigenvalue analysis of the global stiffness matrix and the critical point is detected using a bisection algorithm. The corresponding buckled configurations are

obtained with the help of a branch switching algorithm. The buckling is analysed on single-walled and double-walled carbon nanotubes under different loading conditions. Within these simulations, special focus is spent on the importance of the different types of non-bonded interactions on the morphology of the buckled tubes.

- **Mixed atomistic-continuum model**

  In the mixed atomistic-continuum model, the discrete multi-particle structure of the carbon nanotube is replaced by an appropriate continuum. Furthermore, the constitutive behaviour of the continuum is obtained from the underlying lattice by a homogenisation process. For this purpose, the quasi-continuum method as given in Tadmor *et al.* [52] and Tadmor *et al.* [53] is applied. In particular, this method defines a strain energy density for the continuum on the basis of a reference cell and the interatomic potentials of the associated underlying atomistic structure. For this purpose, the linkage of the atomistic deformation of lattice vectors to that of the continuum is required. In the case of space-filling crystals and homogeneous deformations on the atomic level, this correlation is defined by the classical Cauchy-Born rule as given in Born and Huang [10]. The natural replacement of single-layer crystalline films, such as graphene and individual layers of carbon nanotubes, would be a free formed continuum surface. However, as pointed out by Arroyo [2] and Arroyo and Belytschko [3], the direct application of the classical Cauchy-Born for that type of continuum is not expedient. Consequently, they proposed an extension to the standard Cauchy-Born rule rendering its application to single-layer crystalline films possible. This so-called exponential Cauchy-Born rule allows the modelling of monolayer crystals as free formed continuum surfaces without thickness. Additionally, in their works, a local approximation scheme for that extension relying on the principal curvatures of the considered continuum surface is provided. This idea of the exponential Cauchy-Born rule is incorporated and another approach for its local approximation on the basis of the normal curvature is presented. With the help of the exponential Cauchy-Born rule and its local approximations, the strain energy density for bonded interactions can be integrated into the constitutive model of the continuous replacement of the carbon nanotube. The non-bonded interactions are separately integrated into the constitutive model on the basis of a strain energy double density. In the course of this, in-layer and inter-layer non-bonded interactions are considered. Subsequently, the constitutive model can be used in conjunction with possible external contributions for the definition of a total potential of the continuum surface. This total potential is the basis for the specification of equilibrium configurations. Moreover, it allows to give a criterion for the structural stability of these configurations. For a numerical treatment, the continuous setting is efficiently approximated by the finite element method. This allows to create a discretisation of the continuum model that is independent of the underlying atomistic structure. Consequently, not every single atom has to be tracked and larger systems in comparison to a molecular statics approach can be observed. In a series of numerical studies, Arroyo [2] and Arroyo and Belytschko [3, 4, 5, 6] applied a model of that kind successfully in the buckling analysis of carbon nanotubes. Thereby, finite elements on the basis of subdivision surfaces, as introduced by Cirak *et al.* [18], are applied. In addition, equilibrium configurations of the system are obtained by a direct minimisation of the discretised total potential. Consequently, only the gradients of the total energy with respect to the nodal degrees of freedom are necessary. The studies demonstrate the accuracy of the discretised continuum model by a comparison with full atomistic simulations. On the basis of these publications, the thesis applies a mixed atomistic-continuum model in the structural stability analysis of carbon nanotubes. In particular, the continuous replacement of the carbon nanotube is given by a free formed surface without thickness. Furthermore, the linkage of the continuum deformation to the deformation of the atomistic structure is realised by the exponential Cauchy-Born rule. In doing so, two local approximation schemes are used. The first approach is specified on the basis of the principal curvatures of the surface whereas the second method relies on the normal curvature of the continuum surface. These two approaches are compared against each other by means of numerical simulations. In these numerical simulations, the continuum

surface is discretised by triangular and quadrilateral subdivision finite elements. Equilibrium configurations of the discrete setting are obtained either by a standard Newton-Raphson procedure or by an arc-length method. The detection of instability points is accomplished by an accompanying eigenvalue analysis of the global stiffness matrix in combination with a bisection algorithm. Moreover, a branch switching algorithm allows to reach the corresponding buckled configurations and to follow secondary branches. In order to make these procedures possible, a complete linearisation of the mixed atomistic-continuum model is provided. The buckling behaviour is numerically analysed for different carbon nanotubes under various loading scenarios. In this context, the mixed atomistic-continuum model is checked and validated against the results of a molecular statics approach for the full atomistic structure.

The thesis is organised as follows:
Chapter 2 gives a preliminary overview of the structure of carbon nanotubes. In Section 2.1, the bonding structure, and in Section 2.2, the characterisation of carbon nanotubes, are briefly discussed. Section 2.3 describes the modelling of bonded interactions and Section 2.4 is concerned with the modelling of non-bonded interactions. Chapter 3 introduces the applied molecular statics approach. Section 3.1 specifies the governing equations of molecular statics and in Section 3.2, the structural stability of the associated equilibrium configurations is discussed. The necessary atomistic kinematics with its essential derivatives is the topic in Section 3.3. In Section 3.4, the incorporation of the molecular statics into the finite element framework is presented. This includes the introduction of the atom-related finite element for bonded interactions and the non-linear finite spring element for non-bonded interactions. In Section 3.5, the entire algorithm is applied to the buckling analysis of various carbon nanotubes under different loading scenarios. A summary, in Section 3.6, closes the chapter on molecular statics. Chapter 4 specifies the mixed atomistic-continuum model. A brief overview of the continuum kinematics in Section 4.1, and the standard Cauchy-Born rule in Section 4.2, discusses the space-filling body. In Section 4.3, the kinematics for the continuum surface is presented and, subsequently, Section 4.4 discusses the associated extended Cauchy-Born rules for this solid of reduced dimensionality. Section 4.5 develops the constitutive model for the mixed atomistic-continuum approach. In Section 4.6, the global equilibrium of the carbon nanotube is formulated and in Section 4.7, the associated criterion for structural stability is presented. The numerical treatment of the mixed atomistic-continuum model using the finite element method is highlighted in Section 4.8. Section 4.9 shows the performance of the realised model by means of selected numerical examples on the buckling analysis of carbon nanotubes. The summary, in Section 4.10, completes the chapter on the mixed atomistic-continuum model. A final summary of the numerical studies and concluding remarks appear in Chapter 5. In addition, Appendix A gives supplementary notes concerning the variation and the further linearisation of the mixed atomistic-continuum model. Moreover, the shape functions for finite elements on the basis of subdivision surfaces are described. Finally, the Bibliography completes the thesis.

2 Structure of carbon nanotubes

In this chapter, an introduction to the structure of carbon nanotubes is given. Thereby, on the basis of the graphene sheet, the bonding mechanism of the involved carbon atoms is briefly discussed. Furthermore, the characterisation scheme for the various possible types of carbon nanotubes is given. In doing so, the linkage between the flat graphene and carbon nanotubes is examined. A more advanced treatment on this subject can for instance be found in O'Connell [38], Qian et al. [41] and Dresselhaus et al. [21]. Thereafter, the modelling of bonded interactions by means of interatomic potentials is discussed. In particular, the associated first-order and second-order derivatives with respect to the relevant interatomic measurements are specified. Finally, the modelling of non-bonded interactions, with the important distinction between in-layer and inter-layer non-bonded interactions is described. See classical text books concerned with atomistic simulations, for example Allen and Tildesley [1], Rappé and Casewit [42] and Leach [27] for a detailed discussion on atom interactions and interatomic potentials.

2.1 Bonding structure

Carbon nanotubes are an allotrope of carbon and can be considered as the result of rolling up a graphene sheet. Consequently, the bonding structure between the carbon atoms in nanotubes is related to that of graphene. The graphene sheet as well is an allotrope of carbon and exhibits a planar honeycomb structure. In the course of this, each carbon atom forms three strong covalent bonds with neighbouring carbon atoms. These so-called σ-bonds are separated by an angle of $120°$ and lie within a plane. In addition, the remaining electrons form so-called π-bonds and the related electron cloud of these weak bonds is distributed perpendicular to the plane of the strong σ-bonds. The delocalised out-of-plane π-bonds interact with the π-bonds on the neighbouring layers. In this work, the strong σ-bond formed between two carbon atoms is denoted as "bonded interaction". Additionally, the weaker long-range interaction among different π-bonds is identified as "non-bonded interaction". Moreover, the studies in this work disregard bond breaking and bond rearrangement within the carbon nanotube.

2.2 Characterisation

In the characterisation of carbon nanotubes a distinction is made between single-walled and multi-walled types. Thereby, a single-walled carbon nanotube (SWCNT) can be imagined as the result of rolling up a graphene sheet into cylindrical shape. Following this, multi-walled carbon nanotubes (MWCNT) can be presented as several concentrically rolled graphene sheets. Consequently, the structure of each layer is described by the way of rolling the individual graphene sheets. For that purpose, an integer pair (n_1, n_2) combined with the base vectors $\mathbf{B}_1$ and $\mathbf{B}_2$ of the two-dimensional graphene honeycomb lattice are essential. Based on the illustration in Figure 2.1, these quantities are used to define a chiral vector $\mathbf{C}_{\mathrm{h}}$.

$$\mathbf{C}_{\mathrm{h}} = n_1 \mathbf{B}_1 + n_2 \mathbf{B}_2 \tag{2.1}$$

This vector specifies the circumferential direction of the tube so that after rolling its two end carbon atoms coincide. Furthermore, the circumference of the rolled cylinder is given by the length C_{h} of the chiral vector.

$$C_{\mathrm{h}} = \|\mathbf{C}_{\mathrm{h}}\| = \sqrt{\mathbf{C}_{\mathrm{h}} \cdot \mathbf{C}_{\mathrm{h}}} = A_0 \sqrt{3 \left(n_1^2 + n_1 n_2 + n_2^2\right)} \tag{2.2}$$
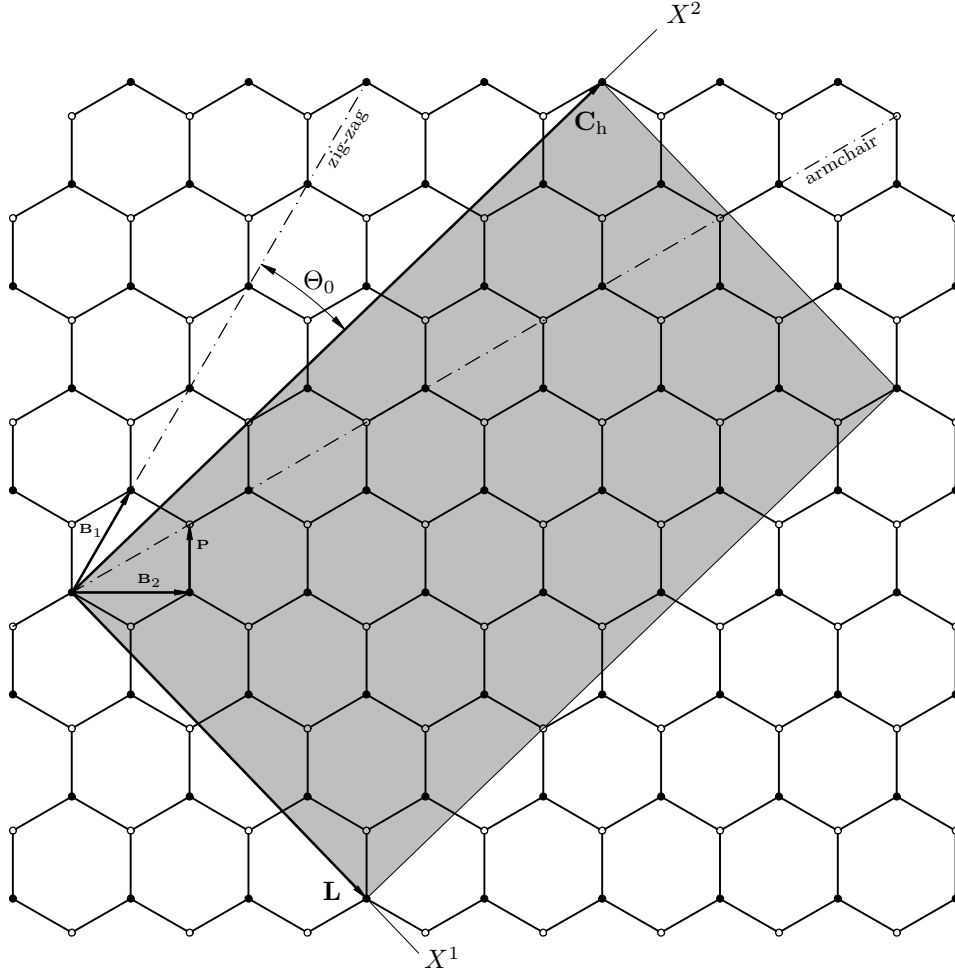
Figure 2.1: Illustration of the chiral vector $\mathbf{C}_h$ defining the rolling direction of the graphene sheet in order to obtain a carbon nanotube layer. The chiral angle Θ_0 and the directions for the zig-zag and armchair carbon nanotubes are indicated. The base vectors $\mathbf{B}_1$ and $\mathbf{B}_2$ of the graphene sheet are specified. The shift vector $\mathbf{P}$ links the two simple triangular sublattices that are depicted by black and white dots.

Consequently, the circumference is solely defined by the chirality (n_1, n_2) of the tube and the carbon-carbon distance A_0 within the graphene sheet. Subsequently, the radius R_0 of the carbon nanotube can be evaluated.

$$R_0 = \frac{C_h}{2\pi} = \frac{A_0}{2\pi}\sqrt{3\left(n_1^2 + n_1 n_2 + n_2^2\right)} \tag{2.3}$$

In addition, the chiral angle Θ_0 is defined as the angle between $\mathbf{C}_h$ and the $\mathbf{B}_1$ direction.

$$\Theta_0 = \arctan\left(\frac{\sqrt{3}n_2}{2n_1 + n_2}\right) \tag{2.4}$$

The characterisation of carbon nanotube layers using the chirality (n_1, n_2) includes two specific types of carbon nanotubes. Thereby, the so-called zig-zag carbon nanotube is characterised by $(n_1, 0)$ or equivalently $\Theta_0 = 0$. Furthermore, two identical integers of the chirality define an armchair carbon nanotube by (n_1, n_1) and an related chiral angle of $\Theta_0 = 30°$. In Figure 2.1,

the corresponding zig-zag and armchair directions are indicated. The various types enclosed by these two special cases are called chiral carbon nanotubes. In the case of multi-walled carbon nanotubes, each individual layer is characterised by its related chirality. Thus, the structure of carbon nanotubes is uniquely defined by the chirality (n_1, n_2). In addition, the vector $\mathbf{L}$ is introduced on the graphene sheet, perpendicular to the chiral vector, in order to specify the length L_0 of the carbon nanotube.

$$L_0 = \|\mathbf{L}\| = \sqrt{\mathbf{L} \cdot \mathbf{L}} \tag{2.5}$$

For the purpose of defining the mapping from the flat graphene sheet to the cylindrical carbon nanotube, the Cartesian coordinates $\left\{X^1, X^2\right\}$ are introduced. Thereby, the X^1 direction is given by the vector $\mathbf{L}$ and the X^2 direction is specified by the chiral vector $\mathbf{C}_\mathrm{h}$. Furthermore, because the hexagonal structure of the graphene sheet is a Bravais 2-lattice, an additional shift vector $\mathbf{P}$ is necessary to spot every carbon atom. Therefore, as illustrated in Figure 2.1, the entire lattice can be viewed as a set of two simple triangular sublattices indicated by black and white dots. Then, the position vectors of all carbon atoms are given by $\mathbf{X}_n = n^1 \mathbf{B}_1 + n^2 \mathbf{B}_2 + m\mathbf{P}$. In this expression n^1 and n^2 are integers whereas, depending on the desired lattice side, m is either zero or one. Subsequently, the Cartesian coordinates $\left\{x^1, x^2, x^3\right\}$ define the rolled configuration of the graphene. Thus, the position vector $\mathbf{x}_n$ of each atom in the carbon nanotube is determined by the related roll-up mapping as:

$$
\begin{aligned}
x_n^1 &= X_n^1 \\
x_n^2 &= R_0 \sin\left(\frac{X_n^2}{R_0}\right) \\
x_n^3 &= -R_0 \cos\left(\frac{X_n^2}{R_0}\right)
\end{aligned}
\tag{2.6}
$$

The handling of multi-walled carbon nanotubes requires the realisation of this mapping for each of the individual layers. In the roll-up procedure from the graphene sheet to the carbon nanotube the bond lengths and the bond angles change. Additionally, in multi-walled carbon nanotubes, the interlayer interactions may not be balanced. The resulting carbon nanotube is therefore geometrically compatible but the structure is not in an equilibrium state. Consequently, the carbon atoms will rearrange in order to reach their equilibrated positions.

2.3 Modelling of bonded interactions

The modelling of bonded interactions in carbon nanotube simulations is often done by means of the so-called Tersoff-Brenner bond-order potential, proposed by Brenner [11] on the basis of the bond-order formalism given by Tersoff [54]. This interatomic potential delivers an analytic potential energy expression capturing the essential chemistry and physics, which can be used for molecular mechanics simulations. Furthermore, the definition of the constitutive model within a mixed atomistic-continuum method is often based on interatomic potentials.

2.3.1 The Tersoff-Brenner interatomic bond-order potential

Within this potential, the energy E_{ij} of a single bond ij between two carbon atoms i and j, as illustrated in Figure 2.2, is described by its bond length a_{ij} and the lengths of neighbouring bonds a_{ik}, a_{il}, a_{jm} and a_{jn} as well as the angles θ_{ijk}, θ_{ijl}, θ_{jim} and θ_{jin} formed with those. The total bonded energy of the structure can then be calculated by the sum over all bonds.

$$\pi_\mathrm{b} = \sum_{ij} E_{ij} = \sum_i \sum_{j>i} E_{ij} \tag{2.7}$$
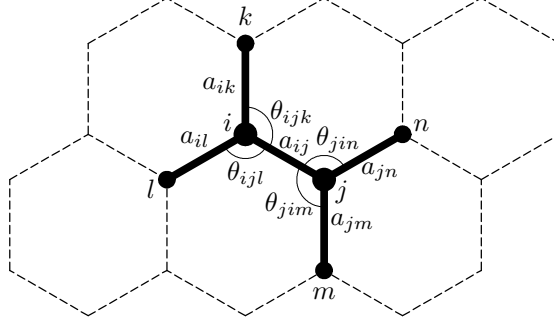
Figure 2.2: Structure of the Tersoff-Brenner bond-order potential for a single carbon-carbon bond with all kinematic measurements essential for energy evaluation.

The expression for the bond-wise energy is given by:

$$E_{ij} = V_{\mathrm{R}}\left(a_{ij}\right) - \bar{B}_{ij}\left(a_{ik}, a_{il}, \theta_{ijk}, \theta_{ijl}; a_{jm}, a_{jn}, \theta_{jim}, \theta_{jin}\right) V_{\mathrm{A}}\left(a_{ij}\right) \tag{2.8}$$

Herein, $V_{\mathrm{R}}(a_{ij})$ represents the repulsive part of the interaction whereas $V_{\mathrm{A}}(a_{ij})$ describes the analogous attractive part.

$$V_{\mathrm{R}}(a_{ij}) = \frac{D^{(\mathrm{e})}}{S - 1} \cdot e^{-\sqrt{2 \cdot S} \cdot \beta \cdot \left(a_{ij} - R^{(\mathrm{e})}\right)} \cdot f_{\mathrm{c}}(a_{ij}) \tag{2.9}$$

$$V_{\mathrm{A}}(a_{ij}) = \frac{D^{(\mathrm{e})} \cdot S}{S - 1} \cdot e^{-\sqrt{\frac{2}{S}} \cdot \beta \cdot \left(a_{ij} - R^{(\mathrm{e})}\right)} \cdot f_{\mathrm{c}}(a_{ij}) \tag{2.10}$$

The term $\bar{B}_{ij}\left(a_{ik}, a_{il}, \theta_{ijk}, \theta_{ijl}; a_{jm}, a_{jn}, \theta_{jim}, \theta_{jin}\right)$ represents the multi-body coupling between the bond from i to j and the local environments of both atoms. It is also known as empirical bond-order function given by the average of the terms associated with each atom in the bond.

$$\bar{B}_{ij}\left(a_{ik}, a_{il}, \theta_{ijk}, \theta_{ijl}; a_{jm}, a_{jn}, \theta_{jim}, \theta_{jin}\right) = \frac{1}{2}\left[B_{ij}\left(a_{ik}, a_{il}, \theta_{ijk}, \theta_{ijl}\right) + B_{ji}\left(a_{jm}, a_{jn}, \theta_{jim}, \theta_{jin}\right)\right] \tag{2.11}$$

$$B_{ij}\left(a_{ik}, a_{il}, \theta_{ijk}, \theta_{ijl}\right) = \left[1 + G(\theta_{ijk}) \cdot f_{\mathrm{c}}(a_{ik}) + G(\theta_{ijl}) \cdot f_{\mathrm{c}}(a_{il})\right]^{-\delta} \tag{2.12}$$

$$B_{ji}\left(a_{jm}, a_{jn}, \theta_{jim}, \theta_{jin}\right) = \left[1 + G(\theta_{jim}) \cdot f_{\mathrm{c}}(a_{jm}) + G(\theta_{jin}) \cdot f_{\mathrm{c}}(a_{jn})\right]^{-\delta} \tag{2.13}$$

So, each of these many-body coupling terms depends on two bond lengths and two valence angles. With the bond angle function

$$G(\theta) = a_0 \cdot \left[1 + \frac{c_0{}^2}{d_0{}^2} - \frac{c_0{}^2}{d_0{}^2 + \left[1 + \cos(\theta)\right]^2}\right] \tag{2.14}$$

and the cut-off function

$$f_{\mathrm{c}}(a) = \begin{cases} 1 & a < R^{(1)} \\ \frac{1}{2} \cdot \left\{1 + \cos\left[\frac{\pi\left(a - R^{(1)}\right)}{R^{(2)} - R^{(1)}}\right]\right\} & R^{(1)} \le a \le R^{(2)} \\ 0 & a > R^{(2)} \end{cases} \tag{2.15}$$

the bond-wise energy can be calculated. The parameters for the interatomic potential are taken from the second parameter set of Brenner [11].

$$
\begin{aligned}
&D^{(e)} = 6.000 \,\text{eV} \ , \ S = 1.22 \ , \ \beta = 21 \,\text{nm}^{-1} \\
&R^{(e)} = 0.1390 \,\text{nm} \\
&R^{(1)} = 0.17 \,\text{nm} \ , \ R^{(2)} = 0.20 \,\text{nm} \\
&\delta = 0.50000 \\
&a_0 = 0.00020813 \ , \ c_0 = 330 \ , \ d_0 = 3.5
\end{aligned}
\tag{2.16}
$$

These values are applied in all numerical simulations, using either the molecular statics approach in Section 3.5 or the mixed atomistic-continuum model in Section 4.9. The first-order and second-order derivatives with respect to the bond lengths and valence angles of the essential sub-functions building the bond-wise energy are given in the following.

- Repulsive interactions function $V_{\text{R}}(a)$

$$
\begin{aligned}
V_{\text{R}}'(a) = &- \sqrt{2 \cdot S} \cdot \beta \cdot \frac{D^{(e)}}{S-1} \cdot e^{-\sqrt{2 \cdot S} \cdot \beta \cdot \left(a - R^{(e)}\right)} \cdot f_{\text{c}}(a) \\
&+ \frac{D^{(e)}}{S-1} \cdot e^{-\sqrt{2 \cdot S} \cdot \beta \cdot \left(a - R^{(e)}\right)} \cdot f_{\text{c}}{}'(a)
\end{aligned}
\tag{2.17}
$$

$$
\begin{aligned}
V_{\text{R}}''(a) = &\left(-\sqrt{2 \cdot S} \cdot \beta\right)^2 \cdot \frac{D^{(e)}}{S-1} \cdot e^{-\sqrt{2 \cdot S} \cdot \beta \cdot \left(a - R^{(e)}\right)} \cdot f_{\text{c}}(a) \\
&- 2\sqrt{2 \cdot S} \cdot \beta \cdot \frac{D^{(e)}}{S-1} \cdot e^{-\sqrt{2 \cdot S} \cdot \beta \cdot \left(a - R^{(e)}\right)} \cdot f_{\text{c}}{}'(a) \\
&+ \frac{D^{(e)}}{S-1} \cdot e^{-\sqrt{2 \cdot S} \cdot \beta \cdot \left(a - R^{(e)}\right)} \cdot f_{\text{c}}{}''(a)
\end{aligned}
\tag{2.18}
$$

- Attractive interactions function $V_{\text{A}}(a)$

$$
\begin{aligned}
V_{\text{A}}'(a) = &- \sqrt{\frac{2}{S}} \cdot \beta \cdot \frac{D^{(e)} \cdot S}{S-1} \cdot e^{-\sqrt{\frac{2}{S}} \cdot \beta \cdot \left(a - R^{(e)}\right)} \cdot f_{\text{c}}(a) \\
&+ \frac{D^{(e)} \cdot S}{S-1} \cdot e^{-\sqrt{\frac{2}{S}} \cdot \beta \cdot \left(a - R^{(e)}\right)} \cdot f_{\text{c}}{}'(a)
\end{aligned}
\tag{2.19}
$$

$$
\begin{aligned}
V_{\text{A}}''(a) = &\left(-\sqrt{\frac{2}{S}} \cdot \beta\right)^2 \cdot \frac{D^{(e)} \cdot S}{S-1} \cdot e^{-\sqrt{\frac{2}{S}} \cdot \beta \cdot \left(a - R^{(e)}\right)} \cdot f_{\text{c}}(a) \\
&- 2\sqrt{\frac{2}{S}} \cdot \beta \cdot \frac{D^{(e)} \cdot S}{S-1} \cdot e^{-\sqrt{\frac{2}{S}} \cdot \beta \cdot \left(a - R^{(e)}\right)} \cdot f_{\text{c}}{}'(a) \\
&+ \frac{D^{(e)} \cdot S}{S-1} \cdot e^{-\sqrt{\frac{2}{S}} \cdot \beta \cdot \left(a - R^{(e)}\right)} \cdot f_{\text{c}}{}''(a)
\end{aligned}
\tag{2.20}
$$

- The multi-body coupling term associated with one atom depends on two bond lengths and two valence angles and is, therefore, rewritten in a compact form for the evaluation of the first-order and second-order derivatives. Depending on the considered atom and its local environment, the appropriate lengths and angles have to be inserted.

$$
B\left(a_1, a_2, \theta_1, \theta_2\right) = \left[1 + G(\theta_1) \cdot f_{\text{c}}(a_1) + G(\theta_2) \cdot f_{\text{c}}(a_2)\right]^{-\delta}
\tag{2.21}
$$

In the following derivatives, i and j are either 1 or 2, and δ_{ij} denotes the Kronecker symbol.

$$\frac{\partial B}{\partial a_i} = -\delta \cdot [1 + G(\theta_1) \cdot f_c(a_1) + G(\theta_2) \cdot f_c(a_2)]^{(-\delta-1)} \cdot G(\theta_i) \cdot f_c{'}(a_i)$$

$$\frac{\partial B}{\partial \theta_i} = -\delta \cdot [1 + G(\theta_1) \cdot f_c(a_1) + G(\theta_2) \cdot f_c(a_2)]^{(-\delta-1)} \cdot G'(\theta_i) \cdot f_c(a_i) \qquad (2.22)$$

$$
\begin{aligned}
\frac{\partial^2 B}{\partial a_i \partial a_j} = &- \delta \cdot (-\delta - 1) \cdot [1 + G(\theta_1) \cdot f_c(a_1) + G(\theta_2) \cdot f_c(a_2)]^{(-\delta-2)} \cdot G(\theta_i) \cdot f_c{'}(a_i) \cdot G(\theta_j) \cdot f_c{'}(a_j) \\
&- \delta \cdot [1 + G(\theta_1) \cdot f_c(a_1) + G(\theta_2) \cdot f_c(a_2)]^{(-\delta-1)} \cdot G(\theta_i) \cdot f_c{''}(a_j) \cdot \delta_{ij} \\
\frac{\partial^2 B}{\partial a_i \partial \theta_j} = &- \delta \cdot (-\delta - 1) \cdot [1 + G(\theta_1) \cdot f_c(a_1) + G(\theta_2) \cdot f_c(a_2)]^{(-\delta-2)} \cdot G(\theta_i) \cdot f_c{'}(a_i) \cdot G'(\theta_j) \cdot f_c(a_j) \\
&- \delta \cdot [1 + G(\theta_1) \cdot f_c(a_1) + G(\theta_2) \cdot f_c(a_2)]^{(-\delta-1)} \cdot G'(\theta_j) \cdot f_c{'}(a_i) \cdot \delta_{ij} \\
\frac{\partial^2 B}{\partial \theta_i \partial a_j} = &- \delta \cdot (-\delta - 1) \cdot [1 + G(\theta_1) \cdot f_c(a_1) + G(\theta_2) \cdot f_c(a_2)]^{(-\delta-2)} \cdot G'(\theta_i) \cdot f_c(a_i) \cdot G(\theta_j) \cdot f_c{'}(a_j) \\
&- \delta \cdot [1 + G(\theta_1) \cdot f_c(a_1) + G(\theta_2) \cdot f_c(a_2)]^{(-\delta-1)} \cdot G'(\theta_i) \cdot f_c{'}(a_j) \cdot \delta_{ij} \\
\frac{\partial^2 B}{\partial \theta_i \partial \theta_j} = &- \delta \cdot (-\delta - 1) \cdot [1 + G(\theta_1) \cdot f_c(a_1) + G(\theta_2) \cdot f_c(a_2)]^{(-\delta-2)} \cdot G'(\theta_i) \cdot f_c(a_i) \cdot G'(\theta_j) \cdot f_c(a_j) \\
&- \delta \cdot [1 + G(\theta_1) \cdot f_c(a_1) + G(\theta_2) \cdot f_c(a_2)]^{(-\delta-1)} \cdot G''(\theta_j) \cdot f_c(a_i) \cdot \delta_{ij} \qquad (2.23)
\end{aligned}
$$

- Bond angle function $G(\theta)$

$$G'(\theta) = \frac{-2 \cdot a_0 \cdot c_0{}^2 \, (1 + \cos(\theta)) \cdot \sin(\theta)}{\left(d_0{}^2 + (1 + \cos(\theta))^2\right)^2} \qquad (2.24)$$

$$G''(\theta) = 2 \cdot a_0 \cdot c_0{}^2 \left\{ \frac{1 - 2 \cdot \cos^2(\theta) - \cos(\theta)}{\left[d_0{}^2 + (1 + \cos(\theta))^2\right]^2} - \frac{4 \cdot (1 + \cos(\theta))^2 \cdot \left(1 - \cos^2(\theta)\right)}{\left[d_0{}^2 + (1 + \cos(\theta))^2\right]^3} \right\} \qquad (2.25)$$

- Cut-off function $f_c(a)$

$$f_c{'}(a) = \begin{cases} 0 & a < R^{(1)} \\ -\frac{1}{2} \cdot \frac{\pi}{R^{(2)} - R^{(1)}} \cdot \sin\left[\frac{\pi\left(a - R^{(1)}\right)}{R^{(2)} - R^{(1)}}\right] & R^{(1)} \le a \le R^{(2)} \\ 0 & a > R^{(2)} \end{cases} \qquad (2.26)$$

$$f_c{''}(a) = \begin{cases} 0 & a < R^{(1)} \\ -\frac{1}{2} \cdot \left[\frac{\pi}{R^{(2)} - R^{(1)}}\right]^2 \cdot \cos\left[\frac{\pi\left(a - R^{(1)}\right)}{R^{(2)} - R^{(1)}}\right] & R^{(1)} \le a \le R^{(2)} \\ 0 & a > R^{(2)} \end{cases} \qquad (2.27)$$

The second-order derivative of the cut-off function is not continuous at the boundaries, where $a = R^{(1)}$ or $a = R^{(2)}$. Because for quadratic convergence of a Newton-Raphson procedure a twice continuously differentiable function is essential, this cut-off function could be replaced by alternative expressions. Nevertheless, this area of bond length is hardly entered and no downsides were recognised in the numerical simulations with the original cut-off function.

2.3.2 The ground state of a graphene sheet

Using the Tersoff-Brenner potential and neglecting non-bonded interactions, the ground state of a flat graphene sheet can be calculated. As a perfect graphene sheet consists of ideal hexagons, all

bond lengths have the same value and all valence angles are the same. Consequently, the valence angle has a value of 120°. In this structure, one carbon atom forms bonds with its three nearest neighbouring atoms and of course one single bond is build by two atoms. As a consequence, the energy per atom in the planar graphene sheet is only a function of the bond length. This function can be seen in Figure 2.3. In this plot, the equilibrium carbon-carbon bond length of $A_0 = 0.14507\,\text{nm}$ and the associated ground state $E_{\text{graphene}} = -7.37563\,\text{eV/atom}$ for the graphene sheet are labelled. The lower and the upper boundaries for the smooth cut-off function are additionally marked.
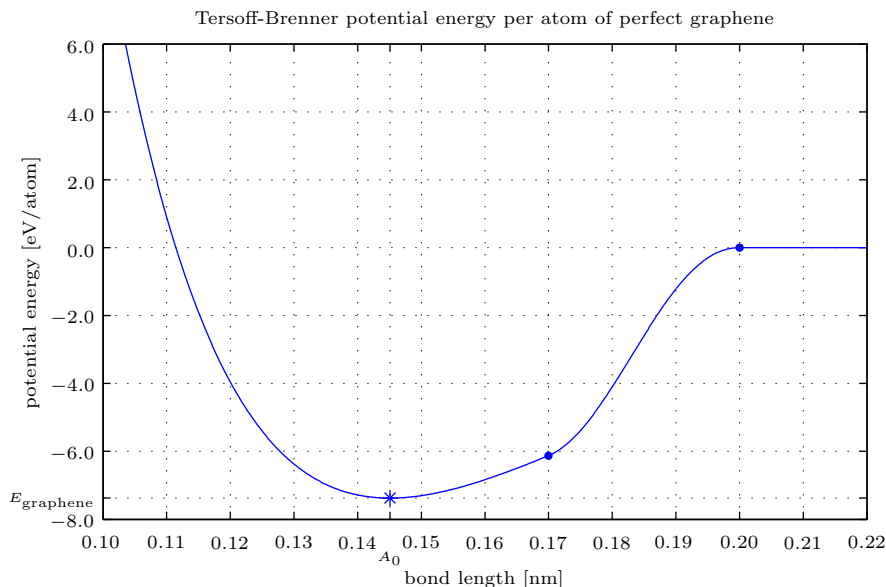
Figure 2.3: The evolution of the Tersoff-Brenner interatomic potential energy per atom in infinite graphene with equal valence angles as a function of the carbon-carbon bond length.

2.4 Modelling of non-bonded interactions

The long-range pair-wise interactions are accounted for in the non-bonded energy. A non-bonded interaction is considered between two atoms of a structure, which are not interacting through covalent bonds. As a consequence, the number of non-bonded pairs in modelling is quite large, and in numerical simulations, an upper cut-off radius is therefore introduced. The non-bonded interactions are modelled by pair-potentials, which depend on the distance a_{ij} between two atoms of the whole structure. The total non-bonded potential π_{nb} of the system is calculated by a sum over all pairs ij of atoms. This expression can further be rewritten by a double sum over all atoms i and j.

$$\pi_{\text{nb}} = \sum_{ij} V_{\text{nb}}\left(a_{ij}\right) = \sum_i \sum_{j > i} V_{\text{nb}}\left(a_{ij}\right)$$

2.4.1 The Lennard-Jones interatomic pair-potential

A commonly used pair potential for the modelling of non-bonded interactions is the Lennard-Jones '6-12' potential. This potential consists of an attractive part and a repulsive part depending on the distance a_{ij} between the two atoms under consideration.

$$V_{\text{nb}}\left(a_{ij}\right) = -\frac{A}{a_{ij}^6} + \frac{B}{a_{ij}^{12}} \tag{2.28}$$

The first-order and second-order derivatives of the Lennard-Jones interatomic pair-potential with respect to the atomic distance read:

$$V'_{\mathrm{nb}}(a_{ij}) = 6\frac{A}{a_{ij}^7} - 12\frac{B}{a_{ij}^{13}} \qquad\qquad V''_{\mathrm{nb}}(a_{ij}) = -42\frac{A}{a_{ij}^8} + 156\frac{B}{a_{ij}^{14}} \qquad (2.29)$$

The constants for the Lennard-Jones '6-12' potential are taken from Girifalco *et al.* [22].

$$
\begin{aligned}
A &= 15.2\,\mathrm{eV\mathring{A}}^6 \\
B &= 24.1 \cdot 10^3 \mathrm{eV\mathring{A}}^{12} \\
\mathring{A} &= 10^{-1}\mathrm{nm}
\end{aligned}
\qquad (2.30)
$$

In the numerical simulations, applying the molecular statics approach in Section 3.5 and the mixed atomistic-continuum model in Section 4.9 these values are used. In Figure 2.4, the evolution of the
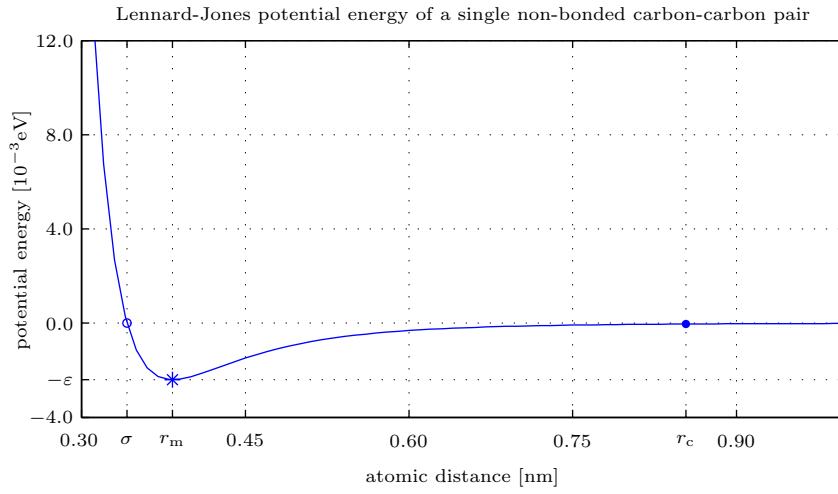
Figure 2.4: The evolution of the Lennard-Jones interatomic potential energy for a single non-bonded carbon-carbon pair as a function of the atomic distance.

Lennard-Jones interatomic pair-potential versus the atomic distance is plotted using the constants given above. In this graph, three interesting points are additionally marked. Thereby, ε is the depth of the potential well and r_{m} is the associated distance at which the minimum $-\varepsilon$ appears. Furthermore, at the atomic distance σ the interatomic potential is zero. The upper cut-off radius for the Lennard-Jones potential is often introduced at a distance $r_{\mathrm{c}} = 2.5\sigma$, in order to reduce the total number of atom-atom interactions. Based on the values of A and B, these constants can be calculated using the correlations:

$$\varepsilon = \frac{A^2}{4B} = 2.39668 \cdot 10^{-3}\,\mathrm{eV} \qquad (2.31)$$

$$\sigma = (B/A)^{1/6} = 0.34148\,\mathrm{nm} \qquad (2.32)$$

$$r_{\mathrm{m}} = 2^{1/6}\sigma = 0.38330\,\mathrm{nm} \qquad (2.33)$$

$$r_{\mathrm{c}} = 2.5\sigma = 0.85369\,\mathrm{nm} \qquad (2.34)$$

The obtained value for the upper cut-off radius serves as guidance for the numerical simulations of carbon nanotubes, using molecular statics in Section 3.5 and the mixed atomistic-continuum model in Section 4.9. By neglecting all non-bonded interactions, exhibiting a distance beyond that barrier, the computational effort of the calculations can be reduced.

2.4.2 The in-layer non-bonded interactions

The modelling of non-bonded interactions within one layer of graphene or one wall of a nanotube needs special attention. On this account, a single atom and its neighbourhood as shown in Figure 2.5, is considered. Within this picture, all covalent bonds that are influenced by the central atom (blank circle) are drawn with a solid black double line. According to Rappé and Casewit [42], the atoms building these bonds (1st and 2nd neighbours or 1-2 and 1-3 interactions) must not be considered when searching for non-bonded interactions of the central atom. In the perfect graphene sheet, these interactions lie inside a circle of radius $A_{\text{1-3}} = \sqrt{3}A_0 = 0.25127\,\text{nm}$ around the central atom. In the derivation of this radius, the honeycomb structure of the lattice and the associated equilibrium carbon-carbon bond length A_0 are considered. All other atoms are in general allowed to build non-bonded pairs with it. The different force fields used in molecular mechanics often scale the 1-4 interactions (3rd neighbours) by a factor of $1/2$ or completely neglect them. When modelling carbon nanotubes, it turns out that these 1-4 interactions lead to high repulsive forces because of small atomic distances. A possibility to overcome this problem is to exclude all atoms forming bonds (solid black lines) with the 2nd neighbours, so that the 1-4 non-bonded interactions are neglected. All these interactions are located in the space of a circle of radius $A_{\text{1-4}} = \sqrt{7}A_0 = 0.38382\,\text{nm}$ around the central atom. In the numerical examples on carbon nanotubes provided in Section 3.5, the results of simulations with and without 1-4 non-bonded interactions are compared based on a molecular statics approach. In order to emphasise that the calculations without 1-4 non-bonded interactions exclude the 1-3 and the 1-2 interactions as well, the phrase up to third neighbours non-bonded interactions excluded is used equivalently. In the same sense, the analysis with the included 1-4 non-bonded interactions is also denoted as up to second neighbours non-bonded interactions excluded. As a consequence of the fast decreasing of the non-bonded interaction described by the Lennard-Jones potential with larger distances, the high number of non-bonded pairs can be reduced by introducing an upper cut-off radius. This means that all pairs of atoms having a distance larger than this specific upper barrier are not considered in the calculation of the non-bonded interactions.
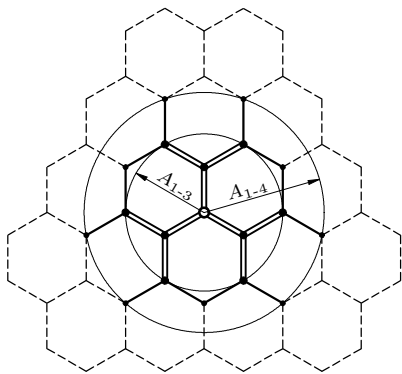
Figure 2.5: Illustration for the valid range of in-layer non-bonded interactions.
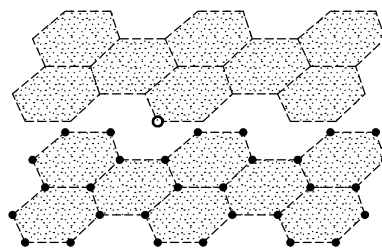
Figure 2.6: Illustration for the range of inter-layer non-bonded interactions.

2.4.3 The inter-layer non-bonded interactions

In contrast to the in-layer interactions, the non-bonded interactions between different layers of graphene or multi-walled nanotubes are not influenced by covalent bonds. This fact is illustrated in Figure 2.6, where an atom of one layer (blank circle) can build non-bonded interactions with all atoms (black dots) of the other layer. Again, an upper cut-off radius is introduced to exclude atomic pairs of large distances from the set of non-bonded interactions.

3 Molecular statics

This chapter provides the important components of a molecular statics approach, in order to study the buckling behaviour of carbon nanotubes at the level of atomistic structures. In the course of this, a special formulation is used, so that the molecular statics model can be integrated into a computational framework on the basis of the classical non-linear finite element formalism of continuum mechanics. This gives the possibility to reuse well established solvers for non-linear systems of equations. In addition, algorithms related to the structural stability analysis are made accessible. In particular, the formulation proposed by Wackerfuß [56] is applied and, consequently, the present derivation partly follows this paper. The chapter is organised as follows: Firstly, the calculation of equilibrium configurations in molecular statics is specified. This is followed by the criterion for structural stability of the atomistic structures. Then, the essential atomistic kinematics are given. Subsequently, the formulation of molecular statics, suitable for an integration into computational frameworks based on the classical finite element formalism, is introduced. Finally, the implemented molecular statics approach is applied to the buckling analysis of carbon nanotubes.

3.1 Equilibrium configurations

In molecular statics, the deformation of an atomistic structure at a temperature of $0\,\mathrm{K}$ is to be considered. This structure of arbitrary shape is composed of a total number of N atoms in interaction with each other. The interactions consider the influence of directly bonded atoms and all pairs of non-bonded atoms. In general, a description within a three-dimensional Euclidean space is used. This allows to state the position of an atom i in the material (Lagrangian) as well as in the spatial (Eulerian) configuration. In the material configuration, specified by the standard basis $\{\mathbf{E}_1, \mathbf{E}_2, \mathbf{E}_3\}$ with Cartesian coordinates $\{X^1, X^2, X^3\}$, the corresponding position vector is denoted by $\mathbf{X}_i$. The vector $\mathbf{x}_i$ in contrast gives the deformed atomic position in the spatial configuration, which is characterised by the standard basis $\{\mathbf{e}_1, \mathbf{e}_2, \mathbf{e}_3\}$ in combination with the Cartesian coordinates $\{x^1, x^2, x^3\}$. Two different atoms i and j in the Eulerian structure feature a distance vector $\mathbf{a}_{ij} = \mathbf{x}_j - \mathbf{x}_i$. This composition in molecular statics is loaded by atom-wise external forces $(\mathbf{f}_{\mathrm{ext}})_i$, which are imposed quasi-statically. Additional displacement boundary conditions are also considered per atom. The total potential energy π of the system now consists of the bonded potential π_{b}, the non-bonded potential π_{nb} and the potential of the external forces π_{ext}.

$$\pi = \pi_{\mathrm{b}} + \pi_{\mathrm{nb}} + \pi_{\mathrm{ext}} \tag{3.1}$$

The potential π_{b}, defining the total energy stored in the atomic bonds, can be defined by so-called interatomic potentials. These interatomic potentials are in general analytic expressions for the properties of the atomic bonds. The interatomic potentials normally have a short-range character, meaning that an atom is only directly influenced by its nearest neighbouring atoms. The characteristics of the energy depend on the bond lengths and bond angles of the structure. These scalar values can directly be calculated by the position vectors of the involved atoms. As a consequence, the bonded potential is a function of the position vectors of all atoms in the structure.

$$\pi_{\mathrm{b}} = \pi_{\mathrm{b}} \left(\mathbf{x}_1, \mathbf{x}_2, \ldots, \mathbf{x}_N \right) \tag{3.2}$$

The non-bonded potential π_{nb} accounts for the interaction of atoms not directly bonded to each other. This van der Waals correlation depends on the distance between the atomic pairs. Therefore,

the non-bonded potential is also a function of the atomic position vectors.

$$\pi_{\text{nb}} = \pi_{\text{nb}} \left(\mathbf{x}_1, \mathbf{x}_2, \dots, \mathbf{x}_N \right) \tag{3.3}$$

The potential of the external forces π_{ext} can be defined on the assumption that the external loads are conservative. Additionally, the external loads are constant so that the related potential can be calculated by the sum of all atom-wise external force contributions. As these external forces are known, the external force potential is a function of the position vectors of the corresponding atoms.

$$\pi_{\text{ext}} = - \sum_{i=1}^{N} \left(\mathbf{f}_{\text{ext}} \right)_i \cdot \mathbf{x}_i = \pi_{\text{ext}} \left(\mathbf{x}_1, \mathbf{x}_2, \dots, \mathbf{x}_N \right) \tag{3.4}$$

Altogether, the total potential of the atomistic structure depends only on the unknown position vectors of its atoms.

$$\pi = \pi \left(\mathbf{x}_1, \mathbf{x}_2, \dots, \mathbf{x}_N \right) \tag{3.5}$$

For a compact writing, the local atomic position vectors $\mathbf{x}_i$ are collected into a global position vector $\mathbf{x}$ and the atom-wise external forces $\left(\mathbf{f}_{\text{ext}} \right)_i$ into a global external force vector $\mathbf{f}_{\text{ext}}$.

$$\mathbf{x} = \begin{bmatrix} \mathbf{x}_1 \\ \mathbf{x}_2 \\ \vdots \\ \mathbf{x}_N \end{bmatrix} \qquad\qquad \mathbf{f}_{\text{ext}} = \begin{bmatrix} \left(\mathbf{f}_{\text{ext}} \right)_1 \\ \left(\mathbf{f}_{\text{ext}} \right)_2 \\ \vdots \\ \left(\mathbf{f}_{\text{ext}} \right)_N \end{bmatrix} \tag{3.6}$$

The equilibrium configuration of the system is characterised by the state of minimal potential energy which is equivalent to the first variation of the total potential being zero. As the position vectors are the only unknowns, this is also equivalent to a discrete minimisation problem.

$$\delta\pi \left(\mathbf{x} \right) = \delta\pi_{\text{b}} \left(\mathbf{x} \right) + \delta\pi_{\text{nb}} \left(\mathbf{x} \right) + \delta\pi_{\text{ext}} \left(\mathbf{x} \right) = 0$$

$$\delta\pi \left(\mathbf{x} \right) = \sum_{i=1}^{N} \left[\frac{\partial\pi_{\text{b}} \left(\mathbf{x} \right)}{\partial\mathbf{x}_i} + \frac{\partial\pi_{\text{nb}} \left(\mathbf{x} \right)}{\partial\mathbf{x}_i} - \left(\mathbf{f}_{\text{ext}} \right)_i \right] \cdot \delta\mathbf{x}_i = 0 \tag{3.7}$$

Taking into account the fact that the virtual displacements $\delta\mathbf{x}_i$ fulfil the displacement constraints but are arbitrary elsewhere, the terms in the bracket give a non-linear system of equations. This system is solved iteratively using the Newton-Raphson approach, thus requiring the linearisation of the varied potential around an initial guess $\tilde{\mathbf{x}}_i$ for the atomic positions.

$$\Delta\delta\pi \left(\tilde{\mathbf{x}} \right) = \Delta\delta\pi_{\text{b}} \left(\tilde{\mathbf{x}} \right) + \Delta\delta\pi_{\text{nb}} \left(\tilde{\mathbf{x}} \right) + \Delta\delta\pi_{\text{ext}} \left(\tilde{\mathbf{x}} \right)$$

$$\Delta\delta\pi \left(\tilde{\mathbf{x}} \right) = \sum_{i=1}^{N} \sum_{j=1}^{N} \left[\frac{\partial^2\pi_{\text{b}} \left(\tilde{\mathbf{x}} \right)}{\partial\tilde{\mathbf{x}}_i \partial\tilde{\mathbf{x}}_j} + \frac{\partial^2\pi_{\text{nb}} \left(\tilde{\mathbf{x}} \right)}{\partial\tilde{\mathbf{x}}_i \partial\tilde{\mathbf{x}}_j} \right] \Delta\tilde{\mathbf{x}}_j \cdot \delta\tilde{\mathbf{x}}_i \tag{3.8}$$

This gives an approximation for the varied potential at the equilibrium state $\mathbf{x}_i$.

$$\delta\pi \left(\mathbf{x} \right) = \delta\pi \left(\tilde{\mathbf{x}} \right) + \Delta\delta\pi \left(\tilde{\mathbf{x}} \right) + \dots = 0$$

$$\delta\pi \left(\mathbf{x} \right) = \sum_{i=1}^{N} \left[\frac{\partial\pi_{\text{b}} \left(\tilde{\mathbf{x}} \right)}{\partial\tilde{\mathbf{x}}_i} + \frac{\partial\pi_{\text{nb}} \left(\tilde{\mathbf{x}} \right)}{\partial\tilde{\mathbf{x}}_i} - \left(\mathbf{f}_{\text{ext}} \right)_i \right] \cdot \delta\tilde{\mathbf{x}}_i + \sum_{i=1}^{N} \sum_{j=1}^{N} \left[\frac{\partial^2\pi_{\text{b}} \left(\tilde{\mathbf{x}} \right)}{\partial\tilde{\mathbf{x}}_i \partial\tilde{\mathbf{x}}_j} + \frac{\partial^2\pi_{\text{nb}} \left(\tilde{\mathbf{x}} \right)}{\partial\tilde{\mathbf{x}}_i \partial\tilde{\mathbf{x}}_j} \right] \Delta\tilde{\mathbf{x}}_j \cdot \delta\tilde{\mathbf{x}}_i = 0$$

$$\delta\pi \left(\mathbf{x} \right) = \sum_{i=1}^{N} \left[\frac{\partial\pi_{\text{b}} \left(\tilde{\mathbf{x}} \right)}{\partial\tilde{\mathbf{x}}_i} + \frac{\partial\pi_{\text{nb}} \left(\tilde{\mathbf{x}} \right)}{\partial\tilde{\mathbf{x}}_i} - \left(\mathbf{f}_{\text{ext}} \right)_i + \sum_{j=1}^{N} \left(\frac{\partial^2\pi_{\text{b}} \left(\tilde{\mathbf{x}} \right)}{\partial\tilde{\mathbf{x}}_i \partial\tilde{\mathbf{x}}_j} + \frac{\partial^2\pi_{\text{nb}} \left(\tilde{\mathbf{x}} \right)}{\partial\tilde{\mathbf{x}}_i \partial\tilde{\mathbf{x}}_j} \right) \Delta\tilde{\mathbf{x}}_j \right] \cdot \delta\tilde{\mathbf{x}}_i = 0 \quad (3.9)$$

Considering the fact that this equation has to be fulfilled for arbitrary virtual displacements $\delta\tilde{\mathbf{x}}_i$, this leads to a linear system of equations to calculate the unknown displacement increments $\Delta\tilde{\mathbf{x}}_j$.

$$\sum_{j=1}^{N} \underbrace{\left[\frac{\partial^2 \pi_{\mathrm{b}}\left(\tilde{\mathbf{x}}\right)}{\partial\tilde{\mathbf{x}}_i\partial\tilde{\mathbf{x}}_j} + \frac{\partial^2 \pi_{\mathrm{nb}}\left(\tilde{\mathbf{x}}\right)}{\partial\tilde{\mathbf{x}}_i\partial\tilde{\mathbf{x}}_j} \right]}_{\mathbf{K}_{ij}(\tilde{\mathbf{x}})} \Delta\tilde{\mathbf{x}}_j = \underbrace{-\frac{\partial \pi_{\mathrm{b}}\left(\tilde{\mathbf{x}}\right)}{\partial\tilde{\mathbf{x}}_i} - \frac{\partial \pi_{\mathrm{nb}}\left(\tilde{\mathbf{x}}\right)}{\partial\tilde{\mathbf{x}}_i}}_{-(\mathbf{f}_{\mathrm{int}})_i(\tilde{\mathbf{x}})} + \left(\mathbf{f}_{\mathrm{ext}}\right)_i \qquad i = 1,\dots,N$$

$$\sum_{j=1}^{N} \mathbf{K}_{ij}\left(\tilde{\mathbf{x}}\right) \Delta\tilde{\mathbf{x}}_j = -\left(\mathbf{f}_{\mathrm{int}}\right)_i\left(\tilde{\mathbf{x}}\right) + \left(\mathbf{f}_{\mathrm{ext}}\right)_i \qquad i = 1,\dots,N \qquad (3.10)$$

With the global stiffness matrix $\mathbf{K}\left(\tilde{\mathbf{x}}\right)$, the global internal force vector $\mathbf{f}_{\mathrm{int}}\left(\tilde{\mathbf{x}}\right)$ and the global external force vector $\mathbf{f}_{\mathrm{ext}}$

$$\mathbf{K}\left(\tilde{\mathbf{x}}\right) = \begin{bmatrix} \mathbf{K}_{11}\left(\tilde{\mathbf{x}}\right) & \cdots & \mathbf{K}_{1N}\left(\tilde{\mathbf{x}}\right) \\ \vdots & \ddots & \vdots \\ \mathbf{K}_{N1}\left(\tilde{\mathbf{x}}\right) & \cdots & \mathbf{K}_{NN}\left(\tilde{\mathbf{x}}\right) \end{bmatrix} \qquad \mathbf{f}_{\mathrm{int}}\left(\tilde{\mathbf{x}}\right) = \begin{bmatrix} \left(\mathbf{f}_{\mathrm{int}}\right)_1\left(\tilde{\mathbf{x}}\right) \\ \vdots \\ \left(\mathbf{f}_{\mathrm{int}}\right)_N\left(\tilde{\mathbf{x}}\right) \end{bmatrix} \qquad \mathbf{f}_{\mathrm{ext}} = \begin{bmatrix} \left(\mathbf{f}_{\mathrm{ext}}\right)_1 \\ \vdots \\ \left(\mathbf{f}_{\mathrm{ext}}\right)_N \end{bmatrix} \qquad (3.11)$$

the linear system of equations can be written as

$$\mathbf{K}\left(\tilde{\mathbf{x}}\right) \Delta\tilde{\mathbf{x}} = -\mathbf{f}_{\mathrm{int}}\left(\tilde{\mathbf{x}}\right) + \mathbf{f}_{\mathrm{ext}} \qquad (3.12)$$

where

$$\Delta\tilde{\mathbf{x}} = \begin{bmatrix} \Delta\tilde{\mathbf{x}}_1 \\ \vdots \\ \Delta\tilde{\mathbf{x}}_N \end{bmatrix} \qquad (3.13)$$

is the global displacement increments vector. This increment vector is used to update the actual atomic positions.

$$\mathbf{x} = \tilde{\mathbf{x}} + \Delta\tilde{\mathbf{x}} \qquad (3.14)$$

Because for non-linear problems one Newton-Raphson iteration is not enough to reach equilibrium states, several iteration steps $(m+1)$ are necessary. For this purpose, the linear system of equations, given in Equation (3.12), and the update rule for the atomic positions, specified in Equation (3.14), are reformulated for an iterative procedure.

$$\mathbf{K}^{(m)}\Delta\mathbf{x}^{(m+1)} = -\mathbf{f}_{\mathrm{int}}^{(m)} + \mathbf{f}_{\mathrm{ext}} \qquad \mathbf{x}^{(m+1)} = \mathbf{x}^{(m)} + \Delta\mathbf{x}^{(m+1)} \qquad m = 0, 1, \dots \qquad (3.15)$$

These iterations are repeated till the energy residuum $\left| \left(-\mathbf{f}_{\mathrm{int}}^{(m)} + \mathbf{f}_{\mathrm{ext}}\right) \cdot \Delta\mathbf{x}^{(m+1)} \right|$ is less or equal a given tolerance. If convergence is achieved, the next load step can be analysed by a new Newton-Raphson iteration loop.

3.2 Stability of equilibrium configurations

Beside the task of finding equilibrium states of the atomistic structure under consideration, it is also of interest to check if this state is stable. This stability is fulfilled if the total energy at the equilibrium state $\pi\left(\mathbf{x}\right)$ is smaller than the one of a slightly perturbed configuration $\pi\left(\mathbf{x} + \delta\mathbf{x}\right)$.

$$\pi\left(\mathbf{x} + \delta\mathbf{x}\right) - \pi\left(\mathbf{x}\right) > 0$$
$$\pi\left(\mathbf{x}_1 + \delta\mathbf{x}_1, \mathbf{x}_2 + \delta\mathbf{x}_2, \dots, \mathbf{x}_N + \delta\mathbf{x}_N\right) - \pi\left(\mathbf{x}_1, \mathbf{x}_2, \dots, \mathbf{x}_N\right) > 0 \qquad (3.16)$$

A truncated Taylor series expansion of the perturbed state gives

$$\pi\left(\mathbf{x}_1 + \delta\mathbf{x}_1, \mathbf{x}_2 + \delta\mathbf{x}_2, \ldots, \mathbf{x}_N + \delta\mathbf{x}_N\right) = \pi\left(\mathbf{x}_1, \mathbf{x}_2, \ldots, \mathbf{x}_N\right) + \delta\pi\left(\mathbf{x}_1, \mathbf{x}_2, \ldots, \mathbf{x}_N\right)$$
$$+ \frac{1}{2}\delta^2\pi\left(\mathbf{x}_1, \mathbf{x}_2, \ldots, \mathbf{x}_N\right) \tag{3.17}$$

By using the stationary condition for the total potential energy $\delta\pi\left(\mathbf{x}_1, \mathbf{x}_2, \ldots, \mathbf{x}_N\right) = 0$, the stability condition reads

$$\delta^2\pi\left(\mathbf{x}_1, \mathbf{x}_2, \ldots, \mathbf{x}_N\right) > 0$$

$$\sum_{i=1}^{N}\sum_{j=1}^{N}\frac{\partial^2\pi\left(\mathbf{x}_1, \mathbf{x}_2, \ldots, \mathbf{x}_N\right)}{\partial\mathbf{x}_i\partial\mathbf{x}_j}\delta\mathbf{x}_j \cdot \delta\mathbf{x}_i > 0 \tag{3.18}$$

Within this expression, the second-order partial derivative of the total potential energy with respect to the position vectors of all atoms in the structure correlates with the global stiffness matrix $\mathbf{K}$ at the equilibrium state. The current state is stable if Equation (3.18) is fulfilled for arbitrary perturbations $\delta\mathbf{x}_i$ and $\delta\mathbf{x}_j$. This condition is achieved by a positive definite global stiffness matrix $\mathbf{K}$. If this condition is not in line, the state is either indifferent $(\delta^2\pi\left(\mathbf{x}_1, \mathbf{x}_2, \ldots, \mathbf{x}_N\right) = 0)$ or unstable $(\delta^2\pi\left(\mathbf{x}_1, \mathbf{x}_2, \ldots, \mathbf{x}_N\right) < 0)$. Especially if it is unstable, a so-called bifurcation into a state with lower energy might be possible. The definiteness of the global stiffness matrix can be checked by the calculation of the eigenvalues ω_i $(i = 1, \ldots, N)$. For the exact detection of these instability points with zero eigenvalues, several methods are available. From this set of approaches, the bisection algorithm is selected. In addition, the corresponding eigenvectors $\boldsymbol{\mu}_i$ give the chance to show the shape of the lower energy mode. These eigenvectors are further essential in a branch switching approach to achieve the appropriate buckled configurations. For that purpose, the method suggested by Wagner and Wriggers [57] is applied. This algorithm relies on the eigenvector $\boldsymbol{\mu}_c$ associated with the critical zero eigenvalue at the bifurcation point. In addition, the global position vector $\mathbf{x}_c$ at the corresponding state of deformation and a scaling factor ν are essential. On the basis of these quantities, the starting vector $\mathbf{x}^{(0)} = \mathbf{x}_c + \nu\boldsymbol{\mu}_c$ for the iterative calculation of the equilibrium state on the postbuckling path is specified. Finally, after successful branch switching, the buckled configuration is obtained and the postbuckling path can be further investigated.

3.3 Atomistic kinematics

The calculation of the bonded potential, using the Tersoff-Brenner interatomic bond-order potential given in Subsection 2.3.1, requires the scalar bond lengths and valence angles formed by the participating atoms. For the evaluation of the non-bonded potential, which applies the Lennard-Jones interatomic pair-potential specified in Subsection 2.4.1, the distance between two atoms is necessary. On this account, Figure 3.1 illustrates a set of atoms with a characteristic bond length and a representative valence angle. In what follows, these quantities and their derivatives with respect to the positions of the atoms involved are given in an exact geometric setting.

3.3.1 The bond vector and the distance vector

For the evaluation of the bond lengths, of the distance between atoms and of the valence angles, the distance vector between two different atoms i and j is necessary. The calculation of the distance vector and its first-order and second-order derivatives with respect to the position vectors of the involved atoms can be performed in the following way. In these expressions, and in the derivations
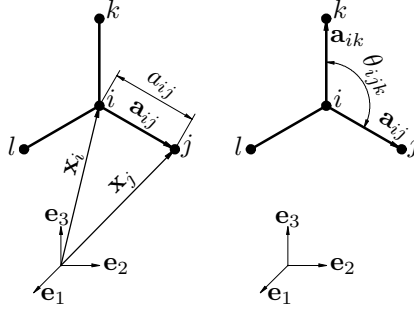
Figure 3.1: The kinematics for a set of interacting atoms. Illustration of the position vectors $\mathbf{x}_i$ and $\mathbf{x}_j$, the bond vectors $\mathbf{a}_{ij}$ and $\mathbf{a}_{ik}$, the bond length a_{ij} and the valence angle θ_{ijk}.

thereafter, α and β are either i or j, and δ_*° denotes the Kronecker symbol.

$$\mathbf{a}_{ij} = \mathbf{x}_j - \mathbf{x}_i \tag{3.19}$$

$$\frac{\partial \mathbf{a}_{ij}}{\partial \mathbf{x}_\alpha} = \mathbf{1}\left(\delta_j^\alpha - \delta_i^\alpha\right) = \mathbf{1}\delta_{ij}^\alpha \tag{3.20}$$

$$\frac{\partial^2 \mathbf{a}_{ij}}{\partial \mathbf{x}_\alpha \partial \mathbf{x}_\beta} = \mathbf{0} \tag{3.21}$$

3.3.2 The bond length and the distance between atoms

The distance a_{ij} between two atoms i and j in the structure directly bonded to each other or building a non-bonded interaction makes use of the distance vector $\mathbf{a}_{ij}$. The interatomic distance itself and its first-order and second-order derivatives with respect to the position vectors of the involved atoms are given by:

$$a_{ij} = \|\mathbf{a}_{ij}\| = [\mathbf{a}_{ij} \cdot \mathbf{a}_{ij}]^{1/2} \tag{3.22}$$

$$\frac{\partial a_{ij}}{\partial \mathbf{x}_\alpha} = \frac{\mathbf{a}_{ij}}{a_{ij}}\left(\delta_j^\alpha - \delta_i^\alpha\right) = \frac{\mathbf{a}_{ij}}{a_{ij}}\delta_{ij}^\alpha \tag{3.23}$$

$$\frac{\partial^2 a_{ij}}{\partial \mathbf{x}_\alpha \partial \mathbf{x}_\beta} = \frac{\delta_{ij}^\alpha \delta_{ij}^\beta}{a_{ij}}\left[\mathbf{1} - \frac{\mathbf{a}_{ij} \otimes \mathbf{a}_{ij}}{a_{ij}^2}\right] \tag{3.24}$$

3.3.3 The valence angle

The valence angle, as illustrated in Figure 3.1, describes an angle included between two bonds arising from a central atom. This angle is necessary for the evaluation of the interatomic potential of bonded interactions. As a consequence of the geometric setting, the calculation is based on the two corresponding bond vectors.

$$\theta_{ijk} = \arccos\left(\frac{\mathbf{a}_{ij}}{a_{ij}} \cdot \frac{\mathbf{a}_{ik}}{a_{ik}}\right) \tag{3.25}$$

Then, the evaluation of the first-order and second-order derivatives of the valence angle with respect to the position vectors of the involved atoms is possible. In the following expressions α and β are either i, j or k. In addition, the abbreviations $\delta_{ij}^\alpha = \left(\delta_j^\alpha - \delta_i^\alpha\right)$ and $\delta_{ik}^\alpha = \left(\delta_k^\alpha - \delta_i^\alpha\right)$ are used, where α can be exchanged by β to get the respective terms.

$$\frac{\partial \theta_{ijk}}{\partial \mathbf{x}_\alpha} = -\frac{1}{\sin\left(\theta_{ijk}\right) a_{ij} a_{ik}}\left[\delta_{ij}^\alpha \mathbf{a}_{ik} + \mathbf{a}_{ij}\delta_{ik}^\alpha - \cos\left(\theta_{ijk}\right)\left(\frac{\mathbf{a}_{ij}}{a_{ij}}\delta_{ij}^\alpha a_{ik} + a_{ij}\frac{\mathbf{a}_{ik}}{a_{ik}}\delta_{ik}^\alpha\right)\right] \tag{3.26}$$

$$\begin{aligned}
\frac{\partial^2 \theta_{ijk}}{\partial \mathbf{x}_\alpha \partial \mathbf{x}_\beta} = & -\frac{\cos\left(\theta_{ijk}\right)}{\sin\left(\theta_{ijk}\right)^3 a_{ij} a_{ik}} \left[\left(\delta_{ij}^\alpha \delta_{ij}^\beta \frac{a_{ik}}{a_{ij}} + \delta_{ik}^\alpha \delta_{ik}^\beta \frac{a_{ij}}{a_{ik}} \right) \left(\frac{\mathbf{a}_{ij}}{a_{ij}} \otimes \frac{\mathbf{a}_{ij}}{a_{ij}} + \frac{\mathbf{a}_{ik}}{a_{ik}} \otimes \frac{\mathbf{a}_{ik}}{a_{ik}} \right) \right] \\
& -\frac{\cos\left(\theta_{ijk}\right)}{\sin\left(\theta_{ijk}\right)^3 a_{ij} a_{ik}} \left[\left(\delta_{ik}^\alpha \delta_{ij}^\beta + \delta_{ij}^\alpha \delta_{ik}^\beta \right) \left(\frac{\mathbf{a}_{ij}}{a_{ij}} \otimes \frac{\mathbf{a}_{ik}}{a_{ik}} + \frac{\mathbf{a}_{ik}}{a_{ik}} \otimes \frac{\mathbf{a}_{ij}}{a_{ij}} \right) \right] \\
& +\frac{1}{\sin\left(\theta_{ijk}\right)^3 a_{ij} a_{ik}} \left[\left(\delta_{ij}^\alpha \delta_{ij}^\beta \frac{a_{ik}}{a_{ij}} + \delta_{ik}^\alpha \delta_{ik}^\beta \frac{a_{ij}}{a_{ik}} \right) \left(\frac{\mathbf{a}_{ij}}{a_{ij}} \otimes \frac{\mathbf{a}_{ik}}{a_{ik}} + \frac{\mathbf{a}_{ik}}{a_{ik}} \otimes \frac{\mathbf{a}_{ij}}{a_{ij}} \right) \right] \\
& +\frac{1}{\sin\left(\theta_{ijk}\right)^3 a_{ij} a_{ik}} \left[\left(\delta_{ij}^\alpha \delta_{ik}^\beta + \delta_{ik}^\alpha \delta_{ij}^\beta \right) \left(\frac{\mathbf{a}_{ij}}{a_{ij}} \otimes \frac{\mathbf{a}_{ij}}{a_{ij}} + \frac{\mathbf{a}_{ik}}{a_{ik}} \otimes \frac{\mathbf{a}_{ik}}{a_{ik}} \right) \right] \\
& -\frac{1}{\sin\left(\theta_{ijk}\right) a_{ij} a_{ik}} \left(\delta_{ij}^\alpha \delta_{ik}^\beta + \delta_{ik}^\alpha \delta_{ij}^\beta \right) \mathbf{1} + \frac{\cos\left(\theta_{ijk}\right)}{\sin\left(\theta_{ijk}\right) a_{ij} a_{ik}} \left(\delta_{ij}^\alpha \delta_{ij}^\beta \frac{a_{ik}}{a_{ij}} + \delta_{ik}^\beta \delta_{ik}^\alpha \frac{a_{ij}}{a_{ik}} \right) \mathbf{1} \\
& -\frac{2\cos\left(\theta_{ijk}\right)}{\sin\left(\theta_{ijk}\right) a_{ij} a_{ik}} \left[\delta_{ij}^\alpha \delta_{ij}^\beta \frac{a_{ik}}{a_{ij}} \frac{\mathbf{a}_{ij}}{a_{ij}} \otimes \frac{\mathbf{a}_{ij}}{a_{ij}} + \delta_{ik}^\alpha \delta_{ik}^\beta \frac{a_{ij}}{a_{ik}} \frac{\mathbf{a}_{ik}}{a_{ik}} \otimes \frac{\mathbf{a}_{ik}}{a_{ik}} \right] \quad (3.27)
\end{aligned}$$

3.4 Molecular statics within the finite element formalism

With the achievements of the previous sections, the search for equilibrium configurations within the molecular statics approach is already possible. For this task, the global force vector and the global stiffness matrix can be directly set up from the definition of the total potential. However, this procedure does not take into consideration the local structure of the interatomic potentials when setting up the global quantities. In contrast, in a classical finite element calculation, the global quantities are assembled from lower dimensional element-wise contributions. As the atomistic structure is discrete from nature, a discretisation and potentially a mesh refinement is not required. To make the assemblage process available for molecular statics, an equivalent to the standard finite element is necessary. This design is possible and known as atom-related finite element. One variant of this type was established by Liu *et al.* [30] and is named atomic-scale finite element (AFEM). Wackerfuß [56] proposed a similar approach also suitable for various interatomic potentials. With such an element-wise description, the extensive use of existing finite element frameworks is possible. This enables the effective use of assemblage algorithms and solvers. Additionally, a decisive advantage is the usage of available stability analysis tools. In particular, bisection algorithms and branch switching procedures are of interest. In what follows, appropriate finite elements will be given for the bonded and the non-bonded interactions.

3.4.1 The atom-related finite element for the Tersoff-Brenner potential

In this section, the equivalent finite element design for the bonded interactions is given on the basis of the approach of Wackerfuß [56]. In an atom-related description, a finite element is defined for each atom of the whole structure by the interaction of this reference atom with its neighbouring atoms. For this formulation, the interacting range of the interatomic potential is essential. This range includes all atoms of the entire structure, which are in direct relation with the reference atom through the description of the interatomic potential. For the Tersoff-Brenner interatomic bond-order potential, this range is illustrated in Figure 3.2. The corresponding patch consists of the reference atom 0, its first neighbours $1, 2$ and 3 and its second neighbours $4, 5, 6, 7, 8$ and 9, resulting in an atom-related 10-node finite element. For this patch, the element-wise energy as well as the element force vector and the element stiffness matrix have to be defined properly. If this is done the same way as in classical finite element methods, double counting of element contributions would occur. In a first step, the bonded energy per bond according to Equation (2.8) is split up
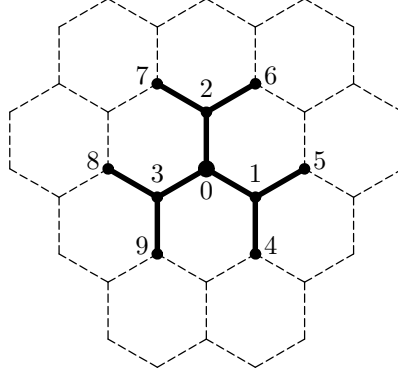
Figure 3.2: The relevant neighbourhood of the reference atom and the structure of the atom-related 10-node finite element equivalent for the Tersoff-Brenner bond-order potential.

into the parts per atom i and j because of $a_{ij} = a_{ji}$ being valid.

$$E_{ij} = + \frac{1}{2} V_{\mathrm{R}} (a_{ij}) - \frac{1}{2} B_{ij} (a_{ik}, a_{il}, \theta_{ijk}, \theta_{ijl}) V_{\mathrm{A}} (a_{ij})$$
$$+ \frac{1}{2} V_{\mathrm{R}} (a_{ji}) - \frac{1}{2} B_{ji} (a_{jm}, a_{jn}, \theta_{jim}, \theta_{jin}) V_{\mathrm{A}} (a_{ji}) \tag{3.28}$$

Then, a list $\mathcal{L}_{ijkl}$ containing the relevant atom interactions (bond lengths a and valence angles θ) of the atom-related 10-node finite element is defined.

$$\mathcal{L}_{ijkl} = \{(0,1,2,3), (0,2,3,1), (0,3,1,2), (1,0,4,5), (1,4,5,0), (1,5,0,4),$$
$$(2,0,6,7), (2,6,7,0), (2,7,0,6), (3,0,8,9), (3,8,9,0), (3,9,0,8)\} \tag{3.29}$$

The use of this list allows the specification of an element-related bonded energy.

$$\pi_{\mathrm{b}}^{e} = \sum_{\mathcal{L}_{ijkl}} \frac{1}{2} \left[V_{\mathrm{R}}(a_{ij}) - B_{ij} (a_{ik}, a_{il}, \theta_{ijk}, \theta_{ijl}) V_{\mathrm{A}}(a_{ij}) \right] \tag{3.30}$$

For the calculation of the total bonded energy of the structure only the first three entries of $\mathcal{L}_{ijkl}$ must be taken to avoid double counting of energy contributions upon assembling. The sum over in total 12 terms is only necessary for the calculation of the element force vector and the element stiffness matrix as it contains all expressions depending on the position of the element central atom. The overlapping of adjacent finite elements can lead to double counting of the elemental contributions in the global force vector as well as in the global stiffness matrix. This double counting is avoided by only considering the influence of the neighbouring nodes on the reference node (node 0) and not the other way round. Starting from the element-related energy π_{b}^{e}, the element force vector $\mathbf{f}_{\mathrm{b}}^{e}$ and the element stiffness matrix $\mathbf{K}_{\mathrm{b}}^{e}$ can be generated by the first-order and second-order derivatives with respect to the positions of the reference node and its neighbouring nodes.

$$\mathbf{f}_{\mathrm{b}}^{e} = \frac{\partial \pi_{\mathrm{b}}^{e}}{\partial \mathbf{x}_0} \tag{3.31}$$

$$\mathbf{K}_{\mathrm{b}}^{e} = \left[\frac{\partial^2 \pi_{\mathrm{b}}^{e}}{\partial \mathbf{x}_0 \partial \mathbf{x}_0} \quad \frac{\partial^2 \pi_{\mathrm{b}}^{e}}{\partial \mathbf{x}_0 \partial \mathbf{x}_1} \quad \cdots \quad \frac{\partial^2 \pi_{\mathrm{b}}^{e}}{\partial \mathbf{x}_0 \partial \mathbf{x}_9} \right] \tag{3.32}$$

The essential first-order and second-order derivatives are:

$$
\frac{\partial \pi_{\mathrm{b}}^{e}}{\partial \mathbf{x}_0} = \sum_{\mathcal{L}_{ijkl}} \frac{1}{2} \left[\frac{\partial V_{\mathrm{R}}}{\partial \mathbf{x}_0} - B_{ij} \frac{\partial V_{\mathrm{A}}}{\partial \mathbf{x}_0} - \frac{\partial B_{ij}}{\partial \mathbf{x}_0} V_{\mathrm{A}} \right]
$$

$$
= \sum_{\mathcal{L}_{ijkl}} \frac{1}{2} \left[(V_{\mathrm{R}}' - B_{ij} V_{\mathrm{A}}') \frac{\partial a_{ij}}{\partial \mathbf{x}_0} - \left(\frac{\partial B_{ij}}{\partial a_{ik}} \frac{\partial a_{ik}}{\partial \mathbf{x}_0} + \frac{\partial B_{ij}}{\partial a_{il}} \frac{\partial a_{il}}{\partial \mathbf{x}_0} + \frac{\partial B_{ij}}{\partial \theta_{ijk}} \frac{\partial \theta_{ijk}}{\partial \mathbf{x}_0} + \frac{\partial B_{ij}}{\partial \theta_{ijl}} \frac{\partial \theta_{ijl}}{\partial \mathbf{x}_0} \right) V_{\mathrm{A}} \right]
$$

$$
\tag{3.33}
$$

$$
\frac{\partial^2 \pi_{\mathrm{b}}^{e}}{\partial \mathbf{x}_0 \partial \mathbf{x}_\alpha} = \sum_{\mathcal{L}_{ijkl}} \frac{1}{2} \left[\frac{\partial^2 V_{\mathrm{R}}}{\partial \mathbf{x}_0 \partial \mathbf{x}_\alpha} - B_{ij} \frac{\partial^2 V_{\mathrm{A}}}{\partial \mathbf{x}_0 \partial \mathbf{x}_\alpha} - \frac{\partial V_{\mathrm{A}}}{\partial \mathbf{x}_0} \otimes \frac{\partial B_{ij}}{\partial \mathbf{x}_\alpha} - \frac{\partial B_{ij}}{\partial \mathbf{x}_0} \otimes \frac{\partial V_{\mathrm{A}}}{\partial \mathbf{x}_\alpha} - \frac{\partial^2 B_{ij}}{\partial \mathbf{x}_0 \partial \mathbf{x}_\alpha} V_{\mathrm{A}} \right]
$$

$$
= \sum_{\mathcal{L}_{ijkl}} \frac{1}{2} \left[(V_{\mathrm{R}}'' - B_{ij} V_{\mathrm{A}}'') \frac{\partial a_{ij}}{\partial \mathbf{x}_0} \otimes \frac{\partial a_{ij}}{\partial \mathbf{x}_\alpha} + (V_{\mathrm{R}}' - B_{ij} V_{\mathrm{A}}') \frac{\partial^2 a_{ij}}{\partial \mathbf{x}_0 \partial \mathbf{x}_\alpha} \right.
$$

$$
- V_{\mathrm{A}}' \frac{\partial a_{ij}}{\partial \mathbf{x}_0} \otimes \left(\frac{\partial B_{ij}}{\partial a_{ik}} \frac{\partial a_{ik}}{\partial \mathbf{x}_\alpha} + \frac{\partial B_{ij}}{\partial a_{il}} \frac{\partial a_{il}}{\partial \mathbf{x}_\alpha} + \frac{\partial B_{ij}}{\partial \theta_{ijk}} \frac{\partial \theta_{ijk}}{\partial \mathbf{x}_\alpha} + \frac{\partial B_{ij}}{\partial \theta_{ijl}} \frac{\partial \theta_{ijl}}{\partial \mathbf{x}_\alpha} \right)
$$

$$
- V_{\mathrm{A}}' \left(\frac{\partial B_{ij}}{\partial a_{ik}} \frac{\partial a_{ik}}{\partial \mathbf{x}_0} + \frac{\partial B_{ij}}{\partial a_{il}} \frac{\partial a_{il}}{\partial \mathbf{x}_0} + \frac{\partial B_{ij}}{\partial \theta_{ijk}} \frac{\partial \theta_{ijk}}{\partial \mathbf{x}_0} + \frac{\partial B_{ij}}{\partial \theta_{ijl}} \frac{\partial \theta_{ijl}}{\partial \mathbf{x}_0} \right) \otimes \frac{\partial a_{ij}}{\partial \mathbf{x}_\alpha}
$$

$$
- \left(\frac{\partial B_{ij}}{\partial a_{ik}} \frac{\partial^2 a_{ik}}{\partial \mathbf{x}_0 \partial \mathbf{x}_\alpha} + \frac{\partial B_{ij}}{\partial a_{il}} \frac{\partial^2 a_{il}}{\partial \mathbf{x}_0 \partial \mathbf{x}_\alpha} + \frac{\partial B_{ij}}{\partial \theta_{ijk}} \frac{\partial^2 \theta_{ijk}}{\partial \mathbf{x}_0 \partial \mathbf{x}_\alpha} + \frac{\partial B_{ij}}{\partial \theta_{ijl}} \frac{\partial^2 \theta_{ijl}}{\partial \mathbf{x}_0 \partial \mathbf{x}_\alpha} \right.
$$

$$
+ \frac{\partial^2 B_{ij}}{\partial a_{ik} \partial a_{ik}} \frac{\partial a_{ik}}{\partial \mathbf{x}_0} \otimes \frac{\partial a_{ik}}{\partial \mathbf{x}_\alpha} + \frac{\partial^2 B_{ij}}{\partial a_{ik} \partial a_{il}} \frac{\partial a_{ik}}{\partial \mathbf{x}_0} \otimes \frac{\partial a_{il}}{\partial \mathbf{x}_\alpha}
$$

$$
+ \frac{\partial^2 B_{ij}}{\partial a_{ik} \partial \theta_{ijk}} \frac{\partial a_{ik}}{\partial \mathbf{x}_0} \otimes \frac{\partial \theta_{ijk}}{\partial \mathbf{x}_\alpha} + \frac{\partial^2 B_{ij}}{\partial a_{ik} \partial \theta_{ijl}} \frac{\partial a_{ik}}{\partial \mathbf{x}_0} \otimes \frac{\partial \theta_{ijl}}{\partial \mathbf{x}_\alpha}
$$

$$
+ \frac{\partial^2 B_{ij}}{\partial a_{il} \partial a_{ik}} \frac{\partial a_{il}}{\partial \mathbf{x}_0} \otimes \frac{\partial a_{ik}}{\partial \mathbf{x}_\alpha} + \frac{\partial^2 B_{ij}}{\partial a_{il} \partial a_{il}} \frac{\partial a_{il}}{\partial \mathbf{x}_0} \otimes \frac{\partial a_{il}}{\partial \mathbf{x}_\alpha}
$$

$$
+ \frac{\partial^2 B_{ij}}{\partial a_{il} \partial \theta_{ijk}} \frac{\partial a_{il}}{\partial \mathbf{x}_0} \otimes \frac{\partial \theta_{ijk}}{\partial \mathbf{x}_\alpha} + \frac{\partial^2 B_{ij}}{\partial a_{il} \partial \theta_{ijl}} \frac{\partial a_{il}}{\partial \mathbf{x}_0} \otimes \frac{\partial \theta_{ijl}}{\partial \mathbf{x}_\alpha}
$$

$$
+ \frac{\partial^2 B_{ij}}{\partial \theta_{ijk} \partial a_{ik}} \frac{\partial \theta_{ijk}}{\partial \mathbf{x}_0} \otimes \frac{\partial a_{ik}}{\partial \mathbf{x}_\alpha} + \frac{\partial^2 B_{ij}}{\partial \theta_{ijk} \partial a_{il}} \frac{\partial \theta_{ijk}}{\partial \mathbf{x}_0} \otimes \frac{\partial a_{il}}{\partial \mathbf{x}_\alpha}
$$

$$
+ \frac{\partial^2 B_{ij}}{\partial \theta_{ijk} \partial \theta_{ijk}} \frac{\partial \theta_{ijk}}{\partial \mathbf{x}_0} \otimes \frac{\partial \theta_{ijk}}{\partial \mathbf{x}_\alpha} + \frac{\partial^2 B_{ij}}{\partial \theta_{ijk} \partial \theta_{ijl}} \frac{\partial \theta_{ijk}}{\partial \mathbf{x}_0} \otimes \frac{\partial \theta_{ijl}}{\partial \mathbf{x}_\alpha}
$$

$$
+ \frac{\partial^2 B_{ij}}{\partial \theta_{ijl} \partial a_{ik}} \frac{\partial \theta_{ijl}}{\partial \mathbf{x}_0} \otimes \frac{\partial a_{ik}}{\partial \mathbf{x}_\alpha} + \frac{\partial^2 B_{ij}}{\partial \theta_{ijl} \partial a_{il}} \frac{\partial \theta_{ijl}}{\partial \mathbf{x}_0} \otimes \frac{\partial a_{il}}{\partial \mathbf{x}_\alpha}
$$

$$
\left. \left. + \frac{\partial^2 B_{ij}}{\partial \theta_{ijl} \partial \theta_{ijk}} \frac{\partial \theta_{ijl}}{\partial \mathbf{x}_0} \otimes \frac{\partial \theta_{ijk}}{\partial \mathbf{x}_\alpha} + \frac{\partial^2 B_{ij}}{\partial \theta_{ijl} \partial \theta_{ijl}} \frac{\partial \theta_{ijl}}{\partial \mathbf{x}_0} \otimes \frac{\partial \theta_{ijl}}{\partial \mathbf{x}_\alpha} \right) V_{\mathrm{A}} \right] \tag{3.34}
$$

where $\alpha = 0, 1, \ldots, 9$ runs over all nodes of the element. As a result of this definition for the elemental contributions, the global force vector and the global stiffness matrix can be assembled line by line. The global stiffness matrix resulting from this process is then symmetric and due to the local character of the interatomic potential also sparse.

3.4.2 The finite element for modelling non-bonded interactions

As already pointed out in Section 2.4, a non-bonded interaction involves two atoms i and j of the structure. It is therefore an obvious choice to model this property by a two-node spring

element. This spring element based on the Lennard-Jones interatomic pair-potential has a non-linear behaviour on the bond length a_{ij} with the element-related potential given as follows.

$$\pi_{\mathrm{nb}}^e = V_{\mathrm{nb}}\left(a_{ij}\right) \tag{3.35}$$

The element force vector $\mathbf{f}_{\mathrm{nb}}^e$ can be calculated by:

$$\mathbf{f}_{\mathrm{nb}}^e = \begin{bmatrix} \frac{\partial V_{\mathrm{nb}}(a_{ij})}{\partial \mathbf{x}_i} \\ \frac{\partial V_{\mathrm{nb}}(a_{ij})}{\partial \mathbf{x}_j} \end{bmatrix} = V_{\mathrm{nb}}'\left(a_{ij}\right) \begin{bmatrix} \frac{\partial a_{ij}}{\partial \mathbf{x}_i} \\ \frac{\partial a_{ij}}{\partial \mathbf{x}_j} \end{bmatrix} = V_{\mathrm{nb}}'\left(a_{ij}\right) \frac{\mathbf{a}_{ij}}{a_{ij}} \begin{bmatrix} -1 \\ +1 \end{bmatrix} \tag{3.36}$$

The element stiffness matrix $\mathbf{K}_{\mathrm{nb}}^e$ is given by:

$$
\begin{aligned}
\mathbf{K}_{\mathrm{nb}}^e &= \begin{bmatrix} \frac{\partial^2 V_{\mathrm{nb}}(a_{ij})}{\partial \mathbf{x}_i \partial \mathbf{x}_i} & \frac{\partial^2 V_{\mathrm{nb}}(a_{ij})}{\partial \mathbf{x}_i \partial \mathbf{x}_j} \\ \frac{\partial^2 V_{\mathrm{nb}}(a_{ij})}{\partial \mathbf{x}_j \partial \mathbf{x}_i} & \frac{\partial^2 V_{\mathrm{nb}}(a_{ij})}{\partial \mathbf{x}_j \partial \mathbf{x}_j} \end{bmatrix} \\[2mm]
&= \begin{bmatrix} V_{\mathrm{nb}}''\left(a_{ij}\right) \frac{\partial a_{ij}}{\partial \mathbf{x}_i} \otimes \frac{\partial a_{ij}}{\partial \mathbf{x}_i} + V_{\mathrm{nb}}'\left(a_{ij}\right) \frac{\partial^2 a_{ij}}{\partial \mathbf{x}_i \partial \mathbf{x}_i} & V_{\mathrm{nb}}''\left(a_{ij}\right) \frac{\partial a_{ij}}{\partial \mathbf{x}_i} \otimes \frac{\partial a_{ij}}{\partial \mathbf{x}_j} + V_{\mathrm{nb}}'\left(a_{ij}\right) \frac{\partial^2 a_{ij}}{\partial \mathbf{x}_i \partial \mathbf{x}_j} \\ V_{\mathrm{nb}}''\left(a_{ij}\right) \frac{\partial a_{ij}}{\partial \mathbf{x}_j} \otimes \frac{\partial a_{ij}}{\partial \mathbf{x}_i} + V_{\mathrm{nb}}'\left(a_{ij}\right) \frac{\partial^2 a_{ij}}{\partial \mathbf{x}_j \partial \mathbf{x}_i} & V_{\mathrm{nb}}''\left(a_{ij}\right) \frac{\partial a_{ij}}{\partial \mathbf{x}_j} \otimes \frac{\partial a_{ij}}{\partial \mathbf{x}_j} + V_{\mathrm{nb}}'\left(a_{ij}\right) \frac{\partial^2 a_{ij}}{\partial \mathbf{x}_j \partial \mathbf{x}_j} \end{bmatrix} \\[2mm]
&= \left[\left(V_{\mathrm{nb}}''\left(a_{ij}\right) - \frac{V_{\mathrm{nb}}'\left(a_{ij}\right)}{a_{ij}} \right) \frac{\mathbf{a}_{ij}}{a_{ij}} \otimes \frac{\mathbf{a}_{ij}}{a_{ij}} + \frac{V_{\mathrm{nb}}'\left(a_{ij}\right)}{a_{ij}} \mathbf{1} \right] \begin{bmatrix} +1 & -1 \\ -1 & +1 \end{bmatrix} \tag{3.37}
\end{aligned}
$$

Applying an appropriate assemblage procedure, this local elemental contributions can be brought to the global level. As a consequence of the non-bonded interactions built by arbitrary pairs of atoms, additional entries in the global stiffness matrix are generated. The long-range character thus ends up in an increased bandwidth of the global stiffness matrix.

3.5 Numerical examples on buckling of carbon nanotubes

The aims of this section are the numerical testing of the molecular statics approach based on the formalism of the finite element method and the investigation into the influence of non-bonded interactions on the buckling behaviour of carbon nanotubes. For this purpose, a stand-alone finite element code including the essential algorithms for the entire buckling analysis was developed. In numerical simulations, various configurations with and without non-bonded interactions are investigated. In order to reduce the total number of possible non-bonded interactions, an upper cut-off radius is introduced in certain simulations to exclude pairs of atoms with a large distance. In the selection of this barrier, the deliberations of Subsection 2.4.1 serve as a guide for the specific cut-off radius in the relevant simulations. The use of such a cut-off radius results in a varying total number of non-bonded interactions depending on the current state of deformation. Therefore, an additional loop around the current load step is accomplished. At the start of each of these runs, a list that contains all relevant non-bonded interactions is updated. In doing so, the distance between all potential pairs of atoms is checked, and those interactions that are beneath the cut-off radius are gathered. Then, the related equilibrium configuration is calculated on the basis of this current set of non-bonded interactions. Once the actual number of non-bonded interactions remains constant, the complemental loop is terminated. Subsequently, the next and following load steps are investigated in the same manner. In the absence of the cut-off radius, a simplified procedure can be applied because the total number of non-bonded interactions is constant throughout the entire loading. Thus, the additional update loop is not needed, and the list of relevant interactions is evaluated just once at the outset of the simulation. The numerical results are given for single-walled (SWCNT) and double-walled (DWCNT) carbon nanotubes under different loading conditions. The simulation results are compared, if available, with corresponding results from the literature.

3.5.1 Single-walled carbon nanotubes under torsional load

The examples on carbon nanotubes under torsional load are performed by a displacement-driven mode. In a first step of the analysis, the tube is relaxed and the resulting state is the basis for the further calculations and the ground state for all energies. The torsional load is applied by rotating both ends of the relaxed tube in opposite direction while holding their axial positions fixed.

Perfect and imperfect structure

In this first twisting example, a (20,0) zig-zag carbon nanotube with a length of 19 honeycomb cells under twisting load is spotted. Calculations are performed for a faultless structure, and for an imperfect structure. The same carbon nanotubes were also simulated by Wackerfuß [56] although different boundary conditions were used. Here, boundary conditions representing the torsional load are implemented as displacement constraints on the outermost atoms of both tube ends. In particular, the axial positions of the considered atoms are fixed whereas their circumferential positions are prescribed. By rotating the atoms with their relaxed radius around the axis of the nanotube, the required displacements are specified. Thereby, the twisting is accomplished by the fact that the atoms of each side are rotated in opposite directions. Within this series of simulations, the non-bonded interactions modelling is not included. The first intent of this example is to show the difference between the unstable and the stable deformation paths. The second objective is to illustrate the possibility of simulating carbon nanotubes with vacancy defects on the basis of the atom-related finite element. The perfect structure has 800 atoms. For the imperfect structure, one carbon atom is removed so that it has 799 remaining atoms. The diagram on the left side in Figure 3.3 presents the evolutions of the total energy, respectively, for the twisted tubes with respect to the twisting angle applied on each side. In the course of this, the number of load increments was
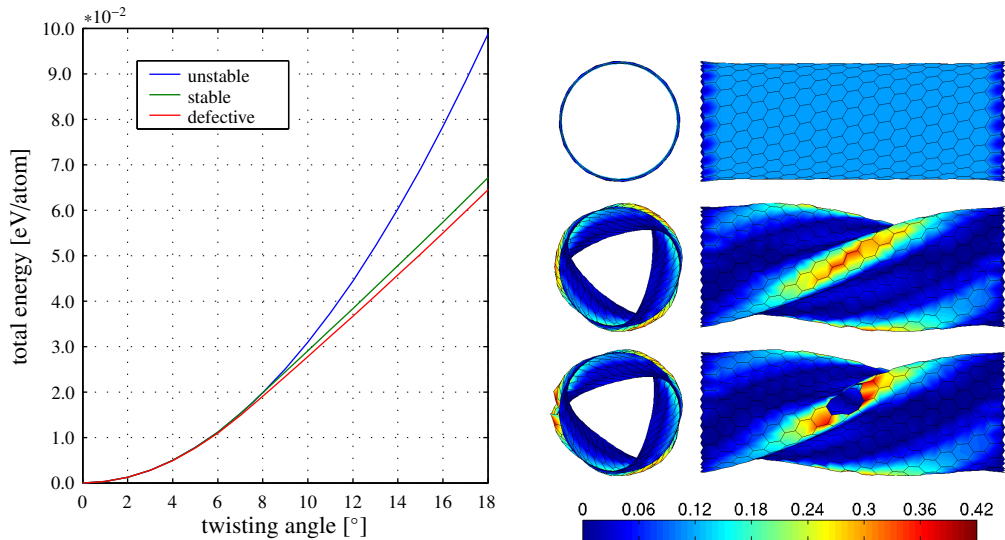
Figure 3.3: Molecular statics approach: The total energy evolutions for the twisted (20,0) carbon nanotubes and the corresponding deformed structures with colour mapping of the local total energy per atom [eV/atom] for the unstable (top), the buckled stable (middle) together with the defective tube (bottom).

21 for both calculations with the perfect nanotube and 19 for the analysis of the defective carbon nanotube. The curves for the perfect tube coincide up to an angle of $7.546°$ where it loses stability. After that point in a first calculation, the unstable path is further followed leading to a nearly quadratic energy plot. The final deformed unstable configuration is given in the topmost images on the right side showing a lateral and a front view. In a second calculation, a branch switch is

performed at the critical point and the resulting buckled configuration is continued twisting. The associated energy versus twisting angle shows a nearly linear behaviour for this stable path. The total energy for the stable path is indeed lower than the total energy for the unstable path after passing the critical point of stability. For this stable path, the corresponding buckled structure is plotted in the central images on the right. The third curve in this figure represents the defective tube. This energy curve alters from an approximately quadratic region to a nearly linear one with increasing twisting angle. The defected nanotube has a lower energy level than the perfect ones throughout the whole loading cycle. The lowermost images on the right side show the two views for the imperfect structure. Within these images, the vacancy defect and the missing bonds can be seen. The colour mapping in all illustrations presents the local change in total energy per atom relative to the relaxed nanotube. Although globally the unstable configuration has the highest value of the average total energy, the locally highest value arises in the imperfect structure near the absent atom. A similar buckled pattern for the ideal tube and a matchable deformed configuration of the defective nanotube were obtained by Wackerfuß [56]. These facts indicate the proper implementation of the atom-related finite element.

Folding under torsional load

In this example, a (10,10) single-walled armchair carbon nanotube with a length of 100 honeycomb cells is twisted. This tube has 4000 carbon atoms in total. The aim of this example is to show the importance of the in-layer non-bonded interactions, when simulating the buckling of single-walled carbon nanotubes. The in-layer non-bonded interactions exclude all pairs of atoms that are within
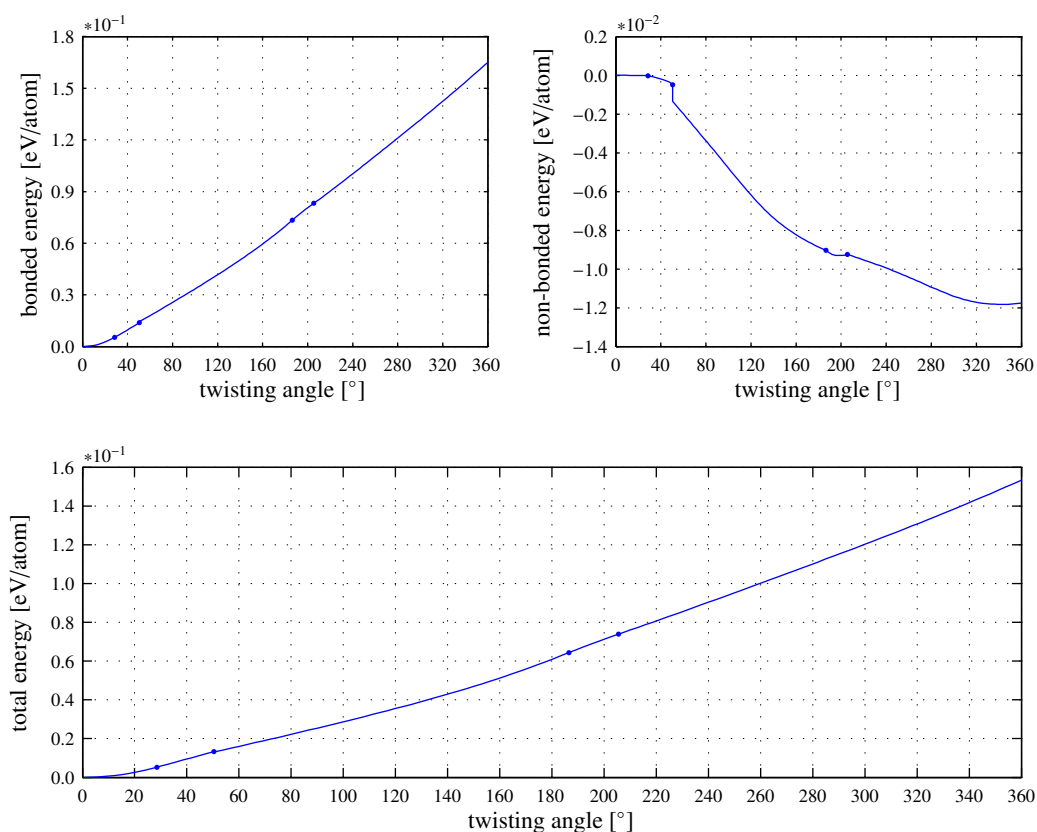
Figure 3.4: Molecular statics approach: The energy evolutions for the twisted (10,10) carbon nanotube with markers at the four instability points. The associated twisting angles of the critical states are $28.557°$, $50.434°$, $186.500°$ and $205.579°$.

three covalent bonds (3rd neighbours or 1-4 interactions) as well as all pairs that have a distance larger than a specific cut-off radius. For this example, an upper cut-off radius of 1.8 nm is applied in order to include potential non-bonded interactions of diametrically opposed atoms right from the beginning of the calculation. In a first step, the tube under consideration is relaxed and the corresponding energies are used as reference. In what follows, the relaxed tube is twisted up to the first bifurcation point at an angle of 28.557°. At this point, the corresponding eigenvector is calculated and a branch switch into the lower energy mode is performed. After further twisting to an angle of 50.434°, the structure reaches another instability point. A bifurcation into the stable
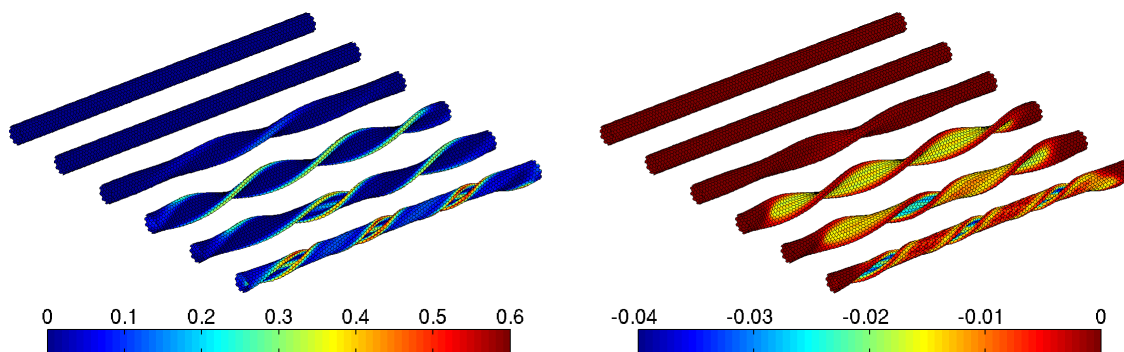
Figure 3.5: Molecular statics approach: The deformed structures of the twisted (10,10) carbon nanotube with colour mapping of the local bonded energy per atom [eV/atom] (left) and the local non-bonded energy per atom [eV/atom] (right) for different twisting angles of 0.0°, 28.557°, 50.434°, 186.500°, 205.579°, 360.0° aligned from rear to front.

path then gives a structure where the opposite walls at the centre of the tube close up to the van der Waals equilibrium distance. If the in-layer non-bonded interactions were not considered, the opposite walls would intersect. On further twisting, this closing proceeds to both ends of the tube. At an angle of 186.500°, the opposite walls of the tube are all closed up and another bifurcation
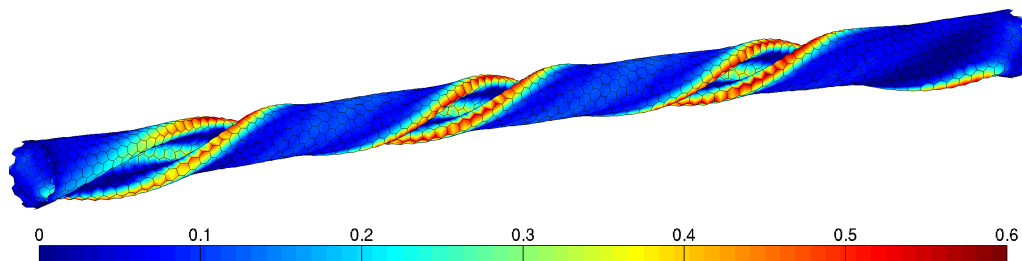
Figure 3.6: Molecular statics approach: The deformed structure of the twisted (10,10) carbon nanotube in the last load step at a twisting angle of 360.0° on each end with colour mapping of the local total energy per atom [eV/atom].

point is detected. The corresponding stable deformation path gives a structure where the walls of the tube start to fold onto itself. At the centre of the tube, this folding is finished at an angle of 205.579°, where the walls come to equilibrium non-bonded distance. The process of folding is then forced to both sides of the tube. At a twisting angle of 360.0° on each end, the loading of the nanotube is finished using a total number of 128 increments. Figure 3.4 shows the evolution of the bonded energy as well as the non-bonded energy and the total energy as a function of the twisting angle. Within these curves, the four instability points are highlighted with markers. The relaxed tube and the deformed structures of the nanotube at the specified bifurcation points can be seen in Figure 3.5 together with the final folded configuration. Thereby, the colour mapping represents the local changes in bonded and non-bonded energy per atom relative to the relaxed tube. In

addition, Figure 3.6 displays the folded carbon nanotube in the last load step at a twisting angle of 360.0° on each end with a colour mapping of the local changes in total energy. Comparable folded structures and related energy curves for this twisted single-walled carbon nanotube were determined by Arroyo [2] and Arroyo and Belytschko [4, 5, 6]. However, this comparison can only be done qualitatively as the detailed specification of their non-bonded interaction modelling is not available. Although this fact is obvious, a similar behaviour of the energy evolutions can be observed. To sum up, the modelling of in-layer non-bonded interactions is of great importance for the simulation of this single-walled carbon nanotube under torsion because otherwise intersection would occur and the folding would not be possible.

3.5.2 Single-walled carbon nanotubes under axial compression

The examples on axially loaded carbon nanotubes are analysed either by a displacement-driven or a force-driven simulation. Again, the first step of the analysis is the relaxation process to achieve a reference configuration for the further calculations and a ground state for the energies.

(8,0) carbon nanotube under axial compression

This example investigates an (8,0) zigzag carbon nanotube with a length of 19 hexagonal cells under displacement-driven axial compression. The atomistic structure is composed of 320 atoms resulting in a modelling with the same amount of atom-related finite elements. Within this example, the non-bonded interactions are not incorporated at all. The deformed structures and the evolution for the total energy can be found in Figure 3.7. The diagram shows the total energy versus axial
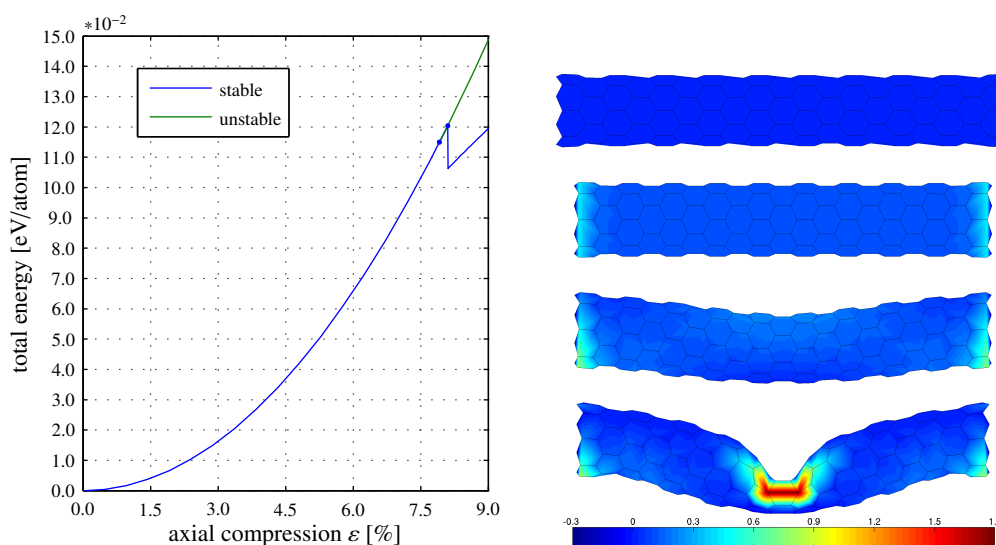
Figure 3.7: Molecular statics approach: The total energy evolutions of the (8,0) carbon nanotube under axial compression. Comparison between the stable and the unstable deformation paths. Deformed structures of the stable path with a colour mapping of the local total energy per atom [eV/atom] for the relaxed tube (topmost), the first bifurcation point (second from top), the buckled tube at the second instability point (third from top) and the final state (undermost).

compression evolution for the stable and the unstable paths of the deformation. Thereby, the final unstable configuration was received after 21 load steps whereas for the entire stable path, 46 increments, mainly due to the necessity of two bisections and the subsequent branch switchings, were necessary. At the beginning, the total energy increases nearly quadratically up to the first critical point. Because of the symmetries of the structure, two zero eigenvalues are present at the

instability point. This point is detected at an axial compression of 7.919% with an corresponding average total energy of 0.1150 eV/atom. The values at the bifurcation point show a perfect match with the results of Wackerfuß [56]. After this bifurcation point, two different paths can be followed. The first possibility is the continuation of the primary path, which is now unstable. The alternative is a branch switch with the eigenform of the critical point leading to the stable postbuckling path with slightly lower energy than the unstable path. The resulting buckled configuration is similar to the Euler-beam-buckling mode with two-sided clamped constraints. On further axial compression, the tube moves sideways more and more, causing a bending load in the tube. At an axial strain of 8.104% and a relative total energy of 0.1204 eV/atom, the next instability occurs. This critical point gives a buckling mode similar to the modes obtained for single-walled carbon nanotubes under bending load of Subsection 3.5.3, building a kink in the middle of the tube. With the branch switch into this path, the total energy curve changes to an approximately linear dependence on the axial strain. The images on the right side of Figure 3.7 give the four most important configurations of the stable path for the (8,0) carbon nanotube under axial compression. The topmost picture is the relaxed nanotube whereas the second picture from top shows the configuration at the first bifurcation point. The next image illustrates the Euler-like buckled tube at the point where it loses its stability. The picture at the bottom presents the final deformed structure with the kink in the middle. All the images show a colour mapping of the local total energy per atom.

(18,0) carbon nanotube under axial compression

This example is about an axially compressed (18,0) zig-zag carbon nanotube with a length of 39 honeycomb cells. On both ends of the tube axial, forces are applied to generate the compression. In order to avoid a global Euler-like buckling mode as observed in the previous example, additional displacement constraints have to be incorporated. A straightforward implementation of these constraints requires the existence of atoms at the four quadrants of the circular cross section of the relaxed tube. This condition is fulfilled by the investigated (18,0) zig-zag carbon nanotube. In addition, because of a length of 39 honeycomb cells, the tube's middle is not occupied by atoms. Thus, the eight atoms located at the four quadrants of the two cross sections that are immediately adjacent on both sides to the middle of the tube are essential. These eight atoms are constrained to move solely in radial direction so that the global buckling mode is prevented. Within this force-driven simulation, the first buckling mode is analysed and the non-linear load-deformation path is calculated with the help of a modified Riks algorithm as given in Hibbitt *et al.* [25]. Further informations on path-following procedures can be found for instance in Riks [43], Wriggers [61] and Bonet and Wood [9]. Three different calculations are performed, where the first simulation is done without modelling non-bonded interactions at all. In a second analysis, non-bonded interactions are excluded up to the 1-4 interactions (3rd neighbours) and with no upper cut-off radius. Finally, in a third calculation, non-bonded interactions are excluded up to the 2nd neighbours (1-3 interactions) and without the implementation of an upper cut-off radius. The instability points are detected using an accompanying eigenvalue analysis and a bisection algorithm. In particular, the obtained critical values of axial compression ε are: 4.491% (all non-bonded interactions excluded), 4.407% (up to third neighbours non-bonded interactions excluded) and 4.192% (up to second neighbours non-bonded interactions excluded). After locating the exact instability point, a branch switching is performed to follow the corresponding postbuckling paths. Figure 3.8 reports the total energy - axial compression ε and the load factor λ - axial compression ε diagrams for all simulations. The number of load increments that were required to specify the respective final buckled configuration is as follows: 99 (all non-bonded interactions excluded), 108 (up to third neighbours non-bonded interactions excluded) and 113 (up to second neighbours non-bonded interactions excluded). With respect to total energy, the behaviour is approximately quadratic in the primary deformation path and changes to a nearly linear curve in the postbuckling regime. The load factor λ - axial compression ε plot starts with a linear part, which is followed by a snap back. This attribute is also observed in the buckling of thin cylindrical shells under axial compression as for instance reported in von Kármán and Tsien [55] and Wohlever and Healey [60]. In their simulations on
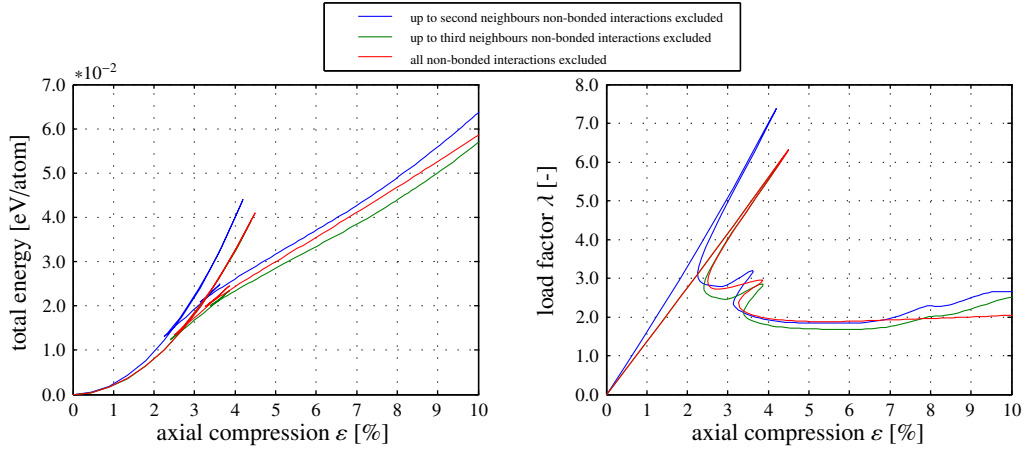
Figure 3.8: Molecular statics approach: The total energy - axial compression ε evolutions and the load factor λ - axial compression ε diagrams of the (18,0) carbon nanotube under force-driven axial compression. Comparison between different variants for modelling the in-layer non-bonded interactions.

axial compression of carbon nanotubes, Pantano *et al.* [39] obtained comparable postbuckling diagrams with an elastic shell theory. By comparing the three simulations, it turns out that the inclusion of the 1-4 non-bonded interactions results in a stiffer response of the tube under compression than the other two analyses. This is due to the repulsive character of these additional "mid-range" interactions that react against the external load in axial direction. Taking the tube without non-bonded interactions as reference, the inclusion of non-bonded interactions leads to a softer (1-4 interactions excluded) or a harder response (1-4 interactions included) of the carbon nanotube in the first part of the postbuckling regime. In the middle region of deformation, the non-bonded interactions soften the global response. At the end of deformation, the inclusion of non-bonded interactions prevents the nanotube from self-intersection and stiffens its behaviour under compression. Figure 3.9 shows the resulting postbuckling pattern with the three perpendicular fins at the end of deformation. The colour mapping indicates the local changes in bonded energy
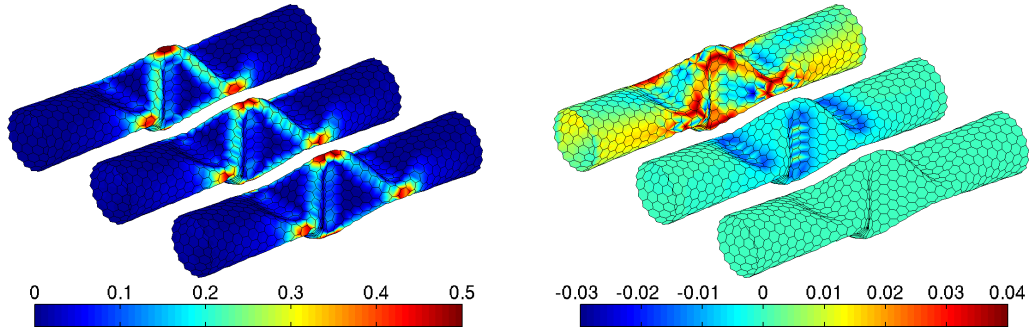
Figure 3.9: Molecular statics approach: The deformed structures of the axially compressed (18,0) carbon nanotube with colour mapping of the local bonded energy per atom [eV/atom] (left) and the local non-bonded energy per atom [eV/atom] (right) for the simulations with included 1-4 non-bonded interactions, excluded 1-4 non-bonded interactions and completely without non-bonded interactions, aligned from rear to front.

(left) and non-bonded energy (right) relative to the relaxed carbon nanotube. At the back, the simulation with included 1-4 non-bonded interactions is illustrated whereas the middle pictures

report the tube with excluded 1-4 non-bonded interactions and the images in the front show the tube without non-bonded interactions. Comparable buckled structures are reported in the literature for example by Arroyo [2], Arroyo and Belytschko [5], Leung *et al.* [29], Liu *et al.* [30], Liu *et al.* [31], Pantano *et al.* [39], Sears and Batra [45], Sun and Liew [50] and Yakobson *et al.* [62] for various carbon nanotubes under axial compression. This example depicts a possible variant for the evaluation of complex non-linear load-deformation graphs with the help of path-following algorithms. The handling of these intricate paths confirms the reliability of the implementation. Within this example, the need for an inclusion of non-bonded interactions is highlighted once more and the influence of their particular modelling is worked out. Additional investigations on the influence of the different variants for modelling non-bonded interactions are performed in the following simulations on carbon nanotubes under bending.

3.5.3 Bending of carbon nanotubes

Here, two types of displacement-driven loading are distinguished: the so-called ideal bending and the sharp bending type, which differ in the way of applying the bending constraints. In a first step for both models, the nanotube is relaxed to achieve an unbent tube. This unbent carbon nanotube owns its characteristic diameter and length, which are further necessary for the calculation of the displacement constraints. In addition, the relaxed carbon nanotube serves as energy ground state. Figure 3.10 illustrates the relaxed carbon nanotube with two constrained ends. Moreover, for a given bending angle α, the locations of these ends are given for the two different types of bending constraints. The detailed evaluation of the prescribed locations is specified in the following.
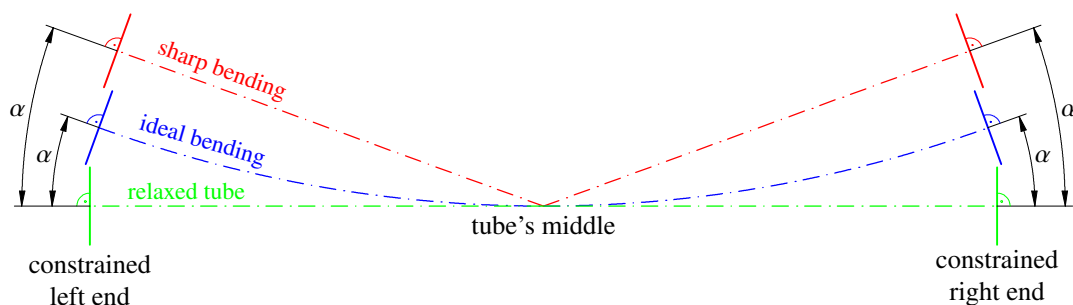
Figure 3.10: Molecular statics approach: Illustration of the displacement-driven ideal bending and sharp bending type. The relaxed carbon nanotube with two constraint ends and the resulting locations for these ends if the displacement constraints dedicated to ideal and sharp bending are applied for the same bending angle.

- **Ideal bending**
  Within the ideal bending, the ends of the tube are rotated rigidly in opposite direction. The positions of the corresponding atoms (two rows per side) can be calculated by assuming that the deformed centerline forms an arc having the fixed length of the relaxed tube. The cross sections of the constrained endings are perpendicular to the ideal deformed axis during the entire loading. In contrast to a pure bending mode, the cross sections of the constrained ends remain circular whereas cross sections in the middle of the bent tube become oval.

- **Sharp bending**
  Within the type of sharp bending, the constraints are imposed as follows. Starting from the relaxed tube, the bending constraints are imposed by rotating both ends of the tube in opposite direction. This rotation is performed about an axis through the tube's middle and perpendicular to the centerline of the relaxed tube. Here, on both ends, two rows of atoms are constrained. These two rows per end therefore undergo a rigid body rotation with constant distance from the pivot. As a consequence, the cross sections of these rows remain circular throughout the whole process of loading.

In Figure 3.10, the dashed-dotted green line represents the centerline of the relaxed tube having its associated length. Applying the indicated bending procedures for a given bending angle α, the locations of the constrained ends can be specified. Thereby, the length of the dashed-dotted blue line (ideal bending) and the length of the dashed-dotted red line (sharp bending) are even and equivalent to the length of the relaxed tube. In addition, it can be seen that for the same bending angle, the sharp bending type generates a larger deformation compared to the ideal bending type.

Single-walled carbon nanotube under ideal bending

This first example deals with a single-walled (10,10) armchair carbon nanotube with a length of 40 honeycomb cells under displacement-driven ideal bending loading. The aim of this example is to show the effect of modelling the in-layer non-bonded interactions. For this purpose, three different settings are distinguished. In the first one, the non-bonded interactions are completely
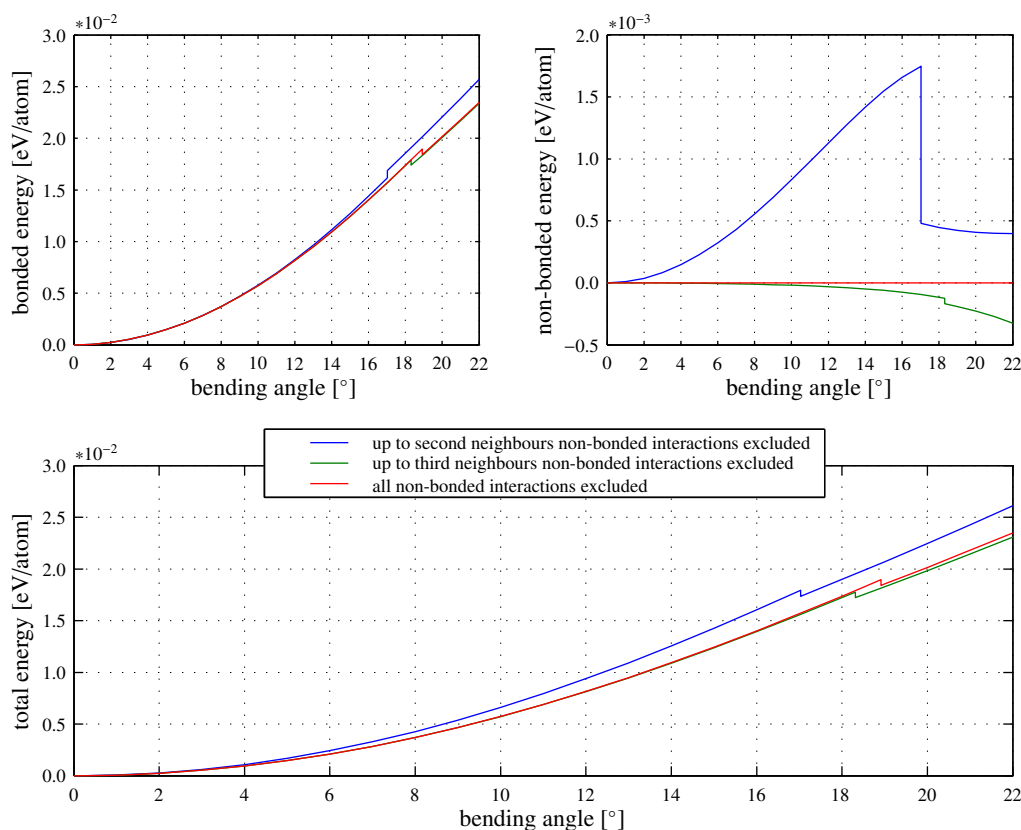
Figure 3.11: Molecular statics approach: The energy evolutions for the ideally bent (10,10) carbon nanotube. Comparison between the different types of modelling in-layer non-bonded interactions.

neglected. In the second case, all non-bonded interactions between atoms up to three bonds apart (1-4 interactions) are disregarded. In the last modelling step, only the non-bonded pairs of atoms up to two bonds distance (1-3 interactions) are excluded. In addition, in the two settings, which consider in-layer non-bonded interactions, an upper cut-off radius of 1.8 nm is implemented. In all cases, the carbon nanotube is bent to the point where the structure loses stability. The associated critical bending angles are 18.914° (all non-bonded interactions excluded), 18.313° (up to third neighbours non-bonded interactions excluded) and 17.030° (up to second neighbours non-bonded interactions excluded). At this point, the corresponding eigenform is superimposed, and the buckled configuration featuring a single kink in the middle of the tube is further bent. The

loading was always applied in 25 steps and ends at a bending angle of 22.0°. Figure 3.11 shows the evolution of the energies for the different simulation setups. From this it can be seen that the case of only excluding non-bonded interactions up to the second neighbours gives slightly different energy plots compared with those of the other two variants. Especially, the non-bonded energy starting with an initial ascent suffers a large decrease at the buckling point. Another interesting fact is the jump of the bonded energy to a higher level after the instability is passed while both remaining variants show a drop in this curve. The combination of both energies leads to a decay in the buckled configuration, which strengthens the principle of minimum energies for the stable path. A clarification and explanation for the occurrence of a jump in the energy evolutions at the corresponding buckling point is given in the studies of Subsection 4.9.3. With regard to the total energy behaviour, the second neighbours variant is subjected to the highest energy level throughout the whole loading process. It can also be seen that the critical buckling angle depends on the type of modelling the non-bonded interactions with the second neighbours variant exhibiting the lowest critical angle. In conclusion, it can be said that the non-bonded interactions modelling with the second neighbours variant imposes additional stretching of bonds. This is because the small distance between atoms only three bonds apart results in high repulsive non-bonded forces. Figure 3.12 shows the mapping of the local bonded and non-bonded energy per atom for the final
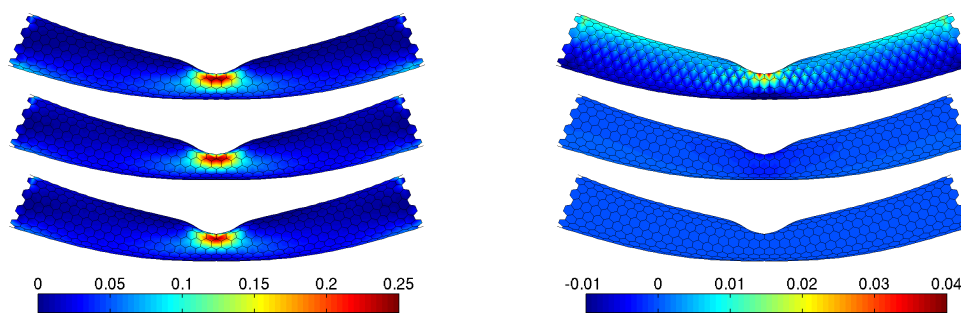
Figure 3.12: Molecular statics approach: The deformed structures of the ideally bent (10,10) carbon nanotube with colour mapping of the local bonded energy per atom [eV/atom] (left) and the local non-bonded energy per atom [eV/atom] (right) for different types of in-layer non-bonded interactions modelling. The topmost structures show the second neighbours variant (1-4 interactions included) and the middle ones the third neighbours variant (1-4 interactions excluded) whereas the lowermost are modelled completely without non-bonded interactions.

configurations of the different variants at 22.0° of bending angle. The colouring gives the relative changes in energies with the relaxed nanotubes as basis. Here again, the locally largest increase in energies can be found in the second neighbours variant.

Single-walled carbon nanotube under sharp bending

In this second example, the single-walled (10,10) armchair nanotube with a length of 40 hexagon cells from the previous simulation is studied again. Now, the loading is applied in the sharp bending variant up to an angle of 22.0 degrees. The non-bonded interactions are once again modelled with the three different variants from before. The energy plots for these settings were computed by means of 25 load increments and are given in Figure 3.13. Again, the second neighbours variant diverges from the other types with its bonded energy being lower and its non-bonded energy being higher during the loading process. The critical bending angle for this variant is lower compared to the others as well. In particular, the obtained critical bending angles are as follows: 11.533° (all non-bonded interactions excluded), 11.339° (up to third neighbours non-bonded interactions excluded) and 10.890° (up to second neighbours non-bonded interactions excluded). When it comes to the total energies, all variants show a decay when switching from the primary path to the buckled
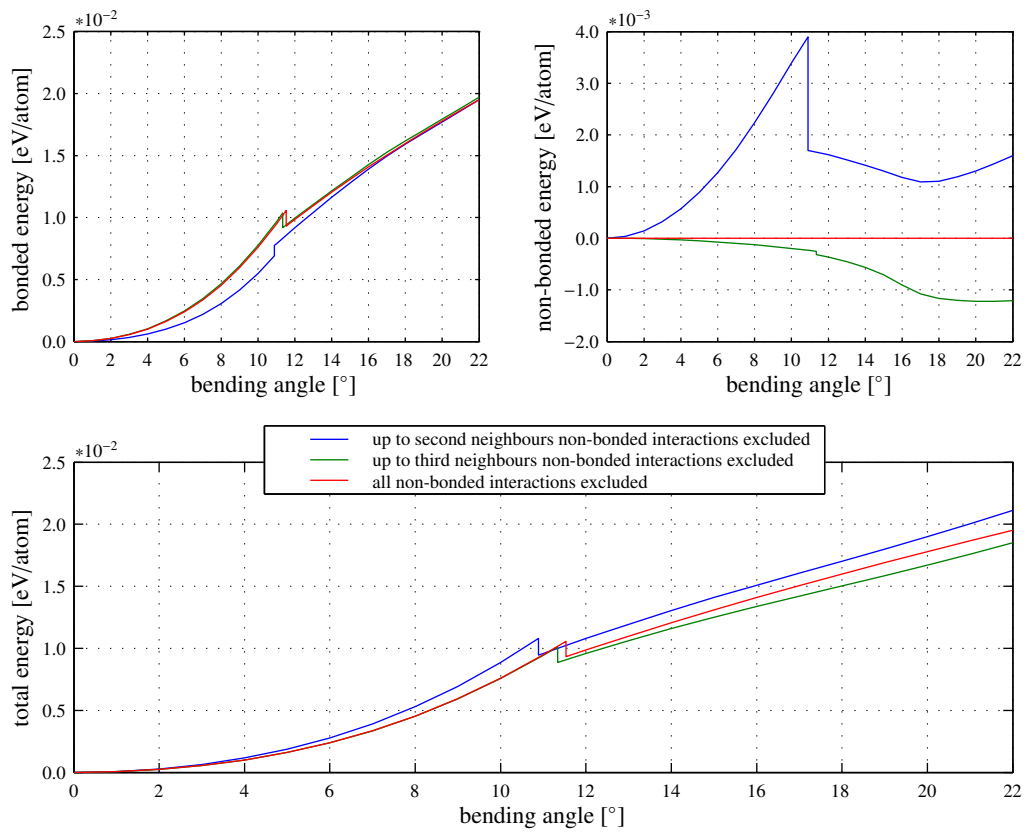
Figure 3.13: Molecular statics approach: The energy evolutions for the sharply bent (10,10) carbon nanotube. Comparison between the different types of modelling in-layer non-bonded interactions.
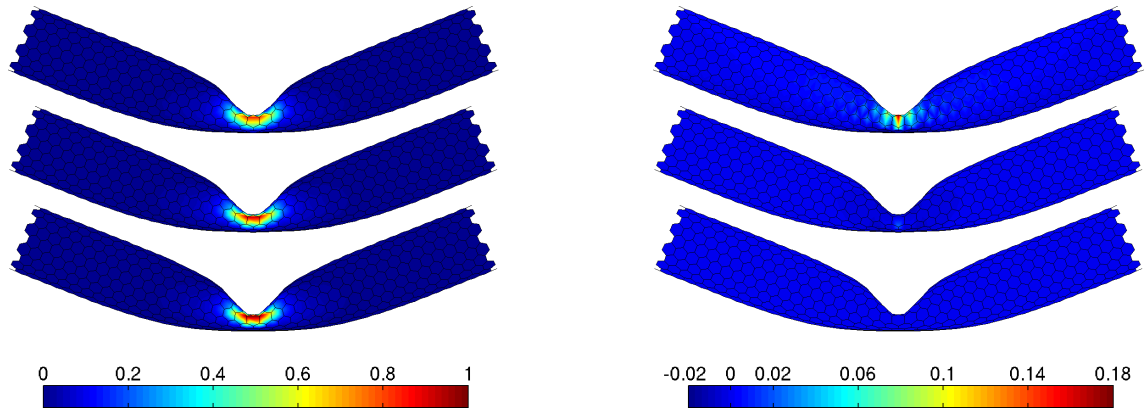
Figure 3.14: Molecular statics approach: The deformed structures of the sharply bent (10,10) carbon nanotube with colour mapping of the local bonded energy per atom [eV/atom] (left) and the local non-bonded energy per atom [eV/atom] (right) for different types of in-layer non-bonded interactions modelling. The topmost structures show the second neighbours variant (1-4 interactions included) and the middle ones the third neighbours variant (1-4 interactions excluded) whereas the lowermost are modelled completely without non-bonded interactions.

configuration branch. These buckled structures show a single bulge in the tube middle section that can be seen in Figure 3.14, which maps the local changes in bonded and non-bonded energy per atom. When the bending angle gets larger then about 17°, the alternate sides of the tube's middle section attain the van der Waals equilibrium distance for the non-bonded interactions. This is characterised by a flattening and a subsequent increase in the non-bonded energy evolutions. In Figure 3.14, it can be seen that the opposite zones of the undermost tube have already moved closer compared with the other variants. This confirms the need for an inclusion of in-layer non-bonded contributions to avoid self-intersections of the tube on further bending. In the case of sharp bending, the locally highest increase in bonded energy is detected in the variant without non-bonded contributions due to the sharper kink.

Single-walled carbon nanotube: ideal bending versus sharp bending

This survey compares the behaviour of the single-walled (10,10) carbon nanotube with a length of 40 honeycomb cells under ideal bending loading with the one of the sharp bending scenario. The objective of this section is to demonstrate the influence of the displacement constraints on the deformation characteristics of the bent nanotubes. From the three variants of modelling the non-
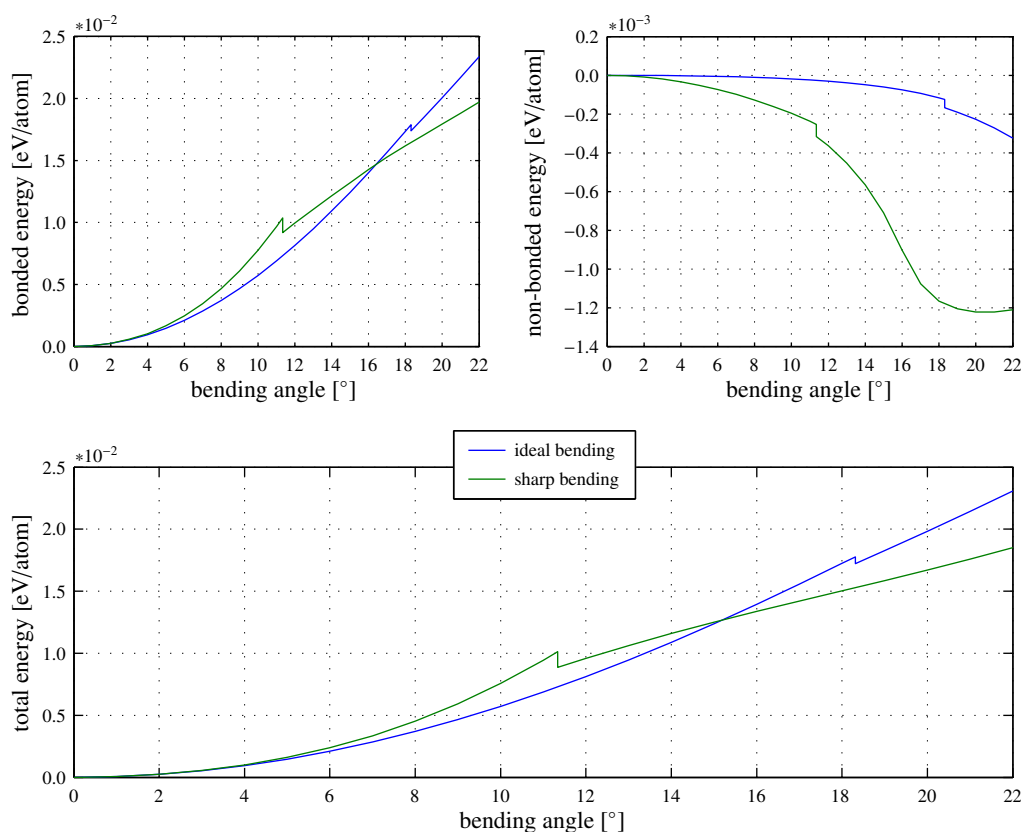
Figure 3.15: Molecular statics approach: The energy evolutions for the comparison between the ideally and sharply bent (10,10) carbon nanotube.

bonded interactions, the one excluding all interactions up to the third neighbours (1-4 interactions) is picked up for comparison. For this, the corresponding results of the preceding studies are reused. Figure 3.15 plots the energy evolutions for both types of loading. The curves for the bonded energy shows that the sharp bending leads to higher values before buckling and to lower values after a certain bending angle. This is a result of the bending displacement constraints that lead to a larger strain in the middle of the tube for the sharp bending mode. As a consequence, the critical

bending angle is reached earlier for this mode, too. To be more accurate, the ideally bent carbon nanotube buckles at a bending angle of 18.313° whereas the sharply bent nanotube loses stability at a bending angle of 11.339°. Nevertheless, both types of loading end up with a single buckle in the nanotube. Similar results of buckled configurations are for instance reported in the papers of Arroyo and Belytschko [3], Cao and Chen [12], Guo *et al.* [23], Iijima *et al.* [26], Mylvaganam *et al.* [36], Pantano *et al.* [40], Sun and Liew [49] and Yakobson *et al.* [62] for bent single-walled carbon nanotubes with mixed dimensions. The change in non-bonded energy relative to the relaxed tube shows a decrease for both loading modes. For the sharp bending mode, an increase in non-bonded energy at higher bending angles can be observed. This is the result of the opposite wall faces that converge to the range of the van der Waals equilibrium distance bewaring the nanotube from self-intersection. The evolution of the total energy shows a jump to lower energy for both loading versions. At the beginning of the loading, the sharp bending mode has a higher total energy level. This fact changes at an angle of about 15° when the ideal bending mode reaches a higher total energy. The deformed structures for the end of loading at 22.0° are given in Figure 3.16 with colour mappings of the relative local changes in bonded and non-bonded energy per atom. The ideally bent tube on the top has a smoother buckle compared with the sharply bent nanotube on the bottom.
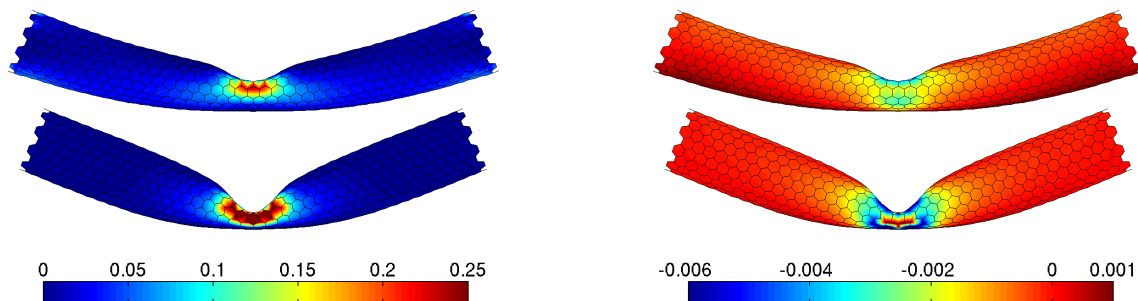
Figure 3.16: Molecular statics approach: Comparison between the deformed structures of the ideally (top row) and the sharply (bottom row) bent (10,10) carbon nanotube with colour mapping of the local bonded energy per atom [eV/atom] (left) and the local non-bonded energy per atom [eV/atom] (right).

Double-walled carbon nanotube under bending

In this example, a (10,10) - (15,15) double-walled carbon nanotube with 50 hexagonal cells in length under bending load is considered. A comparison between sharp and ideal bending is performed. With respect to the non-bonded interactions, the influence of the in-layer and inter-layer interactions is analysed. For the in-layer non-bonded properties, possible interactions are excluded up to the third neighbours (1-4 interactions). In addition, for both types of non-bonded interactions, an upper cut-off radius of 0.9 nm is introduced to reduce the large amount of potential interactions. Whereas the inner layer owns 2020 atoms, the larger outer layer has 3030 atoms. The diameters of the two walls are chosen such that the space between them is approximately the van der Waals equilibrium distance. In a first calculation step, the multi-walled carbon nanotube is relaxed to get a reference configuration. This relaxed tube is the basis for applying the different displacement constraints. Altogether, 23 increments were relevant for each bending procedure to obtain the final buckled structure. Figure 3.17 reports the energy graphs for both types of loading. As already perceived in the numerical examples on single-walled nanotubes, the sharply bent double-walled carbon nanotube again reaches the critical point earlier than the ideally bent tube. In particular, the ideal bending mode gives an associated bending angle of 14.219° and the sharp bending mode results in a bending angle of 9.775°. A response similar to the examples above can also be found in the total energy progress with the ideal bending mode having a lower level
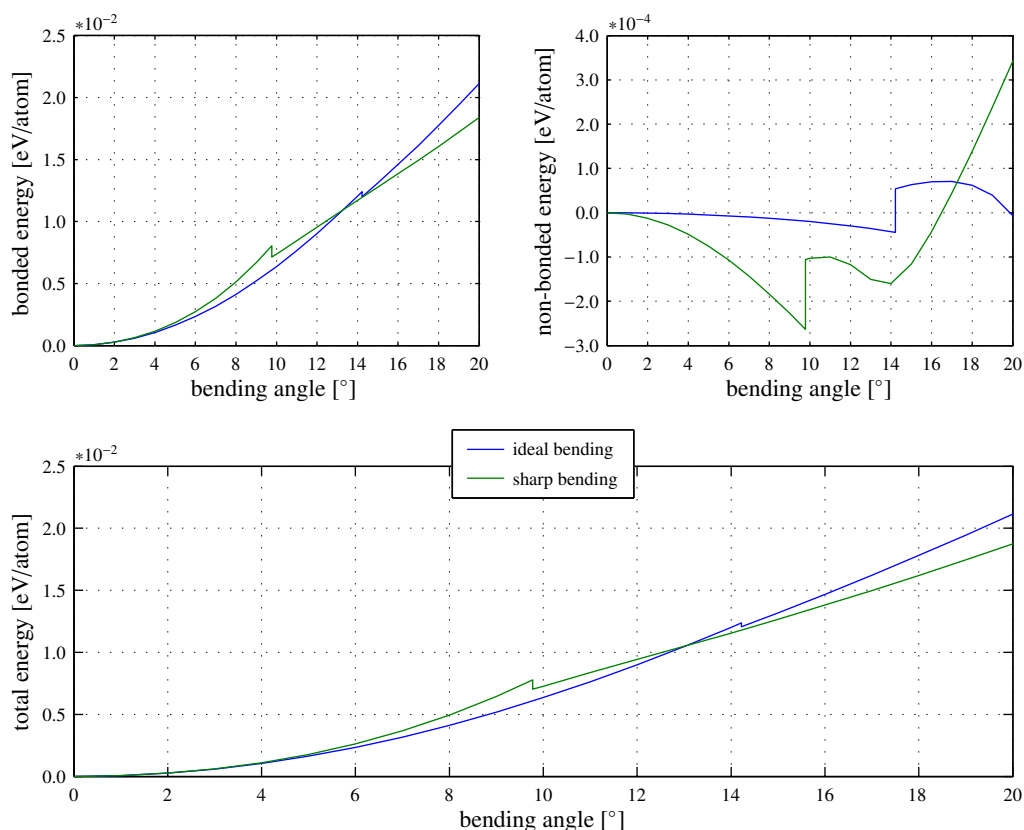
Figure 3.17: Molecular statics approach: The energy evolutions for the comparison between the ideally and sharply bent (10,10) - (15,15) carbon nanotube.

at the beginning and a higher level at the end of deformation. In all curves, the buckling point is characterised by a jump in energy. In Figure 3.18, it can be seen that the buckled configurations exhibit a single kink in the middle of the double-walled tubes. After passing the buckling point, the non-bonded energy jumps to a higher level in both modes. After that, it slightly increases followed by a new decrease to a local minimum. At this stage, the opposite walls of the inner layer come into relevant self-contact within approximately the van der Waals equilibrium distance for the non-bonded interactions. This can be seen in particular for the sharply bent type due to its earlier appearance. The ideally bent tube shows a similar response at a larger bending angle. After passing this local minimum, the approached walls of the inner layer are forced to move closer. This pushes them out of the equilibrium distance, resulting in an increase of the non-bonded energy. Figure 3.18 reports the deformed configurations for the bent double-walled carbon nanotube mapping the local change in both bonded and non-bonded energy relative to the relaxed tube. The three structures at the top represent the ideally bent tube with a fragmentation into outer and inner wall and their combination with translucent outer layer. The same method of illustration is performed for the sharply bent nanotube in the three images at the bottom. It can be observed that the ideal bending mode forms a smoother buckle than the sharp bending mode. Locking at the different walls, the kink in the outer layer is sharper for both types of bending loading. Comparable results for the sharply bent carbon nanotube with the same dimensions can be found in Arroyo [2] and Arroyo and Belytschko [5]. The single kinks in the middle of bent double-walled carbon nanotubes were reported by Iijima *et al.* [26] as well. When focusing on the buckle, the significance of the inter-layer non-bonded interactions comes into play. This type of interactions ensures that the kink develops in both walls of the tube and that penetration does
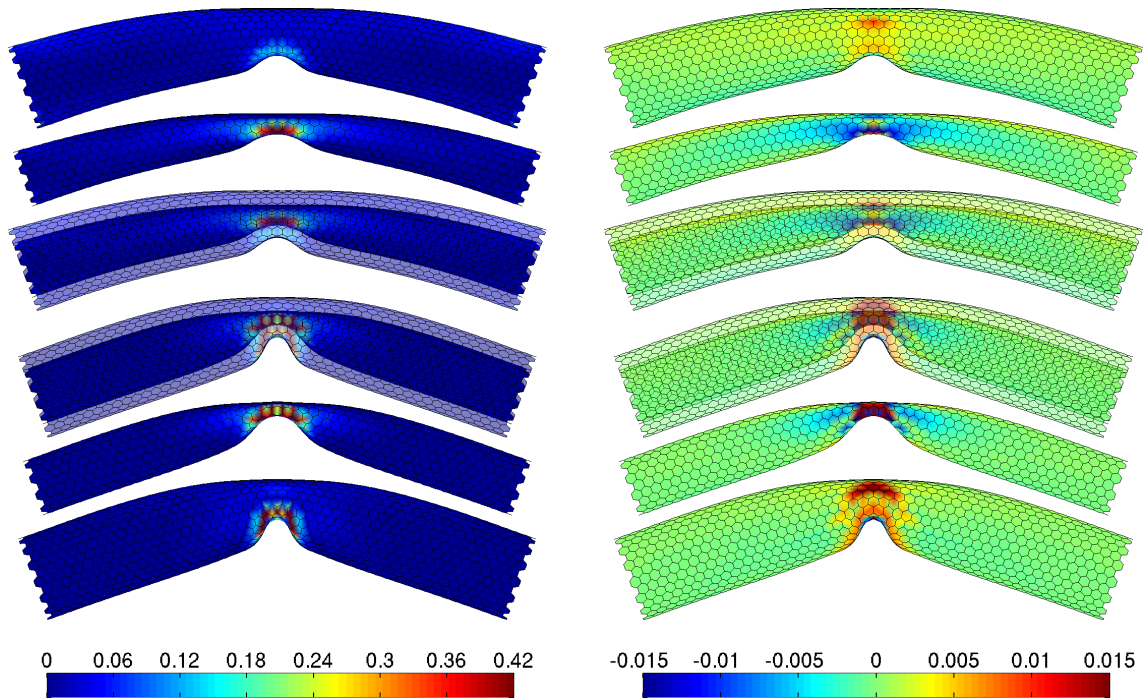
Figure 3.18: Molecular statics approach: Comparison between the deformed structures of the ideally and sharply bent (10,10) - (15,15) carbon nanotubes with colour mapping of the local bonded energy per atom [eV/atom] (left) and the local non-bonded energy per atom [eV/atom] (right). The three images at the top of both sides show the ideally bent nanotube with separated walls and in combination with transparent outer wall. The sharply bent carbon nanotube is displayed in the three images at the bottom of both sides in a joint version with translucent outer layer and a split version with individual walls.

not occur. The relative change in energies at the final deformed configurations is higher in the sharp bending variant for both the bonded and the non-bonded energy. The colour mapping also shows that the inner wall suffers the locally larger changes in energies for both methods. Although the level of change in non-bonded energy is much smaller than the change of bonded energy, in particular, this non-bonded contributions determine the morphology of the kink.

3.6 Summary

A molecular statics approach is applied in order to analyse the buckling behaviour of carbon nanotubes. In particular, the atom-related finite element formulation proposed by Wackerfuß [56] is used. This approach allows the incorporation of molecular statics into the classical finite element framework. As a consequence, efficient and well established algorithms can be reused, which enable the opportunity to analyse nanostructures in a numerical setting. These structures are represented in molecular statics by a discrete number of interacting atoms. The total potential energy of the carbon nanotube considers bonded-interactions, non-bonded interactions and external contributions. Therefrom, equilibrium configurations of the atomistic structure are specified. The resulting non-linear system of equations is solved iteratively, using either a Newton-Raphson approach or an arc-length procedure. Additionally, a criterion for the structural stability of the carbon nanotube is derived. For these purposes, a complete linearisation of the fully non-linear molecular statics model is given. An atom-related finite element for the consideration of bonded interactions is formulated and the associated element force vector and the element stiffness matrix are specified. Furthermore, the non-bonded interactions are implemented into the computational framework by means of a spring finite element. The stability of the structure is observed by an accompanying eigenvalue analysis of the global stiffness matrix, and the critical points are located by a bisection procedure. A branch switching algorithm is applied in order to determine the buckled configuration of the carbon nanotube. The universal applicability of the implemented molecular statics approach is indicated by various numerical simulations of carbon nanotubes under different loading conditions. In the observed examples, in particular, the importance of modelling non-bonded interactions and their influence on the buckling behaviour is emphasised.

The first example on twisted carbon nanotubes is used to study the difference of the unstable and the stable, buckled structure. In addition to these perfect structures, a defective nanotube is simulated for comparison. The second nanotube under torsional loading investigates the modelling of in-layer non-bonded interactions, and it is highlighted that their inclusion is important to avoid the nanotube from self-intersection. This example confirms the handling of complex deformation paths with multiple instability points. Consequently, this simulation relies on a proper stability analysis and a suitable branch switching algorithm.

In the numerical simulations of carbon nanotubes under axial compression, global and local buckling characteristics are observed. The first example exhibits a global Euler-like buckling mode, which on further compression leads to bending and therefore an additional instability point with a localised single kink in the middle of the tube. An additional example deals with a larger carbon nanotube under axial compression, constrained to a local buckling mode. This nanotube is analysed by a path-following procedure, and a non-linear load-deformation plot is derived showing the well-known snap back behaviour from thin shell buckling. In addition, the influence of non-bonded interactions on the buckling behaviour of carbon nanotubes and their type of modelling is studied within this simulation.

In the examples on the bent single-walled and double-walled carbon nanotubes, the influence of modelling non-bonded interactions is analysed. In the bending scenarios, the load is applied in two different ways, denoted as ideal bending and sharp bending. Thereby, the sharp bending constraints lead to a higher local deformation in the tube's middle than the ideal bending type, inducing a smaller buckling angle. In particular, detailed studies into the modelling of in-layer non-bonded interactions are carried out on a single-walled carbon nanotube. The analysis of inter-layer non-bonded interactions is performed by a double-walled carbon nanotube. These studies emphasise that a proper modelling of in-layer and inter-layer non-bonded interactions is important to prevent the carbon nanotubes from self-intersection and penetration.

4 Mixed atomistic-continuum model

This chapter introduces the mixed atomistic-continuum model and its application in the numerical buckling analysis of carbon nanotubes by means of the finite element method. The mixed atomistic-continuum model is based on the quasi-continuum method as given in Tadmor *et al.* [52] and Tadmor *et al.* [53]. In particular, the generalisation of this universal method to curved crystalline monolayer sheets, developed by Arroyo [2] and Arroyo and Belytschko [3, 4, 5, 6], is used and, in a second step, modified. Within this approach, arbitrary shaped single-layer lattices are modelled as free formed continuum surfaces without thickness. The chapter is organised as follows: At the outset, a brief overview of the continuum mechanical treatment of space-filling bodies is given and the linkage of the atomistic deformation to that of the continuum is specified. Then, the continuum mechanical description for solids of reduced dimensionality is presented for the purpose of handling surfaces without thickness. This is followed by a discussion on the correlation between the deformation of the lattice vectors and the deformation of the curved continuum surface. Then, the constitutive model for the continuum approach is formulated on the basis of the quasi-continuum method. In the course of this, the underlying atomistic structure and the associated interatomic potentials are considered and, consequently, the approach is denoted as mixed atomistic-continuum model. Next, the continuous description for the global equilibrium is handled and the corresponding criterion for structural stability is specified. Then, the numerical implementation of the mixed atomistic-continuum model, employing the finite element method, is given. Finally, numerical studies on buckling of carbon nanotubes demonstrate that the mixed atomistic-continuum model is able to reproduce the behaviour of the full atomistic calculation.

4.1 Continuum kinematics for space-filling bodies

This section introduces briefly the continuum mechanical background for the kinematics of space-filling bodies. In general, a space-filling body can be imagined as an open subset of the ambient Euclidean space. However, the following overview concentrates on three-dimensional bodies embedded in a three-dimensional Euclidean space. In particular, the finite kinematics of the continuum is outlined. Firstly, the motion of a body and its related deformation map are presented. Then, the deformation gradient and the right Cauchy-Green deformation tensor are introduced. See classical text books on continuum mechanics for instance Bonet and Wood [9] or Marsden and Hughes [34] for a detailed treatment.

4.1.1 Deformation map

In classical continuum mechanics, the subject under consideration is a continuous body assembled of material particles. This body can be described in different configurations, which are illustrated in Figure 4.1. In the initial setup at time $t = 0$, the particles of the body are characterised by their position X. The associated position vector $\mathbf{X}$ is defined by Cartesian coordinates $\{X^1, X^2, X^3\}$ in the standard basis $\mathcal{B}_0 = \{\mathbf{E}_1, \mathbf{E}_2, \mathbf{E}_3\}$. This undeformed state Ω_0 is called material or Lagrangian configuration. As time passes by, the body deforms and the positions x of the particles at $t \neq 0$ are attained. The dedicated position vector $\mathbf{x}$ is denoted in the standard basis $\mathcal{B} = \{\mathbf{e}_1, \mathbf{e}_2, \mathbf{e}_3\}$ by Cartesian coordinates $\{x^1, x^2, x^3\}$. The corresponding deformed status Ω is called spatial or Eulerian configuration. The motion of particles between the undeformed and the deformed configuration is specified by the deformation map Φ. This map allows the definition of the current particle position vector $\mathbf{x} = \boldsymbol{\Phi}(\mathbf{X}, t)$ as a function of its initial position vector and time. For the purpose of a numerical formulation, an additional parametric or reference body $\bar{\Omega}$ is introduced.
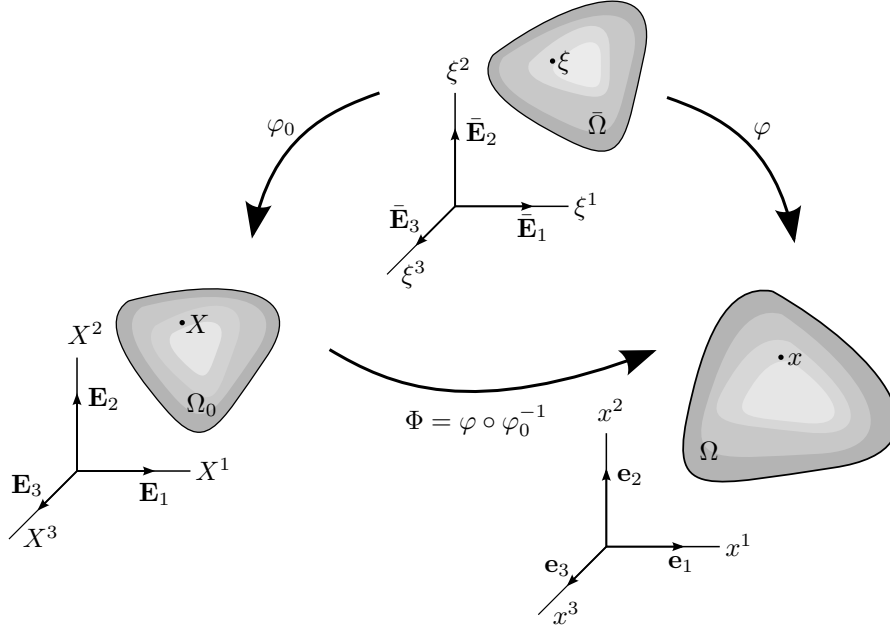
Figure 4.1: Kinematic setting of the space-filling continuous body. The Lagrangian configuration Ω_0, the Eulerian configuration Ω and the parametric body $\bar{\Omega}$ with the corresponding non-linear deformation maps.

In this parameter configuration, the positions of particles are specified by ξ. Additionally, the related position vector $\boldsymbol{\xi}$ is described by Cartesian coordinates $\{\xi^1, \xi^2, \xi^3\}$ in the standard basis $\bar{\mathcal{B}} = \{\bar{\mathbf{E}}_1, \bar{\mathbf{E}}_2, \bar{\mathbf{E}}_3\}$. With the help of this parametric body, an undeformed configuration map φ_0 can be defined. In addition, the parametric body is mapped into the deformed body by the deformed configuration map φ. On the basis of these correlations, the deformation map from the undeformed to the deformed body can finally be rewritten as:

$$\Phi = \varphi \circ \varphi_0^{-1} \tag{4.1}$$

The parameter configuration allows a description of position vectors in the Lagrangian configuration as $\mathbf{X} = \boldsymbol{\varphi}_0(\boldsymbol{\xi})$, or in a more common notation as $\mathbf{X} = \mathbf{X}(\boldsymbol{\xi})$. Furthermore, the position vectors in the Eulerian configuration are denoted as $\mathbf{x} = \boldsymbol{\varphi}(\boldsymbol{\xi}, t)$, or equivalently as $\mathbf{x} = \mathbf{x}(\boldsymbol{\xi}, t)$.

4.1.2 Deformation gradient

The deformation gradient $\mathbf{F}$ is an important quantity in continuum mechanics. As illustrated in Figure 4.2, this quantity allows the linkage of infinitesimal material vectors $d\mathbf{X}$ to their corresponding infinitesimal spatial vectors $d\mathbf{x}$.

$$d\mathbf{x} = \mathbf{F}d\mathbf{X} \tag{4.2}$$

Therefore, the deformation gradient maps vectors from the tangent space $T\Omega_0$ of the undeformed configuration to the tangent space $T\Omega$ of the deformed configurations and is defined as:

$$\mathbf{F} = \frac{\partial \boldsymbol{\Phi}}{\partial \mathbf{X}} = \nabla_{\mathbf{X}} \boldsymbol{\Phi} \tag{4.3}$$
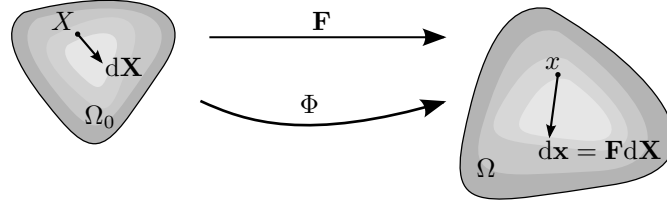
Figure 4.2: The local deformation gradient $\mathbf{F}$ defines a linear map between material and spatial line elements such that $d\mathbf{x} = \mathbf{F}d\mathbf{X}$.

If the motion is expressed in a commonly used notation as $\mathbf{x} = \mathbf{x}(\mathbf{X}, t)$, the deformation gradient can be given in a well-known format as:

$$\mathbf{F} = \frac{\partial \mathbf{x}}{\partial \mathbf{X}} \tag{4.4}$$

As the deformation gradient is part of both the Lagrangian and Eulerian configuration, it is called a two-point tensor. With the introduction of the parametric body, two additional linear tangent maps appear. These are the tangent map of the undeformed configuration $\mathbf{J} = \nabla_{\boldsymbol{\xi}} \mathbf{X}$ and the tangent map of the deformed configuration $\mathbf{j} = \nabla_{\boldsymbol{\xi}} \mathbf{x}$, which are known as Jacobian tensors. On the basis of these quantities, the deformation gradient can be derived by a composition of the two Jacobians in the following form:

$$\mathbf{F} = \frac{\partial \mathbf{x}}{\partial \mathbf{X}} = \frac{\partial \mathbf{x}}{\partial \boldsymbol{\xi}} \frac{\partial \boldsymbol{\xi}}{\partial \mathbf{X}} = \mathbf{j}\,\mathbf{J}^{-1} \tag{4.5}$$

4.1.3 Right Cauchy-Green deformation tensor

The right Cauchy-Green deformation tensor $\mathbf{C}$ is defined in terms of the deformation gradient $\mathbf{F}$.

$$\mathbf{C} = \mathbf{F}^T \mathbf{F} \tag{4.6}$$

If two different elemental vectors $d\mathbf{X}_1$ and $d\mathbf{X}_2$, which deform to $d\mathbf{x}_1$ and $d\mathbf{x}_2$ are considered, a general measure of deformation is given by the change in their scalar product. An illustration of this situation is given in Figure 4.3. Using the right Cauchy-Green deformation tensor $\mathbf{C}$, the
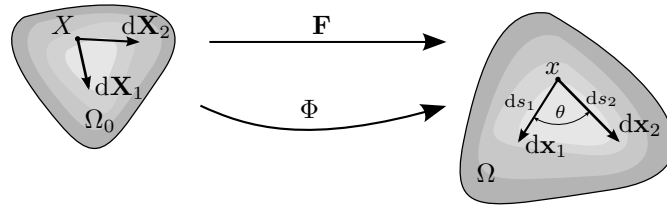
Figure 4.3: Two different elemental vectors $d\mathbf{X}_1$ and $d\mathbf{X}_2$ deforming to $d\mathbf{x}_1$ and $d\mathbf{x}_2$. The lengths ds_1 and ds_2 as well as the enclosed angle θ of the infinitesimal spatial vectors.

scalar product of the infinitesimal spatial vectors can be found in terms of the material vectors.

$$d\mathbf{x}_1 \cdot d\mathbf{x}_2 = d\mathbf{X}_1 \cdot \mathbf{C}d\mathbf{X}_2 \tag{4.7}$$

The change in scalar product includes the stretching of the two vectors and, additionally, the change in their enclosed angle. In terms of the material vectors $d\mathbf{X}_1$ and $d\mathbf{X}_2$ together with the

Green-Lagrange strain tensor $\mathbf{E} = 1/2\,(\mathbf{C} - \mathbf{1})$, this change is defined as:

$$\frac{1}{2}\left(\mathrm{d}\mathbf{x}_1 \cdot \mathrm{d}\mathbf{x}_2 - \mathrm{d}\mathbf{X}_1 \cdot \mathrm{d}\mathbf{X}_2\right) = \frac{1}{2}\left(\mathrm{d}\mathbf{X}_1 \cdot \mathbf{C}\mathrm{d}\mathbf{X}_2 - \mathrm{d}\mathbf{X}_1 \cdot \mathrm{d}\mathbf{X}_2\right)$$
$$= \frac{1}{2}\mathrm{d}\mathbf{X}_1 \cdot (\mathbf{C} - \mathbf{1})\,\mathrm{d}\mathbf{X}_2$$
$$= \mathrm{d}\mathbf{X}_1 \cdot \mathbf{E}\mathrm{d}\mathbf{X}_2 \tag{4.8}$$

The right Cauchy-Green deformation tensor $\mathbf{C}$ allows to calculate the length $\mathrm{d}s$ of an infinitesimal spatial vector $\mathrm{d}\mathbf{x}$ by means of its corresponding infinitesimal material vector $\mathrm{d}\mathbf{X}$.

$$\mathrm{d}s = \|\mathrm{d}\mathbf{x}\| = \sqrt{\mathrm{d}\mathbf{x} \cdot \mathrm{d}\mathbf{x}} = \sqrt{\mathrm{d}\mathbf{X} \cdot \mathbf{C}\mathrm{d}\mathbf{X}} \tag{4.9}$$

Furthermore, the angle θ between two elemental spatial vectors $\mathrm{d}\mathbf{x}_1$ and $\mathrm{d}\mathbf{x}_2$ can be calculated on the basis of their material counterparts $\mathrm{d}\mathbf{X}_1$ and $\mathrm{d}\mathbf{X}_2$ together with the right Cauchy-Green deformation tensor $\mathbf{C}$.

$$\cos\left(\theta\right) = \frac{\mathrm{d}\mathbf{X}_1}{\mathrm{d}s_1} \cdot \mathbf{C}\frac{\mathrm{d}\mathbf{X}_2}{\mathrm{d}s_2} \tag{4.10}$$

4.2 Standard Cauchy-Born rule for space-filling bodies

The aim of this section is to establish a kinematic relation between the continuum and the atomistic structure of the body under consideration. The so-called Cauchy-Born rule, stemming from Born and Huang [10], is a widely accepted fundamental kinematic assumption for the linkage of the atomistic deformation to that of a continuous medium. This rule relies on the assumption that the deformation of the lattice is homogeneous at the atomistic level. Therefore, the deformed lattice can be determined by the deformation gradient $\mathbf{F}$ at the corresponding continuum point. The setting is illustrated in Figure 4.4, displaying the continuum configurations with the underlying atomistic structure, subjected to homogeneous deformation. Starting from an undeformed lattice vector $\mathbf{A}$, the application of the Cauchy-Born rule delivers the deformed lattice vector $\mathbf{a}$.

$$\mathbf{a} = \mathbf{F}\mathbf{A} \tag{4.11}$$

Taking into account the relations from standard continuum mechanics, the geometry of the deformed lattice can be determined. The first relevant quantity is the length a of a deformed
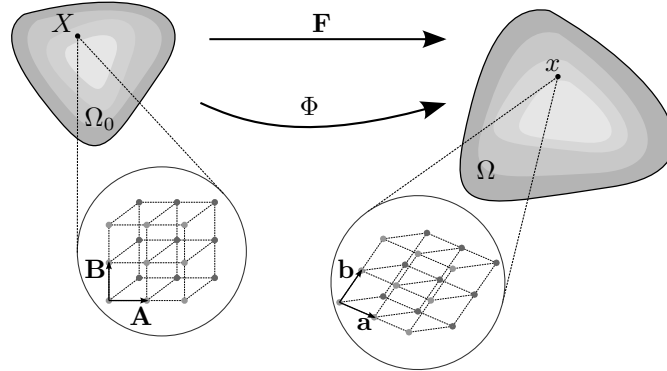
Figure 4.4: Illustration of the standard Cauchy-Born rule for space-filling bodies.

lattice vector $\mathbf{a}$. This value is calculated on the basis of its associated undeformed lattice vector $\mathbf{A}$ and the right Cauchy-Green deformation tensor $\mathbf{C}$.

$$a = \|\mathbf{a}\| = \sqrt{\mathbf{a} \cdot \mathbf{a}} = \sqrt{\mathbf{A} \cdot \mathbf{C}\mathbf{A}} \tag{4.12}$$

Another important factor is the angle θ between two deformed lattice vectors $\mathbf{a}$ and $\mathbf{b}$. Once again, this quantity is evaluated from the corresponding undeformed elements.

$$\cos\left(\theta\right) = \frac{\mathbf{A}}{a} \cdot \mathbf{C} \frac{\mathbf{B}}{b} \tag{4.13}$$

Applying these expressions, the geometry of the embedded deformed lattice is solely specified by the deformation measures of the continuum. As a result of its construction, the standard Cauchy-Born rule is only applicable in the absence of inhomogeneities at the magnitude of atomic spacing. In addition, it is only suitable for space-filling crystals because the deformation gradient maps the tangent space of the undeformed body into the tangent space of the deformed body. To enable the use of the Cauchy-Born rule for inhomogeneous cases and monolayer films, several modifications and extensions were developed. In this context, Leamy *et al.* [28], Guo *et al.* [24], Sunyk and Steinmann [51] and Chandraseker *et al.* [14] extended the standard Cauchy-Born rule by using the gradient of the deformation gradient. This second-order deformation gradient introduces an additional correction term that accounts for the inhomogeneous part of the deformation. Arroyo and Belytschko [3, 5] proposed an extension to the standard Cauchy-Born rule using a concept of differential geometry. This approach is universally applicable in the study of single-layer crystalline films such as carbon nanotubes.

4.3 Continuum kinematics for solids of reduced dimensionality

In this section, the kinematics and the geometric setting for a continuum surface are investigated. With reference to Arroyo [2] and Arroyo and Belytschko [3, 4, 5, 6], this surface is introduced in order to enable the treatment of arbitrary shaped monolayer crystal lattices by means of continuum mechanics. According to the informations given in Section 2.2, the replacement is natural as carbon nanotubes are built of several one atom thick layers of rolled graphene. First, the configurations and the deformation map are specified. Then, the geometric setting of the surface is discussed. Starting with the convected basis, the metric tensor, the curvature tensor and the deformation gradient are introduced. Finally, the normal curvature and, subsequently, the principal curvatures of the continuum surface are presented.

4.3.1 Deformation map

The undeformed configuration Ω_0 and the deformed configuration Ω of the carbon nanotube are represented by arbitrary shaped surfaces in three-dimensional Euclidean spaces. As the surface itself is only two-dimensional, the corresponding reference system $\bar{\Omega}$ is a plane. In what follows, the setting and the necessary kinematic variables are established. Figure 4.5 presents the various configurations and the non-linear deformation maps relating them. The referential body $\bar{\Omega}$ is described by Cartesian coordinates $\{\xi^1, \xi^2\}$ with its standard basis $\bar{\mathcal{B}} = \{\bar{\mathbf{E}}_1, \bar{\mathbf{E}}_2\}$ and the corresponding reciprocal basis $\bar{\mathcal{B}}^* = \{\bar{\mathbf{E}}^1, \bar{\mathbf{E}}^2\}$ is given through $\bar{\mathbf{E}}^\alpha \cdot \bar{\mathbf{E}}_\beta = \delta^\alpha_\beta$, where δ^α_β here and in what follows denotes the Kronecker symbol. The undeformed or Lagrangian configuration Ω_0 at time $t = 0$ is described by Cartesian coordinates $\{X^1, X^2, X^3\}$ with the orthonormal standard basis $\mathcal{B}_0 = \{\mathbf{E}_1, \mathbf{E}_2, \mathbf{E}_3\}$. The associated reciprocal basis $\mathcal{B}_0^* = \{\mathbf{E}^1, \mathbf{E}^2, \mathbf{E}^3\}$ is defined as well. The orthonormal standard basis $\mathcal{B} = \{\mathbf{e}_1, \mathbf{e}_2, \mathbf{e}_3\}$, the related reciprocal basis $\mathcal{B}^* = \{\mathbf{e}^1, \mathbf{e}^2, \mathbf{e}^3\}$ and the Cartesian coordinates $\{x^1, x^2, x^3\}$ define the deformed or Eulerian configuration Ω at time $t \neq 0$. With respect to the parametric space, the undeformed configuration map φ_0 and the deformed configuration map φ can be introduced. With these two distinct maps, the deformation map $\mathbf{\Phi} = \varphi \circ \varphi_0^{-1}$ from the Lagrangian to the Eulerian configuration is given. This map allows to specify the current particle position $\mathbf{x} = \mathbf{\Phi}\left(\mathbf{X}, t\right)$ on the basis of its initial position and time. Furthermore, the application of the undeformed configuration map enables the specification of position vectors in the Lagrangian configuration as $\mathbf{X} = \varphi_0\left(\boldsymbol{\xi}\right)$ or equivalently as $\mathbf{X} = \mathbf{X}\left(\boldsymbol{\xi}\right)$. The position vectors in the Eulerian configuration are denoted as $\mathbf{x} = \varphi\left(\boldsymbol{\xi}, t\right)$ and also in a more usual representation as $\mathbf{x} = \mathbf{x}\left(\boldsymbol{\xi}, t\right)$. Consequently, the position vectors, in both the material and spatial
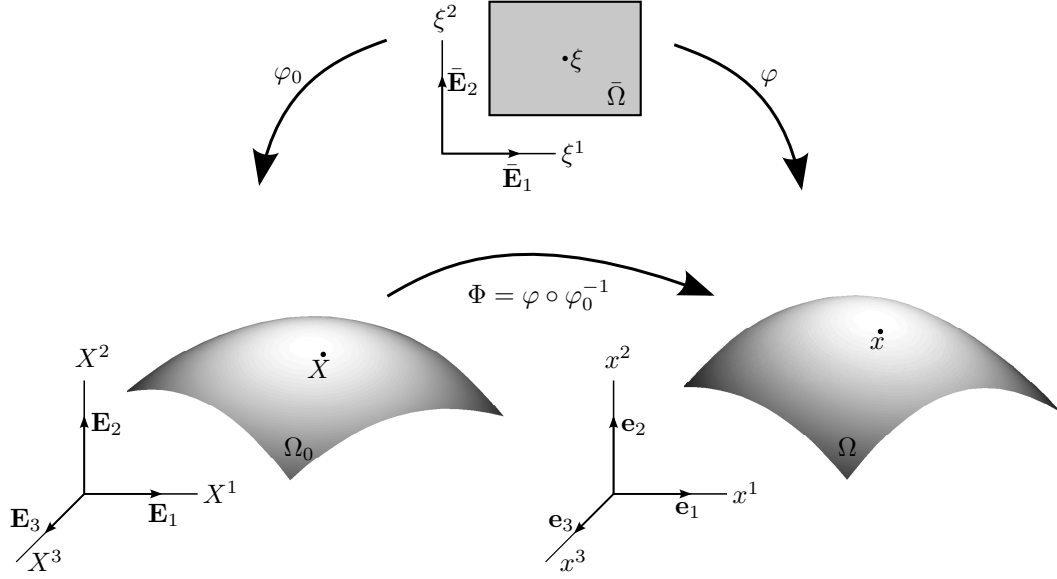
Figure 4.5: Kinematic setting of the continuous surface. The Lagrangian configuration Ω_0, the Eulerian configuration Ω and the parametric body $\bar{\Omega}$ with the corresponding non-linear deformation maps.

setting, are ascertainable from the referential position of the associated particle in the parametric plane.

4.3.2 Convected basis and the tangent plane

As illustrated in Figure 4.6, for the undeformed configuration Ω_0 at point X, and for the deformed configuration Ω at the correlating point x, the plane tangent to the surface can be introduced. Each of these planes represent a linear space, which is denoted as tangent space. In particular, the tangent space $T\Omega_0$ of the undeformed surface is defined by the convected basis $\mathcal{C}_0 = \{\mathbf{G}_1, \mathbf{G}_2\}$. Moreover, the convected basis $\mathcal{C} = \{\mathbf{g}_1, \mathbf{g}_2\}$ specifies the tangent space $T\Omega$ related to the deformed setting. Considering the dependence of the undeformed position vector $\mathbf{X}$ and the deformed position vector $\mathbf{x}$ on the curvilinear coordinates $\{\xi^1, \xi^2\}$ of the parametric space, the covariant base vectors of the tangent plane are defined as:

$$\mathbf{G}_\alpha = \frac{\partial \mathbf{X}}{\partial \xi^\alpha} = \frac{\partial X^A}{\partial \xi^\alpha}\mathbf{E}_A \quad \text{and} \quad \mathbf{g}_\alpha = \frac{\partial \mathbf{x}}{\partial \xi^\alpha} = \frac{\partial x^a}{\partial \xi^\alpha}\mathbf{e}_a \qquad \alpha = 1, 2 \tag{4.14}$$

The corresponding reciprocal bases $\mathcal{C}_0^* = \{\mathbf{G}^1, \mathbf{G}^2\}$ and $\mathcal{C}^* = \{\mathbf{g}^1, \mathbf{g}^2\}$ are defined by the relations $\mathbf{G}^\alpha \cdot \mathbf{G}_\beta = \delta_\beta^\alpha$ and $\mathbf{g}^\alpha \cdot \mathbf{g}_\beta = \delta_\beta^\alpha$. In addition, the unit normals to the undeformed and the deformed body are given by:

$$\mathbf{N} = \frac{\mathbf{G}_1 \times \mathbf{G}_2}{\|\mathbf{G}_1 \times \mathbf{G}_2\|} \quad \text{and} \quad \mathbf{n} = \frac{\mathbf{g}_1 \times \mathbf{g}_2}{\|\mathbf{g}_1 \times \mathbf{g}_2\|} \tag{4.15}$$

Taking into consideration the tangent plane and the normal vectors of the surface, a local convected basis $\widetilde{\mathcal{C}}_0 = \{\mathbf{G}_1, \mathbf{G}_2, \mathbf{N}\}$ for the Lagrangian configuration and a local convected basis $\widetilde{\mathcal{C}} = \{\mathbf{g}_1, \mathbf{g}_2, \mathbf{n}\}$ for the Eulerian configuration can be defined.

The following notations and conventions are as from now used in the current Chapter 4 and in Appendix A. Vectors and tensors are denoted by boldface letters. Furthermore, the components of
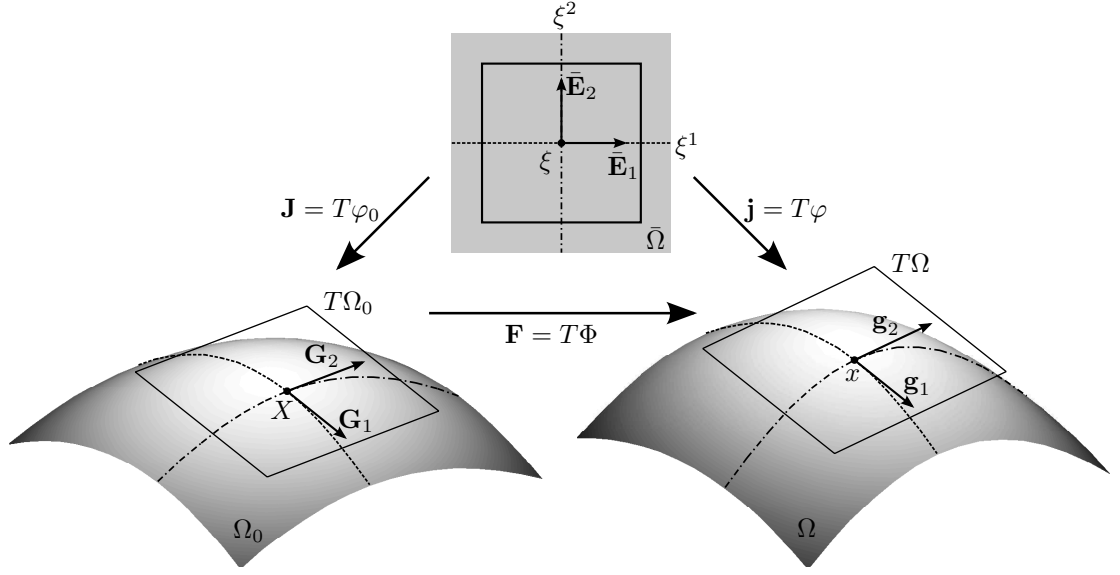
Figure 4.6: The tangent planes of the undeformed and the deformed configuration of the continuous surface with their convected bases and the associated tangent maps.

vectors and tensors in various bases are specified by index notation. Components in the standard basis $\mathcal{B}_0$ of the undeformed configuration are specified by upper case Latin indices (A, B, C, D, E, F) and run in generally from 1 to 2, however, solely for the current Section 4.3, their range is from 1 to 3. Lower case Latin indices (a, b, c, d, e, f, g), running from 1 to 3, denote components in the standard basis $\mathcal{B}$ of the deformed setting. Components in the convected bases $\mathcal{C}_0$ and $\mathcal{C}$ of the associated tangent space, as well as components in the parametric standard basis $\bar{\mathcal{B}}$, are denoted by lower case Greek indices (α, β), which run from 1 to 2. The same indices and ranges are valid for the corresponding reciprocal bases. Moreover, components in the convected basis $\widetilde{\mathcal{C}}$ of the Eulerian configuration are specified by lower case Fraktur indices $(\mathfrak{a}, \mathfrak{b})$, and run from 1 to 3. If the declared indices are repeated in any expression, summation is implied across the associated range. Other indices are not used for the representation of vector and tensor components and, consequently, summation is not implied on occurring repeated indices. Furthermore, the symbol δ equipped with two freely placed indices denotes the Kronecker symbol.

4.3.3 Metric tensor and curvature tensor

With the help of the covariant base vectors of the undeformed and the deformed configuration, the corresponding metric tensors can be calculated with respect to different bases. The material metric tensor $\mathbf{G}$ reads

$$\mathbf{G} = G_{\alpha\beta}\mathbf{G}^\alpha \otimes \mathbf{G}^\beta \tag{4.16}$$

where its covariant components are defined via the covariant base vectors as:

$$G_{\alpha\beta} = \mathbf{G}_\alpha \cdot \mathbf{G}_\beta \tag{4.17}$$

In addition, the material curvature tensor $\mathbf{K}$ is given by:

$$\mathbf{K} = K_{\alpha\beta}\mathbf{G}^\alpha \otimes \mathbf{G}^\beta \tag{4.18}$$

The covariant components depend on the unit normal and the derivatives of the covariant base vectors with respect to the curvilinear coordinates.

$$K_{\alpha\beta} = \mathbf{N} \cdot \mathbf{G}_{\alpha,\beta} \quad \text{with} \quad \mathbf{G}_{\alpha,\beta} = \frac{\partial \mathbf{G}_\alpha}{\partial \xi^\beta} \tag{4.19}$$

The spatial metric tensor $\mathbf{g}$, with covariant components is given by:

$$\mathbf{g} = g_{\alpha\beta}\mathbf{g}^\alpha \otimes \mathbf{g}^\beta \quad \text{with} \quad g_{\alpha\beta} = \mathbf{g}_\alpha \cdot \mathbf{g}_\beta \tag{4.20}$$

The spatial curvature tensor $\mathbf{k}$, expressed in covariant components reads:

$$\mathbf{k} = k_{\alpha\beta}\mathbf{g}^\alpha \otimes \mathbf{g}^\beta \quad \text{where} \quad k_{\alpha\beta} = \mathbf{n} \cdot \mathbf{g}_{\alpha,\beta} \quad \text{with} \quad \mathbf{g}_{\alpha,\beta} = \frac{\partial \mathbf{g}_\alpha}{\partial \xi^\beta} \tag{4.21}$$

Using the metric tensors, the measurement of distances, angles and areas in the undeformed surface Ω_0 and the deformed surface Ω is possible. By means of the curvature tensors, additional information about the surfaces like principal curvatures as well as Gaussian and mean curvature can be stated.

4.3.4 Deformation gradient and pull-back operations

The deformation gradient $\mathbf{F}$ maps elements from the tangent space $T\Omega_0$ of the undeformed surface to the tangent space $T\Omega$ of the deformed configuration via the tangent of the deformation map Φ.

$$\mathbf{F} = T\Phi = T\left(\varphi \circ \varphi_0^{-1}\right) = T\varphi \circ T\varphi_0^{-1} \tag{4.22}$$

For the evaluation of the deformation gradient, the tangent maps

$$\mathbf{J} = T\varphi_0 = \mathbf{G}_\alpha \otimes \bar{\mathbf{E}}^\alpha \quad \text{and} \quad \mathbf{j} = T\varphi = \mathbf{g}_\alpha \otimes \bar{\mathbf{E}}^\alpha \tag{4.23}$$

of the configurations are necessary, with the result that the deformation gradient reads:

$$\mathbf{F} = \left(\mathbf{g}_\alpha \otimes \bar{\mathbf{E}}^\alpha\right) \circ \left(\bar{\mathbf{E}}_\beta \otimes \mathbf{G}^\beta\right) = \delta^\alpha_\beta \mathbf{g}_\alpha \otimes \mathbf{G}^\beta = \mathbf{g}_\alpha \otimes \mathbf{G}^\alpha \tag{4.24}$$

The right Cauchy-Green deformation tensor $\mathbf{C}$ is defined as the pull-back of the spatial metric tensor $\mathbf{g}$.

$$\begin{aligned}
\mathbf{C} &= \Phi^* \mathbf{g} = \mathbf{F}^T \mathbf{g} \mathbf{F} \\
&= g_{\alpha\beta}\mathbf{G}^\alpha \otimes \mathbf{G}^\beta \\
&= g_{\alpha\beta}\frac{\partial \xi^\alpha}{\partial X^A}\frac{\partial \xi^\beta}{\partial X^B}\mathbf{E}^A \otimes \mathbf{E}^B \\
&= C_{AB}\mathbf{E}^A \otimes \mathbf{E}^B
\end{aligned} \tag{4.25}$$

In the same fashion, the pull-back of the spatial curvature tensor $\mathbf{k}$ defines:

$$\begin{aligned}
\mathcal{K} &= \Phi^* \mathbf{k} = \mathbf{F}^T \mathbf{k} \mathbf{F} \\
&= k_{\alpha\beta}\mathbf{G}^\alpha \otimes \mathbf{G}^\beta \\
&= k_{\alpha\beta}\frac{\partial \xi^\alpha}{\partial X^A}\frac{\partial \xi^\beta}{\partial X^B}\mathbf{E}^A \otimes \mathbf{E}^B \\
&= \mathcal{K}_{AB}\mathbf{E}^A \otimes \mathbf{E}^B
\end{aligned} \tag{4.26}$$

4.3.5 Normal curvature and principal curvatures

The normal curvature k, at a point x of the deformed surface, in the direction of the tangential vector $\mathbf{w} = w^\alpha \mathbf{g}_\alpha$, is defined by:

$$k = \frac{w^\alpha k_{\alpha\beta} w^\beta}{w^\alpha g_{\alpha\beta} w^\beta} \tag{4.27}$$

By changing the direction of the tangential vector $\mathbf{w}$, the normal curvature k changes its value. The maximum and minimum of these values are denoted as principal curvatures k_I and k_{II}, and the corresponding directions as principal directions $\mathbf{v}_I$ and $\mathbf{v}_{II}$. The principal curvatures and directions are the solution of the generalised eigenvalue problem

$$\left(\mathbf{k} - k_{I,II} \mathbf{g} \right) \mathbf{v}_{I,II} = \mathbf{0} \tag{4.28}$$

The two principal directions are tangential to the surface and are $\mathbf{g}$-orthogonal vectors.

$$\mathbf{v}_I = (v_I)^\alpha \, \mathbf{g}_\alpha \qquad\qquad \mathbf{v}_{II} = (v_{II})^\alpha \, \mathbf{g}_\alpha \tag{4.29}$$

$$\mathbf{v}_n \cdot \mathbf{g} \, \mathbf{v}_m = (v_n)^\alpha \, g_{\alpha\beta} \, (v_m)^\beta = \delta_{nm} \qquad n, m = I, II \tag{4.30}$$

By appropriate pull-back operations, the spatial normal curvature k can be expressed in the undeformed configuration with $\mathbf{W} = W^A \mathbf{E}_A$ as:

$$k = \frac{W^A \mathcal{K}_{AB} W^B}{W^A C_{AB} W^B} \tag{4.31}$$

The principal curvatures k_I and k_{II}, and the pull-back of the principal directions, namely $\mathbf{V}_I$ and $\mathbf{V}_{II}$, are obtained by solving the generalised eigenvalue problem:

$$\left(\mathcal{K} - k_{I,II} \mathbf{C} \right) \mathbf{V}_{I,II} = \mathbf{0} \tag{4.32}$$

The two eigenvectors $\mathbf{V}_I$ and $\mathbf{V}_{II}$ are now tangential to the undeformed surface and $\mathbf{C}$-orthogonal.

$$\mathbf{V}_I = (V_I)^\alpha \, \mathbf{G}_\alpha \qquad\qquad \mathbf{V}_{II} = (V_{II})^\alpha \, \mathbf{G}_\alpha \tag{4.33}$$

$$\mathbf{V}_n \cdot \mathbf{C} \, \mathbf{V}_m = (V_n)^A \, C_{AB} \, (V_m)^B = \delta_{nm} \qquad n, m = I, II \tag{4.34}$$

In terms of the principal curvatures, the Gaussian curvature

$$K = k_I k_{II} \tag{4.35}$$

and the mean curvature

$$H = \frac{k_I + k_{II}}{2} \tag{4.36}$$

are well defined. As the two principal directions $\mathbf{v}_I$ and $\mathbf{v}_{II}$ are tangential to the deformed surface and are orthogonal unit vectors, they can be used to define a local orthonormal basis $\mathcal{D} = \{\mathbf{v}_I, \mathbf{v}_{II}\}$ of the tangent space. Furthermore, the cross product of the two principal directions defines the unit normal $\mathbf{n} = \mathbf{v}_I \times \mathbf{v}_{II}$, which is equal to the unit normal vector of the deformed surface that is specified in Equation (4.15). Consequently, taking into consideration the principal directions and the unit normal, a local orthonormal basis $\widetilde{\mathcal{D}} = \{\mathbf{v}_I, \mathbf{v}_{II}, \mathbf{n}\}$ for the Eulerian configuration can be defined. Components of vectors in this basis are denoted by a lower case Fraktur index $\mathfrak{c}$ and run from I to III. If the index is repeated, summation across the associated range is implied.

4.4 Cauchy-Born rules for solids of reduced dimensionality

This section is about the linkage of the atomistic lattice deformation to the deformation field of the continuum. When dealing with monolayer crystalline films, it is obvious to treat the substituting continuum solid as a surface. Furthermore, the atoms of the lattice are supposed to lie on this surface and, consequently, the lattice vectors or bonds are chords of the surface. Figure 4.7 shows the undeformed and the deformed continuum with the atoms of the underlying lattices lying on the associated surface. Two representative undeformed lattice vectors $\mathbf{A}$ and $\mathbf{B}$ result due to deformation in their deformed counterparts $\mathbf{a}$ and $\mathbf{b}$. The objective of this section is to characterise
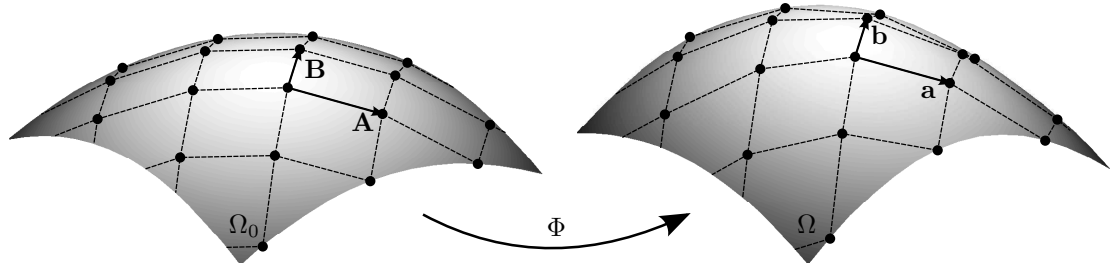
Figure 4.7: The substitute continuum surfaces and the subjacent atomic lattice. The undeformed lattice vectors $\mathbf{A}$ and $\mathbf{B}$ are transformed to the deformed lattice vectors $\mathbf{a}$ and $\mathbf{b}$. In that process, it is supposed that the atoms of the lattice lie on the substituting surfaces.

the geometry of the deformed lattice in terms of continuum deformation measures together with the structure of the undeformed lattice configuration. For this purpose, the undeformed configuration is from now on represented by a plane surface that replaces the flat crystalline sheet. As a consequence of loadings, this sheet deforms and the current configuration is modelled as a curved surface. During
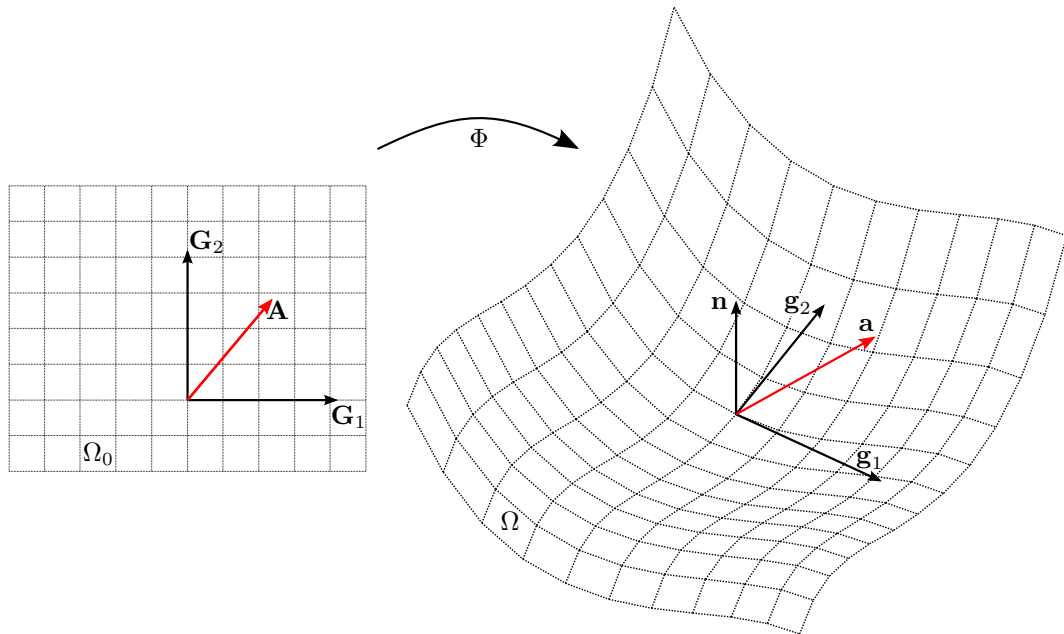
Figure 4.8: The deformation map Φ transforms the undeformed bond vector $\mathbf{A}$ into the exact deformed bond vector $\mathbf{a}$ which is a chord of the continuum surface.

the process of deformation, an undeformed bond vector **A** changes into the associated deformed bond vector **a**. Thereby, the two atoms building a bond are assumed to stay on the surface and the resulting bond is a chord. This general setting is illustrated in Figure 4.8. In the following, several methods for the approximation of the deformed bond vector will be discussed.

4.4.1 Standard Cauchy-Born rule

A first method for the linkage of the continuum deformation to the deformation of the atomistic structure is the use of the standard Cauchy-Born rule. This rule is a widely accepted method, as reviewed in Section 4.2, in the case of space-filling bulk materials. Nevertheless, in the case of solids of reduced dimensionality, the direct application of the standard Cauchy-Born rule leads to some discrepancies. If monolayer crystalline films are modelled as continuum surfaces, the lattice vectors are chords of this surface. An illustration of this fact is given in Figure 4.7 for the entire lattice and in Figure 4.8 for a single bond vector. Thereby, the chords are vectors of finite length that do not belong to the tangent space of the surface. The deformation gradient, however, is only applicable for the mapping of infinitesimal vectors or tangent vectors of the surface. Nevertheless, the usage of the standard Cauchy-Born rule in the treatment of solids of reduced dimensionality maps the undeformed bond vector **A** to a so-called tangent deformed bond vector $\mathbf{w} = \mathbf{F}\mathbf{A}$, which belongs to the tangent space $T\Omega$ of the deformed surface. This situation is presented in Figure
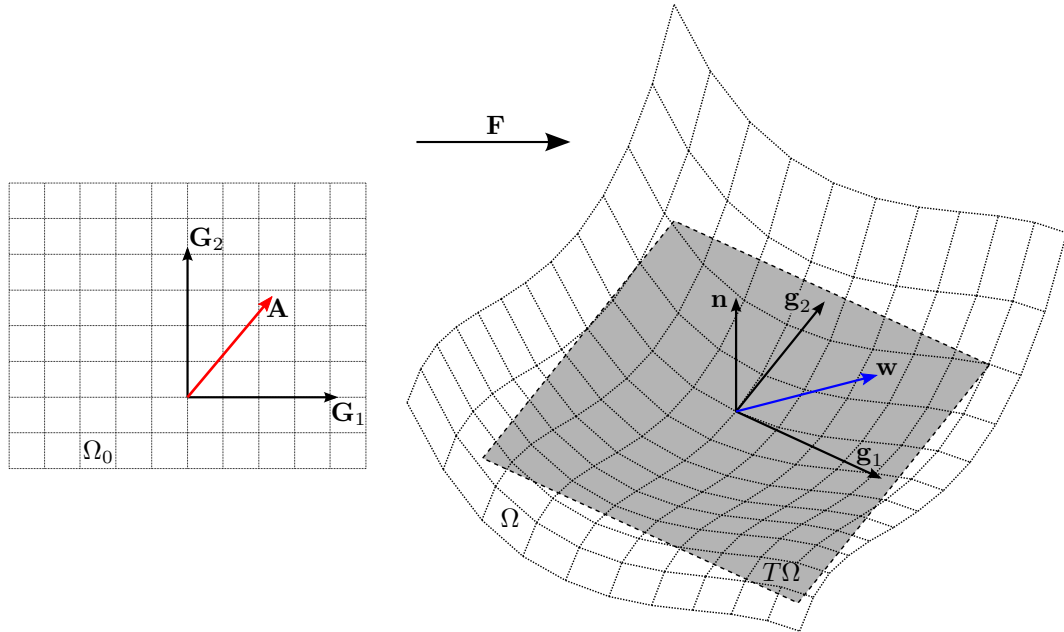
Figure 4.9: In the case of solids of reduced dimensionality, the standard Cauchy-Born rule transforms the undeformed bond vector **A** into the tangent deformed bond vector **w**, which belongs to the tangent space $T\Omega$ of the deformed surface.

4.9, and as pointed out by Arroyo [2] and Arroyo and Belytschko [3] a direct application of the standard Cauchy-Born rule in the case of single-layer lattices is not compatible. However, this deficiency can be improved by various modifications, which are discussed in the following.

4.4.2 Higher order Cauchy-Born rule

With the objective of developing an advanced linkage between atomistic and continuum deformation, so-called higher order Cauchy-Born rules were introduced. Starting from different points,

these approaches lead to the same modifications.

The first variant of such a kind was developed, independently from each other, by Leamy *et al.* [28] and by Guo *et al.* [24]. In the following, the ideas and outcomes of this modification are reproduced. The deformation gradient $\mathbf{F}(\mathbf{X})$ from continuum mechanics maps infinitesimal vectors of the undeformed configuration to infinitesimal vectors of the deformed configuration.

$$\mathrm{d}\mathbf{x} = \mathbf{F}(\mathbf{X})\,\mathrm{d}\mathbf{X} \tag{4.37}$$

In contrast, the standard Cauchy-Born rule maps by definition vectors of finite length via the deformation gradient. As discussed above, this mapping is only exact for homogeneous deformations and, consequently, for a constant deformation gradient along the undeformed bond vector. However, an exact calculation of lattice vectors is possible when taking into account their finite length. For this purpose, Equation (4.37) is integrated once to obtain the deformed lattice vector $\mathbf{a}$ as:

$$\mathbf{a} = \int\limits_{\mathbf{0}}^{\mathbf{a}} \mathrm{d}\mathbf{x} = \int\limits_{\mathbf{0}}^{\mathbf{A}} \frac{\partial \mathbf{x}}{\partial \mathbf{X}}\,\mathrm{d}\mathbf{X} = \int\limits_{\mathbf{0}}^{\mathbf{A}} \mathbf{F}(\mathbf{X})\,\mathrm{d}\mathbf{X} \tag{4.38}$$

The integration requires further information on the change of the deformation gradient $\mathbf{F}(\mathbf{X})$ as a function of the undeformed position $\mathbf{X}$. If $\mathbf{F}(\mathbf{X})$ is expanded into a Taylor series about $\mathbf{X} = \mathbf{0}$, the starting point of the undeformed lattice vector, Cauchy-Born rules of various order can be stated.

$$\mathbf{F}(\mathbf{X}) = \mathbf{F}(\mathbf{0}) + \nabla_{\mathbf{X}}\mathbf{F}(\mathbf{0}) \cdot \mathbf{X} + \nabla_{\mathbf{X}}\nabla_{\mathbf{X}}\mathbf{F}(\mathbf{0}) : \frac{1}{2}(\mathbf{X} \otimes \mathbf{X}) + \ldots \tag{4.39}$$

From this thoughts, the standard Cauchy-Born rule of Equation (4.11) can be recovered if only the constant term of the Taylor series expansion is taken into account.

$$\mathbf{a} = \int\limits_{\mathbf{0}}^{\mathbf{A}} \mathbf{F}(\mathbf{0})\,\mathrm{d}\mathbf{X} = \mathbf{F}(\mathbf{0})\,\mathbf{A} \tag{4.40}$$

A higher order Cauchy-Born rule is obtained via the additional inclusion of the linear part of the Taylor series expansion. Herein, the gradient of the deformation gradient, namely the second-order deformation gradient $\mathbf{G}(\mathbf{0}) = \nabla_{\mathbf{X}}\mathbf{F}(\mathbf{0})$ is essential.

$$\mathbf{a} = \int\limits_{\mathbf{0}}^{\mathbf{A}} \mathbf{F}(\mathbf{X})\,\mathrm{d}\mathbf{X} = \int\limits_{\mathbf{0}}^{\mathbf{A}} [\mathbf{F}(\mathbf{0}) + \mathbf{G}(\mathbf{0}) \cdot \mathbf{X}]\,\mathrm{d}\mathbf{X} \tag{4.41}$$

By a proper parametrisation of the line integral alongside the undeformed bond vector $\mathbf{A}$, the integration is feasible and an enhanced approximation for the deformed lattice vector $\mathbf{a}$ is possible.

$$\mathbf{a} = \mathbf{F}(\mathbf{0})\,\mathbf{A} + \mathbf{G}(\mathbf{0}) : \frac{1}{2}(\mathbf{A} \otimes \mathbf{A}) \tag{4.42}$$

If compared with the standard Cauchy-Born rule, the additional second-order term takes into account the inhomogeneous part of the deformation and adds a correction that brings the deformed bond vector closer to the exact chord. This correction considers the curvature properties that result from deforming the continuum surface. If the deformation is homogeneous, the standard Cauchy-Born rule given in Equation (4.11) is recovered. The inclusion of even higher order terms allows an approximation of better accuracy with the drawback of increasing computational effort. Nevertheless, for highly contorted crystalline sheets, the achieved approximation for the deformed bond vector is not a chord of the surface. The second-order Cauchy-Born rule is illustrated in Figure 4.10. In the course of this, the deformed bond vector is composed of the part from the
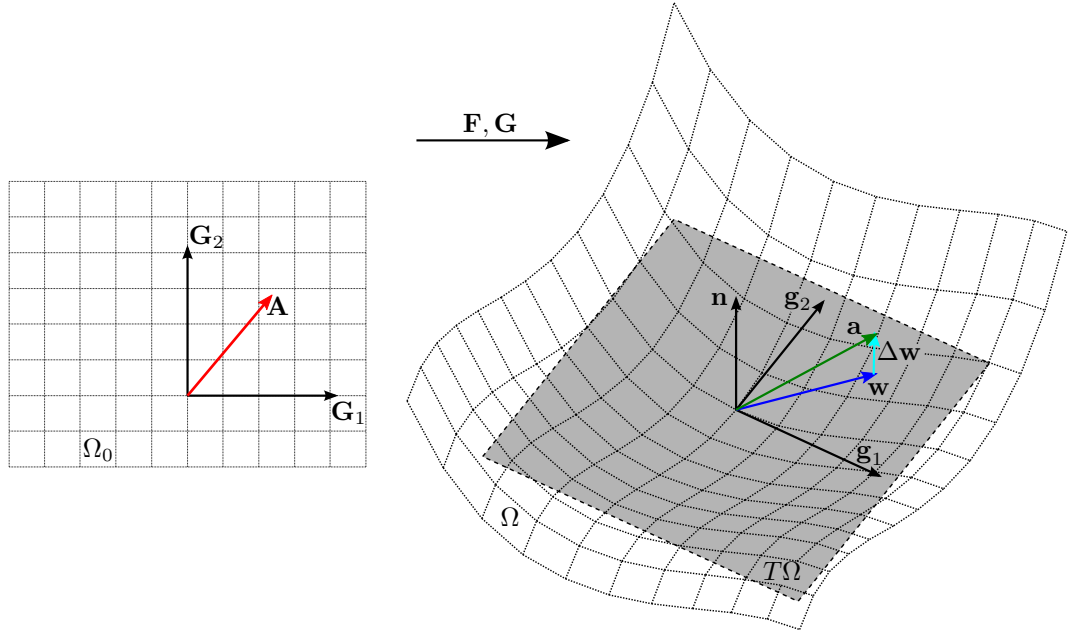
Figure 4.10: The second-order Cauchy-Born rule transforms the undeformed bond vector $\mathbf{A}$ into the deformed bond vector $\mathbf{a}$ by using the deformation gradient $\mathbf{F}$ and the second-order deformation gradient $\mathbf{G}$. The deformation gradient creates the tangent deformed bond vector $\mathbf{w}$ equal to the standard Cauchy-Born rule whereas the second order deformation gradient $\mathbf{G}$ generates the correction term $\Delta\mathbf{w}$ so that $\mathbf{a} = \mathbf{w} + \Delta\mathbf{w}$.

standard Cauchy-Born rule and the additional correction due to its extension. An alternative derivation of this higher order Cauchy-Born rule is feasible if the integration in Equation (4.38) is approximated by the midpoint rule and a subsequent Taylor series expansion.

$$\mathbf{a} = \int_{\mathbf{0}}^{\mathbf{A}} \mathbf{F}(\mathbf{X}) \, \mathrm{d}\mathbf{X} = \mathbf{F}(\mathbf{0} + \mathbf{A}/2)\,\mathbf{A} = \mathbf{F}(\mathbf{0})\,\mathbf{A} + \mathbf{G}(\mathbf{0}) : \frac{1}{2}(\mathbf{A} \otimes \mathbf{A}) \tag{4.43}$$

A second variant for the derivation of the second-order Cauchy-Born rule relies on the deformation map Φ from the undeformed to the deformed configuration. This approach was used by Chandraseker *et al.* [14] and by Sunyk and Steinmann [51]. Thereby, the following deliberations lead to the extended Cauchy-Born rule. A direct application of the deformation map on the two points I and J defining the undeformed lattice vector $\mathbf{A}$ provides their corresponding deformed locations. Subsequently, the connection between these two deformed locations i and j defines the deformed lattice vector $\mathbf{a}$. Without loss of generality, the material position vector of point I is set to $\mathbf{X} = \mathbf{0}$. Then, the material position vector pointing to J is given by $\mathbf{0} + \mathbf{A}$ and the deformed bond vector follows as:

$$\mathbf{a} = \Phi(\mathbf{0} + \mathbf{A}) - \Phi(\mathbf{0}) \tag{4.44}$$

By expanding the first term on the right hand side into a Taylor series expansion about $\mathbf{X} = \mathbf{0}$ and retaining up to the second-order term, the approximation reads:

$$\mathbf{a} = \nabla_{\mathbf{X}}\Phi(\mathbf{0})\mathbf{A} + \nabla_{\mathbf{X}}\nabla_{\mathbf{X}}\Phi(\mathbf{0}) : \frac{1}{2}(\mathbf{A} \otimes \mathbf{A}) \tag{4.45}$$

Finally, using the deformation gradient $\mathbf{F}(\mathbf{0}) = \nabla_{\mathbf{X}}\Phi(\mathbf{0})$ and the second-order deformation gradient $\mathbf{G}(\mathbf{0}) = \nabla_{\mathbf{X}}\nabla_{\mathbf{X}}\Phi(\mathbf{0})$, the second-order Cauchy-Born rule of Equation (4.42) is recovered.

4.4.3 Exponential Cauchy-Born rule

For the investigation of carbon nanotubes, Arroyo [2] and Arroyo and Belytschko [3, 5] proposed an extension to the standard Cauchy-Born rule. The modification is formulated on the basis of the exponential map, denoted as $\mathcal{EXP}$, from the field of differential geometry, which for instance is discussed in do Carmo [20]. Again, this extension is important in the study of monolayer crystalline films, where the lattice vectors are presumed to be chords of the continuum surface. For general undeformed and deformed surfaces, this extension is a three step procedure, which reduces to only two steps if the undeformed continuum is a plane. Starting from the undeformed lattice vector $\mathbf{A}$, which is a chord of the continuum surface, the application of the inverse exponential map $\mathcal{EXP}^{-1}$ delivers the tangent undeformed lattice vector $\mathbf{W}$. If the undeformed surface is planar, the undeformed lattice vector $\mathbf{A}$ and the tangent undeformed lattice vector $\mathbf{W}$ coincide and the first step of the extension is not needed. The vector $\mathbf{W}$ lies in the tangent plane of the undeformed surface and, therefore, can be mapped to the corresponding tangent plane of the deformed continuum by applying the deformation gradient $\mathbf{F}$. This step represents the use of the standard Cauchy-Born rule and results in the tangent deformed lattice vector $\mathbf{w}$. Finally, the exponential map $\mathcal{EXP}$ brings this vector back to the surface. The resulting chord describes the deformed lattice vector $\mathbf{a}$. By combining these steps, the exponential Cauchy-Born rule can be expressed as:

$$\mathbf{a} = \mathcal{EXP}\left[\mathbf{F}\left(\mathbf{X}\right) \mathcal{EXP}^{-1}\left(\mathbf{A}\right)\right] \tag{4.46}$$

The exponential map $\mathcal{EXP}$ requires the determination of the geodesic curves. The calculation of solutions for these curves is not easily done and, therefore, approximations for the exponential map are of interest. Together with the introduction of the exponential Cauchy-Born rule, Arroyo [2] and Arroyo and Belytschko [3, 5] suggested an approximation using the principal directions and the principal curvatures of the continuum surface. Consequently, this scheme is from now on referred to as principal curvatures approach. Another approach for the requested local approximation can be constructed directly on the basis of the local normal curvature of the surface. Hence, this method is denoted as direct curvature approach. The two different approaches are developed in detail in the upcoming derivations. If the exponential Cauchy-Born rule is applied to space-filling crystals, in consequence of its structure, the standard Cauchy-Born rule is exactly recovered.

4.4.4 Approximations of the exponential Cauchy-Born rule

Approximation of the exponential Cauchy-Born rule: principal curvatures approach

In the case of a planar undeformed monolayer crystalline sheet, the exponential Cauchy-Born rule is a two step procedure. The first step of the approach is the use of the standard Cauchy-Born rule in order to map the undeformed bond vector $\mathbf{A}$ of the planar sheet to the tangent deformed bond vector $\mathbf{w}$.

$$\mathbf{w} = \mathbf{FA} \tag{4.47}$$

In a next step, the vector $\mathbf{w}$ from the tangent space of the deformed surface is transformed to the deformed bond vector $\mathbf{a}$ by the local approximation $\mathcal{EXP}^{k_I,k_{II}}$ of the exponential map.

$$\mathbf{a} = \mathcal{EXP}^{k_I,k_{II}} \mathbf{w} \tag{4.48}$$

For this approximation, the metric tensor $\mathbf{g}$ and the curvature tensor $\mathbf{k}$ as well as their related pull-backs $\mathbf{C}$ and $\mathcal{K}$ for the deformed surface are essential. These quantities can be calculated according to the derivations given in Subsection 4.3.3 and Subsection 4.3.4. The principal curvatures k_I, k_{II} and the principal directions $\mathbf{v}_I, \mathbf{v}_{II}$ can then be found either in the current configuration or in the undeformed configuration by solving the corresponding generalised eigenvalue problem given in Equation (4.28) or Equation (4.32). With the help of the principal directions and the unit normal $\mathbf{n} = \mathbf{v}_I \times \mathbf{v}_{II}$, a local orthonormal base system $\widetilde{\mathcal{D}} = \{\mathbf{v}_I, \mathbf{v}_{II}, \mathbf{n}\}$ is defined in the current

configuration in accordance with Subsection 4.3.5. This basis is used for the formulation of the local approximation of the exponential Cauchy-Born rule. The geometric setting and the approximation for the deformed bond vector obtained by the principal curvatures approach is illustrated in Figure 4.11. In order to obtain the approximation, the tangent deformed bond vector $\mathbf{w}$ is split into its
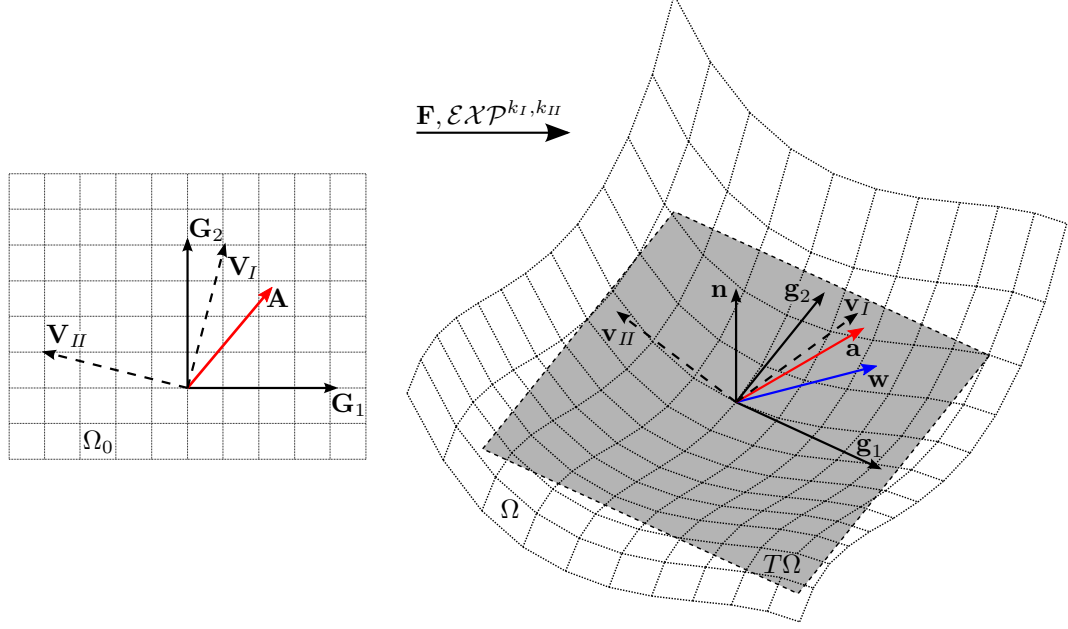
Figure 4.11: The configurations of the continuum surface and the geometric setting for the principal curvatures approach. Illustration of the principal directions, which are essential for the local approximation of the exponential Cauchy-Born rule that transforms the undeformed bond vector $\mathbf{A}$ into the deformed bond vector $\mathbf{a}$.

parts related to the principal directions. For the calculation of these two components, the fact that $\mathbf{v}_I$ and $\mathbf{v}_{II}$ can be obtained by push-forward operations of $\mathbf{V}_I$ and $\mathbf{V}_{II}$ is used.

$$\mathbf{w} = \mathbf{F}\mathbf{A} = w^I \mathbf{v}_I + w^{II} \mathbf{v}_{II} \tag{4.49}$$

$$w^I = \mathbf{w} \cdot \mathbf{v}_I = A^A C_{AB} \left(V_I\right)^B \tag{4.50}$$

$$w^{II} = \mathbf{w} \cdot \mathbf{v}_{II} = A^A C_{AB} \left(V_{II}\right)^B \tag{4.51}$$

The central idea behind this approach is to approximate the exponential map by decoupling the principal directions. This is done by the introduction of a fictitious cylinder for each principal direction with a radius of the inverse principal curvature. Thereof, two individual corrections $\Delta\mathbf{w}_I$ and $\Delta\mathbf{w}_{II}$ are obtained by mapping the tangent deformed bond vector $\mathbf{w}$ exponentially onto these cylinders. A detailed graphical explanation of this process is given in Figure 4.12 and the necessary correction terms are illustrated. In particular, the components of these corrections in the local base system $\widetilde{\mathcal{D}}$ are specified as:

$$[\Delta\mathbf{w}_I]_{\widetilde{\mathcal{D}}} = \begin{bmatrix} \frac{1}{k_I}\sin\left(k_I w^I\right) - w^I \\ 0 \\ \frac{1}{k_I}\left(1 - \cos\left(k_I w^I\right)\right) \end{bmatrix} \qquad [\Delta\mathbf{w}_{II}]_{\widetilde{\mathcal{D}}} = \begin{bmatrix} 0 \\ \frac{1}{k_{II}}\sin\left(k_{II} w^{II}\right) - w^{II} \\ \frac{1}{k_{II}}\left(1 - \cos\left(k_{II} w^{II}\right)\right) \end{bmatrix} \tag{4.52}$$

Applying these two corrections, the approximation of the exponential Cauchy-Born rule, employing the principal curvatures approach, is given by:

$$\mathbf{a} = \mathcal{EXP}^{k_I, k_{II}}\, \mathbf{w} = \mathbf{w} + \Delta\mathbf{w}_I + \Delta\mathbf{w}_{II} \tag{4.53}$$

Thus, the approximated deformed bond vector is obtained by combining the tangent deformed bond vector with the acquired corrections. Finally, its components in the local orthonormal base
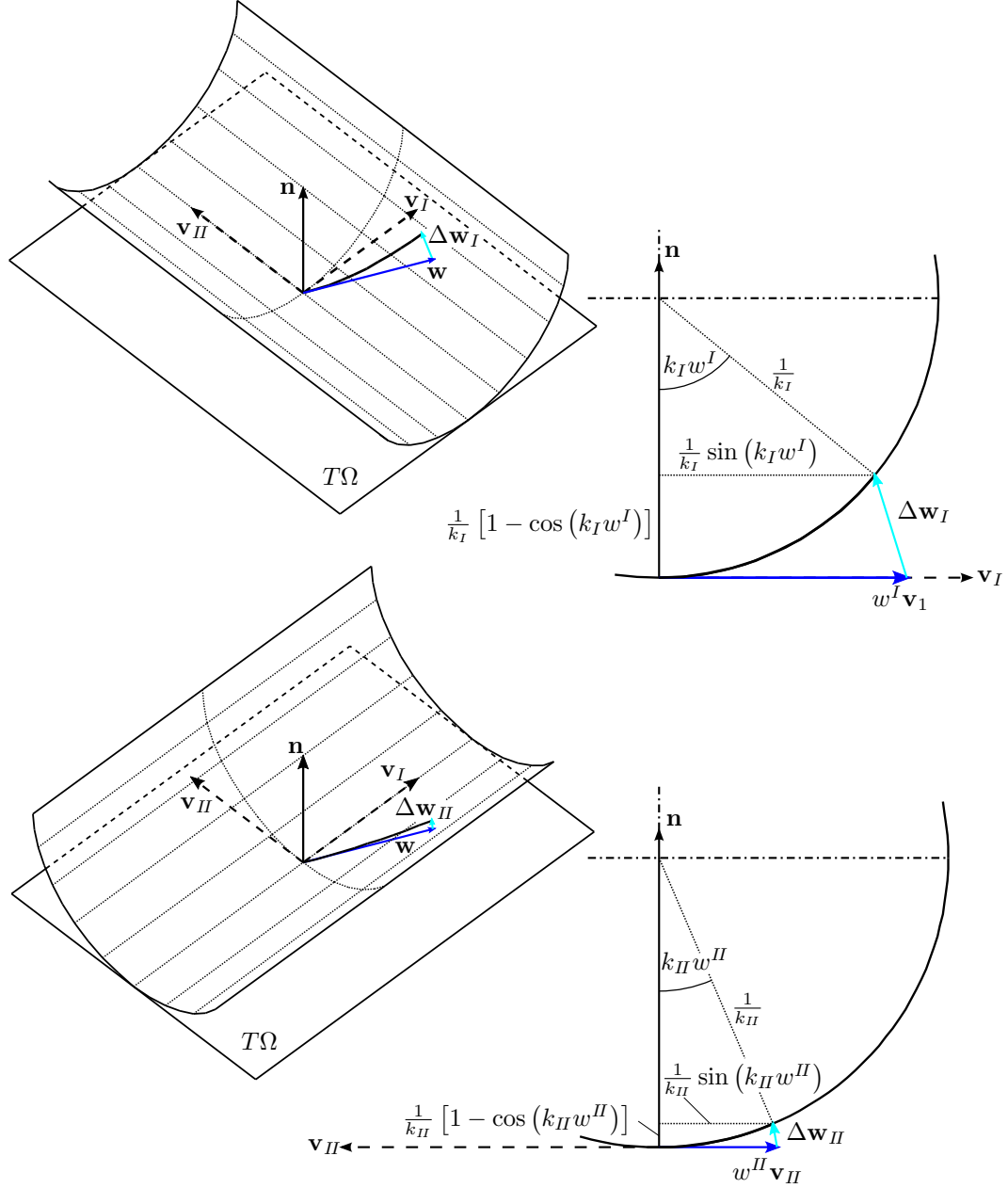
Figure 4.12: The exponential map based on the principal curvatures and the principal directions of the surface for the approximation of the deformed bond vector. The fictitious cylinders for the two decoupled principal directions and the associated correction terms.

system $\widetilde{\mathcal{D}}$ read:

$$[\mathbf{a}]_{\widetilde{\mathcal{D}}} = \begin{bmatrix} \frac{1}{k_I} \sin\left(k_I w^I\right) \\ \frac{1}{k_{II}} \sin\left(k_{II} w^{II}\right) \\ \frac{1}{k_I}\left(1 - \cos\left(k_I w^I\right)\right) + \frac{1}{k_{II}}\left(1 - \cos\left(k_{II} w^{II}\right)\right) \end{bmatrix} \tag{4.54}$$

Starting from the undeformed bond vector $\mathbf{A}$ and taking into consideration that the principal curvatures and the principal directions can be calculated by means of a generalised eigenvalue problem on the reference configuration via the right Cauchy-Green deformation tensor $\mathbf{C}$ and the pull-back of the spatial curvature tensor, namely $\mathcal{K}$, the components of the approximated deformed bond vector $[\mathbf{a}]_{\widetilde{\mathcal{D}}}$ in the local orthonormal basis depend only on quantities expressed in the reference configuration. In conclusion, this approach offers a useful method for the calculation of deformed bond vectors for monolayer crystalline sheets.

Approximation of the exponential Cauchy-Born rule: direct curvature approach

If the undeformed configuration of the considered single-layer lattice is a plane, the exponential Cauchy-Born rule is a two step procedure. The first step of the approach is the application of the standard Cauchy-Born rule. This process maps the undeformed bond vector $\mathbf{A}$ of the planar crystal to the tangent deformed bond vector $\mathbf{w}$.

$$\mathbf{w} = \mathbf{F}\mathbf{A} \tag{4.55}$$

Secondly, the local approximation $\mathcal{EXP}^{k_n}$ of the exponential map is utilised. Thereby, the tangent deformed bond vector $\mathbf{w}$ is transformed to the deformed bond vector $\mathbf{a}$.

$$\mathbf{a} = \mathcal{EXP}^{k_n}\,\mathbf{w} \tag{4.56}$$

The practical realisation of the local approximation is presented in the following. An important feature of the approach is the tangent plane to the deformed surface, which can be specified by the local covariant basis $\mathcal{C} = \{\mathbf{g}_1, \mathbf{g}_2\}$ that is defined according to Subsection 4.3.2. This base system in conjunction with the formulation of the deformation gradient specified in Equation (4.24) allows to give a description for the tangential vector $\mathbf{w}$.

$$\mathbf{w} = \mathbf{F}\mathbf{A} = \left(\mathbf{g}_\alpha \otimes \mathbf{G}^\alpha\right) A^A \mathbf{E}_A = A^A G^\alpha{}_A \mathbf{g}_\alpha = w^\alpha \mathbf{g}_\alpha \tag{4.57}$$

The associated length w of the tangent deformed bond vector $\mathbf{w}$ is given by:

$$w = \|\mathbf{w}\| = (\mathbf{w} \cdot \mathbf{w})^{1/2} = \left(w^\alpha g_{\alpha\beta} w^\beta\right)^{1/2} \tag{4.58}$$

Furthermore, the contravariant base vectors $\mathbf{g}^1$ and $\mathbf{g}^2$ according to Subsection 4.3.2 are introduced. This allows the calculation of the spatial metric tensor $\mathbf{g}$ and the spatial curvature tensor $\mathbf{k}$ on the basis of the derivations given in Subsection 4.3.3. With these quantities, the normal curvature k of the deformed surface in the direction of the tangent deformed bond vector $\mathbf{w} = w^\alpha \mathbf{g}_\alpha$ can be evaluated. The idea of the extension for the exponential map is visualised in Figure 4.13, presenting a part of the continuum surface in both the material and spatial configuration. In the spatial configuration, the local convected basis $\widetilde{\mathcal{C}} = \{\mathbf{g}_1, \mathbf{g}_2, \mathbf{n}\}$ that is defined with reference to Subsection 4.3.2 and a tangent deformed bond vector $\mathbf{w}$ are indicated. In order to obtain an approximation of the deformed bond vector $\mathbf{a}$, the surface is sliced by a plane spanned by the unit normal vector $\mathbf{n}$ and the tangent deformed bond vector $\mathbf{w}$. At the origin, the resulting intersection curve is further replaced by the osculating circle with a radius of the inverse local normal curvature k. Moving the length of the tangent deformed bond vector $\mathbf{w}$, namely w, along this circle an approximation for the deformed atomic position is achieved. A detailed graphical interpretation of this strategy is given in Figure 4.14. Finally, this gives the possibility to specify
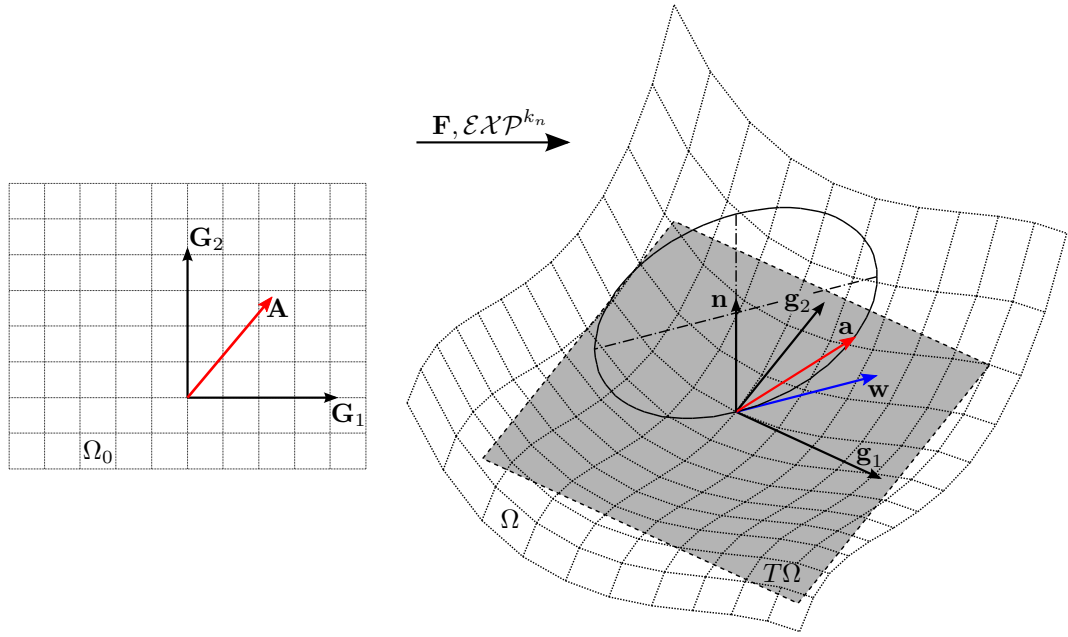
Figure 4.13: The configurations of the continuum surface and the geometric setting for the direct curvature approach. Illustration of the local convected basis for the spatial configuration and the osculating circle of the surface, which are essential for the transformation of the undeformed bond vector **A** to the deformed bond vector **a** by means of the locally approximated exponential Cauchy-Born rule.
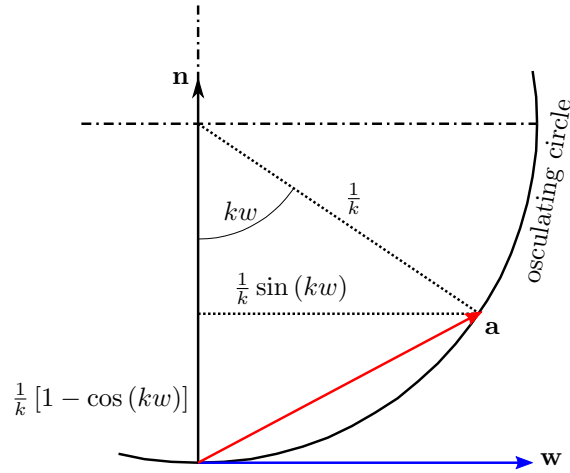
Figure 4.14: The approximation of the exponential map by means of the direct curvature approach. Illustration of the osculating circle and the components of the deformed bond vector.

necessary correction terms for the calculation of the deformed bond vector **a**. As a consequence of the design of this extension, it is referred to as direct curvature approach. In what follows, the essential quantities for this extension of the standard Cauchy-Born rule are stated. The scalar local curvature k of the osculating circle is determined with reference to Equation (4.27) by projecting

k to the unit vector $\mathbf{w}/w$.

$$k = \frac{w^\alpha k_{\alpha\beta} w^\beta}{w^\alpha g_{\alpha\beta} w^\beta} \tag{4.59}$$

When taking into consideration the corrections given in Figure 4.14, the introduced approximation for the exponential map of **w** finally gives the secant vector of the osculating circle that represents the deformed bond vector **a**.

$$\begin{aligned} \mathbf{a} &= \frac{1}{k} \sin(kw) \frac{\mathbf{w}}{w} + \frac{1}{k} \left[1 - \cos(kw) \right] \mathbf{n} \\ &= \frac{1}{k} \sin(kw) \frac{\mathbf{w}}{w} + \frac{2}{k} \sin^2\left(\frac{kw}{2}\right) \mathbf{n} \end{aligned} \tag{4.60}$$

Within this approach, the main steps of calculation are performed on the current configuration and, consequently, pull-back operations carried out on the spatial tensors **g** and **k** are not necessary. To sum up, this extension to the Cauchy-Born rule allows a straightforward calculation of deformed bond vectors for single-layer crystalline surfaces.

4.5 Constitutive model

A material is denoted as elastic if its constitutive behaviour is only a function of the current state of deformation. In addition, if the work that is done during a deformation depends only on the initial state and the final deformed state, the material behaviour is path-independent. Such kinds of materials are known as hyperelastic. For this hyperelastic material response, a strain energy density W can be defined, which represents an energy per unit undeformed volume. To fulfil objectivity, or equivalently frame-indifference, the strain energy density is often defined by invariants of the right Cauchy-Green deformation tensor **C**. Together with some experimentally determined material parameters, the phenomenologically defined macroscopic strain energy density as a function of the right Cauchy-Green deformation tensor **C** reads:

$$W = W(\mathbf{C}) \tag{4.61}$$

A full treatise of constitutive formulations for finite deformations can for instance be found in Bonet and Wood [9], Marsden and Hughes [34], Wriggers [61] and Zienkiewicz and Taylor [65]. In the quasi-continuum method developed by Tadmor *et al.* [52] and Tadmor *et al.* [53], the phenomenological macroscopic strain energy density is replaced by considering directly the properties of the underlying lattice via the interatomic potentials. The important task is to find the correlation between the stored energy of the lattice on the microscopic scale and the strain energy density of the continuum on the macroscopic level. This operation is performed by considering a representative cell of the atomistic structure. For this cell, the energy E_{cell} of the encased deformed lattice structure can be calculated on the basis of interatomic potentials. In addition, the volume or the surface, denoted as V_{cell}, of the corresponding undeformed cell is evaluated. Then, the strain energy density W of the continuum is specified by dividing the energy of the representative cell by its characteristic size.

$$W = \frac{E_{\text{cell}}}{V_{\text{cell}}} \tag{4.62}$$

In what follows, the strain energy density for carbon nanotube and graphene structures is developed. This is done, by considering the contributions of the bonded and the non-bonded energy, separately. However, before working on these energies in detail, the undeformed bond vectors for graphene and, consequently, carbon nanotubes need some advanced handling that is highlighted in the following.

4.5.1 Lattice structure of graphene and the inner displacements

As already pointed out, the flat graphene sheet as illustrated in Figure 4.15 characterises the undeformed body for the mixed atomistic-continuum model. Within this hexagonal lattice, the
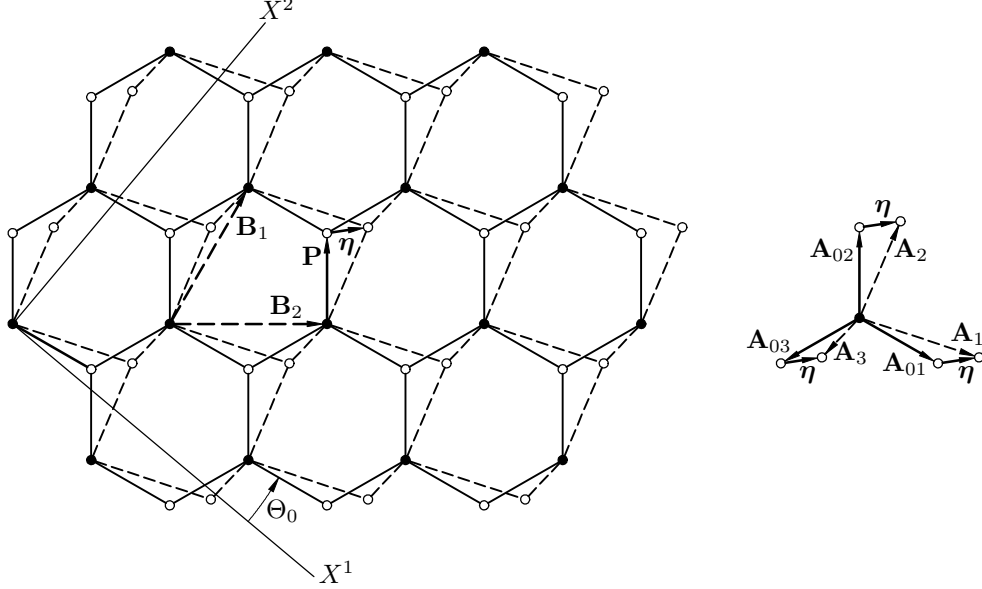
Figure 4.15: The hexagonal Bravais 2-lattice of graphene. The two triangular sublattices are denoted by black and white dots. The solid lines identify the perfect lattice, which has three inequivalent undeformed bonds $\mathbf{A}_{0i}$. The inner displacements $\boldsymbol{\eta}$ between the two sublattices are introduced to ensure the equilibrium of atoms. This inner relaxation results in the dashed lattice with the relaxed undeformed bond vectors $\mathbf{A}_i = \mathbf{A}_{0i} + \boldsymbol{\eta}$.

undeformed bond vectors are defined. This lattice needs some special attention because, as discussed in Section 2.2, its not of a simple Bravais type. To be exact, the hexagonal structure turns out to be a Bravais 2-lattice. Therefore, the lattice can be viewed as a set of two simple triangular sublattices. Thus, in order to spot every atom of the graphene sheet, lattice basis vectors $\mathbf{B}_1$ and $\mathbf{B}_2$ of one sublattice as well as an additional shift vector $\mathbf{P}$ are required. The perfect hexagonal lattice has three inequivalent undeformed bonds $\mathbf{A}_{0i}$ ($i = 1, 2, 3$). These bonds are specified in the local coordinate system of the graphene sheet. The orientation of the bond vectors is defined by the chiral angle Θ_0 and their length by the equilibrium bond length A_0. These two quantities and the alignment of the coordinate system are used in conformance with Section 2.2. Considering the angles inside a regular hexagon, the three inequivalent undeformed bonds are defined as:

$$
\begin{aligned}
\mathbf{A}_{01} &= A_0 \begin{bmatrix} \cos\Theta_0 \\ \sin\Theta_0 \end{bmatrix} \\
\mathbf{A}_{02} &= A_0 \begin{bmatrix} \cos\left(\Theta_0 + 2\pi/3\right) \\ \sin\left(\Theta_0 + 2\pi/3\right) \end{bmatrix} \\
\mathbf{A}_{03} &= A_0 \begin{bmatrix} \cos\left(\Theta_0 - 2\pi/3\right) \\ \sin\left(\Theta_0 - 2\pi/3\right) \end{bmatrix}
\end{aligned}
\tag{4.63}
$$

If applying any of the discussed Cauchy-Born rules to the undeformed bond vectors of the Bravais 2-lattice of graphene, additional requirements concerning a homogeneous deformation have to be considered. In particular, with regard to standard theories of inner crystal elasticity, as for instance

discussed in Martin [35] and Cousins [19], the assumption of homogeneous deformation is made for each of the sublattices. This results in a rearrangement of the distinct atoms against each other and, consequently, in modified bond vectors. A proper description of the structure, therefore, needs some additional variables to account for relative shifts between the simple lattices. With reference to Arroyo [2], Arroyo and Belytschko [3, 4, 5], Cousins [19], Martin [35] and Tadmor *et al.* [53], these so-called inner displacements are included via the shift vector $\boldsymbol{\eta}$. Moreover, this inner displacement vector is defined in the undeformed configuration to guarantee invariance against rigid-body rotation. Adding the inner displacement vector $\boldsymbol{\eta}$ to each of the three undeformed bond vectors $\mathbf{A}_{0i}$, the three undeformed bond vectors $\mathbf{A}_i$ $(i = 1, 2, 3)$ of the relaxed lattice are obtained.

$$\mathbf{A}_i = \mathbf{A}_{0i} + \boldsymbol{\eta} \tag{4.64}$$

As the inner displacements describe some kind of relaxation of atom positions, the three inequivalent vectors $\mathbf{A}_i$ of the graphene sheet are denoted as relaxed undeformed bond vectors. Taking into consideration a deformation of the continuum, these relaxed undeformed bond vectors are transformed to their deformed counterparts by applying an appropriate variant of the extended Cauchy-Born rules given in Section 4.4 for the continuum surface.

4.5.2 Strain energy density for bonded interactions

The definition of the strain energy density for bonded interactions requires a suitable interatomic potential for the graphene sheet and, consequently, the carbon nanotube. One member from this appropriate set is the Tersoff-Brenner bond-order potential, which is often used for carbon nanotubes. It expresses the energy in one bond by the corresponding bond length and the lengths of adjacent bonds as well as the angles formed with neighbouring bonds. A detailed investigation of this potential is given in Subsection 2.3.1. This description can be reused in the formulation of a constitutive law for the mixed atomistic-continuum model, however, a slight modification of the many-body coupling term is necessary. At the outset, in each point of the continuum surface, a fictitious atomistic structure of the graphene sheet is imagined. Then, for the formulation of the strain energy density a representative cell has to be defined on the basis of this underlying structure. In Figure 4.16, a cut-out of a graphene sheet is illustrated together with a proper representative cell. This areal cell is hexagonal and contains three full bonds. The cell also has one full atom located in its centre and, in addition, it shares three atoms with two neighbouring cells. Altogether, the representative hexagonal cell contains an average of two atoms. Considering the equilibrium bond length A_0 of the graphene sheet, as specified in Subsection 2.3.2, the area of the cell is:

$$S_{\text{cell}} = S_0 = \frac{3\sqrt{3}}{2} A_0^2 \tag{4.65}$$

The calculation of the cell-based energy requires a summation of the appropriate bond-wise energies. For that purpose, the three bonds within the representative cell in their deformed setting have to be considered. The related energy of each of these bonds can be specified by the Tersoff-Brenner potential. Nevertheless, if taking a closer look at the definition of the Tersoff-Brenner potential in Subsection 2.3.1, the many-body coupling term needs attention. This term incorporates the local environment of both atoms that are building a bond together. Therefore, besides the three bonds within the representative cell, also the six directly attached bonds and their geometric setting influences the energy within the cell. To circumvent this problem, the atomistic structure is assumed to be the same in both local environments. As a consequence, the corresponding multi-body coupling term depends only on the local environment of the central atom which is a member of all bonds in the cell. Finally, this allows to calculate the energy of the representative cell solely from bond lengths and valence angles emerging from within the cell. For this task, the central atom and the three bonds of the cell are considered in their deformed configuration as illustrated in Figure 4.16. In order to obtain a compact notation of the energy per cell, the bond lengths and valence angles are relabelled as well. These scalar quantities can be
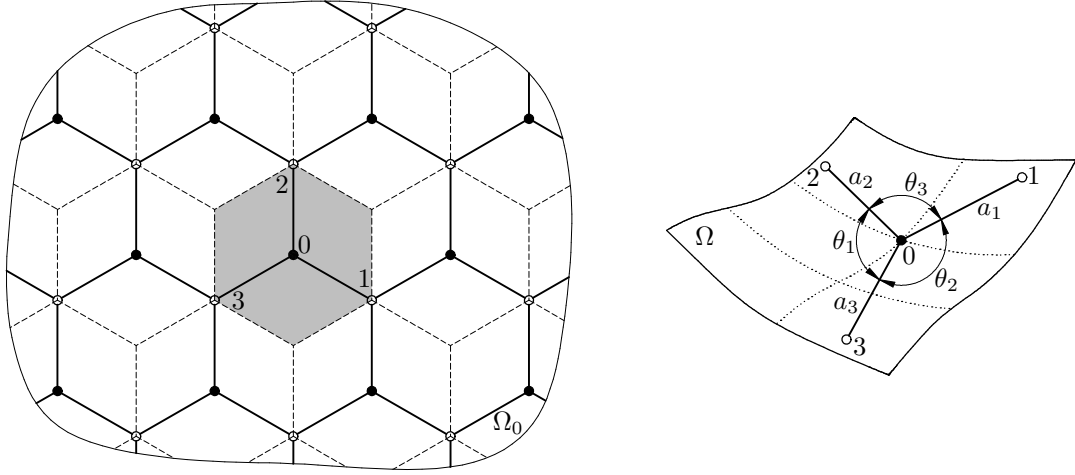
Figure 4.16: Derivation of the strain energy density for bonded interactions in carbon nanotubes. Illustration of a cut-out of the undeformed graphene sheet with its appropriate shaded representative hexagonal cell. This cell contains three bonds and an average of two atoms. Visualisation of the deformed bonds of the representative cell with their appendant bond lengths a_i and valence angles θ_i $(i = 1, 2, 3)$.

calculated directly from the deformed bond vectors. Resulting from the executions of Subsection 4.5.1, these vectors are influenced by the undeformed bond vectors of the graphene sheet and the inner displacements. A proper variant of the Cauchy-Born rule provides the desired deformed bond vector and wields additional influence. In this work, the focus lies on the exponential Cauchy-Born rule outlined in Subsection 4.4.3 and, especially, on the two different approximations of this rule given in Subsection 4.4.4. Based on the chosen approximation, the bond lengths a_i and the valence angles θ_i $(i = 1, 2, 3)$ depend on different local strain measures as well.

- Approximation of the exponential Cauchy-Born rule: principal curvatures approach

$$a_i = a_i \left(\mathbf{C}, \boldsymbol{\mathcal{K}}; \mathbf{A}_i \right) = a_i \left(\mathbf{C}, \boldsymbol{\mathcal{K}}, \boldsymbol{\eta}; \mathbf{A}_{0i} \right) \tag{4.66}$$

$$\theta_i = \theta_i \left(\mathbf{C}, \boldsymbol{\mathcal{K}}; \mathbf{A}_j, \mathbf{A}_k \right) = \theta_i \left(\mathbf{C}, \boldsymbol{\mathcal{K}}, \boldsymbol{\eta}; \mathbf{A}_{0j}, \mathbf{A}_{0k} \right) \tag{4.67}$$

- Approximation of the exponential Cauchy-Born rule: direct curvature approach

$$a_i = a_i \left(\mathbf{g}, \mathbf{k}; \mathbf{A}_i \right) = a_i \left(\mathbf{g}, \mathbf{k}, \boldsymbol{\eta}; \mathbf{A}_{0i} \right) \tag{4.68}$$

$$\theta_i = \theta_i \left(\mathbf{g}, \mathbf{k}; \mathbf{A}_j, \mathbf{A}_k \right) = \theta_i \left(\mathbf{g}, \mathbf{k}, \boldsymbol{\eta}; \mathbf{A}_{0j}, \mathbf{A}_{0k} \right) \tag{4.69}$$

With this notation and the Tersoff-Brenner potential, the cell-based energy of the deformed cell is given by a sum over the three bonds i with $\{i, j, k\}$ being an even permutation of $\{1, 2, 3\}$.

$$E_{\text{cell}} = \sum_{i=1}^{3} \left[V_{\text{R}} \left(a_i \right) - B_i \left(a_j, a_k, \theta_k, \theta_j \right) V_{\text{A}} \left(a_i \right) \right] \tag{4.70}$$

Taking into consideration Subsection 2.3.1, the adapted repulsive and attractive components of the Tersoff-Brenner potential as well as the cut-off function for the introduced notation are defined as:

$$V_{\text{R}}(a_i) = \frac{D^{(\text{e})}}{S-1} \cdot e^{-\sqrt{2 \cdot S} \cdot \beta \cdot \left(a_i - R^{(\text{e})}\right)} \cdot f_{\text{c}}(a_i) \tag{4.71}$$

$$V_{\text{A}}(a_i) = \frac{D^{(\text{e})} \cdot S}{S-1} \cdot e^{-\sqrt{\frac{2}{S}} \cdot \beta \cdot \left(a_i - R^{(\text{e})}\right)} \cdot f_{\text{c}}(a_i) \tag{4.72}$$

$$f_{\text{c}}(a_i) = \begin{cases} 1 & a_i < R^{(1)} \\ \frac{1}{2} \cdot \left\{ 1 + \cos\left[\frac{\pi\left(a_i - R^{(1)}\right)}{R^{(2)} - R^{(1)}} \right] \right\} & R^{(1)} \leq a_i \leq R^{(2)} \\ 0 & R^{(2)} < a_i \end{cases} \tag{4.73}$$

Furthermore, the simplified many-body coupling term that only includes the local environment of the central atom is given by:

$$B_i = \left[1 + G(\theta_k) \cdot f_{\text{c}}(a_j) + G(\theta_j) \cdot f_{\text{c}}(a_k) \right]^{-\delta}$$
$$G(\theta_i) = a_0 \cdot \left[1 + \frac{c_0{}^2}{d_0{}^2} - \frac{c_0{}^2}{d_0{}^2 + (1 + \cos\theta_i)^2} \right] \tag{4.74}$$

For the evaluation of all these terms, the constants provided in Subsection 2.3.1, are used. Finally, as the energy and the area of the representative cell are defined, the relevant strain energy density for bonded interactions is given by:

$$W = \frac{E_{\text{cell}}}{S_{\text{cell}}} = \frac{1}{S_0} \sum_{i=1}^{3} \left[V_{\text{R}}\left(a_i\right) - B_i\left(a_j, a_k, \theta_k, \theta_j\right) V_{\text{A}}\left(a_i\right) \right] \tag{4.75}$$

The two local approximations of the exponential Cauchy-Born rule lead to a dependence of the strain energy density on the relevant local deformation measures at the observed continuum point. Furthermore, both variants base on the undeformed bond vectors and the inner displacements.

- Approximation of the exponential Cauchy-Born rule: principal curvatures approach

$$W = W\left(\mathbf{C}, \boldsymbol{\mathcal{K}}, \boldsymbol{\eta}; \mathbf{A}_{0i}\right) \tag{4.76}$$

- Approximation of the exponential Cauchy-Born rule: direct curvature approach

$$W = W\left(\mathbf{g}, \mathbf{k}, \boldsymbol{\eta}; \mathbf{A}_{0i}\right) \tag{4.77}$$

The obvious dependence of the strain energy density on the fixed undeformed lattice vectors $\mathbf{A}_{0i}$ will be omitted in the further executions without loss of generality.

4.5.3 Inner relaxation

As observed in Subsection 4.5.2, the inner displacements $\boldsymbol{\eta}$, which where introduced in Subsection 4.5.1 on the undeformed graphene sheet, influence the constitutive model of the bonded interactions. With reference to Arroyo [2], Arroyo and Belytschko [3, 5] and Tadmor *et al.* [53], the inner displacements are viewed as internal variables and can be eliminated at the constitutive level. For this purpose, a deformation of the continuum surface is assumed and the minimisation of the strain energy density W with respect to the inner displacements $\boldsymbol{\eta}$ is carried out. This process is called inner relaxation and yields $\hat{\boldsymbol{\eta}}$, the relaxed inner displacements.

$$\frac{\partial W}{\partial \boldsymbol{\eta}} = \mathbf{0} \quad \Rightarrow \quad \boldsymbol{\eta} = \hat{\boldsymbol{\eta}} \tag{4.78}$$

The resulting non-linear system of equations is solved iteratively by expanding $\partial W / \partial \boldsymbol{\eta}$ into a Taylor series expansion, delivering an update rule for the inner displacements.

$$\frac{\partial W}{\partial \boldsymbol{\eta}} \left(\boldsymbol{\eta} + \Delta \boldsymbol{\eta} \right) = \frac{\partial W}{\partial \boldsymbol{\eta}} \left(\boldsymbol{\eta} \right) + \frac{\partial^2 W}{\partial \boldsymbol{\eta} \partial \boldsymbol{\eta}} \left(\boldsymbol{\eta} \right) : \Delta \boldsymbol{\eta} + \ldots = \mathbf{0} \tag{4.79}$$

$$\Delta \boldsymbol{\eta} = - \left[\frac{\partial^2 W}{\partial \boldsymbol{\eta} \partial \boldsymbol{\eta}} \left(\boldsymbol{\eta} \right) \right]^{-1} : \frac{\partial W}{\partial \boldsymbol{\eta}} \left(\boldsymbol{\eta} \right) \tag{4.80}$$

For this minimisation process, the first-order and second-order derivatives of the strain energy density W with respect to the inner displacements $\boldsymbol{\eta}$ are necessary. The explicit expressions for these quantities are given in Appendix A.1 and for comparison in Arroyo [2] and Arroyo and Belytschko [5]. After minimisation, a relaxed strain energy density is obtained, which implies that the dependence on the inner displacements is eliminated. According to Tadmor *et al.* [53], the minimisation can be history dependent. Consequently, if the load is applied incrementally, it is necessary to store the obtained inner displacements of the actual load step. After that, these stored values serve as starting point for the Newton-Raphson iterations of the inner relaxation procedure in the following increment.

4.5.4 Strain energy double density for non-bonded interactions

The non-bonded or van der Waals interactions include the influence of non-bonded pairs of atoms. As observed in Section 2.4, there are two types of interactions that arise in the simulation of carbon nanotubes. At first, there are the in-layer non-bonded interactions appearing in single-walled tubes and in the individual layers of multi-walled carbon nanotubes. This type requires a specific treatment in its modelling, because only pairs of atoms that are not covalently bonded have to be included. The second type considers the inter-layer non-bonded interactions that occur in multi-walled carbon nanotubes. Within this type, each atom of a specific layer can build a non-bonded pair with all atoms of the other layers. In combination, these two types are of particular importance for the simulations because of their influence on the morphology of the deformed structures. Especially, in the buckled configurations, these interactions beware the carbon nanotubes from self-intersection and penetration. This fact is confirmed by the numerical simulations given in Section 3.5 using molecular statics and in Section 4.9 applying the mixed atomistic-continuum model. The non-bonded interactions are usually described by a pair potential. Here, according to the discussion in Subsection 2.4.1, a Lennard-Jones pair potential is used. This interatomic potential consists of an attractive and a repulsive part, which depend on the distance between the two atoms building the non-bonded pair. With regard to the mixed atomistic-continuum model, this distance is denoted as d and in combination with the constants given in Subsection 2.4.1 the adapted formulation of the pair potential reads:

$$V_{\mathrm{nb}} \left(d \right) = - \frac{A}{d^6} + \frac{B}{d^{12}} \tag{4.81}$$

Thereof, the non-bonded energy double density W_{nb} for the mixed atomistic-continuum model is defined by considering two distinct representative cells of the hexagonal type that is illustrated in Figure 4.16. Moreover, with reference to the observations of Subsection 4.5.2, each of these cells owns an area S_0 and contains two atoms. Within the continuum model, the discrete location of the atoms is not accessible. However, the distance $d \left(\mathbf{x}, \mathbf{y} \right)$ between two arbitrary points $\mathbf{x}$ and $\mathbf{y}$ in the deformed configuration of the surface is well defined and given by:

$$d \left(\mathbf{x}, \mathbf{y} \right) = \| \mathbf{x} - \mathbf{y} \| = \left[\left(\mathbf{x} - \mathbf{y} \right) \cdot \left(\mathbf{x} - \mathbf{y} \right) \right]^{1/2} \tag{4.82}$$

Finally, the strain energy double density for non-bonded interactions is defined as:

$$W_{\mathrm{nb}} = V_{\mathrm{nb}} \left(d \left(\mathbf{x}, \mathbf{y} \right) \right) \frac{2}{S_0} \frac{2}{S_0} \tag{4.83}$$

To sum up, the modelling of non-bonded interactions in the mixed atomistic-continuum model depends on the distance between two points on the continuum surface. Furthermore, this distance is characterised by the position vectors of the involved points in the deformed surface. If evaluating this non-bonded energy double density, the distances have to be carefully inspected such that pairs of bonded atoms are not additionally included via in-layer non-bonded interactions.

4.6 Global equilibrium

From the achievements of Section 4.5, the total potential Π of the carbon nanotube using the mixed atomistic-continuum model can be stated. This total potential Π consists of the potential Π_{b} of the bonded interactions, the potential Π_{nb} of the non-bonded interactions and the potential Π_{ext} of the external loads. These individual terms generally depend on the deformation map, which links the undeformed and the deformed configuration. As a consequence of the fixed undeformed configuration, the total potential Π depends on the current state of deformation $\mathbf{x}$, exclusively.

$$\Pi = \Pi_{\mathrm{b}} + \Pi_{\mathrm{nb}} + \Pi_{\mathrm{ext}} \tag{4.84}$$

The potential Π_{b} of the bonded interactions can be expressed using the strain energy density, which is defined according to Subsection 4.5.2 in combination with the process of inner relaxation stated in Subsection 4.5.3. As a consequence of the inner relaxation, the strain energy density W is evaluated at the state of relaxed inner displacements $\boldsymbol{\eta} = \hat{\boldsymbol{\eta}}$. The integration of this relaxed strain energy density over the initial planar body Ω_0 delivers the required potential Π_{b} of the bonded interactions. In the following derivations, it is implied that the strain energy density and all ensuing terms are evaluated at the state of relaxed inner displacements. Based on the chosen local approximation of the exponential Cauchy-Born rule, different expressions are obtained as a function of the related local strain measures.

- Approximation of the exponential Cauchy-Born rule: principal curvatures approach

$$\Pi_{\mathrm{b}} = \int\limits_{\Omega_0} W\left(\mathbf{C}, \boldsymbol{\mathcal{K}}; \boldsymbol{\eta}\left(\mathbf{C}, \boldsymbol{\mathcal{K}}\right)\right) \, \mathrm{d}\Omega_0 \tag{4.85}$$

- Approximation of the exponential Cauchy-Born rule: direct curvature approach

$$\Pi_{\mathrm{b}} = \int\limits_{\Omega_0} W\left(\mathbf{g}, \mathbf{k}; \boldsymbol{\eta}\left(\mathbf{g}, \mathbf{k}\right)\right) \, \mathrm{d}\Omega_0 \tag{4.86}$$

The potential Π_{nb} of the non-bonded or van der Waals interactions between non-bonded pairs of atoms relies on Subsection 4.5.4 and the strain energy double density W_{nb} stated there. Herein, the influence of the in-layer and the inter-layer non-bonded interactions is considered.

$$\Pi_{\mathrm{nb}} = \frac{1}{2} \int\limits_{\Omega_0} \int\limits_{\Omega_0 - B_X} W_{\mathrm{nb}}\left(d\right) \, \mathrm{d}\Omega_{0Y} \, \mathrm{d}\Omega_{0X} \tag{4.87}$$

For the in-layer interactions, the fact that this potential must not affect bonded atoms is important. Therefore, at a distinct point $\mathbf{X}\left(\mathbf{x}\right)$ of the undeformed surface a circle with a specific radius is introduced, and the domain $\Omega_0 - B_X$ identifies the remaining exterior area. This is the allowed zone for the co-partner location $\mathbf{Y}\left(\mathbf{y}\right)$ of the in-layer non-bonded interaction in order to exclude bonded atoms from this potential. For the inter-layer non-bonded interactions, this circle vanishes because the two forming atoms are located on different deformed surfaces, thus, on diverse undeformed domains. Consequently, inter-layer interactions can reach the highly repulsive range of the non-bonded potential that prevents the layers from penetration. The limit radius for the restriction of in-layer non-bonded interactions is chosen on the basis of Subsection 2.4.2.

The potential Π_{ext} of the external loads can be defined if the external contributions are conservative. Additionally, the external contributions are assumed to be applied as a constant force field $\mathbf{f}$, on the atoms of the structure. Considering a representative hexagonal cell, according to Subsection 4.5.2, the continuum counterpart of the external loads in the mixed atomistic-continuum model is given by a body force per unit undeformed area. The representative cell owns an area S_0 and contains two atoms. Consequently, the potential Π_{ext} of the external loads for the mixed atomistic-continuum model can be defined in the following form.

$$\Pi_{\text{ext}} = -\int_{\Omega_0} \frac{2}{S_0}\, \mathbf{f} \cdot \mathbf{x}\, \mathrm{d}\Omega_0 \tag{4.88}$$

On the basis of the description for the total potential Π, the global equilibrium configurations of the system are characterised by the stationary condition at time $t + \Delta t$.

$$^{t+\Delta t}\delta\Pi = {}^{t+\Delta t}\delta\Pi_{\text{b}} + {}^{t+\Delta t}\delta\Pi_{\text{nb}} + {}^{t+\Delta t}\delta\Pi_{\text{ext}} = 0 \tag{4.89}$$

In view of the later use of the finite element method and the resulting system of non-linear equations, various solution approaches are possible. Numerical methods that only require gradients, like the non-linear conjugate gradients method or quasi-Newton methods are directly based on Equation (4.89). Beyond that, the commonly used Newton-Raphson solution method needs an additional linearisation of the stationary condition. In doing so, the variations of the bonded Π_{b} and the non-bonded Π_{nb} potential are approximated at time t via linearisation. Furthermore, the considered external contributions, given at time $t + \Delta t$, eventuate in a displacement independent variation of the potential Π_{ext} of external loads.

$$\Delta^t\delta\Pi_{\text{b}} + \Delta^t\delta\Pi_{\text{nb}} + \ldots = -{}^{t+\Delta t}\delta\Pi_{\text{ext}} - {}^{t}\delta\Pi_{\text{b}} - {}^{t}\delta\Pi_{\text{nb}} \tag{4.90}$$

In what follows, the variations and the linearised variations for the bonded Π_{b} and the non-bonded Π_{nb} potential are formulated. Moreover, the variation and the linearised variation of the external potential Π_{ext} are specified. As stated above, the components of the total potential Π depend solely on the current configuration $\mathbf{x}$ of the continuum surface. Consequently, only the associated variation $\delta\mathbf{x}$ and the increment $\Delta\mathbf{x}$ have to be considered.

Once again, based on the chosen local approximation for the exponential Cauchy-Born rule, two different formulations for the bonded potential and, consequently, for the variation $\delta\Pi_{\text{b}}$ and its increment $\Delta\delta\Pi_{\text{b}}$, have to be distinguished.

- Approximation of the exponential Cauchy-Born rule: principal curvatures approach

$$\delta\Pi_{\text{b}} = \int_{\Omega_0} \frac{\mathrm{d}W}{\mathrm{d}\frac{1}{2}\mathbf{C}} : \delta\frac{1}{2}\mathbf{C} + \frac{\mathrm{d}W}{\mathrm{d}\boldsymbol{\mathcal{K}}} : \delta\boldsymbol{\mathcal{K}}\, \mathrm{d}\Omega_0 \tag{4.91}$$

$$\Delta\delta\Pi_{\text{b}} = \int_{\Omega_0} \left[\left(\frac{\mathrm{d}^2W}{\mathrm{d}\frac{1}{2}\mathbf{C}\, \mathrm{d}\frac{1}{2}\mathbf{C}} : \Delta\frac{1}{2}\mathbf{C} + \frac{\mathrm{d}^2W}{\mathrm{d}\frac{1}{2}\mathbf{C}\, \mathrm{d}\boldsymbol{\mathcal{K}}} : \Delta\boldsymbol{\mathcal{K}} \right) : \delta\frac{1}{2}\mathbf{C} + \mathbf{S} : \Delta\delta\frac{1}{2}\mathbf{C} \right.$$
$$\left. + \left(\frac{\mathrm{d}^2W}{\mathrm{d}\boldsymbol{\mathcal{K}}\, \mathrm{d}\frac{1}{2}\mathbf{C}} : \Delta\frac{1}{2}\mathbf{C} + \frac{\mathrm{d}^2W}{\mathrm{d}\boldsymbol{\mathcal{K}}\, \mathrm{d}\boldsymbol{\mathcal{K}}} : \Delta\boldsymbol{\mathcal{K}} \right) : \delta\boldsymbol{\mathcal{K}} + \mathbf{M} : \Delta\delta\boldsymbol{\mathcal{K}} \right] \mathrm{d}\Omega_0 \quad (4.92)$$

In this formulation, all quantities are calculated on the initial (Lagrangian) configuration. Thereby, $\frac{\mathrm{d}W}{\mathrm{d}\frac{1}{2}\mathbf{C}}$ is identified as second Piola-Kirchhoff membrane tensor $\mathbf{S}$ and $\frac{\mathrm{d}W}{\mathrm{d}\boldsymbol{\mathcal{K}}}$ is denoted as second Piola-Kirchhoff bending tensor $\mathbf{M}$.

- Approximation of the exponential Cauchy-Born rule: direct curvature approach

$$\delta\Pi_{\text{b}} = \int_{\Omega_0} \frac{\mathrm{d}W}{\mathrm{d}\frac{1}{2}\mathbf{g}} : \delta\frac{1}{2}\mathbf{g} + \frac{\mathrm{d}W}{\mathrm{d}\mathbf{k}} : \delta\mathbf{k}\, \mathrm{d}\Omega_0 \tag{4.93}$$

$$\Delta\delta\Pi_{\mathrm{b}} = \int\limits_{\Omega_0} \Bigg[\left(\frac{\mathrm{d}^2 W}{\mathrm{d}\frac{1}{2}\mathbf{g}\,\mathrm{d}\frac{1}{2}\mathbf{g}} : \Delta\frac{1}{2}\mathbf{g} + \frac{\mathrm{d}^2 W}{\mathrm{d}\frac{1}{2}\mathbf{g}\,\mathrm{d}\mathbf{k}} : \Delta\mathbf{k} \right) : \delta\frac{1}{2}\mathbf{g} + \boldsymbol{\tau} : \Delta\delta\frac{1}{2}\mathbf{g}$$

$$+ \left(\frac{\mathrm{d}^2 W}{\mathrm{d}\mathbf{k}\,\mathrm{d}\frac{1}{2}\mathbf{g}} : \Delta\frac{1}{2}\mathbf{g} + \frac{\mathrm{d}^2 W}{\mathrm{d}\mathbf{k}\,\mathrm{d}\mathbf{k}} : \Delta\mathbf{k} \right) : \delta\mathbf{k} + \mathbf{m} : \Delta\delta\mathbf{k} \Bigg] \, \mathrm{d}\Omega_0 \qquad (4.94)$$

In contrast to the aforementioned approach, this formulation is defined on the spatial (Eulerian) configuration. Consequently, $\frac{\mathrm{d}W}{\mathrm{d}\frac{1}{2}\mathbf{g}}$ is called Kirchhoff membrane tensor $\boldsymbol{\tau}$ and the term $\frac{\mathrm{d}W}{\mathrm{d}\mathbf{k}}$ is declared as Kirchhoff bending tensor $\mathbf{m}$.

It has to be pointed out that by an appropriate push-forward operation, the principal curvatures approach can be characterised on the current configuration as well. On the other hand, the direct curvature approach may be treated on the initial configuration by applying a suitable pull-back of the involved terms. Nevertheless, both formulations need the first-order and second-order total derivatives of the strain energy density with respect to the corresponding strain measures. In the course of this, it has to be emphasised that the relaxed strain energy density depends on the relaxed inner displacements $\boldsymbol{\eta} = \hat{\boldsymbol{\eta}}$, which are in turn a function of the strain measures. In order to obtain a compact notation of the required derivatives, the strain measures are symbolised by $(\,)$ and $[\,]$. For the principal curvatures approach, $(\,)$ and $[\,]$ are either $\frac{1}{2}\mathbf{C}$ or $\mathcal{K}$ whereas for the direct curvature approach these brackets are either $\frac{1}{2}\mathbf{g}$ or $\mathbf{k}$. The first-order total derivative of the strain energy density with respect to $(\,)$ is given by:

$$\frac{\mathrm{d}W}{\mathrm{d}(\,)} = \frac{\partial W}{\partial(\,)} + \frac{\partial W}{\partial\boldsymbol{\eta}} : \frac{\partial\boldsymbol{\eta}}{\partial(\,)} \qquad (4.95)$$

Considering the fact that an ideal inner relaxation is performed, the second term drops out due to Equation (4.78) and the total derivative of the strain energy density can be replaced by the related partial derivative at the state of relaxed inner displacements. However, the full expression of Equation (4.95) is essential for its further total derivatives. Otherwise, the influence of the inner relaxation on the second-order derivatives of the strain energy density is omitted and the corresponding correction term is missing. With this fact in mind, the second-order total derivative of the strain energy density with respect to $[\,]$ reads:

$$\frac{\mathrm{d}^2 W}{\mathrm{d}(\,)\,\mathrm{d}[\,]} = \frac{\partial}{\partial[\,]}\left(\frac{\mathrm{d}W}{\mathrm{d}(\,)}\right) + \frac{\partial}{\partial\boldsymbol{\eta}}\left(\frac{\mathrm{d}W}{\mathrm{d}(\,)}\right) : \frac{\partial\boldsymbol{\eta}}{\partial[\,]}$$

$$= \frac{\partial}{\partial[\,]}\left(\frac{\partial W}{\partial(\,)}\right) + \frac{\partial}{\partial[\,]}\left(\frac{\partial W}{\partial\boldsymbol{\eta}}\right) : \frac{\partial\boldsymbol{\eta}}{\partial(\,)} + \frac{\partial W}{\partial\boldsymbol{\eta}} : \frac{\partial}{\partial[\,]}\left(\frac{\partial\boldsymbol{\eta}}{\partial(\,)}\right)$$

$$+ \left[\frac{\partial}{\partial\boldsymbol{\eta}}\left(\frac{\partial W}{\partial(\,)}\right) + \frac{\partial}{\partial\boldsymbol{\eta}}\left(\frac{\partial W}{\partial\boldsymbol{\eta}}\right) : \frac{\partial\boldsymbol{\eta}}{\partial(\,)} + \frac{\partial W}{\partial\boldsymbol{\eta}} : \frac{\partial}{\partial\boldsymbol{\eta}}\left(\frac{\partial\boldsymbol{\eta}}{\partial(\,)}\right)\right] : \frac{\partial\boldsymbol{\eta}}{\partial[\,]} \qquad (4.96)$$

This expression is further simplified by using the fulfilment of the inner relaxation. Therefore, the total derivative of Equation (4.78) with respect to $(\,)$ is computed.

$$\frac{\mathrm{d}}{\mathrm{d}(\,)}\left(\frac{\partial W}{\partial\boldsymbol{\eta}}\right) = \frac{\partial}{\partial(\,)}\left(\frac{\partial W}{\partial\boldsymbol{\eta}}\right) + \frac{\partial}{\partial\boldsymbol{\eta}}\left(\frac{\partial W}{\partial\boldsymbol{\eta}}\right) : \frac{\partial\boldsymbol{\eta}}{\partial(\,)} = \mathbf{0} \qquad (4.97)$$

This equation allows to give a characterisation for the partial derivative of the inner displacements $\boldsymbol{\eta}$ with respect to the strain measures, which are again symbolised by $(\,)$.

$$\frac{\partial\boldsymbol{\eta}}{\partial(\,)} = -\left[\frac{\partial^2 W}{\partial\boldsymbol{\eta}\partial\boldsymbol{\eta}}\right]^{-1} : \frac{\partial^2 W}{\partial\boldsymbol{\eta}\partial(\,)} \qquad (4.98)$$

Taking into account of Equation (4.97), Equation (4.98) and the ideal inner relaxation of Equation (4.78), the second-order total derivative of the strain energy density simplifies to:

$$\frac{\mathrm{d}^2 W}{\mathrm{d}(\,)\,\mathrm{d}[\,]} = \frac{\partial^2 W}{\partial(\,)\partial[\,]} - \frac{\partial^2 W}{\partial\boldsymbol{\eta}\partial[\,]} : \left[\frac{\partial^2 W}{\partial\boldsymbol{\eta}\partial\boldsymbol{\eta}}\right]^{-1} : \frac{\partial^2 W}{\partial\boldsymbol{\eta}\partial(\,)} \qquad (4.99)$$

It is pointed out again that within this expression, the relaxed strain energy density is considered and, consequently, all terms are evaluated at the relaxed inner displacements $\boldsymbol{\eta} = \hat{\boldsymbol{\eta}}$. The necessary quantities for the evaluation of the first-order and second-order partial derivatives of the strain energy density with respect to the proper strain measures are listed explicitly in Appendix A.1. The variations of the strain measures and their increments are given in Subappendix A.3.1.

The variation $\delta\Pi_{\mathrm{nb}}$ and its increment $\Delta\delta\Pi_{\mathrm{nb}}$ follow directly from the definition of the non-bonded potential Π_{nb} in Equation (4.87).

$$\delta\Pi_{\mathrm{nb}} = \frac{1}{2} \int\limits_{\Omega_0} \int\limits_{\Omega_0 - B_X} \frac{\partial W_{\mathrm{nb}}}{\partial d} : \delta d \; \mathrm{d}\Omega_{0Y} \; \mathrm{d}\Omega_{0X} \tag{4.100}$$

$$\Delta\delta\Pi_{\mathrm{nb}} = \frac{1}{2} \int\limits_{\Omega_0} \int\limits_{\Omega_0 - B_X} \left[\left(\frac{\partial^2 W_{\mathrm{nb}}}{\partial d \partial d} : \Delta d \right) : \delta d + \frac{\partial W_{\mathrm{nb}}}{\partial d} : \Delta\delta d \right] \; \mathrm{d}\Omega_{0Y} \; \mathrm{d}\Omega_{0X} \tag{4.101}$$

The first-order and second-order derivatives of the strain energy double density W_{nb} with respect to the distance $d(\mathbf{x}, \mathbf{y})$ of two points on the deformed surface can be calculated in a straightforward manner and are given in Appendix A.2. Additionally, the variation δd, the increment Δd and the increment $\Delta\delta d$ are essential.

$$d(\mathbf{x}, \mathbf{y}) = \|\mathbf{x} - \mathbf{y}\| = [(\mathbf{x} - \mathbf{y}) \cdot (\mathbf{x} - \mathbf{y})]^{1/2} \tag{4.102}$$

$$\delta d(\mathbf{x}, \mathbf{y}) = \frac{1}{d(\mathbf{x}, \mathbf{y})} (\delta\mathbf{x} - \delta\mathbf{y}) \cdot (\mathbf{x} - \mathbf{y}) \tag{4.103}$$

$$\Delta d(\mathbf{x}, \mathbf{y}) = \frac{1}{d(\mathbf{x}, \mathbf{y})} (\Delta\mathbf{x} - \Delta\mathbf{y}) \cdot (\mathbf{x} - \mathbf{y}) \tag{4.104}$$

$$\Delta\delta d(\mathbf{x}, \mathbf{y}) = -\frac{1}{[d(\mathbf{x}, \mathbf{y})]^3} [(\Delta\mathbf{x} - \Delta\mathbf{y}) \cdot (\mathbf{x} - \mathbf{y})] \cdot [(\delta\mathbf{x} - \delta\mathbf{y}) \cdot (\mathbf{x} - \mathbf{y})]$$
$$+ \frac{1}{d(\mathbf{x}, \mathbf{y})} (\delta\mathbf{x} - \delta\mathbf{y}) \cdot (\Delta\mathbf{x} - \Delta\mathbf{y}) \tag{4.105}$$

The variation $\delta\Pi_{\mathrm{ext}}$ results from the potential due to external loads defined in Equation (4.88).

$$\delta\Pi_{\mathrm{ext}} = -\int\limits_{\Omega_0} \frac{2}{S_0} \mathbf{f} \cdot \delta\mathbf{x} \; \mathrm{d}\Omega_0 \tag{4.106}$$

Due to the consideration of a constant force field $\mathbf{f}$, this variation is independent of the deformation and, consequently, its increment $\Delta\delta\Pi_{\mathrm{ext}}$ vanishes.

4.7 Stability of global equilibrium

On the basis of the previous Section 4.6, equilibrium configurations of the continuum surface for the mixed atomistic-continuum model can be calculated. In addition, the structural stability of this states is significant for a buckling analysis. In order to give a criterion for stable configurations, the total potential of neighbouring states is compared. If the total potential $\Pi(\mathbf{x})$ at the equilibrium state is smaller than the total potential $\Pi(\mathbf{x} + \delta\mathbf{x})$ of an infinitesimally perturbed configuration, the observed equilibrium configuration is designated to be stable.

$$\Pi(\mathbf{x} + \delta\mathbf{x}) - \Pi(\mathbf{x}) > 0 \tag{4.107}$$

Next, the infinitesimally perturbed configuration can be approximated by a truncated Taylor series expansion around the equilibrium state.

$$\Pi\left(\mathbf{x} + \delta\mathbf{x}\right) = \Pi\left(\mathbf{x}\right) + \delta\Pi\left(\mathbf{x}\right) + \frac{1}{2}\delta^2\Pi\left(\mathbf{x}\right) \tag{4.108}$$

Moreover, for the equilibrium configuration, the stationary condition $\delta\Pi\left(\mathbf{x}\right) = 0$ is valid and, consequently, the stability condition reads:

$$\delta^2\Pi\left(\mathbf{x}\right) > 0 \tag{4.109}$$

On the contrary, the observed equilibrium state is indifferent if $\delta^2\Pi\left(\mathbf{x}\right) = 0$ or even unstable if $\delta^2\Pi\left(\mathbf{x}\right) < 0$. In particular, at unstable configurations, a neighbouring state with lower potential energy is possible.

4.8 Numerical implementation

This section supplies information about the numerical implementation of the mixed atomistic-continuum model on the basis of the finite element method. For a full treatment on the concepts of the finite element method see classical textbooks for instance Bathe [7], Wriggers [61] and Zienkiewicz and Taylor [64, 65]. The application of the finite element method for the approximation of the mixed atomistic-continuum model requires a proper choice of the finite element space. For that purpose, suitable finite elements are specified. The calculation of equilibrium configurations is performed by discretising the linearised stationary condition and employing an iterative solution procedure. The necessary expressions for setting up the finite element equations are specified. In particular, considering the bonded and the non-bonded interactions as well as external contributions, the relevant element force vectors and element stiffness matrices are provided.

4.8.1 Finite element approximation employing subdivision finite elements

The constitutive model for the simulation of carbon nanotubes, derived in Section 4.5, sets essential conditions on the finite element space. This is because the two distinct approximations of the exponential Cauchy-Born rule deliver a strain energy density that depends on the spatial curvature tensor and, therefore, the total potential of bonded interactions alike. As a consequence, the finite element space has to provide bounded second square integrable derivatives. This requirement on the finite element shape functions is evident from the definition of the spatial curvature tensor in Equation (4.21). One possibility to observe this request is the use of finite elements on the basis of subdivision surfaces. Subdivision surfaces are tools for shaping curves and surfaces, which were developed in the area of computer graphics. Thereby, the main fields of application are animation movies, computer games and computer aided geometry design. However, subdivision surfaces were also applied as finite elements for special purposes. In this context, Cirak and Ortiz [17] and Cirak *et al.* [18] successfully introduced the idea of subdivision surfaces to the finite element analysis of thin shells. In particular, a triangular type of subdivision surfaces according to Loop [33] is used. The call for comparable quadrilateral subdivision finite elements is satisfied by the scheme of Catmull and Clark [13]. These two schemes offer the desirable property that a polynomial representation of the surface within an element is possible and, hence, the shape functions of the finite element are well defined. In what follows, the characteristics and the patches of the triangular and quadrilateral subdivision finite elements are specified.

Triangular subdivision finite element

This type of finite element is non-local and offers an approximative character. The illustration in Figure 4.17 depicts a referential finite element patch that is mapped into the undeformed and the deformed configuration by the concept of isoparametry. The three distinct configurations
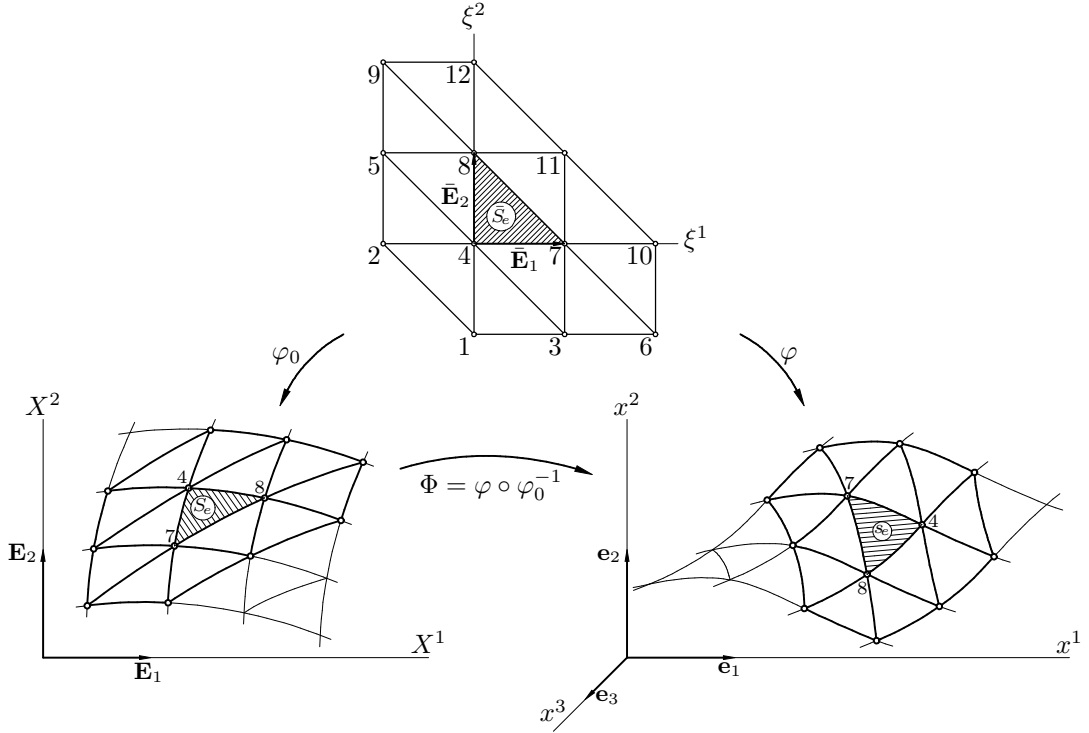
Figure 4.17: The triangular subdivision finite element. Illustration of the reference configuration and the mapped material (graphene sheet) and spatial (carbon nanotube) configuration of the triangular subdivision finite element patch.

of the finite element and their bases are defined according to Subsection 4.3.1. The non-local character results from the fact that the approximated field within the shaded central face depends not only on nodal values of its corners. In addition, the coefficients of the nodes in its first neighbourhood are important as well. This results in 12 shape functions for the whole patch, nonetheless, the parametrisation is executed solely for the considered central element 4-7-8, which is referred to as finite element. Explicit expressions for the shape functions $N_I\left(\xi^1, \xi^2\right)$ are given in Subappendix A.4.1. Herein, the index I characterises the local node number while ξ^1 and ξ^2 are the local curvilinear coordinates of the unit triangle in the parametric space. This allows to state an approximated position vector within the finite element in its Lagrangian and Eulerian configuration on the basis of the shape functions and the related nodal coefficients.

Quadrilateral subdivision finite element

The quadrilateral non-local subdivision finite element patch is illustrated in Figure 4.18. Herein, the referential patch consists of the central quad, termed as finite element, and its eight surrounding quads. Following the isoparametric concept, this reference element is mapped into each undeformed and deformed finite element. In doing so, the three distinct configurations and their bases are defined in conformance with Subsection 4.3.1. Again, the non-locality is characterised by the additional influence of the nodal coefficients of the surrounding nodes on the approximation field inside the central quad that is enclosed by the corner nodes 6-7-10-11. Thus, in total 16 shape functions are necessary for the parametrisation of the finite element. Based on the local curvilinear coordinates ξ^1 and ξ^2, for each local node I in the patch, a shape function $N_I\left(\xi^1, \xi^2\right)$ is defined according to Subappendix A.4.2. Using these shape functions and the nodal coefficients, the approximation of a position vector inside the finite element is possible. Thus, its material and
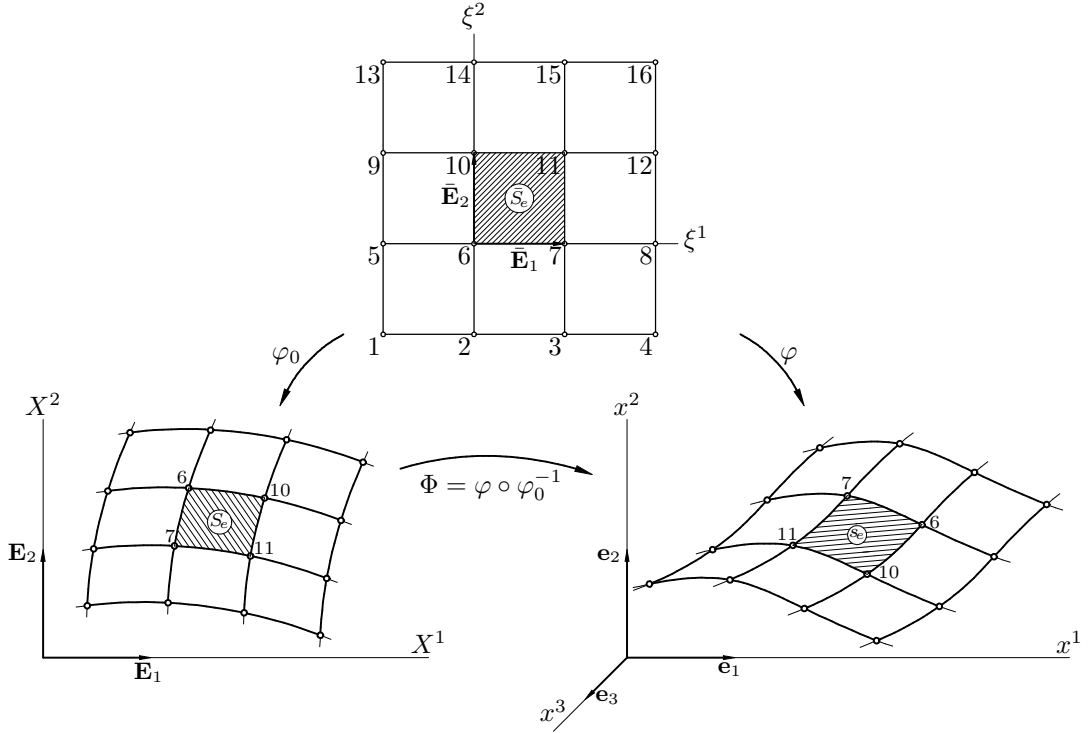
Figure 4.18: The quadrilateral subdivision finite element. Illustration of the reference configuration and the mapped material (graphene sheet) and spatial (carbon nanotube) configuration of the quadrilateral subdivision finite element patch.

spatial description are well defined.

Configurations of the finite element

The description of the approximated geometry by a finite element requires a set of nodal coefficients in combination with the appropriate shape functions. In the case of the subdivision finite elements, the nodes of the patch exhibit only translational degrees of freedom. However, using either the triangular or the quadrilateral finite element, the resulting parametrised surface is smooth. This circumstance is received due to their non-local character. Taking everything into account, the approximations of the position vectors, for the geometry of the finite elements in the material (Lagrangian) $\mathbf{X}$ and spatial (Eulerian) $\mathbf{x}$ configuration, are given by:

$$\mathbf{X} = N_I\left(\xi^1, \xi^2\right) \mathbf{X}_I \tag{4.110}$$

$$\mathbf{x} = N_I\left(\xi^1, \xi^2\right) \mathbf{x}_I \tag{4.111}$$

In these expressions and in what follows, summation on the local node index I is performed. In addition, the quantities $\mathbf{X}_I$ and $\mathbf{x}_I$ depict the nodal coordinates in the material and spatial configuration, respectively. The shape functions $N_I\left(\xi^1, \xi^2\right)$ are selected depending on the type of discretisation. For that purpose, the triangular finite element ($I = 1, \ldots, 12$) and the quadrilateral finite element ($I = 1, \ldots, 16$), which where introduced above are available. Applying the finite element approximation, the covariant base vectors of the undeformed configuration, which are defined in Equation (4.14), are obtained in their discrete form as:

$$\mathbf{G}_\alpha = \frac{\partial \mathbf{X}}{\partial \xi^\alpha} = (N_I)_{,\alpha} \mathbf{X}_I = (N_I)_{,\alpha} \left(X_I\right)^A \mathbf{E}_A \tag{4.112}$$

Herein, $(N_I)_{,\alpha}$ denotes the first-order partial derivative of the shape function N_I with respect to the curvilinear coordinate ξ^α. In a similar manner, considering Equation (4.14), the approximated covariant base vectors of the surface in its deformed configuration are given by:

$$\mathbf{g}_\alpha = \frac{\partial \mathbf{x}}{\partial \xi^\alpha} = (N_I)_{,\alpha}\, \mathbf{x}_I = (N_I)_{,\alpha}\, (x_I)^a\, \mathbf{e}_a \tag{4.113}$$

Subsequently, the discretised initial Jacobian tensor, following Equation (4.23), reads:

$$\mathbf{J} = \mathbf{G}_\alpha \otimes \bar{\mathbf{E}}^\alpha = (N_I)_{,\alpha}\, (X_I)^A\, \mathbf{E}_A \otimes \bar{\mathbf{E}}^\alpha \tag{4.114}$$

This Jacobian tensor, strictly speaking its inverse, is important for the pull-back operations performed on the spatial metric tensor and the spatial curvature tensor. Therefore, especially its components

$$J^A{}_\alpha = (N_I)_{,\alpha}\, (X_I)^A \tag{4.115}$$

with respect to the bases $\mathbf{E}_A$ and $\bar{\mathbf{E}}^\alpha$ are of interest. The discretised current configuration Jacobian tensor according, to Equation (4.23), is given by:

$$\mathbf{j} = \mathbf{g}_\alpha \otimes \bar{\mathbf{E}}^\alpha = (N_I)_{,\alpha}\, (x_I)^A\, \mathbf{e}_a \otimes \bar{\mathbf{E}}^\alpha \tag{4.116}$$

This quantity is specified for the sake of completeness although it is not explicitly needed in the implementation. Furthermore, for the spatial curvature tensor, the derivative of the covariant base vectors in the deformed surface with respect to the local curvilinear coordinate ξ^β is necessary.

$$\mathbf{g}_{\alpha,\beta} = \frac{\partial \mathbf{g}_\alpha}{\partial \xi^\beta} = \frac{\partial^2 \mathbf{x}}{\partial \xi^\alpha \partial \xi^\beta} = (N_I)_{,\alpha\beta}\, \mathbf{x}_I = (N_I)_{,\alpha\beta}\, (x_I)^a\, \mathbf{e}_a \tag{4.117}$$

In that expression, $(N_I)_{,\alpha\beta}$ denotes the second-order partial derivative of the shape function N_I with respect to the curvilinear coordinates ξ^α and ξ^β. On the basis of these approximations, the essential strain measures $\mathbf{g}, \mathbf{k}$ and, consequently, $\mathbf{C}, \mathcal{K}$ can be calculated according to Subsection 4.3.3 and Subsection 4.3.4 in a straightforward manner. In addition to that, the analogies to the variations of the strain measures and the increments of these variations, namely their derivatives with respect to the degrees of freedom, follow the representation of Subappendix A.3.2.

4.8.2 Global equilibrium in the discrete setting

In order to obtain the finite element equations for the global equilibrium that is derived in its continuous setting in Section 4.6, a discretisation by means of subdivision finite elements is applied. In that process, the undeformed domain Ω_0 and the deformed domain Ω are partitioned into a set of n_{el} elements. This fragmentation, additionally, introduces a specific number n_{n} of global nodes K with various feasible and dedicated coefficients. Each finite element e owns its undeformed area S_e as well as its deformed area s_e. Moreover, two distinct elements do not overlap. Consequently, the entire undeformed body $\Omega_0 = \bigcup_{e=1}^{n_{\mathrm{el}}} S_e$ is the union of all element-related undeformed domains. The identical thought delivers $\Omega = \bigcup_{e=1}^{n_{\mathrm{el}}} s_e$ for the deformed domain. As a consequence of this discretisation, the overall quantities of the considered domain are obtained by collecting the individual elemental contributions. According to Subsection 4.8.1, the use of subdivision finite elements solely introduces translational degrees of freedom. Therefore, the nodal position vector $\mathbf{X}_K$ in the material configuration as well as the nodal position vector $\mathbf{x}_K$ in spatial configuration are assigned to each global node K of the discretisation. In addition, the virtual displacements $\delta\mathbf{x}$ and the increments $\Delta\mathbf{x}$ are approximated in accordance with the geometry by finite elements and their associated shape functions. Consequently, a vector of virtual displacements $\delta\mathbf{x}_K$ and a vector of displacement increments $\Delta\mathbf{x}_K$ is assigned to each node of the finite element mesh. The calculation of global equilibrium configurations for a specified external load level is characterised

by the associated stationary condition given for the continuous setting in Equation (4.89). As a consequence of the discretisation by finite elements and the introduction of nodal coefficients, a non-linear system of equations originates. This system of equations is further linearised in order to enable an iterative solution procedure. Therefore, on the basis of the linearisation given in Equation (4.90), a linear system of equations has to be solved repeatedly. For this purpose, the variations of the total potential and their increments in the discrete setting are given below.

$$\delta\Pi = \delta\Pi_{\text{b}} + \delta\Pi_{\text{nb}} + \delta\Pi_{\text{ext}}$$

$$\delta\Pi = \sum_{K=1}^{n_{\text{n}}} \left[\frac{\partial\Pi_{\text{b}}}{\partial\mathbf{x}_K} + \frac{\partial\Pi_{\text{nb}}}{\partial\mathbf{x}_K} + \frac{\partial\Pi_{\text{ext}}}{\partial\mathbf{x}_K} \right] \cdot \delta\mathbf{x}_K$$

$$\delta\Pi = \sum_{K=1}^{n_{\text{n}}} \left[(\mathbf{f}_{\text{b}})_K + (\mathbf{f}_{\text{nb}})_K - (\mathbf{f}_{\text{ext}})_K \right] \cdot \delta\mathbf{x}_K$$

$$\delta\Pi = \sum_{K=1}^{n_{\text{n}}} \left[(\mathbf{f}_{\text{int}})_K - (\mathbf{f}_{\text{ext}})_K \right] \cdot \delta\mathbf{x}_K \tag{4.118}$$

The expressions $(\mathbf{f}_{\text{b}})_K$ and $(\mathbf{f}_{\text{nb}})_K$ denote the global force sub-vectors associated with the global node K. These forces arise from the bonded interactions and the non-bonded interactions, which are, additionally, collected into a global internal force sub-vector $(\mathbf{f}_{\text{int}})_K$. Consequently, the global external force sub-vector $(\mathbf{f}_{\text{ext}})_K$ considers the contributions of external loads related to node K.

$$\Delta\delta\Pi = \Delta\delta\Pi_{\text{b}} + \Delta\delta\Pi_{\text{nb}} + \Delta\delta\Pi_{\text{ext}}$$

$$\Delta\delta\Pi = \sum_{K=1}^{n_{\text{n}}} \left\{ \sum_{L=1}^{n_{\text{n}}} \left[\frac{\partial^2\Pi_{\text{b}}}{\partial\mathbf{x}_K\partial\mathbf{x}_L} + \frac{\partial^2\Pi_{\text{nb}}}{\partial\mathbf{x}_K\partial\mathbf{x}_L} \right] \Delta\mathbf{x}_L \right\} \cdot \delta\mathbf{x}_K$$

$$\Delta\delta\Pi = \sum_{K=1}^{n_{\text{n}}} \left\{ \sum_{L=1}^{n_{\text{n}}} \left[(\mathbf{K}_{\text{b}})_{KL} + (\mathbf{K}_{\text{nb}})_{KL} \right] \Delta\mathbf{x}_L \right\} \cdot \delta\mathbf{x}_K$$

$$\Delta\delta\Pi = \sum_{K=1}^{n_{\text{n}}} \left\{ \sum_{L=1}^{n_{\text{n}}} (\mathbf{K})_{KL} \Delta\mathbf{x}_L \right\} \cdot \delta\mathbf{x}_K \tag{4.119}$$

The sub-matrices $(\mathbf{K}_{\text{b}})_{KL}$ and $(\mathbf{K}_{\text{nb}})_{KL}$ of the global stiffness matrix incorporate the bonded and the non-bonded interactions. Moreover, these individual sub-matrices are combined to a tangent stiffness sub-matrix $(\mathbf{K})_{KL}$ associated with the global nodes K and L.

The concatenation of the discrete forms of the variations and the linearised variations, under consideration of arbitrary virtual displacements $\delta\mathbf{x}$, delivers a linear system of equations. Consequently, the finite element equations for the iteration $(m+1)$ of the global equilibrium can be set up.

$$\sum_{L=1}^{n_{\text{n}}} \left(\mathbf{K}^{(m)} \right)_{KL} \Delta\mathbf{x}_L^{(m+1)} = - \left(\mathbf{f}_{\text{int}}^{(m)} \right)_K + (\mathbf{f}_{\text{ext}})_K \qquad K = 1, \ldots, n_{\text{n}} \quad \text{and} \quad m = 0, 1, \ldots \tag{4.120}$$

Furthermore, this index representation of the finite element equations can be transformed into a matrix notation. In the course of this, the introduction of the global tangent stiffness matrix $\mathbf{K}^{(m)}$ and the global vector $\Delta\mathbf{x}^{(m+1)}$ of displacement increments is necessary.

$$\mathbf{K}^{(m)} = \begin{bmatrix} \left(\mathbf{K}^{(m)} \right)_{11} & \cdots & \left(\mathbf{K}^{(m)} \right)_{1n_{\text{n}}} \\ \vdots & \ddots & \vdots \\ \left(\mathbf{K}^{(m)} \right)_{n_{\text{n}}1} & \cdots & \left(\mathbf{K}^{(m)} \right)_{n_{\text{n}}n_{\text{n}}} \end{bmatrix} \qquad \Delta\mathbf{x}^{(m+1)} = \begin{bmatrix} \Delta\mathbf{x}_1^{(m+1)} \\ \vdots \\ \Delta\mathbf{x}_{n_{\text{n}}}^{(m+1)} \end{bmatrix} \tag{4.121}$$

In addition, the global internal force vector $\mathbf{f}_{\text{int}}^{(m)}$ and the global external force vector $\mathbf{f}_{\text{ext}}$ are accordingly defined.

$$\mathbf{f}_{\text{int}}^{(m)} = \begin{bmatrix} \left(\mathbf{f}_{\text{int}}^{(m)}\right)_1 \\ \vdots \\ \left(\mathbf{f}_{\text{int}}^{(m)}\right)_{n_{\text{n}}} \end{bmatrix} \qquad \mathbf{f}_{\text{ext}} = \begin{bmatrix} (\mathbf{f}_{\text{ext}})_1 \\ \vdots \\ (\mathbf{f}_{\text{ext}})_{n_{\text{n}}} \end{bmatrix} \qquad (4.122)$$

As a consequence, the linear system of equations for the iteration $(m + 1)$ of a Newton-Raphson procedure can be written as:

$$\mathbf{K}^{(m)} \Delta \mathbf{x}^{(m+1)} = -\mathbf{f}_{\text{int}}^{(m)} + \mathbf{f}_{\text{ext}} \qquad (4.123)$$

This system is solved to obtain the increments $\Delta \mathbf{x}^{(m+1)}$ of the global nodal position vector $\mathbf{x}^{(m)}$ and, subsequently, an update of these positions is realised.

$$\mathbf{x}^{(m+1)} = \mathbf{x}^{(m)} + \Delta \mathbf{x}^{(m+1)} \qquad (4.124)$$

The iterations are repeated till the energy residuum $\left| \left(-\mathbf{f}_{\text{int}}^{(m)} + \mathbf{f}_{\text{ext}}\right) \cdot \Delta \mathbf{x}^{(m+1)} \right|$ is less or equal a given tolerance. If convergence is achieved, the next load step can be investigated.

In the following, the essential element-wise contributions to the global force vectors and the global stiffness matrix are specified. In particular, the bonded and the non-bonded interactions are observed and the associated element force vectors and the element stiffness matrices are defined. Furthermore, the element-related external force vector resulting from the external loads is given. Thereby, index notation is used and the conventions given in Subsection 4.3.2 are applied. In addition, the indices I and J characterise local nodes within a finite element whereas the indices K and L represent global nodes of the entire discretisation. Following this conventions, the components of global and element force vectors are specified by a node index and a coordinate index. In the same fashion, the components of global and element stiffness matrices are characterised by two node indices and two coordinate indices.

Potential of bonded interactions

With reference to Equation (4.85) and Equation (4.86), the potential Π_{b} of bonded interactions is defined by the integral of the relaxed strain energy density over the undeformed domain. The relaxed strain energy density is obtained by evaluating the strain energy density W, which is given according to Equation (4.76) and Equation (4.77) for the two types of approximations of the exponential Cauchy-Born rule, at the state of relaxed inner displacements $\boldsymbol{\eta} = \hat{\boldsymbol{\eta}}$, received from the minimisation process as specified in Equation (4.78). Due to the discretisation of the continuous surface by means of finite elements, the integral over the undeformed domain Ω_0 can be split into a sum of element-wise integrals.

$$\Pi_{\text{b}} = \int\limits_{\Omega_0} W \, d\Omega_0 = \sum_{e=1}^{n_{\text{el}}} \int\limits_{S_e} W \, dS_e = \sum_{e=1}^{n_{\text{el}}} \Pi_{\text{b}}^e \qquad (4.125)$$

Furthermore, the integrals within the element-related bonded potential Π_{b}^e are transformed to correlated integrals on the reference element. At this stage, the determinant of the initial Jacobian tensor is crucial. Finally, the exact integration is approximated by numerical quadrature. Therefore, quadrature points $q = 1, \ldots, n_{\text{qb}}$ at the referential coordinates (ξ_q^1, ξ_q^2) with their corresponding weights w_q are introduced. As a consequence, the relaxed strain energy density and the determinant of the initial Jacobian tensor $\det(\mathbf{J})$ have to be evaluated at this quadrature

points.

$$\Pi_{\rm b}^e = \int\limits_{\bar{S}_e} W \det\left(\mathbf{J}\right)\,{\rm d}\bar{S}_e \approx \sum_{q=1}^{n_{\rm qb}} W\big|_{\left(\xi_q^1,\xi_q^2\right)} \det\left(\mathbf{J}\right)\big|_{\left(\xi_q^1,\xi_q^2\right)} w_q \tag{4.126}$$

The representation of the relaxed strain energy density for the numerical integration requires the relaxed inner displacements $\boldsymbol{\eta} = \hat{\boldsymbol{\eta}}$. These have to be calculated for each quadrature point according to Subsection 4.5.3 via an internal Newton-Raphson procedure.

Internal forces due to bonded interactions

In the discrete setting of the finite element method, the virtual displacements within an element are approximated in the same fashion as the geometry by shape functions and nodal coefficients. On this account, for each global node K the related virtual displacement vector $\delta\mathbf{x}_K$ is introduced. This allows to give the discrete form of the variated bonded potential as:

$$\delta\Pi_{\rm b} = \sum_{K=1}^{n_{\rm n}} \frac{\partial\Pi_{\rm b}}{\partial\mathbf{x}_K} \cdot \delta\mathbf{x}_K = \sum_{K=1}^{n_{\rm n}} \left(\mathbf{f}_{\rm b}\right)_K \cdot \delta\mathbf{x}_K \tag{4.127}$$

Within this expression, the derivative of the bonded potential with respect to the global nodal coefficients defines the global force sub-vector $\left(\mathbf{f}_{\rm b}\right)_K$ of the discrete system. An element force vector $\left(\mathbf{f}_{\rm b}^e\right)_I$ can be defined, if the corresponding coefficients $\delta\mathbf{x}_I$ of the local nodes I are extracted from the global ones. Then, the derivative of the element-wise bonded potential $\Pi_{\rm b}^e$ with respect to the components $(x_I)^a$ of the actual local displacement vector gives the corresponding components of the internal force vector. Following these thoughts, the force vector components $(f_{\rm b}^e)_{Ia}$ for the two formulations of the extended Cauchy-Born rule are assignable in their numerical integration complying form.

- Approximation of the exponential Cauchy-Born rule: principal curvatures approach

$$\left(f_{\rm b}^e\right)_{Ia} = \sum_{q=1}^{n_{\rm qb}} \left[\frac{{\rm d}W}{{\rm d}\frac{1}{2}C_{AB}} \frac{\partial\frac{1}{2}C_{AB}}{\partial(x_I)^a} + \frac{{\rm d}W}{{\rm d}\mathcal{K}_{AB}} \frac{\partial\mathcal{K}_{AB}}{\partial(x_I)^a}\right]_{\left(\xi_q^1,\xi_q^2\right)} \det\left(\mathbf{J}\right)\big|_{\left(\xi_q^1,\xi_q^2\right)} w_q \tag{4.128}$$

- Approximation of the exponential Cauchy-Born rule: direct curvature approach

$$\left(f_{\rm b}^e\right)_{Ia} = \sum_{q=1}^{n_{\rm qb}} \left[\frac{{\rm d}W}{{\rm d}\frac{1}{2}g_{\alpha\beta}} \frac{\partial\frac{1}{2}g_{\alpha\beta}}{\partial(x_I)^a} + \frac{{\rm d}W}{{\rm d}k_{\alpha\beta}} \frac{\partial k_{\alpha\beta}}{\partial(x_I)^a}\right]_{\left(\xi_q^1,\xi_q^2\right)} \det\left(\mathbf{J}\right)\big|_{\left(\xi_q^1,\xi_q^2\right)} w_q \tag{4.129}$$

By an appropriate assemble procedure, these various local element force vector components $(f_{\rm b}^e)_{Ia}$ are converted into the unique global force vector $\left(\mathbf{f}_{\rm b}\right)_K$. The components of this global force vector $(f_{\rm b})_{Ka}$ are specified according to the global node number K and the coordinate direction a. In the computational implementation, the force vectors are effectively stored in this two-dimensional representation, exhibiting a node index and a coordinate index. The total first-order derivative of the strain energy density can be calculated by following the deliberations given in Section 4.6 and, subsequently, considering Appendix A.1 and the statements therein with the discrete strain measures acting as input. The derivatives of the strain measures with respect to the components of the actual displacement vector are stated in Subappendix A.3.2.

Tangent stiffness matrix due to bonded interactions

For the application of the Newton-Raphson procedure, the increment of the variated bonded potential is crucial. Therefore, displacement increments $\Delta\mathbf{x}_L$ are introduced in each global node L of the discretisation. The displacement increments within each finite element are approximated on

the basis of these nodal coefficients and the shape functions. With regard to the global displacement increments, the discrete form of the increment of the variated bonded potential can be stated as:

$$\Delta \delta \Pi_{\mathrm{b}} = \sum_{K=1}^{n_{\mathrm{n}}} \left[\sum_{L=1}^{n_{\mathrm{n}}} \frac{\partial^2 \Pi_{\mathrm{b}}}{\partial \mathbf{x}_K \partial \mathbf{x}_L} \Delta \mathbf{x}_L \right] \cdot \delta \mathbf{x}_K = \sum_{K=1}^{n_{\mathrm{n}}} \left[\sum_{L=1}^{n_{\mathrm{n}}} (\mathbf{K}_{\mathrm{b}})_{KL} \, \Delta \mathbf{x}_L \right] \cdot \delta \mathbf{x}_K \qquad (4.130)$$

Herein, the second-order partial derivative of the bonded potential with respect to the global nodal coefficients identifies the sub-matrices $(\mathbf{K}_{\mathrm{b}})_{KL}$ of the global stiffness matrix. In order to make use of the intention of the finite element method, appropriate element stiffness matrices can be introduced. For that purpose, the element-wise bonded potential Π_{b}^e is derivated twice with respect to the components of the actual local displacement vectors $(x_I)^a$ and $(x_J)^b$. Therein, the indices I and J refer to the local node number within the element while a and b are indices related to the base vectors of the coordinate frame. The realisation of the derivatives in the given notation delivers the element stiffness matrix components $(K_{\mathrm{b}}^e)_{IaJb}$ for the two different approximations of the exponential Cauchy-Born rule under consideration of numerical integration.

- Approximation of the exponential Cauchy-Born rule: principal curvatures approach

$$
\begin{aligned}
(K_{\mathrm{b}}^e)_{IaJb} = \sum_{q=1}^{n_{\mathrm{qb}}} \Bigg[& \left(\frac{\mathrm{d}^2 W}{\mathrm{d}\frac{1}{2}C_{AB}\, \mathrm{d}\frac{1}{2}C_{CD}} \frac{\partial \frac{1}{2}C_{CD}}{\partial (x_J)^b} + \frac{\mathrm{d}^2 W}{\mathrm{d}\frac{1}{2}C_{AB}\, \mathrm{d}\mathcal{K}_{CD}} \frac{\partial \mathcal{K}_{CD}}{\partial (x_J)^b} \right) \frac{\partial \frac{1}{2}C_{AB}}{\partial (x_I)^a} \\
& + \left(\frac{\mathrm{d}^2 W}{\mathrm{d}\mathcal{K}_{AB}\, \mathrm{d}\frac{1}{2}C_{CD}} \frac{\partial \frac{1}{2}C_{CD}}{\partial (x_J)^b} + \frac{\mathrm{d}^2 W}{\mathrm{d}\mathcal{K}_{AB}\, \mathrm{d}\mathcal{K}_{CD}} \frac{\partial \mathcal{K}_{CD}}{\partial (x_J)^b} \right) \frac{\partial \mathcal{K}_{AB}}{\partial (x_I)^a} \\
& + S^{AB} \frac{\partial^2 \frac{1}{2}C_{AB}}{\partial (x_I)^a \partial (x_J)^b} + M^{AB} \frac{\partial^2 \mathcal{K}_{AB}}{\partial (x_I)^a \partial (x_J)^b} \Bigg]_{(\xi_q^1, \xi_q^2)} \det(\mathbf{J}) \big|_{(\xi_q^1, \xi_q^2)} w_q
\end{aligned}
$$
$$(4.131)$$

The components of the second Piola-Kirchhoff membrane tensor S^{AB} are defined as $\frac{\mathrm{d}W}{\mathrm{d}\frac{1}{2}C_{AB}}$ and, moreover, $\frac{\mathrm{d}W}{\mathrm{d}\mathcal{K}_{AB}}$ identifies the second Piola-Kirchhoff bending tensor components M^{AB}.

- Approximation of the exponential Cauchy-Born rule: direct curvature approach

$$
\begin{aligned}
(K_{\mathrm{b}}^e)_{IaJb} = \sum_{q=1}^{n_{\mathrm{qb}}} \Bigg[& \left(\frac{\mathrm{d}^2 W}{\mathrm{d}\frac{1}{2}g_{\alpha\beta}\, \mathrm{d}\frac{1}{2}g_{\gamma\delta}} \frac{\partial \frac{1}{2}g_{\gamma\delta}}{\partial (x_J)^b} + \frac{\mathrm{d}^2 W}{\mathrm{d}\frac{1}{2}g_{\alpha\beta}\, \mathrm{d}k_{\gamma\delta}} \frac{\partial k_{\gamma\delta}}{\partial (x_J)^b} \right) \frac{\partial \frac{1}{2}g_{\alpha\beta}}{\partial (x_I)^a} \\
& + \left(\frac{\mathrm{d}^2 W}{\mathrm{d}k_{\alpha\beta}\, \mathrm{d}\frac{1}{2}g_{\gamma\delta}} \frac{\partial \frac{1}{2}g_{\gamma\delta}}{\partial (x_J)^b} + \frac{\mathrm{d}^2 W}{\mathrm{d}k_{\alpha\beta}\, \mathrm{d}k_{\gamma\delta}} \frac{\partial k_{\gamma\delta}}{\partial (x_J)^b} \right) \frac{\partial k_{\alpha\beta}}{\partial (x_I)^a} \\
& + \tau^{\alpha\beta} \frac{\partial^2 \frac{1}{2}g_{\alpha\beta}}{\partial (x_I)^a \partial (x_J)^b} + m^{\alpha\beta} \frac{\partial^2 k_{\alpha\beta}}{\partial (x_I)^a \partial (x_J)^b} \Bigg]_{(\xi_q^1, \xi_q^2)} \det(\mathbf{J}) \big|_{(\xi_q^1, \xi_q^2)} w_q \quad (4.132)
\end{aligned}
$$

In this expression, $\frac{\mathrm{d}W}{\mathrm{d}\frac{1}{2}g_{\alpha\beta}}$ denotes the Kirchhoff membrane tensor components $\tau^{\alpha\beta}$. Furthermore, the Kirchhoff bending tensor components $m^{\alpha\beta}$ are given by $\frac{\mathrm{d}W}{\mathrm{d}k_{\alpha\beta}}$.

Once more, these local element stiffness matrix components $(K_{\mathrm{b}}^e)_{IaJb}$ are assembled to obtain the global stiffness matrix components $(K_{\mathrm{b}})_{KaLb}$ by using the correlation between the local nodes I, J and the global nodes K, L. Subsequently, the sub-matrices $(\mathbf{K}_{\mathrm{b}})_{KL}$ can be specified. Nevertheless, in the computational implementation the stiffness matrices are stored in their four-dimensional structure, having two node indices as well as two coordinate indices. This specific notation delivers

an effective setup of the individual quantities. The calculation of the first-order and second-order total derivatives of the strain energy density with respect to the strain measures follows Section 4.6 and, additionally, Appendix A.1. Thereby, the discrete strain measures, calculated at the quadrature points, are serving as input for the evaluation. The first-order and second-order derivatives of the strain measures with respect to the components of the actual displacement vector are stated in Subappendix A.3.2.

Potential of non-bonded interactions

The potential Π_{nb} of non-bonded interactions according to Equation (4.87) is defined as an integral of the strain energy double density W_{nb}. In the discrete setting, the in-layer non-bonded interactions within an element are disregarded such that possible point-to-point distances in the regime of the bonded interactions are prevented from the outset. Then, the double integral over the adequate domains is replaced by a double sum over the elements, denoted by e and f. The integrals over the elements are further transformed to correlated integrals on the reference element. In addition, the fact that each pair of elements has to be considered only once is used to save steps of calculation.

$$\Pi_{\mathrm{nb}} = \frac{1}{2} \int\limits_{\Omega_0} \int\limits_{\Omega_0 - B_X} W_{\mathrm{nb}}\left(d\right) \, \mathrm{d}\Omega_{0Y} \, \mathrm{d}\Omega_{0X} \tag{4.133}$$

$$= \sum_{e=1}^{n_{\mathrm{el}}} \int\limits_{\bar{S}_e} \left[\sum_{f=e+1}^{n_{\mathrm{el}}} \int\limits_{\bar{S}_f} W_{\mathrm{nb}}\left(d^{ef}\right) \, \det\left(\mathbf{J}^f\right) \, \mathrm{d}\bar{S}_f \right] \det\left(\mathbf{J}^e\right) \mathrm{d}\bar{S}_e \tag{4.134}$$

In this expression, the deformed distance of two arbitrary points, one in each element, is denoted as d^{ef}. Subsequently, the paired element-related non-bonded energy occurring between two elements e and $f > e$ follows as:

$$\Pi_{\mathrm{nb}}^{ef} = \int\limits_{\bar{S}_e} \int\limits_{\bar{S}_f} W_{\mathrm{nb}}\left(d^{ef}\right) \, \det\left(\mathbf{J}^f\right) \mathrm{d}\bar{S}_f \, \det\left(\mathbf{J}^e\right) \mathrm{d}\bar{S}_e \tag{4.135}$$

Now, the exact integration is replaced by a numerical quadrature. Therefore, for element e quadrature points $q^e = 1, \ldots, n_{\mathrm{qnb}}^e$ at the referential coordinates $(\xi_{q^e}^1, \xi_{q^e}^2)$ with their corresponding weights w_{q^e} are introduced. Similarly, the points $q^f = 1, \ldots, n_{\mathrm{qnb}}^f$ at the referential coordinates $(\xi_{q^f}^1, \xi_{q^f}^2)$ with their corresponding weights w_{q^f} are defined as quadrature points for element f. Although not necessarily required, the number of non-bonded quadrature points is in general the same for all elements. As already pointed out in the continuous setting, this potential must not affect bonded interactions. This special requirement solely affects the in-layer non-bonded interactions of two finite elements on the same carbon nanotube layer. In Subsection 2.4.2 , these interactions are examined directly on the atomistic structure. In the course of this, the exclusion of 1-2 and 1-3 interactions from the set of non-bonded interactions is emphasised. Additionally, the separate consideration of 1-4 non-bonded interactions is discussed. However, in the mixed atomistic-continuum approach, the atomistic structure is not accessible. Consequently, another criterion for the identification of valid in-layer non-bonded interactions is necessary. For that purpose, the non-bonded interaction distances $A_{1\text{-}3}$ or $A_{1\text{-}4}$ of the undeformed graphene sheet, which are defined in Subsection 2.4.2 are used as lower limits. In doing so, in-layer non-bonded interactions are only considered for pairs of integration points of which the undeformed distance is larger than the specific threshold value. The evaluation of valid pairs of in-layer non-bonded integration points is, therefore, performed on the basis of the undeformed plane continuum surface. Additionally, in multi-walled carbon nanotubes or bundles of carbon nanotubes, inter-layer non-bonded interactions are essential. This type of interaction is not influenced by the potential of the bonded interactions. Consequently, inter-layer non-bonded interactions are generally taken into

account for all pairs of integration points of which the associated finite elements are located on different layers. In order to reduce the total number of non-bonded interactions, an extra upper cut-off radius is specified in accordance with Subsection 2.4.1. In doing so, all non-bonded interactions exhibiting a distance larger than the upper cut-off radius are not considered. The distances for this comparison are calculated on the deformed configuration of the continuum surface. Furthermore, the evaluation of the strain energy double density W_{nb} also requires the deformed distance $d^{ef}_{(q^e,q^f)}$ between quadrature point q^e in element e and q^f in element f. For the discrete setting, these two points are connected by the distance vector

$$\mathbf{d}^{ef}_{(q^e,q^f)} = \left(d^{ef}_{(q^e,q^f)}\right)^a \mathbf{e}_a = \mathbf{x}^e_{q^e} - \mathbf{x}^f_{q^f} \tag{4.136}$$

where the indices q^e and q^f denote the evaluation of the position vectors within the elements at the dedicated curvilinear coordinates of the quadrature points. According to Equation (4.111), these positions are defined in the discrete setting by the shape functions and the spatial nodal coordinates of element e and f, respectively.

$$\mathbf{x}^e_{q^e} = N^e_I \left(\xi^1_{q^e}, \xi^2_{q^e}\right) \mathbf{x}^e_I \tag{4.137}$$

$$\mathbf{x}^f_{q^f} = N^f_I \left(\xi^1_{q^f}, \xi^2_{q^f}\right) \mathbf{x}^f_I \tag{4.138}$$

Subsequently, the corresponding approximated form of the scalar distance value follows directly as:

$$d^{ef}_{(q^e,q^f)} = \|\mathbf{x}^e_{q^e} - \mathbf{x}^f_{q^f}\| = \|N^e_I \left(\xi^1_{q^e}, \xi^2_{q^e}\right) \mathbf{x}^e_I - N^f_I \left(\xi^1_{q^f}, \xi^2_{q^f}\right) \mathbf{x}^f_I\| \tag{4.139}$$

Then, the numerically approximated non-bonded energy between two distinct elements is given by:

$$\Pi^{ef}_{\mathrm{nb}} = \sum_{q^e=1}^{n^e_{\mathrm{qnb}}} \sum_{q^f=1}^{n^f_{\mathrm{qnb}}} W_{\mathrm{nb}} \left(d^{ef}_{(q^e,q^f)}\right) \underbrace{\det\left(\mathbf{J}^f\right)\big|_{\left(\xi^1_{q^f},\xi^2_{q^f}\right)} w_{q^f}}_{w^f_{q^f}} \underbrace{\det\left(\mathbf{J}^e\right)\big|_{\left(\xi^1_{q^e},\xi^2_{q^e}\right)} w_{q^e}}_{w^e_{q^e}} \tag{4.140}$$

For a compact notation, here and henceforth, extended weights $w^e_{q^e}$ and $w^f_{q^f}$ are used. These are defined as scaled standard weights of the quadrature points. The scaling factor is specified by the determinant of the initial Jacobian tensor, evaluated at the appendant quadrature point.

Internal forces due to non-bonded interactions

Following the same train of thoughts as in the derivation of the internal forces due to bonded interactions, the discrete form of the variated non-bonded potential is defined as:

$$\delta\Pi_{\mathrm{nb}} = \sum_{K=1}^{n_{\mathrm{n}}} \frac{\partial \Pi_{\mathrm{nb}}}{\partial \mathbf{x}_K} \cdot \delta\mathbf{x}_K = \sum_{K=1}^{n_{\mathrm{n}}} (\mathbf{f}_{\mathrm{nb}})_K \cdot \delta\mathbf{x}_K \tag{4.141}$$

The derivative of the non-bonded potential with respect to the global nodal coefficients $\mathbf{x}_K$ defines the global non-bonded force sub-vector $(\mathbf{f}_{\mathrm{nb}})_K$ of the discrete system. The element force vectors due to non-bonded interactions follow from the definition of the non-bonded potential occurring between two elements e and $f > e$ as given above. The dependence on two distinct finite elements results in force vectors related to the local nodes of both of them. Therefore, the derivatives of the interaction distance $d^{ef}_{(q^e,q^f)}$ with respect to the components of the local element-wise actual

displacement vectors are necessary. Using Equation (4.139), these terms are obtained as:

$$\frac{\partial d^{ef}_{(q^e,q^f)}}{\partial (x_I^e)^a} = +\frac{\left(d^{ef}_{(q^e,q^f)}\right)^a}{d^{ef}_{(q^e,q^f)}} N_I^e \left(\xi^1_{q^e},\xi^2_{q^e}\right) \tag{4.142}$$

$$\frac{\partial d^{ef}_{(q^e,q^f)}}{\partial \left(x_I^f\right)^a} = -\frac{\left(d^{ef}_{(q^e,q^f)}\right)^a}{d^{ef}_{(q^e,q^f)}} N_I^f \left(\xi^1_{q^f},\xi^2_{q^f}\right) \tag{4.143}$$

Then, in a first step, the non-bonded forces $(\mathbf{f}_{\mathrm{nb}}^e)_I$ in the nodes of element e are obtained by the derivative of the element-pair-related non-bonded interactions potential with respect to the components $(x_I^e)^a$ of the local actual displacement vector corresponding to element e. Under consideration of Equation (4.142), these force vector components can be written as:

$$(f_{\mathrm{nb}}^e)_{Ia} = \frac{\partial \Pi_{\mathrm{nb}}^{ef}}{\partial (x_I^e)^a} = +\sum_{q^e=1}^{n_{\mathrm{qnb}}^e} \sum_{q^f=1}^{n_{\mathrm{qnb}}^f} W'_{\mathrm{nb}} \left(d^{ef}_{(q^e,q^f)}\right) \frac{\left(d^{ef}_{(q^e,q^f)}\right)^a}{d^{ef}_{(q^e,q^f)}} N_I^e \left(\xi^1_{q^e},\xi^2_{q^e}\right) w^f_{q^f}\, w^e_{q^e} \tag{4.144}$$

Secondly, in the nodes of element f the non-bonded forces $\left(\mathbf{f}_{\mathrm{nb}}^f\right)_I$ appear. By calculating the derivative of the element-pair-related non-bonded energy with respect to the components $\left(x_I^f\right)^a$ of the local actual displacement vector for element f and using Equation (4.143), the force vector components are:

$$\left(f_{\mathrm{nb}}^f\right)_{Ia} = \frac{\partial \Pi_{\mathrm{nb}}^{ef}}{\partial \left(x_I^f\right)^a} = -\sum_{q^e=1}^{n_{\mathrm{qnb}}^e} \sum_{q^f=1}^{n_{\mathrm{qnb}}^f} W'_{\mathrm{nb}} \left(d^{ef}_{(q^e,q^f)}\right) \frac{\left(d^{ef}_{(q^e,q^f)}\right)^a}{d^{ef}_{(q^e,q^f)}} N_I^f \left(\xi^1_{q^f},\xi^2_{q^f}\right) w^f_{q^f}\, w^e_{q^e} \tag{4.145}$$

For the evaluation of the first-order derivative of the strain energy double density with respect to the point-to-point distance the expressions given in Appendix A.2 are applied. The global non-bonded force vector components $(f_{\mathrm{nb}})_{Ka}$ according to the global node number K and the coordinate direction a are obtained by an assemblage of the elemental contributions. With that, the global non-bonded force sub-vectors $(\mathbf{f}_{\mathrm{nb}})_K$ are specified as well. In the computational implementation, the index notation, utilising a node index and a coordinate index is used again. This allows to store the various non-bonded force vector components in a two-dimensional representation.

Tangent stiffness matrix due to non-bonded interactions

The discrete form of the increment of the variated non-bonded potential is essential for the Newton-Raphson procedure. Thereby, the way of proceeding follows the sequence given within the discussion for bonded interactions. This allows to state the discrete form of the incremental variated non-bonded potential as:

$$\Delta\delta\Pi_{\mathrm{nb}} = \sum_{K=1}^{n_{\mathrm{n}}} \left[\sum_{L=1}^{n_{\mathrm{n}}} \frac{\partial^2 \Pi_{\mathrm{nb}}}{\partial \mathbf{x}_K \partial \mathbf{x}_L} \Delta\mathbf{x}_L\right] \cdot \delta\mathbf{x}_K = \sum_{K=1}^{n_{\mathrm{n}}} \left[\sum_{L=1}^{n_{\mathrm{n}}} (\mathbf{K}_{\mathrm{nb}})_{KL}\, \Delta\mathbf{x}_L\right] \cdot \delta\mathbf{x}_K \tag{4.146}$$

The sub-matrices $(\mathbf{K}_{\mathrm{nb}})_{KL}$ of the global stiffness matrix are given by the second-order partial derivative of the non-bonded potential with respect to the global nodal coefficients. Based on the paired element-related non-bonded energy Π_{nb}^{ef}, coupled element stiffness matrices, incorporating two finite elements e and $f > e$, can be specified. For this reason, the various second-order derivatives of the interaction distance $d^{ef}_{(q^e,q^f)}$ with respect to the components of the local element-wise actual displacement vectors are essential. Starting from the associated first-order derivatives,

given in Equation (4.142) and Equation (4.143), those terms are obtained as:

$$\frac{\partial^2 d^{ef}_{(q^e,q^f)}}{\partial(x^e_I)^a \partial(x^e_J)^b} = + \left[\frac{\delta^{ab}}{d^{ef}_{(q^e,q^f)}} - \frac{\left(d^{ef}_{(q^e,q^f)}\right)^a \left(d^{ef}_{(q^e,q^f)}\right)^b}{\left[d^{ef}_{(q^e,q^f)}\right]^3} \right] N^e_I \left(\xi^1_{q^e}, \xi^2_{q^e}\right) N^e_J \left(\xi^1_{q^e}, \xi^2_{q^e}\right) \tag{4.147}$$

$$\frac{\partial^2 d^{ef}_{(q^e,q^f)}}{\partial(x^e_I)^a \partial\left(x^f_J\right)^b} = - \left[\frac{\delta^{ab}}{d^{ef}_{(q^e,q^f)}} - \frac{\left(d^{ef}_{(q^e,q^f)}\right)^a \left(d^{ef}_{(q^e,q^f)}\right)^b}{\left[d^{ef}_{(q^e,q^f)}\right]^3} \right] N^e_I \left(\xi^1_{q^e}, \xi^2_{q^e}\right) N^f_J \left(\xi^1_{q^f}, \xi^2_{q^f}\right) \tag{4.148}$$

$$\frac{\partial^2 d^{ef}_{(q^e,q^f)}}{\partial\left(x^f_I\right)^a \partial(x^e_J)^b} = - \left[\frac{\delta^{ab}}{d^{ef}_{(q^e,q^f)}} - \frac{\left(d^{ef}_{(q^e,q^f)}\right)^a \left(d^{ef}_{(q^e,q^f)}\right)^b}{\left[d^{ef}_{(q^e,q^f)}\right]^3} \right] N^f_I \left(\xi^1_{q^f}, \xi^2_{q^f}\right) N^e_J \left(\xi^1_{q^e}, \xi^2_{q^e}\right) \tag{4.149}$$

$$\frac{\partial^2 d^{ef}_{(q^e,q^f)}}{\partial\left(x^f_I\right)^a \partial\left(x^f_J\right)^b} = + \left[\frac{\delta^{ab}}{d^{ef}_{(q^e,q^f)}} - \frac{\left(d^{ef}_{(q^e,q^f)}\right)^a \left(d^{ef}_{(q^e,q^f)}\right)^b}{\left[d^{ef}_{(q^e,q^f)}\right]^3} \right] N^f_I \left(\xi^1_{q^f}, \xi^2_{q^f}\right) N^f_J \left(\xi^1_{q^f}, \xi^2_{q^f}\right) \tag{4.150}$$

It can be seen from this that all four expressions share the same expression in square brackets, which is, therefore, abbreviated into one single quantity.

$$\widetilde{\mathcal{D}}^{ab} = \frac{1}{d^{ef}_{(q^e,q^f)}} \left[\delta^{ab} - \mathcal{D}^{ab} \right] \tag{4.151}$$

Herein, an additional second short-form is introduced, which is given by:

$$\mathcal{D}^{ab} = \frac{\left(d^{ef}_{(q^e,q^f)}\right)^a \left(d^{ef}_{(q^e,q^f)}\right)^b}{\left[d^{ef}_{(q^e,q^f)}\right]^2} \tag{4.152}$$

This allows to specify the four element-pair-related non-bonded stiffness matrices. In the course of this, the term

$$\left(\mathcal{W}^{ef}_{nb}\right)^{ab} = W'_{nb}\left(d^{ef}_{(q^e,q^f)}\right) \widetilde{\mathcal{D}}^{ab} + W''_{nb}\left(d^{ef}_{(q^e,q^f)}\right) \mathcal{D}^{ab} \tag{4.153}$$

appears in all four expressions so that its collection into an other short-form is advantageous.

$$\left(K^{ee}_{nb}\right)_{IaJb} = \frac{\partial^2 \Pi^{ef}_{nb}}{\partial(x^e_I)^a \partial(x^e_J)^b} = + \sum_{q^e=1}^{n^e_{qnb}} \sum_{q^f=1}^{n^f_{qnb}} \left(\mathcal{W}^{ef}_{nb}\right)^{ab} N^e_I \left(\xi^1_{q^e}, \xi^2_{q^e}\right) N^e_J \left(\xi^1_{q^e}, \xi^2_{q^e}\right) w^f_{q^f} \, w^e_{q^e} \tag{4.154}$$

$$\left(K^{ef}_{nb}\right)_{IaJb} = \frac{\partial^2 \Pi^{ef}_{nb}}{\partial(x^e_I)^a \partial(x^f_J)^b} = - \sum_{q^e=1}^{n^e_{qnb}} \sum_{q^f=1}^{n^f_{qnb}} \left(\mathcal{W}^{ef}_{nb}\right)^{ab} N^e_I \left(\xi^1_{q^e}, \xi^2_{q^e}\right) N^f_J \left(\xi^1_{q^f}, \xi^2_{q^f}\right) w^f_{q^f} \, w^e_{q^e} \tag{4.155}$$

$$\left(K^{fe}_{nb}\right)_{IaJb} = \frac{\partial^2 \Pi^{ef}_{nb}}{\partial(x^f_I)^a \partial(x^e_J)^b} = - \sum_{q^e=1}^{n^e_{qnb}} \sum_{q^f=1}^{n^f_{qnb}} \left(\mathcal{W}^{ef}_{nb}\right)^{ab} N^f_I \left(\xi^1_{q^f}, \xi^2_{q^f}\right) N^e_J \left(\xi^1_{q^e}, \xi^2_{q^e}\right) w^f_{q^f} \, w^e_{q^e} \tag{4.156}$$

$$\left(K^{ff}_{nb}\right)_{IaJb} = \frac{\partial^2 \Pi^{ef}_{nb}}{\partial(x^f_I)^a \partial(x^f_J)^b} = + \sum_{q^e=1}^{n^e_{qnb}} \sum_{q^f=1}^{n^f_{qnb}} \left(\mathcal{W}^{ef}_{nb}\right)^{ab} N^f_I \left(\xi^1_{q^f}, \xi^2_{q^f}\right) N^f_J \left(\xi^1_{q^f}, \xi^2_{q^f}\right) w^f_{q^f} \, w^e_{q^e} \tag{4.157}$$

These local element-pair-related non-bonded stiffness matrix components are used within the computational implementation in their four-dimensional notation. This allows a convenient and

straightforward evaluation of these quantities. The utilisation of the first-order and second-order derivatives of the strain energy double density with respect to the point-to-point distance is explicitly specified in Appendix A.2. In a final step, the correlation between the local nodes I, J and the global nodes K, L enables the assemblage of the global non-bonded stiffness matrix components $(K_{\mathrm{nb}})_{KaLb}$ and, consequently, the related sub-matrices $(\mathbf{K}_{\mathrm{nb}})_{KL}$.

Potential of external loads

The potential Π_{ext} of external loads is defined according to Equation (4.88) by an integration of the external contributions over the undeformed domain of the continuum surface. This integral can be further split into a sum of element-wise integrals using the finite element discretisation.

$$\Pi_{\mathrm{ext}} = -\int_{\Omega_0} \frac{2}{S_0}\, \mathbf{f} \cdot \mathbf{x}\, \mathrm{d}\Omega_0 = \sum_{e=1}^{n_{\mathrm{el}}} \left[-\int_{S_e} \frac{2}{S_0}\, \mathbf{f} \cdot \mathbf{x}\, \mathrm{d}S_e \right] = \sum_{e=1}^{n_{\mathrm{el}}} \Pi_{\mathrm{ext}}^e \qquad (4.158)$$

Subsequently, the integral within the undeformed element is transformed to the correlated integral on the reference element involving the initial Jacobian tensor. Additionally, the application of a numerical quadrature replaces the exact integration. Therefore, quadrature points $\hat{q} = 1, \ldots, n_{\mathrm{qext}}$ with weights $w_{\hat{q}}$ at the referential coordinates $(\xi_{\hat{q}}^1, \xi_{\hat{q}}^2)$ are introduced and the essential quantities are evaluated at these points.

$$\Pi_{\mathrm{ext}}^e = -\int_{\bar{S}_e} \frac{2}{S_0}\, \mathbf{f} \cdot \mathbf{x} \det(\mathbf{J})\, \mathrm{d}\bar{S}_e \approx -\frac{2}{S_0} \sum_{\hat{q}=1}^{n_{\mathrm{qext}}} \mathbf{f} \cdot \mathbf{x}\big|_{(\xi_{\hat{q}}^1, \xi_{\hat{q}}^2)} \det(\mathbf{J})\big|_{(\xi_{\hat{q}}^1, \xi_{\hat{q}}^2)} w_{\hat{q}} \qquad (4.159)$$

For the evaluation of the external potential within the finite element, the approximated position vector at the quadrature points is necessary. This position is given by the shape functions and the spatial nodal coordinates of the element according to Equation (4.111) as:

$$\mathbf{x}\big|_{(\xi_{\hat{q}}^1, \xi_{\hat{q}}^2)} = N_I\left(\xi_{\hat{q}}^1, \xi_{\hat{q}}^2\right) \mathbf{x}_I \qquad (4.160)$$

External forces

In accordance to the derivation of the internal forces due to bonded and non-bonded interactions, the discrete form of the variated potential of external forces is defined as:

$$\delta\Pi_{\mathrm{ext}} = -\sum_{K=1}^{n_{\mathrm{n}}} \left[-\frac{\partial \Pi_{\mathrm{ext}}}{\partial \mathbf{x}_K} \right] \cdot \delta\mathbf{x}_K = -\sum_{K=1}^{n_{\mathrm{n}}} (\mathbf{f}_{\mathrm{ext}})_K \cdot \delta\mathbf{x}_K \qquad (4.161)$$

Thereby, the negative derivative of the potential due to external forces with respect to the global nodal coefficients $\mathbf{x}_K$ defines the global external force sub-vector $(\mathbf{f}_{\mathrm{ext}})_K$, related to the global node K of the discrete system. The element-wise external force vector components $(f_{\mathrm{ext}}^e)_{Ia}$ can be specified by the derivative of the negative element-wise external potential Π_{ext}^e with respect to the components $(x_I)^a$ of the actual local position vector.

$$(f_{\mathrm{ext}}^e)_{Ia} = -\frac{\partial \Pi_{\mathrm{ext}}^e}{\partial (x_I)^a} = \frac{2}{S_0} \sum_{\hat{q}=1}^{n_{\mathrm{qext}}} (f)^a\, N_I\left(\xi_{\hat{q}}^1, \xi_{\hat{q}}^2\right) \det(\mathbf{J})\big|_{(\xi_{\hat{q}}^1, \xi_{\hat{q}}^2)} w_{\hat{q}} \qquad (4.162)$$

The local element-related external force vector components $(f_{\mathrm{ext}}^e)_{Ia}$ can then be assembled into the global external force vector components $(f_{\mathrm{ext}})_{Ka}$ by the appropriate correlation between local nodes I and global nodes K. Consequently, the global external force sub-vectors $(\mathbf{f}_{\mathrm{ext}})_K$ are defined. In the computational implementation, the related components are again stored in the two-dimensional representation, holding a node index and a coordinate index. The permitted external contributions result in an external force vector, which is independent of the deformation.

4.8.3 Stability of global equilibrium in the discrete setting

In Section 4.7, the condition for the structural stability of equilibrium configurations is specified for the continuous case on the basis of the second variation of the total potential energy. In the finite element method, this criterion is defined accordingly and, thus, the second variation of the total potential energy in the discrete setting is necessary.

$$\delta^2\Pi = \delta^2\Pi_{\mathrm{b}} + \delta^2\Pi_{\mathrm{nb}} + \delta^2\Pi_{\mathrm{ext}}$$

$$\delta^2\Pi = \sum_{K=1}^{n_{\mathrm{n}}} \left\{ \sum_{L=1}^{n_{\mathrm{n}}} \left[\frac{\partial^2\Pi_{\mathrm{b}}}{\partial\mathbf{x}_K \partial\mathbf{x}_L} + \frac{\partial^2\Pi_{\mathrm{nb}}}{\partial\mathbf{x}_K \partial\mathbf{x}_L} \right] \delta\mathbf{x}_L \right\} \cdot \delta\mathbf{x}_K$$

$$\delta^2\Pi = \sum_{K=1}^{n_{\mathrm{n}}} \left\{ \sum_{L=1}^{n_{\mathrm{n}}} \left[(\mathbf{K}_{\mathrm{b}})_{KL} + (\mathbf{K}_{\mathrm{nb}})_{KL} \right] \delta\mathbf{x}_L \right\} \cdot \delta\mathbf{x}_K$$

$$\delta^2\Pi = \sum_{K=1}^{n_{\mathrm{n}}} \left\{ \sum_{L=1}^{n_{\mathrm{n}}} (\mathbf{K})_{KL} \, \delta\mathbf{x}_L \right\} \cdot \delta\mathbf{x}_K \tag{4.163}$$

The derivation of this term is closely related to the increments of the variation of the total potential energy, which is specified in Equation (4.119). Consequently, in the discrete setting, the second variation of the total potential energy includes the global stiffness matrix of the equilibrium state. In accordance to Equation (4.109), the discrete stability criterion reads:

$$\delta^2\Pi = \sum_{K=1}^{n_{\mathrm{n}}} \left\{ \sum_{L=1}^{n_{\mathrm{n}}} (\mathbf{K})_{KL} \, \delta\mathbf{x}_L \right\} \cdot \delta\mathbf{x}_K > 0 \tag{4.164}$$

In order to obtain a more compact notation, the global virtual displacements vector $\delta\mathbf{x}$ and the global tangent stiffness matrix $\mathbf{K}$ are expressed in matrix notation.

$$\delta\mathbf{x} = \begin{bmatrix} \delta\mathbf{x}_1 \\ \vdots \\ \delta\mathbf{x}_{n_{\mathrm{n}}} \end{bmatrix} \qquad \mathbf{K} = \begin{bmatrix} (\mathbf{K})_{11} & \cdots & (\mathbf{K})_{1n_{\mathrm{n}}} \\ \vdots & \ddots & \vdots \\ (\mathbf{K})_{n_{\mathrm{n}}1} & \cdots & (\mathbf{K})_{n_{\mathrm{n}}n_{\mathrm{n}}} \end{bmatrix} \tag{4.165}$$

Now, the stability criterion can be rewritten using matrix algebra.

$$\delta^2\Pi = \delta\mathbf{x}^T \mathbf{K} \, \delta\mathbf{x} > 0 \tag{4.166}$$

This basic condition for stability has to be fulfilled for arbitrary perturbations $\delta\mathbf{x}$. As a consequence, the observed equilibrium configuration is stable if the global tangent stiffness matrix $\mathbf{K}$ is positive definite. The calculation of the eigenvalues ω_i $(i = 1, \ldots, n_{\mathrm{n}})$, of the global stiffness matrix $\mathbf{K}$, enables the determination of its definiteness. From this it follows that an instability point is characterised by the occurrence of a zero eigenvalue. Additionally, the eigenvector $\boldsymbol{\mu}_i$ identifies the shape of the configuration, associated to eigenvalue ω_i. This is why these eigenvectors are essential for problems exhibiting bifurcation points, because in the treatment of secondary branches they can be used to achieve the appropriate buckled configurations. For this reason, the branch switching approach suggested by Wagner and Wriggers [57] is applied. This algorithm provides a starting vector $\mathbf{x}^{(0)}$ for the iterative calculation of the equilibrium state on the secondary branch.

$$\mathbf{x}^{(0)} = \mathbf{x}_{\mathrm{c}} + \nu\boldsymbol{\mu}_{\mathrm{c}} \tag{4.167}$$

Therein, the vector $\mathbf{x}_{\mathrm{c}}$ denotes the state of deformation at the detected critical point. Furthermore, the associated eigenvector $\boldsymbol{\mu}_{\mathrm{c}}$ and a scaling factor ν are essential. A successful branch switch generates the requested equilibrium configuration on the secondary path. Consequently, the buckled configuration is obtained and the postbuckling path can be further investigated.

4.9 Numerical simulations on buckling of carbon nanotubes

The aim of this section is the application of the mixed atomistic-continuum model in the buckling analysis of carbon nanotubes. The validation of the model is done by a check against the results obtained by the full atomistic simulation using the molecular statics approach. In particular, the equilibrium configurations and the appendant energy evolutions of both methods are compared. Moreover, the characteristic deformation parameters, which specify the critical states of structural stability in both approaches are checked against each other. In this verifications, the molecular statics approach is taken as reference for the specification of accuracy statements and relative errors for the mixed atomistic-continuum model. In addition, a comparison between the different approximation schemes for the exponential Cauchy-Born rule is performed. The modelling of in-layer and inter-layer non-bonded interactions in the context of the mixed atomistic-continuum model is investigated. For these purposes, various carbon nanotubes under different loading scenarios are considered. The numerical simulations are realised with the implementation of a stand-alone finite element framework. In the course of this, the calculation of equilibrium configurations is accomplished by means of a classical Newton-Raphson procedure or an arc-length method. See for instance Wriggers [61] and Zienkiewicz and Taylor [65] for a collection of solution algorithms for non-linear systems of equations. With respect to stability, an accompanying eigenvalue analysis of the global stiffness matrix is carried out, and the critical configurations are detected using a bisection algorithm. To gain insight into the postbuckling behaviour of carbon nanotubes, a branch switching is performed. In the numerical examples that consider non-bonded interactions, certain simulations include an upper cut-off radius in order to reduce the amount of possible non-bonded interactions. In the selection of the specific threshold value, the derivations of Subsection 2.4.1 serve as guidance. The use of an upper cut-off radius requires an additional loop around the iterations of the current load step. This is because the actual set of non-bonded interactions depends on the current state of deformation. Consequently, the current load step is repeatedly evaluated, and at the start of each iteration loop a list that contains all relevant non-bonded interactions is updated. Thereby, the distance between all potential pairs of non-bonded integration points is examined and those interactions that are beneath the cut-off radius are considered. On the basis of this current set of non-bonded interactions, the equilibrium configuration of the intermediate state is calculated. If the initially varying number of non-bonded interactions remains constant, the complemental loop is terminated. After this, the next and subsequent load steps are handled in the same manner. This procedure simplifies if the upper cut-off radius is not used and, consequently, the total number of non-bonded interactions is the same throughout the entire loading. Then, the additional update loop is not required and the relevant set of interactions is evaluated just once at the start of the numerical simulation. With this computational framework in hand, numerical simulations on the basis of the discretised mixed atomistic-continuum model are performed for several types of carbon nanotubes under different loading cases. The obtained results are checked against the molecular statics approach and, if available, with corresponding simulations from the literature.

4.9.1 Rolling of the graphene sheet to a carbon nanotube

The first step within all the simulations is the establishment of a relaxed carbon nanotube. This process starts from the flat continuum surface, representing the undeformed graphene sheet. With reference to Section 2.2, the graphene sheet for a specific carbon nanotube has a length L_0 and a height C_{h}. This rectangular slab of graphene is the undeformed body of the mixed atomistic-continuum model and is, consequently, discretised by finite elements. In particular, referring to Subsection 4.8.1, subdivision finite elements are applied. In the continuum setup, the rolling of the undeformed planar graphene sheet produces a cylindrical surface. This cylinder is the initial deformed configuration that owns, according to Equation (2.3), a radius R_0. However, due to the approximative character of the considered shape functions, a computational radius R_{C} of the control mesh is needed. This fictitious radius is given by $R_{\mathrm{C}} = R_0 / (8/12 + 4/12 \cdot \cos{(2\pi/n_{\mathrm{cd}})})$.

For this specification, a structured grid with equally sized quadrangles is assumed. Furthermore, it becomes additionally necessary that the number of quadrangles in the circumferential direction n_{cd} of the grid is even. The number of quadrangles in the longitudinal direction n_{ld} is not restricted. On the basis of this grid, the mesh of a quadrilateral finite element discretisation is specified as $n_{\mathrm{ld}} \times n_{\mathrm{cd}}$ in the numerical simulations. In line with this, $2 \times n_{\mathrm{ld}} \times n_{\mathrm{cd}}$ characterises the finite element mesh of a triangular discretisation, which is obtained by cutting the quadrangles of the grid into halves. With reference to the numerical experiments realised by Arroyo [2], the numerical integration of the relaxed strain energy density for bonded interactions using the triangular finite element is performed by two integration points. If quadrilateral finite elements are applied, the numerical integration of the relaxed strain energy density for bonded interactions is realised by means of four integration points. For each global node K of the discretisation, the mapping of the Lagrangian nodal position vector $\mathbf{X}_K$ of the plane mesh to the Eulerian nodal position vector $\mathbf{x}_K$ of the fictitious cylindrical mesh can be specified.

$$
\begin{aligned}
x_K^1 &= X_K^1 \\
x_K^2 &= R_{\mathrm{C}} \sin\left(\frac{X_K^2}{R_0}\right) \\
x_K^3 &= -R_{\mathrm{C}} \cos\left(\frac{X_K^2}{R_0}\right)
\end{aligned}
\tag{4.168}
$$

The resulting tube is then geometrically compatible, but the cylindrical surface is not in an equilibrium state. In the transition from the graphene sheet to the cylinder, the bond lengths a_i and valence angles θ_i $(i = 1, 2, 3)$ change due to the repositioning of the atoms. As a consequence, the potential Π_b of the bonded interactions, specified according to Equation (4.85) or Equation (4.86), is affected. Furthermore, the potential Π_{nb} of the non-bonded interactions, given in Equation (4.87) changes. Thus, in order to achieve a global equilibrium configuration of the structure, the constitutive model has to be fulfilled. This process is performed in an initial step of calculation, leading to the relaxed carbon nanotube, which is the initial state for the further loadings and the ground state for all energies.

4.9.2 An (18,0) carbon nanotube under axial compression

This series of numerical simulations investigates an (18,0) zig-zag carbon nanotube with a length of 8.7 nm. The tube under consideration is loaded by axial compressive forces, which are applied antagonistic on both ends of the cylinder. Within these simulations, the non-bonded interactions are completely neglected in order to put the focus on the different approaches for the extended Cauchy-Born rules. Additionally, a discretisation on the basis of the triangular and quadrilateral subdivision finite elements enables a direct comparison of the corresponding results. The external load is implemented by increasing axial forces, applied on the first row of finite element nodes on each side of the tube. Additionally, these nodes are constrained to move only radially with reference to the perfect cylindrical tube. In order to avoid a global buckling mode, similar to the Euler-beam-buckling, the nodes on the four quadrants of the circular cross section, in the middle of the tube, are constrained in radial direction. The first step of each simulation is the relaxation process. This initial step generates a reference configuration for the further loading. In addition, the relaxed carbon nanotube represents the ground state for the energies. To evaluate the non-linear load-deformation path, a modified Riks algorithm, as given in Hibbitt *et al.* [25], together with an accompanying eigenvalue analysis of the global stiffness matrix is carried out. Additional informations on path-following procedures can be found for instance in Riks [43], Wriggers [61] and Bonet and Wood [9]. The important bifurcation points are found via bisection and an associated branch switching is performed.

Comparison between the principal curvatures approach and the direct curvature approach

The aim of this simulation is to make a comparison between the two different approximations of the exponential Cauchy-Born rule that were discussed in Subsection 4.4.4. Additionally, these continuum approaches are checked against the solution obtained by molecular statics in Subsection 3.5.2. In the course of this, the first eigenform of the axially compressed (18,0) zig-zag carbon nanotube is studied. For the numerical calculations, in the continuum setting, the graphene sheet and, therefore, also the carbon nanotube is discretised by 2x48x24 triangular subdivision elements. Consequently, the finite element mesh has 1176 relevant nodes. The structure of the associated molecular statics simulation consists of 1440 carbon atoms. The right hand side of Figure 4.19 demonstrates the obtained load factor λ - axial compression ε diagrams. These
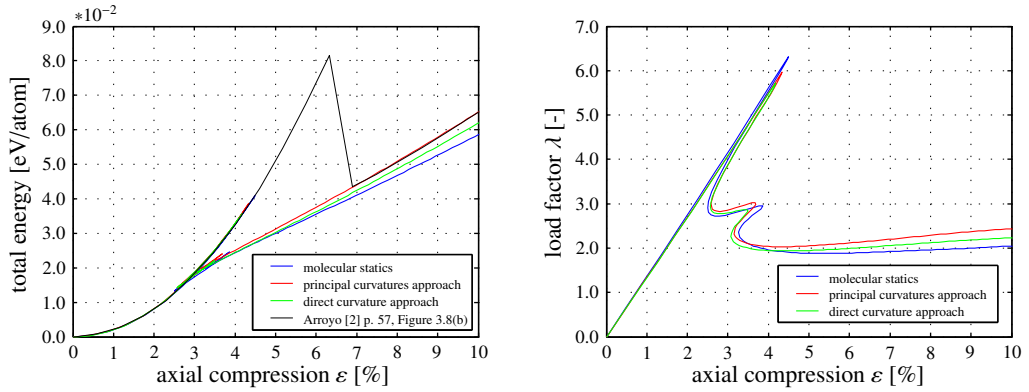
Figure 4.19: Mixed atomistic-continuum model: The total energy - axial compression ε and load factor λ - axial compression ε diagrams for the first eigenform of the (18,0) carbon nanotube under axial compression. Comparison between the principal curvatures and direct curvature approach and their check against the results obtained by molecular statics.

curves are characterised by a linear correlation between load and axial compression until the first instability point is reached. In the outset of this linear part, both continuum approaches are almost indistinguishable. In addition, the slope of these lines agrees very well with the corresponding slope of the molecular statics path. Then, the direct curvature approach loses stability slightly before the principal curvature approach. In spite of that, the continuum methods exhibit a lower critical load level than the molecular statics simulation. However, as reported in Table 4.1, the values of axial compression for the predicted instability points are located close together. Subsequently, the branch

	molecular statics	principal curvatures approach	direct curvature approach
critical axial compression	4.491%	4.338%	4.174%
relative error	-	3.4%	7.1%

Table 4.1: Mixed atomistic-continuum model: The critical value of compression for the axially loaded (18,0) carbon nanotube. Comparison between the principal curvatures and direct curvature approach and their check against the results obtained by molecular statics. The relative errors for the principal curvatures and direct curvature approach.

switching results in a snap back regime of the corresponding secondary paths. This postbuckling regions are further followed up to an axial compression of 10.0% using an arc-length method. From this it can be seen that both continuum approaches and the molecular statics show the same trend

in the evolution of the postbuckling branch. However, the direct curvature method exhibits a lower load level at the same extent of compression than the principal curvatures approach. Furthermore, in the last part of compression, the lowest load level can be seen for the molecular statics calculation. Similar postbuckling diagrams of compressed carbon nanotubes were obtained by Pantano *et al.* [39] using an elastic shell theory. Furthermore, the snap back attribute is known from the buckling of thin cylindrical shells under axial compression as for instance observed in von Kármán and Tsien [55] and Wohlever and Healey [60]. In the left side of Figure 4.19, the average total energy is plotted over the axial compression and the results obtained with the two different continuum methods are compared with Arroyo's solution (see Figure 3.8(b) of [2]) and the results obtained from molecular statics. Here, both continuum approaches show a similar trend again and the model based on the direct curvature approach gives the lower energy level at the same axial compression. Nonetheless, the lowest energy level is found in the calculations using molecular statics. Another important point is the fact that the energy curve obtained by Arroyo [2] via direct minimisation methods coincides in the important fields with the corresponding curve evaluated with the modified Riks method. The relative errors of total energy at an axial compression of 10.0% are 11.2% (principal curvatures approach) and 5.7% (direct curvature approach). The stiffer response of the continuum approaches results partly from the homogenisation process within the mixed atomistic-continuum approach. This process can suppress the development of locally severe deformations by a smoothing character. In particular, this smoothing has less influence if the dimensions of the finite element are in the scale of the atomic bond length. In the case under consideration, this suggestion is satisfied. However, there are also fewer degrees of freedom in the finite element mesh than in the atomistic structure. This circumstance results in an additional stiffening of the continuum model. Consequently, one can improve the agreement by a finer discretisation, adding more degrees of freedom and obtaining even smaller finite elements. In that case, the advantage of the continuum approach, to reduce the degrees of freedom compared to a molecular mechanics calculation, gets lost. It is then more appropriate to directly use a molecular mechanics approach. The softer response of the direct curvature approach compared to the principal curvatures method originates from the individual treatment of each of the three bond vectors within the unit cell. In Figure 4.20,
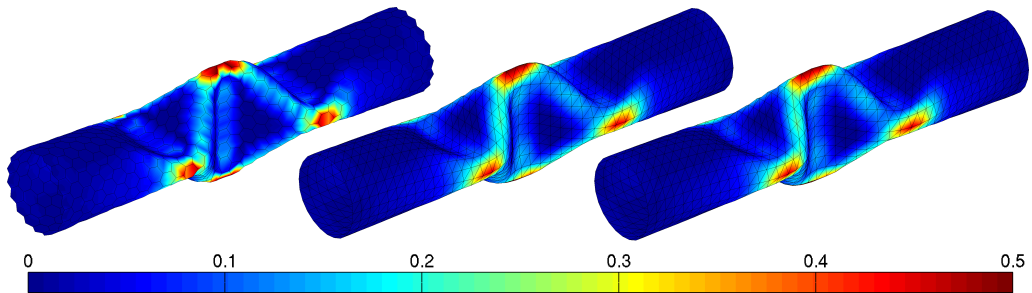
Figure 4.20: Mixed atomistic-continuum model: The final buckled configurations of the (18,0) SWCNT under axial compression with a colour mapping of the local total energy per atom [eV/atom]. Comparison between the molecular statics (left), the principal curvatures approach (middle) and the direct curvature approach (right).

the resulting postbuckling patterns at the end of deformation are presented. This structure exhibits three flattenings, perpendicular to each other, in the middle of the tube. The colouring corresponds to a mapping of the averaged local total energy. In the literature, various carbon nanotubes under axial compression were investigated for instance by Arroyo [2], Arroyo and Belytschko [5], Leung *et al.* [29], Liu *et al.* [30], Liu *et al.* [31], Pantano *et al.* [39], Sears and Batra [45], Sun and Liew [50] and Yakobson *et al.* [62] and comparable buckled structures are reported.

Comparison between the first and second eigenform of buckling

In this numerical calculation, the first and second eigenform of the (18,0) zig-zag carbon nanotube under axial compression are investigated. For that purpose, the constitutive model, resulting from the principal curvatures approach is used. Furthermore, the tube is discretised by means of quadrilateral or triangular subdivision finite elements. The quadrilateral mesh contains 64x32 elements and the triangular discretisation has 2x64x32 finite elements. Consequently, both discretisations are generated by the same amount of nodes. The determined load factor λ - axial compression ε and the total energy - axial compression ε curves are given in Figure 4.21. Thereby, the plots related to the first eigenform are similar to the ones obtained in the example before that. In a further simulation, the first instability point is bypassed and the second bifurcation point is
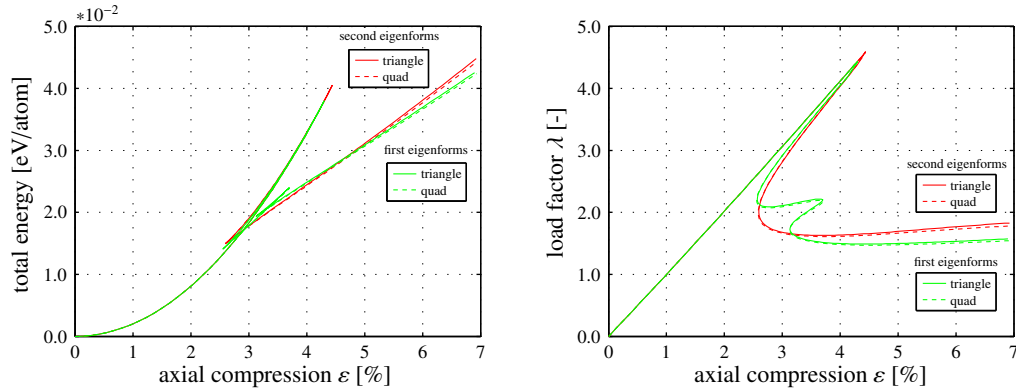
Figure 4.21: Mixed atomistic-continuum model: The total energy - axial compression ε and load factor λ - axial compression ε evolutions for the first and second eigenform of the (18,0) carbon nanotube under axial compression. Comparison between the response obtained by triangular and quadrilateral subdivision finite elements.

detected. Again, a branch switching enables the evaluation of the associated postbuckling path, which exhibits a snap back behaviour. The numerically obtained values of axial compression at the first and second instability point are reported in Table 4.2. This list indicates that the influence of the applied finite element type on the calculation of the critical states is vanishingly low. At the end

	critical axial compression	
	first eigenform	second eigenform
triangle	4.303%	4.439%
quad	4.303%	4.439%

Table 4.2: Mixed atomistic-continuum model: The critical values of compression for the first and second eigenform of the axially loaded (18,0) carbon nanotube. Comparison between the response obtained by triangular and quadrilateral subdivision finite elements.

of loading, the load factor as well as the total energy for the second eigenform are higher than the values for the first eigenform. In addition, the simulations show that in the postbuckling region the quadrilateral finite element gives a slightly softer response than the triangular finite element. The images in Figure 4.22 display the buckled configurations related to the first and second eigenform of the axially compressed (18,0) carbon nanotube. In particular, it can be seen that the first eigenform develops three perpendicular fins, whereas the second eigenform only consists of two. Additionally, the colouring represents the averaged local total energy. Similar to the behaviour of the global energy response, the locally higher values of averaged total energy are found in the

triangle - first eigenform   triangle - second eigenform

0   0.1   0.2   0.3   0.4   0.5

quad - first eigenform   quad - second eigenform
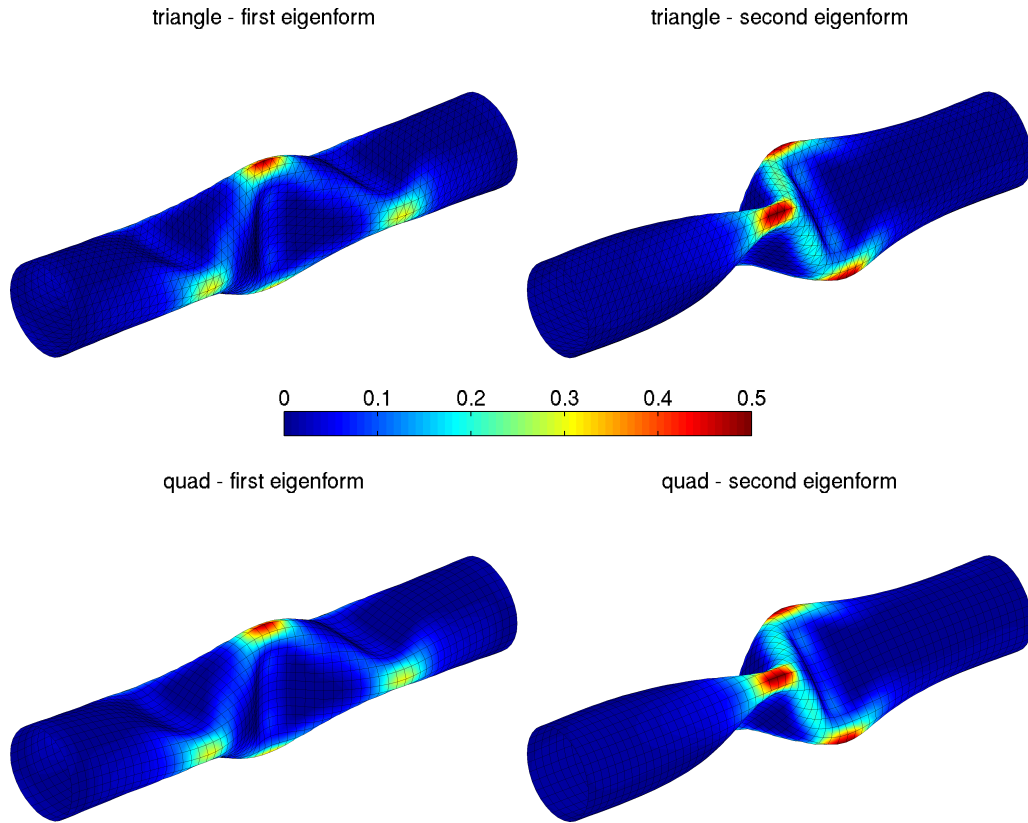
Figure 4.22: Mixed atomistic-continuum model: The final buckled configurations related to the first and second eigenform of the (18,0) SWCNT under axial compression with a colour mapping of the local total energy per atom [eV/atom]. Comparison between the response obtained by triangular and quadrilateral subdivision finite elements.

buckled configuration of the second eigenform.

This series of numerical simulations on the buckling of an (18,0) carbon nanotube under axial compression provided some interesting insights. With regard to the applied approximations of the exponential Cauchy-Born rule, the direct curvature approach and the principal curvatures approach deliver analogous results. The check against the molecular statics calculation provides an agreement of the obtained total energy and load factor evolutions. Additionally, the type of finite element slightly influences the behaviour of the carbon nanotube, despite the fact that the discretisations are based on the same set of nodes. Furthermore, the application of an arc-length method allows to follow complex non-linear load-deformation paths. Finally, the accompanying structural stability analysis and the branch switching procedure enable the evaluation of buckled configurations and associated postbuckling paths.

4.9.3 A (10,10) carbon nanotube under sharp bending

In this numerical simulations, a (10,10) single-walled carbon nanotube with a length of 40 hexagonal cells under displacement-driven bending load is investigated. The approximation of the exponential map for the mixed atomistic-continuum model is performed by the direct curvature approach. The same carbon nanotube is also discussed in Subsection 3.5.3 using molecular statics and, consequently, the associated results are taken for comparison. In the course of this, it is observed

that the sharp bending type is subjected to the higher local deformation compared with the ideal bending type. Additionally, the need for in-layer non-bonded interactions, in order to prevent the tube from self-intersection, is more important in this mode. For these reasons, the displacement constraints in the following simulations are applied according to the sharp bending type. Thus, after the initial relaxation step, on both ends two rows of finite element nodes are constrained. In particular, these nodes are rotated about an axis through the tube's middle and perpendicular to the centerline of the relaxed tube. Consequently, these two rows perform a rigid body rotation with constant distance from the pivot and the generated cross sections on both ends of the carbon nanotube remain circular throughout the whole process of loading. The Newton-Raphson procedure is applied to obtain equilibrium configurations of the loaded tubes and an accompanying eigenvalue analysis is carried out. A bisection and a branch switching algorithm are used to detect instability points and to achieve the associated buckled configurations. The relaxed carbon nanotube represents the reference state for bonded and non-bonded energies. In a first series of simulations, the influence of the finite element mesh on the buckling behaviour is studied. Secondly, the stability of the equilibrium path of the displacement-driven simulation is analysed. Thirdly, the modelling of non-bonded interactions in the mixed atomistic-continuum approach is discussed.

Studies into the influence of the finite element mesh on the buckling behaviour

The aim of this study is to examine the influence of the finite element mesh on the buckling behaviour of carbon nanotubes. On this account, the continuum model is discretised using quadrilateral subdivision finite elements and for three different simulations the element size is varied. The calculations are checked against the results obtained by molecular statics in Subsection 3.5.3, where the corresponding atomistic structure consists of 1620 atoms. The first mesh contains 20x80 quadrilateral subdivision finite elements and 1620 nodes. In the second mesh, 40x40 finite elements, generated by 1640 nodes, are utilised. Compared to the molecular statics approach, these two meshes have a similar amount of degrees of freedom. Finally, an even finer mesh, owning 3240 nodes and 40x80 quadrilateral subdivision finite elements is used. In the performed simulations,

Figure 4.23: Mixed atomistic-continuum model: The total energy - bending angle evolutions for the (10,10) carbon nanotube under sharp bending. Comparison between simulations with different discretisations and their check against the results obtained by molecular statics. The buckled configuration for the mixed atomistic-continuum approach (40x40 quadrilateral finite elements) at the end of deformation in a front and top view with colour mapping of the local total energy per atom [eV/atom].

the non-bonded interactions are neglected in order to concentrate on the influence of the bonded interactions. The determined total energy - bending angle evolutions are given in the left side of Figure 4.23. Thereby, all simulations were performed using a total of 24 load steps. In the prebuckling regime, the results of the molecular statics approach and all three discretisations of

the mixed atomistic-continuum model are in remarkable agreement. In particular, as can be seen from Table 4.3, this is also true for the bending angle at the instability point. Thus, for the

	molecular statics	mixed atomistic-continuum model		
		20x80 □	40x40 □	40x80 □
critical bending angle	11.533°	11.694°	11.606°	11.670°
relative error	-	1.4%	0.6%	1.2%

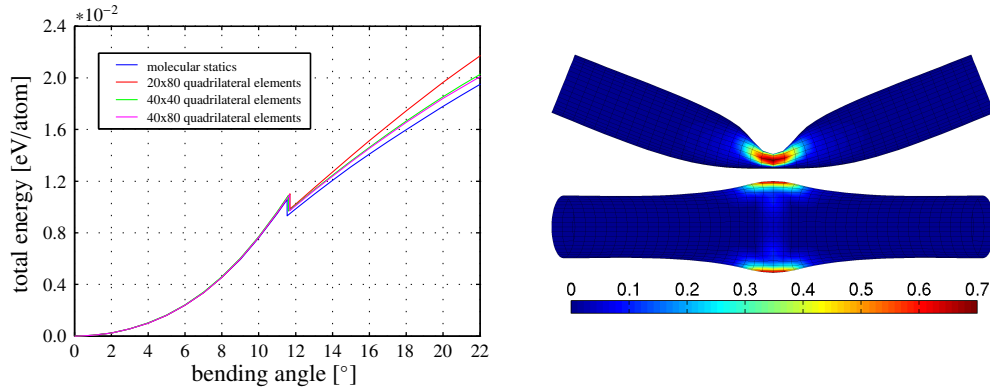Table 4.3: Mixed atomistic-continuum model: The critical bending angle for the (10,10) carbon nanotube under sharp bending. Comparison between different quadrilateral discretisations and their relative errors with reference to the molecular statics approach.

unbuckled tube, the fineness of the discretisation has only little influence on the global behaviour. The branch switching into the postbuckling path is indicated in the energy evolutions by a jump to a lower level. The corresponding buckled configuration shows a single kink in the middle of the tube. Then, after buckling, the displacement constraints are applied up to a bending angle of 22.0°. In the postbuckling regime, the influence of the mesh on the global behaviour is obvious from the plots. Although, the mesh with 20x80 elements and the mesh with 40x40 elements, have almost the same number of nodes, the last-mentioned discretisation provides the better agreement to the molecular statics calculation. Thus, in the mesh with the larger amount of nodes in circumferential direction the smoothing property of the mixed atomistic-continuum approach has a smaller effect, and the local deformations at the atomistic level are well approximated. In the last reported step, the relative errors of the total energy are 11.3% (20x80 quadrilateral elements) and 3.9% (40x40 quadrilateral elements). An even better correlation is obtained by the finest mesh (40x80 quadrilateral elements) with a relative error of 2.9%. However, the additional slight improvement with the finest mesh has to be paid by a large increase in computational effort. It can be seen from this fact that a mesh refinement allows the mixed atomistic-continuum approach to reproduce the locally intricate deformations of the atomistic structure. The buckled configuration of the sharply bent carbon nanotube, for the mixed atomistic-continuum approach with 40x40 quadrilateral finite elements, is illustrated in the right hand side of Figure 4.23 for the last load step. In particular, a front and top view of the tube depict the single kink in the middle and the colouring represents the averaged local total energy. This simulation shows that the continuum modelling error and the discretisation error can be reduced to an adequate level. Nevertheless, it is not meaningful to use a finite element model that has even more degrees of freedom than the atomistic system.

Studies into the behaviour and the stability of the equilibrium path

In this simulations, the behaviour and the stability of the equilibrium path for the displacement-driven sharp bending load are analysed. The aim of this study is the clarification and explanation of the jumps in the total energy evolutions, which arise at the buckling points of carbon nanotubes under bending load. For this purpose, the discretisation of the tube with 40x40 quadrilateral finite elements of the foregoing investigations is reused. Moreover, non-bonded interactions are not modelled within this example. The analysis of the equilibrium path is performed by a numerical simulation, which contains two bending directions. In doing so, several characteristic variables of the considered buckling problem were observed and the results are plotted in Figure 4.24. At the top, the evolution of the total energy with respect to the applied bending angle is visualised and an enlargement of the region around the critical points is provided. At the bottom, the behaviours of the norm of the global force vector and the first eigenvalue of the global stiffness matrix as functions of the bending angle are given. In each of these plots, a curve representing the loading and the unloading of the tube are presented. At first, the carbon nanotube is loaded by increasing the bending angle according to the sharp bending mode. Observing the progress of the first eigenvalue of the global stiffness matrix, this loading path reaches a critical state in point 1 at a bending angle of 11.606°. At this point, the corresponding eigenform is superimposed onto the actual state
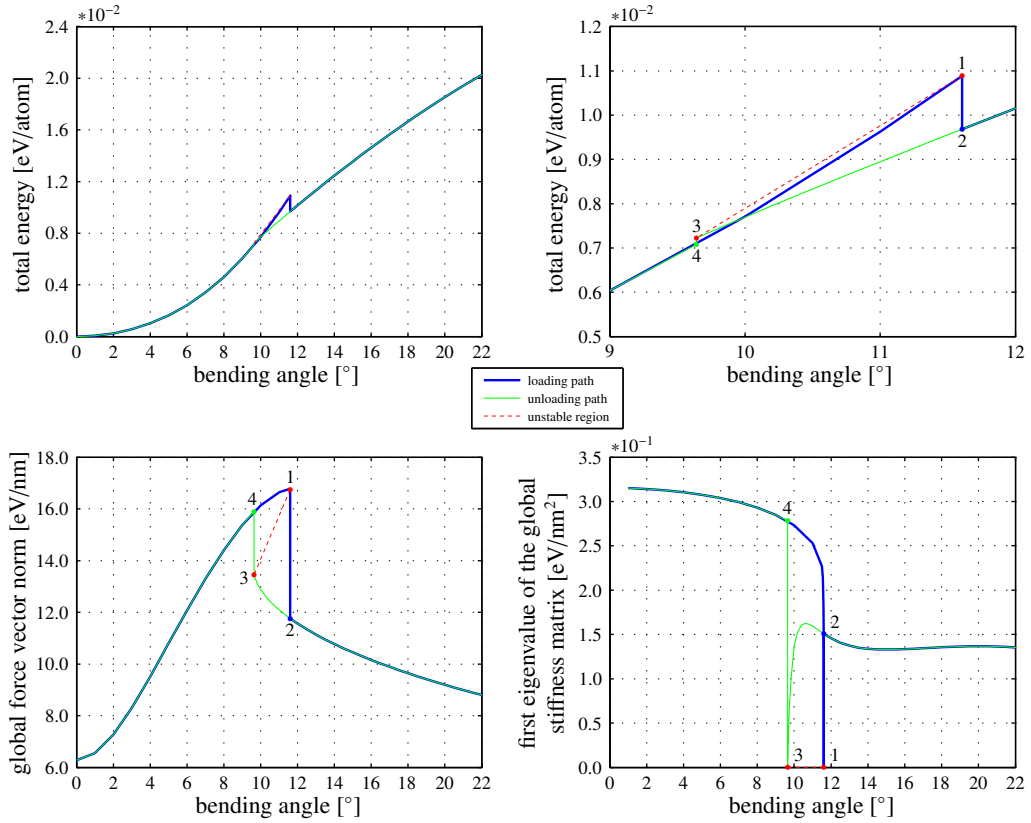
Figure 4.24: Mixed atomistic-continuum model: Studies into the behaviour and the stability of the equilibrium path of the (10,10) carbon nanotube under sharp bending. The evolutions of the total energy, the norm of the global force vector and the first eigenvalue of the global stiffness matrix as functions of the bending angle.

of deformation. Thereby, the bending angle is kept constant and the stable equilibrium state 2 is obtained. In the passage from 1 to 2, the carbon nanotube buckles and a single kink in its middle originates. The corresponding configurations of the tube with an additional visualisation of the middle cross sections are displayed in Figure 4.25. After buckling, the total energy as well as the global force vector norm reach a smaller level than in the unbuckled state. With reference to Bažant and Cedolin [8], this phenomenon is called snap down. The buckled carbon nanotube is further loaded up to a bending angle of 22.0°. Then, the tube is unloaded by displacement constraints that represent a decreasing bending angle. In this unloading process, the initial buckled equilibrium state 2 is passed. Afterwards, the monitoring of the first eigenvalue of the global stiffness matrix indicates a critical state of the unloading path, which is reached at a bending angle of 9.641° in point 3. The closest stable equilibrium state in the case of a further decrease in bending angle is located on the initial loading path at point 4. In the transition from 3 to 4, the bulge of the carbon nanotube vanishes and the total energy jumps to a higher value located at the initial loading path. In the same fashion, the norm of the global force vector increases to the corresponding value of the loading path. After this, the unloading path follows the loading path in reverse direction. In Figure 4.25, the state of deformation associated to the critical point 3 and the unbuckled structure corresponding to point 4 are provided. The indicated path between the two critical points 1 and 3 represents an unstable region of the displacement-driven simulation and its real behaviour is not determinable. However, if in the superimposition of the eigenform at the critical point 1 of the loading path, the bending angle is adjusted to the corresponding value at the critical point 3 of the

unloading path, this equilibrium state on the postbuckling path can directly be reached. As this has no influence on the further tracking of the equilibrium path in the postbuckling zone of the bent carbon nanotubes, at the critical state of deformation, the associated eigenform is superimposed at a constant bending angle. This procedure is applied in the simulations of carbon nanotubes under bending load presented in Subsection 3.5.3, Subsection 4.9.3 and Subsection 4.9.4.
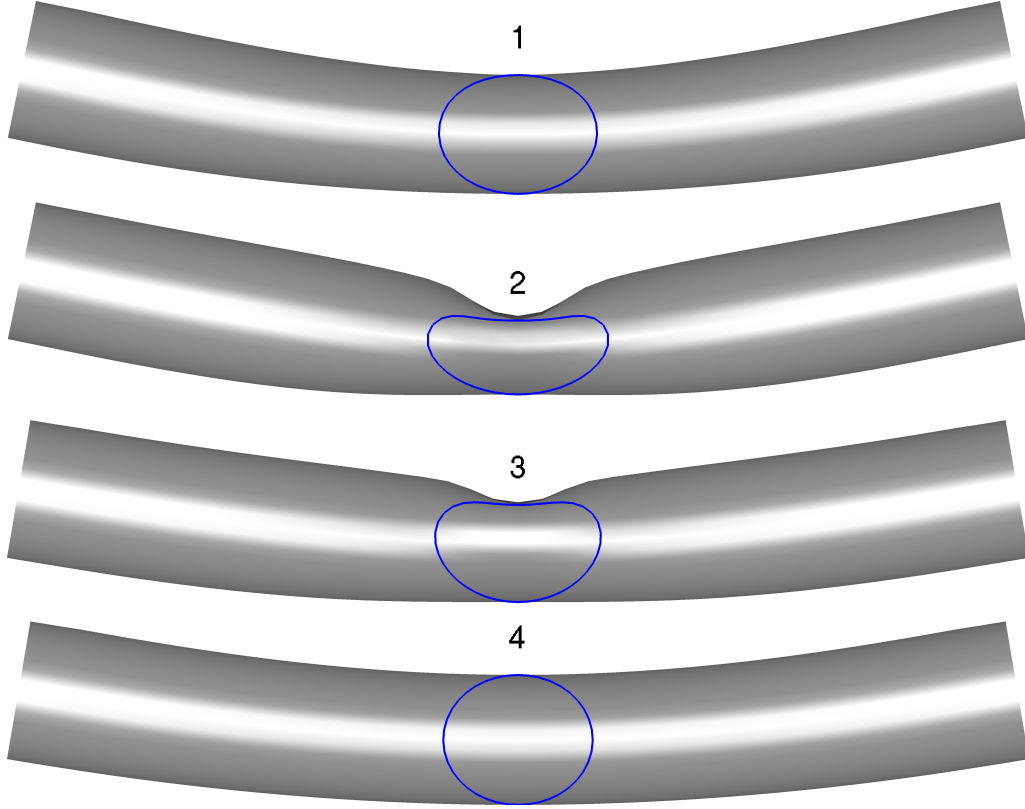
Figure 4.25: Mixed atomistic-continuum model: The deformed configurations and the corresponding middle cross sections of the (10,10) carbon nanotube under sharp bending at the four specific points of the equilibrium path. The deformed tube at the critical point 1 of the loading path (topmost), the buckled state 2 of the loading path (second from top), the buckled carbon nanotube at the critical point 3 of the unloading path (third from top) and the unbuckled state 4 of the unloading path (undermost).

Studies into the non-bonded interactions in the mixed atomistic-continuum model

In the following simulations, the modelling of in-layer non-bonded interactions in the mixed atomistic-continuum model is investigated. Based on the discussions of the preceding simulations, the tube is once again discretised with 40x40 quadrilateral finite elements. Furthermore, for the evaluation of non-bonded interactions, two different numbers of non-bonded integration points are used. In a first calculation, 4 integration points for non-bonded interactions are used whereas in a second simulation only 1 non-bonded integration point is considered. In order to exclude non-bonded interactions between atoms up to the 3rd neighbourhood, a lower cut-off radius is introduced. According to Subsection 2.4.2, the related 1-4 interaction distance is characterised by $A_{1\text{-}4} = 0.38382\,\text{nm}$ and, consequently, this value serves as lower cut-off radius. 4.26. Furthermore, an upper cutting radius of $1.8\,\text{nm}$ is implemented so that the total amount of possible non-bonded interactions is reduced. The results from the mixed atomistic-continuum model are checked
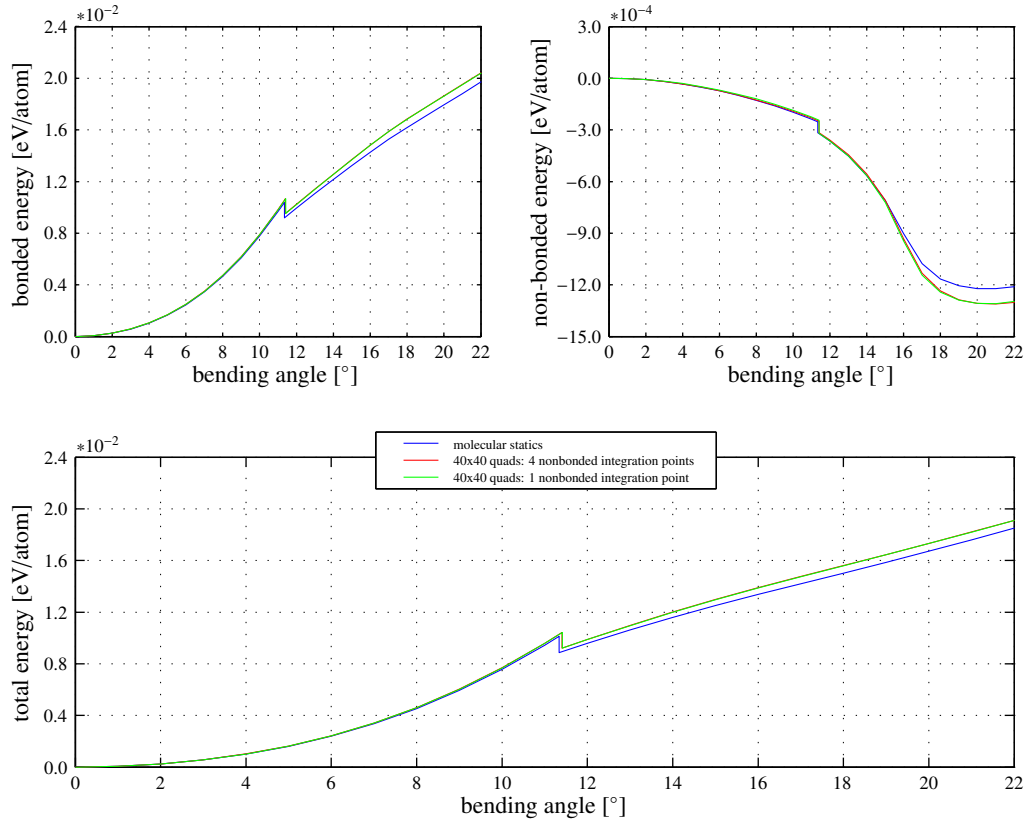
Figure 4.26: Mixed atomistic-continuum model: The energy evolutions for the (10,10) carbon nanotube under sharp bending. Comparison between simulations with different amounts of non-bonded integration points and their check against the results obtained by molecular statics.

against the molecular statics simulation of the associated atomistic structure. The buckled carbon nanotube shows a single kink in the middle and the complete energy curves for all simulations are presented in Figure Thereby, the loading was applied in a total of 24 increments, ending at a bending angle of 22.0°. From this it can be seen that the bonded energy shows a similar behaviour to the results of the preceding studies on the influence of discretisation. In particular, the two types of modelling non-bonded interactions are almost indistinguishable from each other. The same matter of fact can be seen with regard to the non-bonded interactions. In addition, with respect to non-bonded interactions, the comparison against the molecular statics gives a remarkable agreement over a wide range. At higher bending angles, the curves begin to separate, resulting in a nearly constant offset in the last part of deformation. This separation is mostly influenced by the fact that the continuum model is not capable to completely reproduce the local deformations in the kink of the tube. Nevertheless, the non-bonded energy of the mixed atomistic-continuum model shows a similar behaviour at higher bending angles compared to the molecular statics approach. In particular, the minimum and the subsequent increase of the non-bonded energy are well predicted. This is the region where the opposite wall faces converge to the equilibrium distance of non-bonded interactions and, thus, prevent the carbon nanotube from self-intersection. For the last load step at a bending angle of 22.0°, Table 4.4 reports the relative errors of the individual energy terms, obtained by the mixed atomistic-continuum model with different amounts of non-bonded integration points. In Figure 4.27, the solution of the continuum model with 1 non-bonded integration point is displayed as translucent surface, and the results from molecular statics are

	non-bonded integration points	
	4	1
bonded energy	3.5%	3.4%
non-bonded energy	7.5%	7.0%
total energy	3.3%	3.2%

Table 4.4: Mixed atomistic-continuum model: The relative errors of the individual energies at a bending angle of 22.0° for the (10,10) carbon nanotube under sharp bending. Comparison between simulations with different amounts of non-bonded integration points and their validation against the molecular statics approach.
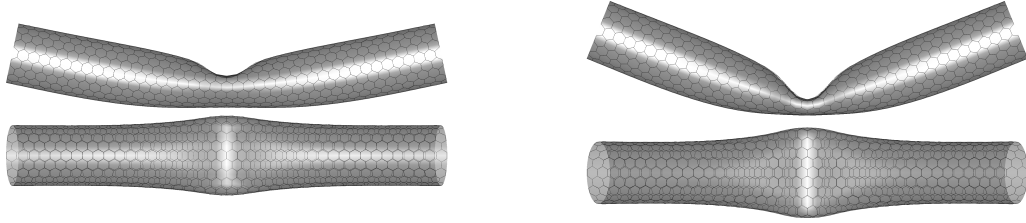
Figure 4.27: Mixed atomistic-continuum model: The superimposed deformed configurations of the molecular statics calculation (line-pattern) and the mixed atomistic-continuum solution (transparent gray surface) obtained with 40x40 quadrilateral finite elements and 1 non-bonded integration point. The front and top view of the buckled structure at a bending angle of 12.0° (left) and 22.0° (right).
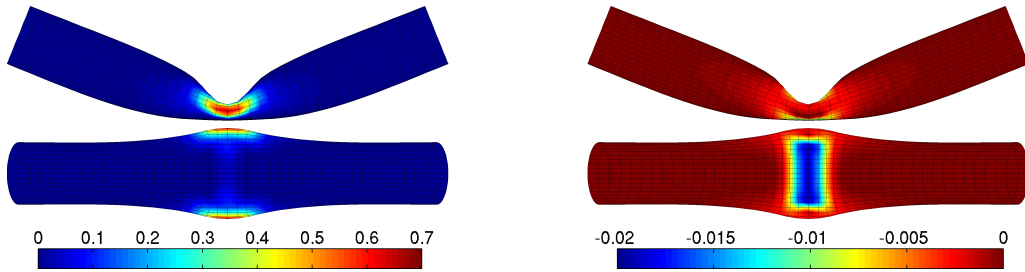
Figure 4.28: Mixed atomistic-continuum model: The buckled configuration for the (10,10) carbon nanotube under sharp bending load (40x40 quadrilateral finite elements and 1 non-bonded integration point) at the end of deformation in a front and top view with colour mapping of the local bonded energy per atom [eV/atom] (left) and the local non-bonded energy per atom [eV/atom] (right).

overlayed. Thereby, the images on the left side present a front and top view of the buckled structure at a bending angle of 12.0°. The pictures on the right side show the deformed tube for the last load step. At both load levels, the deformed structures are in good agreement. The evolution of the total energy is mainly determined by the bonded energy combined with a minor influence of the non-bonded energy. The consideration of in-layer non-bonded interactions leads to a small reduction of the critical bending angle compared to the simulations without them. This variation is observed for the mixed atomistic-continuum model and the molecular statics approach. In the course of this, the relative errors of the predicted critical bending angle are 0.6%

(4 non-bonded integration points) and 0.7% (1 non-bonded integration point). In Figure 4.28, the continuum solution at the last load step, obtained with 1 non-bonded integration point, is illustrated in a front and top view. The colouring on the left side corresponds to a mapping of the averaged local bonded energy. In contrast, the colour mapping on the right side represents the averaged local non-bonded energy. The effect of the in-layer non-bonded interactions on the prevention of self-intersection is evident at the dint in the middle of the tube. The simulations demonstrate the ability of the mixed atomistic-continuum model to properly model the non-bonded interactions. Furthermore, the amount of non-bonded integration points has a negligible influence on the behaviour of the carbon nanotube. This is true for the applied finite element size, where the dimensions of the finite elements are in the magnitude of the atomic bond lengths. However, based on the coarseness of the mesh, an appropriate number of non-bonded integration points is essential in order to accurately resolve the non-bonded interactions. In particular, very large finite elements could otherwise lead to self-intersection or penetration, due to the lacking of sampling points for possible non-bonded interactions. With respect to the total energy evolution, the influence of the non-bonded energy is small in comparison to the contribution from bonded energy. Nevertheless, the consideration of in-layer non-bonded interactions is important to avoid the carbon nanotube from self-intersection.

4.9.4 A (10,10) - (15,15) carbon nanotube under sharp bending

In this example, a (10,10) - (15,15) double-walled carbon nanotube with 50 hexagonal cells in its length under bending load is considered. The results of the mixed atomistic-continuum model are compared with those obtained from a separate molecular statics simulation. With respect to the non-bonded properties, the inter-layer interactions are analysed. In the mixed atomistic-continuum model, the evaluation of non-bonded interactions is carried out with 1 integration point per element. In order to reduce the large amount of possible non-bonded interactions, an upper cut-off radius of 0.9 nm is implemented in the simulations. After the relaxation process, the tube is bent by imposing displacement boundary conditions on both sides of the tube. This is done by rotating both ends about an axis through the tube's middle and perpendicular to the centerline of the relaxed tube. In accordance with previous numerical examples on bent carbon nanotubes, this mode is denoted as sharp bending. Here, on both ends, two rows of finite element nodes or two rows of atoms are constrained. These two rows perform a rigid body rotation with constant distance from the pivot. As a consequence, the end cross sections of the carbon nanotube remain circular throughout the whole process of loading. Equilibrium configurations are calculated by means of a Newton-Raphson procedure and the relaxed tube serves as reference state. The onset of buckling is detected using an accompanying eigenvalue analysis together with a bisection algorithm. The shape of the buckled carbon nanotube is then achieved by branch switching. For the molecular statics approach, the full atomistic structure of the carbon nanotube, which is composed of 5050 atoms, is considered. In a first verification step of the mixed atomistic-continuum model, the tube is discretised by 5000 triangular finite elements (2x50x20 + 2x50x30) using 2550 nodes, and the simulation is performed for the two different local exponential Cauchy-Born rule approximations. In addition, for the direct curvature approach, a calculation with a finer mesh, consisting of 10000 triangular elements (2x100x20 + 2x100x30) and 5050 nodes, is performed. Figure 4.29 reports the evolutions of the energies for these simulations as functions of the bending angle. In the area of the unbuckled tube, all three continuum simulations agree well for both the bonded and the total energy. Additionally, the agreement with the independent molecular statics solution is remarkable. The critical state and the development of the buckled configuration is characterised in any case by a jump in the curves of the individual energies. The predicted values for the bending angle at the instability point are reported in Table 4.5 along with the relative errors for the mixed atomistic-continuum model with reference to the molecular statics approach. The corresponding buckled configuration exhibits a single kink in the middle of the double-walled carbon nanotube. After buckling, the bending is continued to an angle of 18.0°, using a total of 20 load steps. In the postbuckling regime, the direct curvature model shows a slightly lower bonded and total energy
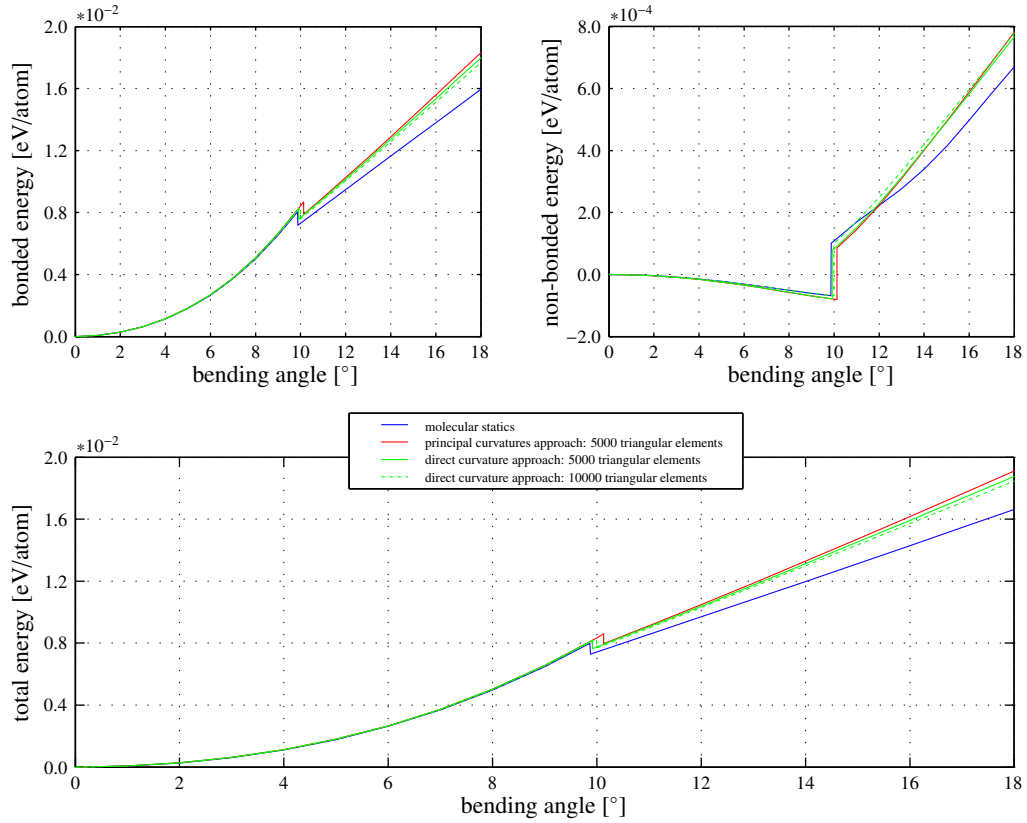
Figure 4.29: Mixed atomistic-continuum model: The energy evolutions for the (10,10) - (15,15) double-walled carbon nanotube under sharp bending. Comparison between the principal curvatures and direct curvature approach and their check against the results obtained by molecular statics. Additional investigations into the influence of the finite element discretisation on the global energy response.

	molecular statics	principal curvatures approach	direct curvature approach	
		5000 △	5000 △	10000 △
critical bending angle	9.867°	10.131°	9.914°	9.992°
relative error	-	2.7%	0.5%	1.3%

Table 4.5: Mixed atomistic-continuum model: The critical bending angle for the (10,10) - (15,15) double-walled carbon nanotube under sharp bending. Comparison between the principal curvatures and direct curvature approach and investigations into the influence of the different triangular discretisations. Specification of the relative errors of the mixed atomistic-continuum model with reference to the molecular statics approach.

for the same finite element mesh compared to the principal curvatures approach. In the case of non-bonded energies, both methods agree well over the entire loading. The transition to the finer mesh leads to a further decrease in all energies. However, the total energy level, related to the molecular statics simulation, cannot be reached. For the purpose of verification, in Table 4.6, the relative errors of the total energy for the different simulations performed with the mixed atomistic-continuum model are reported for the bending angles of 11.0° and 18.0°. From this

	principal curvatures approach	direct curvature approach	
	5000 △	5000 △	10000 △
11.0°	6.4%	5.7%	4.8%
18.0°	14.9%	12.9%	11.0%

Table 4.6: Mixed atomistic-continuum model: The relative errors of the total energy at bending angles of 11.0° and 18.0° for the (10,10) - (15,15) double-walled carbon nanotube under sharp bending. Comparison between the different simulations using the mixed atomistic-continuum model and their validation against the molecular statics approach.
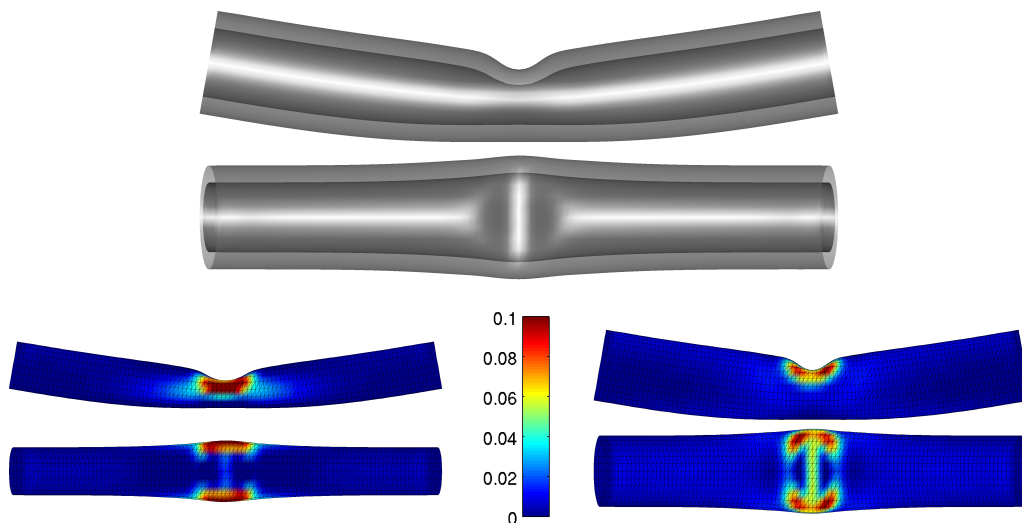
Figure 4.30: Mixed atomistic-continuum model: The buckled configuration at the instability point for the (10,10) - (15,15) DWCNT under sharp bending load in a front and top view. The numerical results are given for the direct curvature approach using a discretisation with 10000 triangular finite elements. At the head, a combined state with translucent outer wall, and at the bottom, the separated walls with colour mapping of the local total energy per atom [eV/atom].

it can be seen that the accuracy of the mixed atomistic-continuum model with reference to the molecular statics approach suffers a decrease at higher bending angles. This can be assigned to the smoothing property of the continuum approaches. In particular, this influence increases with the amount of complex local deformations, which arise at higher bending angles. In this regard, the refined mesh, which has the same amount of degrees of freedom as the atomistic structure, gives a slight improvement. However, the computational effort increases and a further mesh refinement is not suggestive because then the benefits of the mixed atomistic-continuum model are not utilised, and a full atomistic simulation is more favourable. Nonetheless, the mixed atomistic-continuum model is able to represent the critical bending angle with remarkable accuracy. In particular, this can be achieved with finite element meshes that contain fewer degrees of freedom than a molecular statics approach would have to take into account. Figure 4.30 shows the continuum structure of the double-walled carbon nanotube for the simulation with the fine mesh at the critical point in the buckled configuration. Within these images, the buckled shape of the tube, with its single kink in the middle, affecting both layers is illustrated in a front and a top view. In the transparent illustration on top, it can be seen that the inter-layer non-bonded interactions prevent the two walls from penetration. The two sets of images at the bottom display the separated inner and
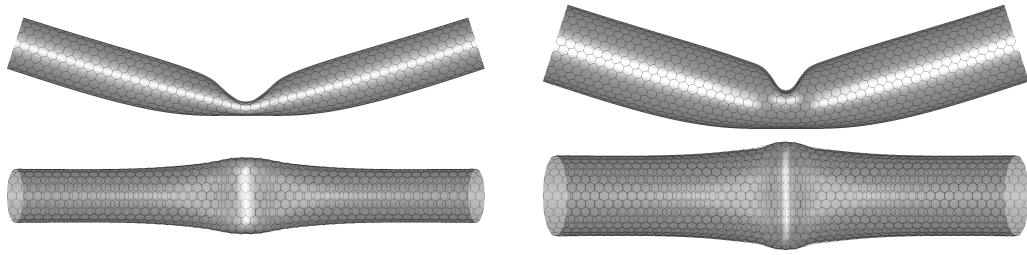
Figure 4.31: Mixed atomistic-continuum model: The superimposed deformed configurations of the molecular statics simulation (line-pattern) and the mixed atomistic-continuum solution (transparent gray surface), obtained by the direct curvature approach using a discretisation with 10000 triangular finite elements.

outer wall of the carbon nanotube. The colour mapping of the averaged local total energy points out that the inner wall suffers a higher strain at the buckle compared to the outer layer. In contrast to that, the sharper kink appears in the outer wall. Similar results for the behaviour of the energies and the shape of the buckle can be found in Arroyo [2], Arroyo and Belytschko [5] and Iijima *et al.* [26]. Additionally, in Figure 4.31, the continuum solution is displayed as translucent surface and the atomistic result is overlayed. From this is can be seen that the deformed structures of both methods are in good agreement. However, the kink in both layers is slightly wider and deeper for the atomistic model. Thus, the local deformations are lower and, consequently, the total energy of the molecular statics simulation is beneath the total energy of the mixed atomistic-continuum approaches. Furthermore, it can be seen that, although the magnitude of change in non-bonded energy is observable smaller compared with the change in bonded energy, the non-bonded interactions have large influence on the morphology of the buckled configuration. In the case of disregarded inter-layer non-bonded interactions, the buckle would not develop in both layers of the tube and penetration would occur.

4.9.5 A (10,10) carbon nanotube under torsional load

In this example, a (10,10) carbon nanotube with 25 hexagonal cells in axial direction under twisting is observed. The aim of this simulation is to highlight the significance of modelling in-layer non-bonded interactions. In addition, this example is taken to show the different unstable and buckled configurations, feasible for this special loading. After the tube has been relaxed, the twisting load is imposed by rotating both ends in opposite direction about the tube's central axis while keeping their axial position fixed. Here, one row of finite element nodes is constrained on each side, resulting in circular end sections throughout the whole loading. Again, a Newton-Raphson procedure is used for calculating equilibrium configurations. With regard to the upcoming energy inspections, the relaxed carbon nanotube defines the reference configuration. Buckling points are further detected by an accompanying eigenvalue analysis combined with a bisection algorithm. The shift between unstable and stable buckled paths is done by means of a branch switching approach. For the numerical investigation, the tube is discretised into 2x25x20 triangular subdivision elements. The continuum modelling of the in-layer non-bonded interactions is done with 1 integration point per element. To exclude the non-bonded interaction between pairs of integration points that are within the bonded distance, a lower cutting radius of $0.3\,\mathrm{nm}$ is introduced. This magnitude is chosen on the basis of the non-bonded interaction distances $A_{1\text{-}3}$ and $A_{1\text{-}4}$ of the undeformed graphene sheet, which are defined in Subsection 2.4.2. In particular, the implemented radius excludes all 1-3 non-bonded interactions and, additionally, the three nearest atom interactions in the 3rd neighbourhood of the graphene sheet. Moreover, an upper cut-off radius of $1.8\,\mathrm{nm}$ is applied. Due to this specific value, possible non-bonded interactions between diametrically opposed sampling points are considered right from the beginning of the simulation. Figure 4.32 plots the
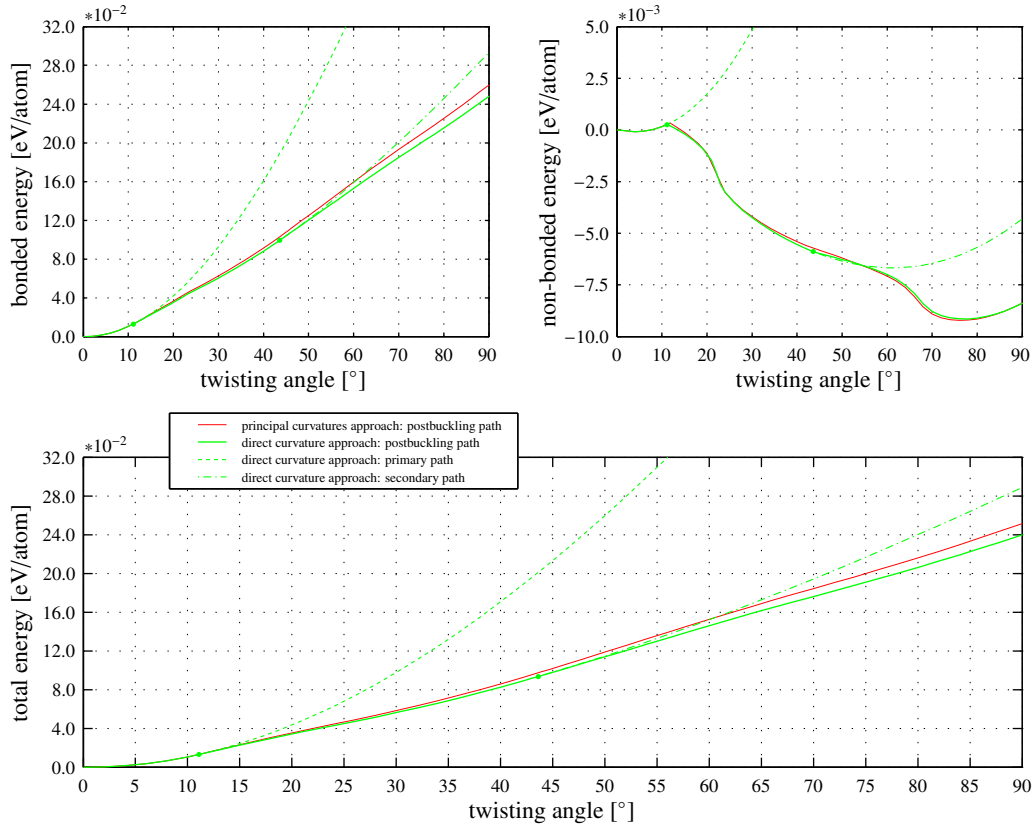
Figure 4.32: Mixed atomistic-continuum model: The energy evolutions for the twisted (10,10)
carbon nanotube. Comparison between the principal curvatures and direct curvature
approach and additional studies related to unstable paths and secondary branches.

diagrams for the different energies versus the twisting angle. In doing so, the different stable and
unstable energy paths obtained by the direct curvature approach are plotted. In addition, the
entire stable path for the principal curvatures approach is shown for comparison. The carbon
nanotube under consideration exhibits two structural instabilities. In the following, the results of
the mixed atomistic-continuum simulation by means of the direct curvature approach are discussed
and the associated deformation paths are explained. The first bifurcation point raises at a twisting
angle of 11.094° and is denoted by a marker in the energy diagrams. From this point on, two
different paths can be followed. The first one is the unstable path of deformation and is denoted
by dashed lines. By means of branch switching, a second path with lower total energy and a
non-uniform deformation mode is possible. This postbuckling path leaves the nearly quadratic
regime of the bonded energy and leads to a kink in the non-bonded energy. The structure of
this buckled configuration is given in the left snapshot of Figure 4.33. On further twisting, the
opposite walls of the tube draw nearer and finally come up to the equilibrium distance for the van
der Waals interactions. This fact can be seen in the decrease of the non-bonded energy. Without
modelling in-layer non-bonded interactions, self-intersection of the tube's walls would occur in this
area of deformation. The flattened twisted structure loses its stability at the marked angle of
43.609° once more. The continuation of this unstable path is now given by the dashed-dotted
lines. Again, branch switching allows the calculation of the buckled structure, which is illustrated
in the middle image of Figure 4.33. From this point on, the tube starts to fold onto itself and
the non-bonded energy tends to a minimum. On further twisting, the walls of the folded carbon
nanotube ribbon are forced closer together. This is evident in the increase of the non-bonded
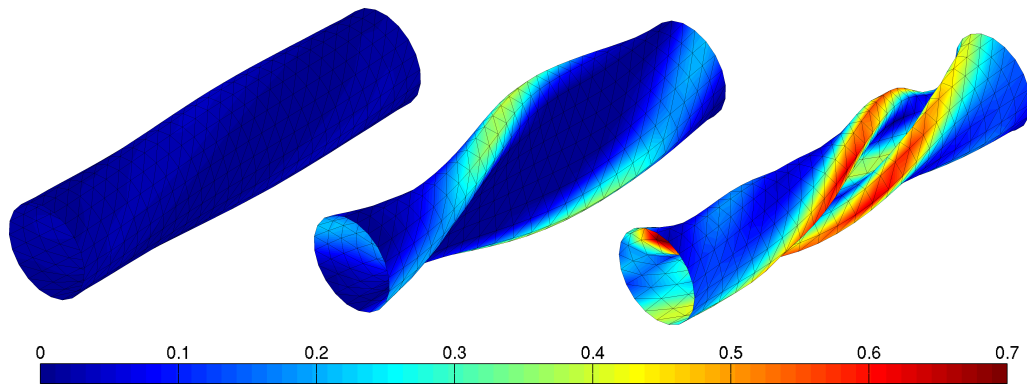
Figure 4.33: Mixed atomistic-continuum model: The buckled configurations of the (10,10) carbon nanotube under torsional load. The numerical results are given for the direct curvature approach and the colour mapping depicts the local total energy per atom [eV/atom]. Visualisation of the buckled structures immediately after the first critical point (left), after branch switching at the second point of instability (middle) and at the end of loading at a twisting angle of 90.0° on each end of the carbon nanotube.

energy and leads to a hardening of the carbon nanotube's twisting response. The loading is ended at a twisting angle of 90.0° on each end and the corresponding deformed configuration is shown in the right image of Figure 4.33. The curves explained so far are based on simulations performed with the direct curvature approach for the approximation of the exponential Cauchy-Born rule. For comparison, the deformation curves of the carbon nanotube are also determined with the principal curvatures approximation of the mixed atomistic-continuum model. The critical twisting angles for this simulation are 11.750° (first instability) and 44.650° (second instability). Thus, the principal curvatures and the direct curvature approach predict critical twisting angles which lie close together. From the simulations it follows that the direct curvature approach leads to slightly lower bonded and total energies and, therefore, to a softer twisting response of the carbon nanotube. Furthermore, a remarkable correspondence is seen in the evolution of the non-bonded energy. Similar twisted carbon nanotubes with comparable deformed configurations were studied by Arroyo and Belytschko [3] and Sun and Liew [50]. With this example, the handling of multiple bifurcation points and the following of stable and unstable deformation paths is demonstrated. This structural stability analysis makes the use of a bisection algorithm in combination with an accompanying eigenvalue calculation of the global stiffness matrix and an additional branch switching procedure indispensable. In addition, this example exhibits the importance of modelling in-layer non-bonded interactions in the case of simulating single-walled carbon nanotubes. In particular, the simulations demonstrate that the mixed atomistic-continuum model is able to reliably model non-bonded interactions. This fact is relevant, as the in-layer non-bonded interactions largely influence the morphology of the buckled configurations and, moreover, prevent the single-walled carbon nanotube from self-intersection.

4.10 Summary

A mixed atomistic-continuum model is applied for the buckling analysis of carbon nanotubes. In this approach, developed by Arroyo [2] and Arroyo and Belytschko [3] on the basis of the quasi-continuum method as given in Tadmor *et al.* [52] and Tadmor *et al.* [53], the discrete atomistic structure is replaced by a continuum surface without thickness. The associated constitutive model is directly obtained from the structure of the underlying atomistic system by means of interatomic potentials. In the course of this, the inner elasticity of the complex honeycomb lattice is considered. The strain energy density for bonded interactions requires the linkage of the atomistic deformation to that of the continuum surface by an extended Cauchy-Born rule. For this purpose, Arroyo [2] and Arroyo and Belytschko [3] proposed the exponential Cauchy-Born rule in combination with a local approximation scheme that relies on the principal curvatures of the considered continuum surface. Adapting this suggestion, another approach for the local approximation of the exponential Cauchy-Born rule is presented on the basis of the normal curvature. In addition, the non-bonded interactions are separately incorporated into the constitutive model by means of a strain energy double density. The definition of the total potential supplies the foundation for the specification of equilibrium configurations. Furthermore, a criterion for the structural stability of configurations is derived therefrom. In the numerical treatment, the continuum surface is approximated by subdivision finite elements and equilibrium configurations of the carbon nanotubes are obtained either by a standard Newton-Raphson procedure or by an arc-length method. For these purposes, a complete linearisation of the mixed atomistic-continuum model is provided. In particular, the evaluation of the element force vectors and the element stiffness matrices for bonded and non-bonded interactions is specified in detail. The detection of instability points is achieved by an accompanying eigenvalue analysis of the global stiffness matrix in combination with a bisection algorithm. Moreover, a branch switching algorithm allows the handling of secondary branches. The mixed atomistic-continuum model is applied in the numerical simulations of various carbon nanotubes under different loading conditions. Thereby, the principal curvatures approach and the direct curvature approach, for the approximation of the exponential Cauchy-Born rule, are used side by side and the obtained results are compared. In addition, molecular statics simulations of the full atomistic structure are performed. Consequently, the deformed configurations and the energy evolutions of both models are checked against each other.

The first example considers a force-driven, axially compressed single-walled carbon nanotube. Firstly, this setup is used to compare the two different local approximations for the exponential Cauchy-Born rule. Additionally, the simulations with the mixed atomistic-continuum model are checked against the results obtained by molecular statics. Secondly, the first and second eigenform for the loaded carbon nanotube are calculated on the basis of the mixed atomistic-continuum model. Within this example, an arc-length method is used in order to follow secondary branches.

In the second example, a single-walled carbon nanotube under sharp bending constraints is investigated. First, the influence of the finite element mesh on the buckling behaviour is studied. Second, the behaviour and the stability of the equilibrium path are analysed. Third, the modelling of in-layer non-bonded interactions in the mixed atomistic-continuum model is discussed. In the first and third subtask, the results obtained by the continuum approach are compared with a molecular statics calculation of the full atomistic model.

A double-walled carbon nanotube under sharp bending constraints is investigated in the third example. In doing so, the modelling and the influence of inter-layer non-bonded interactions is studied and their importance for the prevention of penetration is highlighted. Additionally, the finite element mesh is varied in terms of the element size. Again, a molecular statics simulation is applied for the purpose of comparison.

The fourth numerical example handles a twisted single-walled carbon nanotube. Thereby, the importance of modelling in-layer non-bonded interactions within the mixed atomistic-continuum model is emphasised in order to avoid self-intersection of single-walled carbon nanotubes. Moreover, different unstable and stable paths of the loaded tube are followed and the handling of multiple bifurcation points is demonstrated.

5 Summary and conclusion

This thesis is concerned with the numerical buckling analysis of carbon nanotubes. Thereby, the nanostructure is modelled by two different approaches. Firstly, the discrete system of atoms is directly considered and molecular statics is used. Secondly, the multi-particle structure is replaced by a continuum surface and the mixed atomistic-continuum model is applied. Both approaches are integrated into a stand-alone computational framework that is based on the formalism of the finite element method. For this purpose, the governing equations of molecular statics are formulated in a partitioned form using finite element equivalents. The continuous description of the mixed atomistic-continuum model is discretised and handled on the basis of finite elements. Consequently, it is made possible that both approaches share the main features of the framework. In this regard, solution procedures for non-linear systems of equations and algorithms related to the structural stability analysis can be emphasised. Applying the implemented computational framework, the buckling of various carbon nanotubes in different loading scenarios is studied. In the course of this, simulations using the molecular statics approach and the mixed atomistic-continuum model are performed. The following conclusions can be drawn from these numerical investigations:

- **Molecular statics approach**

  The integration of molecular statics into the computational framework using the finite element formalism provides an efficient method for the intended structural stability analysis of carbon nanotubes. In the observed examples, in particular, the importance of modelling non-bonded interactions and their influence on the buckling behaviour are emphasised. With regard to the in-layer non-bonded interactions, the numerical simulations reveal that their inclusion is important to avoid the nanotubes from self-intersection. Thus, it is natural to employ this type of non-bonded interactions in the analysis of carbon nanotubes. Furthermore, it is observed that the consideration of 1–4 non-bonded interactions influences the buckling behaviour by introducing additional repulsive forces between the atoms of the structure. On the basis of this observation, it is suggested for one to neglect these 1–4 non-bonded interactions in the buckling analysis of carbon nanotubes. Concerning the inter-layer non-bonded interactions, the related numerical investigations demonstrate their crucial impact on the buckled configurations. In particular, they prevent the individual walls of carbon nanotubes from penetration. For this reason, in the simulation of multi-walled carbon nanotubes, it is highly recommended to incorporate inter-layer non-bonded interactions in addition to in-layer non-bonded interactions.

- **Mixed atomistic-continuum model**

  The mixed atomistic-continuum model provides an alternative to the full atomistic simulation of nanostructures. In particular, the numerical realisation using the finite element method allows an efficient analysis of carbon nanotubes. In the computational examples, the mixed atomistic-continuum model is checked against the molecular statics approach. This verification depicts a remarkable agreement of both methods in the case of unbuckled carbon nanotubes and moderate local deformations. In particular, the critical configurations with respect to structural stability are accurately predicted. In the buckled configurations, the occurrence of large local deformations reveals deviations from the molecular statics reference solution. This can be partially assigned to the smoothing property of the mixed atomistic-continuum model, treating the discrete arrangement of atoms as a continuum surface. In this regard, the different approximations of the exponential Cauchy-Born rule are additionally investigated. It can be seen from this that the direct curvature approach leads to a slightly softer response when compared to the principal curvature approach. The energy evolutions

obtained by the first-mentioned approach are therefore closer to the full atomistic simulation of molecular statics. Moreover, the accuracy of the mixed atomistic-continuum model is mainly controlled by the finite element discretisation. On this account, numerical simulations with different meshes are performed and it turns out that under moderate local deformations the influence of the discretisation is minimal. However, the emerging of severe deformations requires a sufficiently fine mesh in order to properly reproduce complex local features of buckled carbon nanotubes. In addition, the effect of the applied finite element type is examined. From this it follows that for the same amount of nodes the quadrilateral finite element gives a slightly softer response than the triangular finite element. With respect to modelling non-bonded interactions, the numerical investigations demonstrate a remarkable agreement of the mixed atomistic-continuum model with the molecular statics approach. Consequently, the continuum surfaces, representing the walls of the carbon nanotube, are prevented from self-intersection and penetration.

A molecular statics approach and a mixed atomistic-continuum model are applied in order to study the buckling behaviour of carbon nanotubes. On this account, various loading cases are considered and a collection of numerical examples is presented. These simulations provide the critical points of structural stability and the associated buckled configurations of the carbon nanotubes.

A Supplementary notes on the mixed atomistic-continuum model

This Appendix provides supplementary notes concerning the variation and the further linearisation of the mixed atomistic-continuum model. In addition, finite elements, which are suitable for a discretisation of the mixed atomistic-continuum model, are presented.

A.1 Derivatives of the strain energy density with respect to inner displacements and strain measures

In this Appendix, explicit expressions for the first-order and second-order derivatives of the strain energy density for bonded interactions with respect to the inner displacements and the strain measures are given. These derivatives are necessary for the inner relaxation and the description of the global equilibrium for the mixed atomistic-continuum model. According to Subsection 4.5.2, the strain energy density W for the bonded interactions is a function of the bond lengths and the valence angles within the representative cell. With reference to Subsection 4.5.1, these lengths and angles are linked to the inner displacements η via the lattice structure of graphene. In addition, as a result of the local approximations for the exponential Cauchy-Born rule given in Subsection 4.4.4, the bond lengths and the valence angles depend on the local strain measures of the deformed surface. For the principal curvatures approach, the measures are $\mathbf{C}$ and $\mathcal{K}$ whereas for the direct curvature approach the deformation is characterised by $\mathbf{g}$ and $\mathbf{k}$. In order to achieve a compact notation, the three bond lengths and the three valence angles of the representative cell are gathered in an array $\mathbf{p}$, where p_o is its o-th component ($o = 1, \ldots, 6$).

$$\mathbf{p} = [a_1, a_2, a_3, \theta_1, \theta_2, \theta_3] \tag{A.1}$$

The various derivatives with respect to the inner displacements $\boldsymbol{\eta}$ and the different strain measures ($\mathbf{C}$, $\mathcal{K}$, $\mathbf{g}$, $\mathbf{k}$) are symbolised by ( ) and [ ]. This allows to represent the first-order and second-order derivatives of W by using the chain rule as:

$$\frac{\partial W}{\partial (\,)} = \sum_{o=1}^{6} \frac{\partial W}{\partial p_o} \frac{\partial p_o}{\partial (\,)} \tag{A.2}$$

$$\frac{\partial^2 W}{\partial (\,) \partial [\,]} = \sum_{p=1}^{6} \sum_{o=1}^{6} \frac{\partial^2 W}{\partial p_o \partial p_p} \frac{\partial p_o}{\partial (\,)} \otimes \frac{\partial p_p}{\partial [\,]} + \sum_{o=1}^{6} \frac{\partial W}{\partial p_o} \frac{\partial^2 p_o}{\partial (\,) \partial [\,]} \tag{A.3}$$

A.1.1 First-order and second-order derivatives of the strain energy density with respect to bond lengths and valence angles

With reference to Subsection 4.5.2, the strain energy density W for the bonded interactions, as a function of the bond lengths and the valence angles within the representative cell, is given by the sum over the three bonds i, where $\{i, j, k\}$ is an even permutation of $\{1, 2, 3\}$.

$$W = \frac{1}{S_0} \sum_{i=1}^{3} \left[V_{\mathrm{R}}(a_i) - B_i(a_j, a_k, \theta_k, \theta_j) V_{\mathrm{A}}(a_i) \right] \tag{A.4}$$

The many-body coupling terms are used in a shortened notation, where the dependences on the bond lengths and valence angles are omitted.

$$B_1 = B_1 \left(a_2, a_3, \theta_3, \theta_2 \right) \tag{A.5}$$

$$B_2 = B_2 \left(a_3, a_1, \theta_1, \theta_3 \right) \tag{A.6}$$

$$B_3 = B_3 \left(a_1, a_2, \theta_2, \theta_1 \right) \tag{A.7}$$

Then, the first-order derivatives with respect to the bond lengths and valence angles are:

$$\frac{\partial W}{\partial a_1} = \frac{1}{S_0} \left[V_R'(a_1) - B_1 V_A'(a_1) - \frac{\partial B_2}{\partial a_1} V_A(a_2) - \frac{\partial B_3}{\partial a_1} V_A(a_3) \right] \tag{A.8}$$

$$\frac{\partial W}{\partial a_2} = \frac{1}{S_0} \left[V_R'(a_2) - \frac{\partial B_1}{\partial a_2} V_A(a_1) - B_2 V_A'(a_2) - \frac{\partial B_3}{\partial a_2} V_A(a_3) \right] \tag{A.9}$$

$$\frac{\partial W}{\partial a_3} = \frac{1}{S_0} \left[V_R'(a_3) - \frac{\partial B_1}{\partial a_3} V_A(a_1) - \frac{\partial B_2}{\partial a_3} V_A(a_2) - B_3 V_A'(a_3) \right] \tag{A.10}$$

$$\frac{\partial W}{\partial \theta_1} = \frac{1}{S_0} \left[-\frac{\partial B_2}{\partial \theta_1} V_A(a_2) - \frac{\partial B_3}{\partial \theta_1} V_A(a_3) \right] \tag{A.11}$$

$$\frac{\partial W}{\partial \theta_2} = \frac{1}{S_0} \left[-\frac{\partial B_1}{\partial \theta_2} V_A(a_1) - \frac{\partial B_3}{\partial \theta_2} V_A(a_3) \right] \tag{A.12}$$

$$\frac{\partial W}{\partial \theta_3} = \frac{1}{S_0} \left[-\frac{\partial B_1}{\partial \theta_3} V_A(a_1) - \frac{\partial B_2}{\partial \theta_3} V_A(a_2) \right] \tag{A.13}$$

In addition, the second-order derivatives with respect to the bond lengths and valence angles are:

$$\frac{\partial^2 W}{\partial a_1 \partial a_1} = \frac{1}{S_0} \left[V_R''(a_1) - B_1 V_A''(a_1) - \frac{\partial^2 B_2}{\partial a_1 \partial a_1} V_A(a_2) - \frac{\partial^2 B_3}{\partial a_1 \partial a_1} V_A(a_3) \right] \tag{A.14}$$

$$\frac{\partial^2 W}{\partial a_1 \partial a_2} = \frac{1}{S_0} \left[-\frac{\partial B_1}{\partial a_2} V_A'(a_1) - \frac{\partial B_2}{\partial a_1} V_A'(a_2) - \frac{\partial^2 B_3}{\partial a_1 \partial a_2} V_A(a_3) \right] \tag{A.15}$$

$$\frac{\partial^2 W}{\partial a_1 \partial a_3} = \frac{1}{S_0} \left[-\frac{\partial B_1}{\partial a_3} V_A'(a_1) - \frac{\partial^2 B_2}{\partial a_1 \partial a_3} V_A(a_2) - \frac{\partial B_3}{\partial a_1} V_A'(a_3) \right] \tag{A.16}$$

$$\frac{\partial^2 W}{\partial a_1 \partial \theta_1} = \frac{1}{S_0} \left[-\frac{\partial^2 B_2}{\partial a_1 \partial \theta_1} V_A(a_2) - \frac{\partial^2 B_3}{\partial a_1 \partial \theta_1} V_A(a_3) \right] \tag{A.17}$$

$$\frac{\partial^2 W}{\partial a_1 \partial \theta_2} = \frac{1}{S_0} \left[-\frac{\partial B_1}{\partial \theta_2} V_A'(a_1) - \frac{\partial^2 B_3}{\partial a_1 \partial \theta_2} V_A(a_3) \right] \tag{A.18}$$

$$\frac{\partial^2 W}{\partial a_1 \partial \theta_3} = \frac{1}{S_0} \left[-\frac{\partial B_1}{\partial \theta_3} V_A'(a_1) - \frac{\partial^2 B_2}{\partial a_1 \partial \theta_3} V_A(a_2) \right] \tag{A.19}$$

$$\frac{\partial^2 W}{\partial a_2 \partial a_1} = \frac{1}{S_0} \left[-\frac{\partial B_1}{\partial a_2} V_A'(a_1) - \frac{\partial B_2}{\partial a_1} V_A'(a_2) - \frac{\partial^2 B_3}{\partial a_2 \partial a_1} V_A(a_3) \right] \tag{A.20}$$

$$\frac{\partial^2 W}{\partial a_2 \partial a_2} = \frac{1}{S_0} \left[V_R''(a_2) - \frac{\partial^2 B_1}{\partial a_2 \partial a_2} V_A(a_1) - B_2 V_A''(a_2) - \frac{\partial^2 B_3}{\partial a_2 \partial a_2} V_A(a_3) \right] \tag{A.21}$$

$$\frac{\partial^2 W}{\partial a_2 \partial a_3} = \frac{1}{S_0} \left[-\frac{\partial^2 B_1}{\partial a_2 \partial a_3} V_A(a_1) - \frac{\partial B_2}{\partial a_3} V_A'(a_2) - \frac{\partial B_3}{\partial a_2} V_A'(a_3) \right] \tag{A.22}$$

$$\frac{\partial^2 W}{\partial a_2 \partial \theta_1} = \frac{1}{S_0} \left[-\frac{\partial B_2}{\partial \theta_1} V_A'(a_2) - \frac{\partial^2 B_3}{\partial a_2 \partial \theta_1} V_A(a_3) \right] \tag{A.23}$$

$$\frac{\partial^2 W}{\partial a_2 \partial \theta_2} = \frac{1}{S_0} \left[-\frac{\partial^2 B_1}{\partial a_2 \partial \theta_2} V_A(a_1) - \frac{\partial^2 B_3}{\partial a_2 \partial \theta_2} V_A(a_3) \right] \tag{A.24}$$

$$\frac{\partial^2 W}{\partial a_2 \partial \theta_3} = \frac{1}{S_0} \left[-\frac{\partial^2 B_1}{\partial a_2 \partial \theta_3} V_A(a_1) - \frac{\partial B_2}{\partial \theta_3} V_A'(a_2) \right] \tag{A.25}$$

$$\frac{\partial^2 W}{\partial a_3 \partial a_1} = \frac{1}{S_0} \left[-\frac{\partial B_1}{\partial a_3} V_{\mathrm{A}}'(a_1) - \frac{\partial^2 B_2}{\partial a_3 \partial a_1} V_{\mathrm{A}}(a_2) - \frac{\partial B_3}{\partial a_1} V_{\mathrm{A}}'(a_3) \right] \tag{A.26}$$

$$\frac{\partial^2 W}{\partial a_3 \partial a_2} = \frac{1}{S_0} \left[-\frac{\partial^2 B_1}{\partial a_3 \partial a_2} V_{\mathrm{A}}(a_1) - \frac{\partial B_2}{\partial a_3} V_{\mathrm{A}}'(a_2) - \frac{\partial B_3}{\partial a_2} V_{\mathrm{A}}'(a_3) \right] \tag{A.27}$$

$$\frac{\partial^2 W}{\partial a_3 \partial a_3} = \frac{1}{S_0} \left[V_{\mathrm{R}}''(a_3) - \frac{\partial^2 B_1}{\partial a_3 \partial a_3} V_{\mathrm{A}}(a_1) - \frac{\partial^2 B_2}{\partial a_3 \partial a_3} V_{\mathrm{A}}(a_2) - B_3 V_{\mathrm{A}}''(a_3) \right] \tag{A.28}$$

$$\frac{\partial^2 W}{\partial a_3 \partial \theta_1} = \frac{1}{S_0} \left[-\frac{\partial^2 B_2}{\partial a_3 \partial \theta_1} V_{\mathrm{A}}(a_2) - \frac{\partial B_3}{\partial \theta_1} V_{\mathrm{A}}'(a_3) \right] \tag{A.29}$$

$$\frac{\partial^2 W}{\partial a_3 \partial \theta_2} = \frac{1}{S_0} \left[-\frac{\partial^2 B_1}{\partial a_3 \partial \theta_2} V_{\mathrm{A}}(a_1) - \frac{\partial B_3}{\partial \theta_2} V_{\mathrm{A}}'(a_3) \right] \tag{A.30}$$

$$\frac{\partial^2 W}{\partial a_3 \partial \theta_3} = \frac{1}{S_0} \left[-\frac{\partial^2 B_1}{\partial a_3 \partial \theta_3} V_{\mathrm{A}}(a_1) - \frac{\partial^2 B_2}{\partial a_3 \partial \theta_3} V_{\mathrm{A}}(a_2) \right] \tag{A.31}$$

$$\frac{\partial^2 W}{\partial \theta_1 \partial a_1} = \frac{1}{S_0} \left[-\frac{\partial^2 B_2}{\partial \theta_1 \partial a_1} V_{\mathrm{A}}(a_2) - \frac{\partial^2 B_3}{\partial \theta_1 \partial a_1} V_{\mathrm{A}}(a_3) \right] \tag{A.32}$$

$$\frac{\partial^2 W}{\partial \theta_1 \partial a_2} = \frac{1}{S_0} \left[-\frac{\partial B_2}{\partial \theta_1} V_{\mathrm{A}}'(a_2) - \frac{\partial^2 B_3}{\partial \theta_1 \partial a_2} V_{\mathrm{A}}(a_3) \right] \tag{A.33}$$

$$\frac{\partial^2 W}{\partial \theta_1 \partial a_3} = \frac{1}{S_0} \left[-\frac{\partial^2 B_2}{\partial \theta_1 \partial a_3} V_{\mathrm{A}}(a_2) - \frac{\partial B_3}{\partial \theta_1} V_{\mathrm{A}}'(a_3) \right] \tag{A.34}$$

$$\frac{\partial^2 W}{\partial \theta_1 \partial \theta_1} = \frac{1}{S_0} \left[-\frac{\partial^2 B_2}{\partial \theta_1 \partial \theta_1} V_{\mathrm{A}}(a_2) - \frac{\partial^2 B_3}{\partial \theta_1 \partial \theta_1} V_{\mathrm{A}}(a_3) \right] \tag{A.35}$$

$$\frac{\partial^2 W}{\partial \theta_1 \partial \theta_2} = \frac{1}{S_0} \left[-\frac{\partial^2 B_3}{\partial \theta_1 \partial \theta_2} V_{\mathrm{A}}(a_3) \right] \tag{A.36}$$

$$\frac{\partial^2 W}{\partial \theta_1 \partial \theta_3} = \frac{1}{S_0} \left[-\frac{\partial^2 B_2}{\partial \theta_1 \partial \theta_3} V_{\mathrm{A}}(a_2) \right] \tag{A.37}$$

$$\frac{\partial^2 W}{\partial \theta_2 \partial a_1} = \frac{1}{S_0} \left[-\frac{\partial B_1}{\partial \theta_2} V_{\mathrm{A}}'(a_1) - \frac{\partial^2 B_3}{\partial \theta_2 \partial a_1} V_{\mathrm{A}}(a_3) \right] \tag{A.38}$$

$$\frac{\partial^2 W}{\partial \theta_2 \partial a_2} = \frac{1}{S_0} \left[-\frac{\partial^2 B_1}{\partial \theta_2 \partial a_2} V_{\mathrm{A}}(a_1) - \frac{\partial^2 B_3}{\partial \theta_2 \partial a_2} V_{\mathrm{A}}(a_3) \right] \tag{A.39}$$

$$\frac{\partial^2 W}{\partial \theta_2 \partial a_3} = \frac{1}{S_0} \left[-\frac{\partial^2 B_1}{\partial \theta_2 \partial a_3} V_{\mathrm{A}}(a_1) - \frac{\partial B_3}{\partial \theta_2} V_{\mathrm{A}}'(a_3) \right] \tag{A.40}$$

$$\frac{\partial^2 W}{\partial \theta_2 \partial \theta_1} = \frac{1}{S_0} \left[-\frac{\partial^2 B_3}{\partial \theta_2 \partial \theta_1} V_{\mathrm{A}}(a_3) \right] \tag{A.41}$$

$$\frac{\partial^2 W}{\partial \theta_2 \partial \theta_2} = \frac{1}{S_0} \left[-\frac{\partial^2 B_1}{\partial \theta_2 \partial \theta_2} V_{\mathrm{A}}(a_1) - \frac{\partial^2 B_3}{\partial \theta_2 \partial \theta_2} V_{\mathrm{A}}(a_3) \right] \tag{A.42}$$

$$\frac{\partial^2 W}{\partial \theta_2 \partial \theta_3} = \frac{1}{S_0} \left[-\frac{\partial^2 B_1}{\partial \theta_2 \partial \theta_3} V_{\mathrm{A}}(a_1) \right] \tag{A.43}$$

$$\frac{\partial^2 W}{\partial \theta_3 \partial a_1} = \frac{1}{S_0}\left[-\frac{\partial B_1}{\partial \theta_3}V'_{\mathrm{A}}(a_1) - \frac{\partial^2 B_2}{\partial \theta_3 \partial a_1}V_{\mathrm{A}}(a_2)\right] \tag{A.44}$$

$$\frac{\partial^2 W}{\partial \theta_3 \partial a_2} = \frac{1}{S_0}\left[-\frac{\partial^2 B_1}{\partial \theta_3 \partial a_2}V_{\mathrm{A}}(a_1) - \frac{\partial B_2}{\partial \theta_3}V'_{\mathrm{A}}(a_2)\right] \tag{A.45}$$

$$\frac{\partial^2 W}{\partial \theta_3 \partial a_3} = \frac{1}{S_0}\left[-\frac{\partial^2 B_1}{\partial \theta_3 \partial a_3}V_{\mathrm{A}}(a_1) - \frac{\partial^2 B_2}{\partial \theta_3 \partial a_3}V_{\mathrm{A}}(a_2)\right] \tag{A.46}$$

$$\frac{\partial^2 W}{\partial \theta_3 \partial \theta_1} = \frac{1}{S_0}\left[-\frac{\partial^2 B_2}{\partial \theta_3 \partial \theta_1}V_{\mathrm{A}}(a_2)\right] \tag{A.47}$$

$$\frac{\partial^2 W}{\partial \theta_3 \partial \theta_2} = \frac{1}{S_0}\left[-\frac{\partial^2 B_1}{\partial \theta_3 \partial \theta_2}V_{\mathrm{A}}(a_1)\right] \tag{A.48}$$

$$\frac{\partial^2 W}{\partial \theta_3 \partial \theta_3} = \frac{1}{S_0}\left[-\frac{\partial^2 B_1}{\partial \theta_3 \partial \theta_3}V_{\mathrm{A}}(a_1) - \frac{\partial^2 B_2}{\partial \theta_3 \partial \theta_3}V_{\mathrm{A}}(a_2)\right] \tag{A.49}$$

The evaluation of the expressions given above, requires the first-order and second-order derivatives of the sub-functions that specify the bond-wise energy with respect to the bond lengths and valence angles. For this purpose, Subsection 2.3.1 can be reused, which specifies the essential derivatives in a generally applicable notation.

A.1.2 First-order and second-order derivatives of bond lengths and valence angles with respect to inner displacements and strain measures

The first-order and second-order derivatives of the bond lengths a_i and the valence angles θ_i ($i = 1, 2, 3$) with respect to the inner displacements and the strain measures depend on the chosen approximation for the exponential Cauchy-Born rule. Therefore, these two approaches are discussed consecutively in the following segments. Within both derivations, the function

$$\mathcal{S}(x) = \frac{\sin(x)}{x} \tag{A.50}$$

is necessary. In addition its first-order and second-order derivatives, which are given by

$$\mathcal{S}'(x) = \frac{\cos(x)}{x} - \frac{\sin(x)}{x^2} = \frac{\cos(x) - \mathcal{S}(x)}{x} \tag{A.51}$$

$$\mathcal{S}''(x) = -\frac{\cos(x) - \mathcal{S}(x)}{x^2} - \frac{\sin(x) + \mathcal{S}'(x)}{x} = -\frac{\sin(x) + 2\mathcal{S}'(x)}{x} \tag{A.52}$$

are relevant. As pointed out by Arroyo [2], in the numerical evaluation, these functions have to be used carefully if x tends to zero. Such a point is obtained if one of the principal curvatures or the currently considered normal curvature is zero. In order to avoid this problem, these functions are replaced by a truncated Taylor series expansion.

Approximation of the exponential Cauchy-Born rule: principal curvatures approach

With reference to Equation (4.54) of Subsection 4.4.4, the components of the approximated deformed bond vector $\mathbf{a}$ in the local orthonormal base system $\widetilde{\mathcal{D}} = \{\mathbf{v}_I, \mathbf{v}_{II}, \mathbf{n}\}$ are given as:

$$[\mathbf{a}_i]_{\widetilde{\mathcal{D}}} = \begin{bmatrix} \mathcal{S}\left(k_I w_i^I\right)w_i^I \\ \mathcal{S}\left(k_{II} w_i^{II}\right)w^{II} \\ \frac{k_I w_i^I}{2}\mathcal{S}^2\left(\frac{k_I w_i^I}{2}\right)w_i^I + \frac{k_{II} w_i^{II}}{2}\mathcal{S}^2\left(\frac{k_{II} w_i^{II}}{2}\right)w_i^{II} \end{bmatrix} \tag{A.53}$$

The length of the deformed lattice vector a_i is expressed by using its components in the local orthonormal base system.

$$a_i = \left[(a_i)^{\mathfrak{c}} (a_i)^{\mathfrak{c}} \right]^{1/2} \tag{A.54}$$

The deformed valence angle θ_i between two deformed lattice vectors $\mathbf{a}_j$ and $\mathbf{a}_k$ follows from the scalar product between these vectors and their corresponding lengths.

$$\cos(\theta_i) = \frac{(a_j)^{\mathfrak{c}} (a_k)^{\mathfrak{c}}}{a_j a_k} \tag{A.55}$$

$$\theta_i = \arccos\left[\frac{(a_j)^{\mathfrak{c}} (a_k)^{\mathfrak{c}}}{a_j a_k} \right] \tag{A.56}$$

Within all these expressions, $(\ )^{\mathfrak{c}}$ denotes the $\mathfrak{c}$-th component of the observed vector in the local orthonormal basis $\widetilde{\mathcal{D}}$ of the Eulerian configuration and a summation on this index $\mathfrak{c}$ is implied. Beyond that, $\{i, j, k\}$ is an even permutation of $\{1, 2, 3\}$.

Based on Equation (A.54), the first-order and second-order derivatives of the bond length a_i with respect to the inner displacements $\boldsymbol{\eta}$, the right Cauchy-Green deformation tensor $\mathbf{C}$ and the pullback of the spatial curvature tensor, namely $\mathcal{K}$, are ascertainable. In the course of this, these quantities are symbolised by $(\ )$ and $[\ ]$.

$$\frac{\partial a_i}{\partial(\ )} = \frac{1}{a_i} \frac{\partial (a_i)^{\mathfrak{c}}}{\partial(\ )} (a_i)^{\mathfrak{c}} \tag{A.57}$$

$$\frac{\partial^2 a_i}{\partial(\ )\partial[\ ]} = \frac{1}{a_i} \left[-\frac{\partial a_i}{\partial(\ )} \otimes \frac{\partial a_i}{\partial[\ ]} + \frac{\partial^2 (a_i)^{\mathfrak{c}}}{\partial(\ )\partial[\ ]} (a_i)^{\mathfrak{c}} + \frac{\partial (a_i)^{\mathfrak{c}}}{\partial(\ )} \otimes \frac{\partial (a_i)^{\mathfrak{c}}}{\partial[\ ]} \right] \tag{A.58}$$

Applying the same notation as above and using Equation (A.55), the required derivatives of the deformed valence angle θ_i are obtained as:

$$\frac{\partial \theta_i}{\partial(\ )} = -\frac{1}{\sin(\theta_i) a_j a_k} \left[\frac{\partial (a_j)^{\mathfrak{c}}}{\partial(\ )} (a_k)^{\mathfrak{c}} + (a_j)^{\mathfrak{c}} \frac{\partial (a_k)^{\mathfrak{c}}}{\partial(\ )} - \cos(\theta_i) \left(\frac{\partial a_j}{\partial(\ )} a_k + a_j \frac{\partial a_k}{\partial(\ )} \right) \right] \tag{A.59}$$

$$
\begin{aligned}
\frac{\partial^2 \theta_i}{\partial(\ )\partial[\ ]} = {} & -\frac{\cos(\theta_i)}{\sin(\theta_i)} \frac{\partial \theta_i}{\partial(\ )} \otimes \frac{\partial \theta_i}{\partial[\ ]} \\
& -\frac{1}{a_j a_k} \left[\left(\frac{\partial a_j}{\partial(\ )} a_k + a_j \frac{\partial a_k}{\partial(\ )} \right) \otimes \frac{\partial \theta_i}{\partial[\ ]} + \frac{\partial \theta_i}{\partial(\ )} \otimes \left(\frac{\partial a_j}{\partial[\ ]} a_k + a_j \frac{\partial a_k}{\partial[\ ]} \right) \right] \\
& -\frac{1}{\sin(\theta_i) a_j a_k} \left[\frac{\partial^2 (a_j)^{\mathfrak{c}}}{\partial(\ )\partial[\ ]} (a_k)^{\mathfrak{c}} + (a_j)^{\mathfrak{c}} \frac{\partial^2 (a_k)^{\mathfrak{c}}}{\partial(\ )\partial[\ ]} \right] \\
& -\frac{1}{\sin(\theta_i) a_j a_k} \left[\frac{\partial (a_j)^{\mathfrak{c}}}{\partial(\ )} \otimes \frac{\partial (a_k)^{\mathfrak{c}}}{\partial[\ ]} + \frac{\partial (a_k)^{\mathfrak{c}}}{\partial(\ )} \otimes \frac{\partial (a_j)^{\mathfrak{c}}}{\partial[\ ]} \right] \\
& +\frac{\cos(\theta_i)}{\sin(\theta_i) a_j a_k} \left[\frac{\partial^2 a_j}{\partial(\ )\partial[\ ]} a_k + a_j \frac{\partial^2 a_k}{\partial(\ )\partial[\ ]} + \frac{\partial a_j}{\partial(\ )} \otimes \frac{\partial a_k}{\partial[\ ]} + \frac{\partial a_k}{\partial(\ )} \otimes \frac{\partial a_j}{\partial[\ ]} \right]
\end{aligned} \tag{A.60}
$$

These expressions need the first-order and second-order derivatives of the deformed lattice vector components $(a_i)^{\mathfrak{c}}$ with respect to either $\mathbf{C}, \mathcal{K}$ or $\boldsymbol{\eta}$, whereby, once again, these measures are indicated by $(\ )$ and $[\ ]$. The first two components are associated to the principal directions $\mathbf{v}_n$ with $n = I, II$. These show a similar structure so that their derivatives can be given in one expression.

For this task, the abbreviations $\mathcal{S}_I = \mathcal{S}\left(k_I w^I\right)$ and $\mathcal{S}_{II} = \mathcal{S}\left(k_{II} w^{II}\right)$ are introduced.

$$
\left(a_i\right)^n = w_i^n \mathcal{S}_n \tag{A.61}
$$

$$
\frac{\partial\left(a_i\right)^n}{\partial\left(\right)} = \frac{\partial w_i^n}{\partial\left(\right)}\mathcal{S}_n + w_i^n \mathcal{S}_n'\left(\frac{\partial k_n}{\partial\left(\right)}w_i^n + k_n\frac{\partial w_i^n}{\partial\left(\right)}\right) \tag{A.62}
$$

$$
\begin{aligned}
\frac{\partial^2\left(a_i\right)^n}{\partial\left(\right)\partial\left[\,\right]} = {} & \frac{\partial^2 w_i^n}{\partial\left(\right)\partial\left[\,\right]}\mathcal{S}_n + \frac{\partial w_i^n}{\partial\left(\right)}\otimes\mathcal{S}_n'\left(\frac{\partial k_n}{\partial\left[\,\right]}w_i^n + k_n\frac{\partial w_i^n}{\partial\left[\,\right]}\right) + \mathcal{S}_n'\left(\frac{\partial k_n}{\partial\left(\right)}w_i^n + k_n\frac{\partial w_i^n}{\partial\left(\right)}\right)\otimes\frac{\partial w_i^n}{\partial\left[\,\right]} \\
& + w_i^n \mathcal{S}_n''\left(\frac{\partial k_n}{\partial\left(\right)}w_i^n + k_n\frac{\partial w_i^n}{\partial\left(\right)}\right)\otimes\left(\frac{\partial k_n}{\partial\left[\,\right]}w_i^n + k_n\frac{\partial w_i^n}{\partial\left[\,\right]}\right) \\
& + w_i^n \mathcal{S}_n'\left(\frac{\partial^2 k_n}{\partial\left(\right)\partial\left[\,\right]}w_i^n + \frac{\partial k_n}{\partial\left(\right)}\otimes\frac{\partial w_i^n}{\partial\left[\,\right]} + \frac{\partial w_i^n}{\partial\left(\right)}\otimes\frac{\partial k_n}{\partial\left[\,\right]} + k_n\frac{\partial^2 w_i^n}{\partial\left(\right)\partial\left[\,\right]}\right) \tag{A.63}
\end{aligned}
$$

For the derivatives of the third component, related to the unit normal $\mathbf{n}$, the two abbreviations $\mathcal{S}_{I/2} = \mathcal{S}\left(\frac{k_I w^I}{2}\right)$ and $\mathcal{S}_{II/2} = \mathcal{S}\left(\frac{k_{II} w^{II}}{2}\right)$ are introduced.

$$
(a_i)^{III} = \frac{k_I \left(w_i^I\right)^2}{2}\mathcal{S}_{I/2}^2 + \frac{k_{II}\left(w_i^{II}\right)^2}{2}\mathcal{S}_{II/2}^2 \tag{A.64}
$$

$$
\frac{\partial (a_i)^{III}}{\partial(\,)} = \left(\frac{\partial k_I}{\partial(\,)}\frac{w_i^I}{2} + k_I\frac{\partial w_i^I}{\partial(\,)}\right)w_i^I\mathcal{S}_{I/2}^2 + \frac{k_I\left(w_i^I\right)^2}{2}\mathcal{S}_{I/2}\mathcal{S}_{I/2}'\left(\frac{\partial k_I}{\partial(\,)}w_i^I + k_I\frac{\partial w_i^I}{\partial(\,)}\right)
$$
$$
+ \left(\frac{\partial k_{II}}{\partial(\,)}\frac{w_i^{II}}{2} + k_{II}\frac{\partial w_i^{II}}{\partial(\,)}\right)w_i^{II}\mathcal{S}_{II/2}^2 + \frac{k_{II}\left(w_i^{II}\right)^2}{2}\mathcal{S}_{II/2}\mathcal{S}_{II/2}'\left(\frac{\partial k_{II}}{\partial(\,)}w_i^{II} + k_{II}\frac{\partial w_i^{II}}{\partial(\,)}\right) \tag{A.65}
$$

$$
\frac{\partial^2 (a_i)^{III}}{\partial(\,)\partial[\,]} = w_i^I\mathcal{S}_{I/2}^2\left(\frac{\partial^2 k_I}{\partial(\,)\partial[\,]}\frac{w_i^I}{2} + \frac{\partial k_I}{\partial(\,)}\otimes\frac{\partial w_i^I}{\partial[\,]} + \frac{\partial w_i^I}{\partial(\,)}\otimes\frac{\partial k_I}{\partial[\,]} + k_I\frac{\partial^2 w_i^I}{\partial(\,)\partial[\,]}\right)
$$
$$
+ k_I\mathcal{S}_{I/2}^2\frac{\partial w_i^I}{\partial(\,)}\otimes\frac{\partial w_i^I}{\partial[\,]}
$$
$$
+ w_i^I D_{12}\mathcal{S}_{I/2}'\left[\left(\frac{\partial k_I}{\partial(\,)}\frac{w_i^I}{2} + k_I\frac{\partial w_i^I}{\partial(\,)}\right)\otimes\left(\frac{\partial k_I}{\partial[\,]}w_i^I + k_I\frac{\partial w_i^I}{\partial[\,]}\right)\right]
$$
$$
+ w_i^I D_{12}\mathcal{S}_{I/2}'\left[\left(\frac{\partial k_I}{\partial(\,)}w_i^I + k_I\frac{\partial w_i^I}{\partial(\,)}\right)\otimes\left(\frac{\partial k_I}{\partial[\,]}\frac{w_i^I}{2} + k_I\frac{\partial w_i^I}{\partial[\,]}\right)\right]
$$
$$
+ \frac{k_I\left(w_i^I\right)^2}{4}\left(\mathcal{S}_{I/2}'\mathcal{S}_{I/2}' + \mathcal{S}_{I/2}\mathcal{S}_{I/2}''\right)\left(\frac{\partial k_I}{\partial(\,)}w_i^I + k_I\frac{\partial w_i^I}{\partial(\,)}\right)\otimes\left(\frac{\partial k_I}{\partial[\,]}w_i^I + k_I\frac{\partial w_i^I}{\partial[\,]}\right)
$$
$$
+ \frac{k_I\left(w_i^I\right)^2}{2}\mathcal{S}_{I/2}\mathcal{S}_{I/2}'\left(\frac{\partial^2 k_I}{\partial(\,)\partial[\,]}w_i^I + \frac{\partial k_I}{\partial(\,)}\otimes\frac{\partial w_i^I}{\partial[\,]} + \frac{\partial w_i^I}{\partial(\,)}\otimes\frac{\partial k_I}{\partial[\,]} + k_I\frac{\partial^2 w_i^I}{\partial(\,)\partial[\,]}\right)
$$
$$
+ w_i^{II}\mathcal{S}_{II/2}^2\left(\frac{\partial^2 k_{II}}{\partial(\,)\partial[\,]}\frac{w_i^{II}}{2} + \frac{\partial k_{II}}{\partial(\,)}\otimes\frac{\partial w_i^{II}}{\partial[\,]} + \frac{\partial w_i^{II}}{\partial(\,)}\otimes\frac{\partial k_{II}}{\partial[\,]} + k_{II}\frac{\partial^2 w_i^{II}}{\partial(\,)\partial[\,]}\right)
$$
$$
+ k_{II}\mathcal{S}_{II/2}^2\frac{\partial w_i^{II}}{\partial(\,)}\otimes\frac{\partial w_i^{II}}{\partial[\,]}
$$
$$
+ w_i^{II} D_{22}\mathcal{S}_{II/2}'\left[\left(\frac{\partial k_{II}}{\partial(\,)}\frac{w_i^{II}}{2} + k_{II}\frac{\partial w_i^{II}}{\partial(\,)}\right)\otimes\left(\frac{\partial k_{II}}{\partial[\,]}w_i^{II} + k_{II}\frac{\partial w_i^{II}}{\partial[\,]}\right)\right]
$$
$$
+ w_i^{II} D_{22}\mathcal{S}_{II/2}'\left[\left(\frac{\partial k_{II}}{\partial(\,)}w_i^{II} + k_{II}\frac{\partial w_i^{II}}{\partial(\,)}\right)\otimes\left(\frac{\partial k_{II}}{\partial[\,]}\frac{w_i^{II}}{2} + k_{II}\frac{\partial w_i^{II}}{\partial[\,]}\right)\right]
$$
$$
+ \frac{k_{II}\left(w_i^{II}\right)^2}{4}\left(\mathcal{S}_{II/2}'\mathcal{S}_{II/2}'\right)\left(\frac{\partial k_{II}}{\partial(\,)}w_i^{II} + k_{II}\frac{\partial w_i^{II}}{\partial(\,)}\right)\otimes\left(\frac{\partial k_{II}}{\partial[\,]}w_i^{II} + k_{II}\frac{\partial w_i^{II}}{\partial[\,]}\right)
$$
$$
+ \frac{k_{II}\left(w_i^{II}\right)^2}{4}\left(\mathcal{S}_{II/2}\mathcal{S}_{II/2}''\right)\left(\frac{\partial k_{II}}{\partial(\,)}w_i^{II} + k_{II}\frac{\partial w_i^{II}}{\partial(\,)}\right)\otimes\left(\frac{\partial k_{II}}{\partial[\,]}w_i^{II} + k_{II}\frac{\partial w_i^{II}}{\partial[\,]}\right)
$$
$$
+ \frac{k_{II}\left(w_i^{II}\right)^2}{2}\mathcal{S}_{II/2}\mathcal{S}_{II/2}'\left(\frac{\partial^2 k_{II}}{\partial(\,)\partial[\,]}w_i^{II} + k_{II}\frac{\partial^2 w_i^{II}}{\partial(\,)\partial[\,]}\right)
$$
$$
+ \frac{k_{II}\left(w_i^{II}\right)^2}{2}\mathcal{S}_{II/2}\mathcal{S}_{II/2}'\left(\frac{\partial k_{II}}{\partial(\,)}\otimes\frac{\partial w_i^{II}}{\partial[\,]} + \frac{\partial w_i^{II}}{\partial(\,)}\otimes\frac{\partial k_{II}}{\partial[\,]}\right) \tag{A.66}
$$

Next, the first-order and second-order derivatives of the tangent deformed lattice vector components with respect to the inner displacements and the strain measures are calculated. Within the following expressions, index notation is used and the conventions given in Subsection 4.3.2 are applied. Therefore, the components of the independent quantities are represented in the standard

bases of the undeformed configuration, resulting in:

$$\boldsymbol{\eta} = \eta^A \mathbf{E}_A \tag{A.67}$$

$$\mathbf{C} = C_{AB} \mathbf{E}^A \otimes \mathbf{E}^B \tag{A.68}$$

$$\boldsymbol{\mathcal{K}} = \mathcal{K}_{AB} \mathbf{E}^A \otimes \mathbf{E}^B \tag{A.69}$$

The components w_i^n of the tangent deformed lattice vector, related to the two principal directions $\mathbf{v}_n$ $(n = I, II)$, are evaluated according to Equation (4.50) and Equation (4.51). The dependence on the inner displacements is obtained by using Equation (4.64).

$$w_i^n = C_{AB} \left(A_i\right)^A \left(V_n\right)^B \tag{A.70}$$

$$w_i^n = C_{AB} \left(A_{i0} + \eta\right)^A \left(V_n\right)^B \tag{A.71}$$

The first-order derivatives of w_i^n are:

$$\frac{\partial w_i^n}{\partial \eta^C} = C_{CB} \left(V_n\right)^B \tag{A.72}$$

$$\frac{\partial w_i^n}{\partial C_{CD}} = \frac{1}{2} \left(\delta_A^C \delta_B^D + \delta_A^D \delta_B^C\right) \left(A_i\right)^A \left(V_n\right)^B + C_{AB} \left(A_i\right)^A \frac{\partial \left(V_n\right)^B}{\partial C_{CD}} \tag{A.73}$$

$$\frac{\partial w_i^n}{\partial \kappa_{CD}} = C_{AB} \left(A_i\right)^A \frac{\partial \left(V_n\right)^B}{\partial \kappa_{CD}} \tag{A.74}$$

Now, the second-order derivatives of w_i^n follow as:

$$\frac{\partial^2 w_i^n}{\partial \eta^C \partial \eta^E} = 0 \tag{A.75}$$

$$\frac{\partial^2 w_i^n}{\partial \eta^C \partial C_{EF}} = \frac{1}{2} \left(\delta_C^E \delta_B^F + \delta_C^F \delta_B^E\right) \left(V_n\right)^B + C_{CB} \frac{\partial \left(V_n\right)^B}{\partial C_{EF}} \tag{A.76}$$

$$\frac{\partial^2 w_i^n}{\partial \eta^C \partial \kappa_{EF}} = C_{CB} \frac{\partial \left(V_n\right)^B}{\partial \kappa_{EF}} \tag{A.77}$$

$$\frac{\partial^2 w_i^n}{\partial C_{CD} \partial \eta^E} = \frac{1}{2} \left(\delta_E^C \delta_B^D + \delta_E^D \delta_B^C\right) \left(V_n\right)^B + C_{EB} \frac{\partial \left(V_n\right)^B}{\partial C_{CD}} \tag{A.78}$$

$$\frac{\partial^2 w_i^n}{\partial C_{CD} \partial C_{EF}} = \frac{1}{2} \left(\delta_A^C \delta_B^D + \delta_D^D \delta_C^C\right) \left(A_i\right)^A \frac{\partial \left(V_n\right)^B}{\partial C_{EF}} + \frac{1}{2} \left(\delta_A^E \delta_B^F + \delta_A^F \delta_B^E\right) \left(A_i\right)^A \frac{\partial \left(V_n\right)^B}{\partial C_{CD}}$$
$$+ C_{AB} \left(A_i\right)^A \frac{\partial^2 \left(V_n\right)^B}{\partial C_{CD} \partial C_{EF}} \tag{A.79}$$

$$\frac{\partial^2 w_i^n}{\partial C_{CD} \partial \kappa_{EF}} = \frac{1}{2} \left(\delta_A^C \delta_B^D + \delta_A^D \delta_B^C\right) \left(A_i\right)^A \frac{\partial \left(V_n\right)^B}{\partial \kappa_{EF}} + C_{AB} \left(A_i\right)^A \frac{\partial^2 \left(V_n\right)^B}{\partial C_{CD} \partial \kappa_{EF}} \tag{A.80}$$

$$\frac{\partial^2 w_i^n}{\partial \kappa_{CD} \partial \eta^E} = C_{EB} \frac{\partial \left(V_n\right)^B}{\partial \kappa_{CD}} \tag{A.81}$$

$$\frac{\partial^2 w_i^n}{\partial \kappa_{CD} \partial C_{EF}} = \frac{1}{2} \left(\delta_A^E \delta_B^F + \delta_A^F \delta_B^E\right) \left(A_i\right)^A \frac{\partial \left(V_n\right)^B}{\partial \kappa_{CD}} + C_{AB} \left(A_i\right)^A \frac{\partial^2 \left(V_n\right)^B}{\partial \kappa_{CD} \partial C_{EF}} \tag{A.82}$$

$$\frac{\partial^2 w_i^n}{\partial \kappa_{CD} \partial \kappa_{EF}} = C_{AB} \left(A_i\right)^A \frac{\partial^2 \left(V_n\right)^B}{\partial \kappa_{CD} \partial \kappa_{EF}} \tag{A.83}$$

A Supplementary notes on the mixed atomistic-continuum model

Referring to Arroyo [2] and Arroyo and Belytschko [5], the first-order derivatives of the principal curvatures k_n $(n = I, II$ and $k_I \neq k_{II})$ of the deformed surface with respect to $\mathcal{K}$ and $\mathbf{C}$ read:

$$\frac{\partial k_n}{\partial \kappa_{CD}} = (V_n)^C (V_n)^D \tag{A.84}$$

$$\frac{\partial k_n}{\partial C_{CD}} = -k_n \frac{\partial k_n}{\partial \kappa_{CD}} \tag{A.85}$$

On this basis, the second-order derivatives can be calculated as:

$$\frac{\partial^2 k_n}{\partial \kappa_{CD} \partial \kappa_{EF}} = \frac{\partial (V_n)^C}{\partial \kappa_{EF}} (V_n)^D + (V_n)^C \frac{\partial (V_n)^D}{\partial \kappa_{EF}} \tag{A.86}$$

$$\frac{\partial^2 k_n}{\partial \kappa_{CD} \partial C_{EF}} = \frac{\partial (V_n)^C}{\partial C_{EF}} (V_n)^D + (V_n)^C \frac{\partial (V_n)^D}{\partial C_{EF}} \tag{A.87}$$

$$\frac{\partial^2 k_n}{\partial C_{CD} \partial \kappa_{EF}} = -\frac{\partial k_n}{\partial \kappa_{CD}} \frac{\partial k_n}{\partial \kappa_{EF}} - k_n \frac{\partial^2 k_n}{\partial \kappa_{CD} \partial \kappa_{EF}} \tag{A.88}$$

$$\frac{\partial^2 k_n}{\partial C_{CD} \partial C_{EF}} = k_n \left(\frac{\partial k_n}{\partial \kappa_{CD}} \frac{\partial k_n}{\partial \kappa_{EF}} - \frac{\partial^2 k_n}{\partial \kappa_{CD} \partial C_{EF}} \right) \tag{A.89}$$

Again, with reference to Arroyo [2] and Arroyo and Belytschko [5], the first-order derivatives of the principal directions $\mathbf{V}_n$ $(n = I, II$ and $k_I \neq k_{II})$ of the deformed surface with respect to $\mathcal{K}$ and $\mathbf{C}$, whereby $\{n, m\}$ is a permutation of $\{I, II\}$, are given as:

$$\frac{\partial (V_n)^A}{\partial \kappa_{CD}} = \frac{1}{2 (k_n - k_m)} (V_m)^A \left[(V_n)^C (V_m)^D + (V_m)^C (V_n)^D \right] \tag{A.90}$$

$$\frac{\partial (V_n)^A}{\partial C_{CD}} = -\frac{1}{2} (V_n)^A (V_n)^C (V_n)^D - k_n \frac{\partial (V_n)^A}{\partial \kappa_{CD}} \tag{A.91}$$

A Supplementary notes on the mixed atomistic-continuum model

Further calculations provide the second-order derivatives of the principal directions as:

$$
\begin{aligned}
\frac{\partial^2 (V_n)^A}{\partial \kappa_{CD} \partial \kappa_{EF}} &= -\frac{1}{4\left(k_n - k_m\right)^2} (V_m)^A \left[(V_m)^C (V_n)^D + (V_n)^C (V_m)^D\right] \left[(V_m)^E (V_n)^F + (V_n)^E (V_m)^F\right] \\
&\quad + \frac{1}{2\left(k_n - k_m\right)^2} (V_m)^A \left[(V_m)^E (V_m)^F - (V_n)^E (V_n)^F\right] \left[(V_m)^C (V_n)^D + (V_n)^C (V_m)^D\right] \\
&\quad + \frac{1}{2\left(k_n - k_m\right)^2} (V_m)^A \left[(V_m)^C (V_m)^D - (V_n)^C (V_n)^D\right] \left[(V_m)^E (V_n)^F + (V_n)^E (V_m)^F\right]
\end{aligned}
$$

(A.92)

$$
\begin{aligned}
\frac{\partial^2 (V_n)^A}{\partial \kappa_{CD} \partial C_{EF}} &= \frac{k_m}{4\left(k_n - k_m\right)^2} (V_n)^A \left[(V_m)^C (V_n)^D + (V_n)^C (V_m)^D\right] \left[(V_m)^E (V_n)^F + (V_n)^E (V_m)^F\right] \\
&\quad - \frac{k_n}{2\left(k_n - k_m\right)^2} (V_m)^A (V_m)^C (V_m)^D \left[(V_m)^E (V_n)^F + (V_n)^E (V_m)^F\right] \\
&\quad - \frac{k_n}{2\left(k_n - k_m\right)^2} (V_m)^A (V_m)^E (V_m)^F \left[(V_m)^C (V_n)^D + (V_n)^C (V_m)^D\right] \\
&\quad + \frac{k_n + k_m}{4\left(k_n - k_m\right)^2} (V_m)^A (V_n)^E (V_n)^F \left[(V_m)^C (V_n)^D + (V_n)^C (V_m)^D\right] \\
&\quad + \frac{k_m}{2\left(k_n - k_m\right)^2} (V_m)^A (V_n)^C (V_n)^D \left[(V_m)^E (V_n)^F + (V_n)^E (V_m)^F\right]
\end{aligned}
$$

(A.93)

$$
\begin{aligned}
\frac{\partial^2 (V_n)^A}{\partial C_{CD} \partial \kappa_{EF}} &= \frac{k_m}{4\left(k_n - k_m\right)^2} (V_n)^A \left[(V_m)^C (V_n)^D + (V_n)^C (V_m)^D\right] \left[(V_m)^E (V_n)^F + (V_n)^E (V_m)^F\right] \\
&\quad - \frac{k_n}{2\left(k_n - k_m\right)^2} (V_m)^A (V_m)^C (V_m)^D \left[(V_m)^E (V_n)^F + (V_n)^E (V_m)^F\right] \\
&\quad - \frac{k_n}{2\left(k_n - k_m\right)^2} (V_m)^A (V_m)^E (V_m)^F \left[(V_m)^C (V_n)^D + (V_n)^C (V_m)^D\right] \\
&\quad + \frac{k_n + k_m}{4\left(k_n - k_m\right)^2} (V_m)^A (V_n)^C (V_n)^D \left[(V_m)^E (V_n)^F + (V_n)^E (V_m)^F\right] \\
&\quad + \frac{k_m}{2\left(k_n - k_m\right)^2} (V_m)^A (V_n)^E (V_n)^F \left[(V_m)^C (V_n)^D + (V_n)^C (V_m)^D\right]
\end{aligned}
$$

(A.94)

$$
\begin{aligned}
\frac{\partial^2 (V_n)^A}{\partial C_{CD} \partial C_{EF}} &= \frac{3}{4} (V_n)^A (V_n)^C (V_n)^D (V_n)^E (V_n)^F \\
&\quad \frac{k_n^2 - 2k_n k_m}{4\left(k_n - k_m\right)^2} (V_n)^A \left[(V_m)^C (V_n)^D + (V_n)^C (V_m)^D\right] \left[(V_m)^E (V_n)^F + (V_n)^E (V_m)^F\right] \\
&\quad \frac{k_n^2 - 3k_n k_m}{4\left(k_n - k_m\right)^2} (V_m)^A (V_n)^C (V_n)^D \left[(V_m)^E (V_n)^F + (V_n)^E (V_m)^F\right] \\
&\quad \frac{k_n^2 - 3k_n k_m}{4\left(k_n - k_m\right)^2} (V_m)^A (V_n)^E (V_n)^F \left[(V_m)^C (V_n)^D + (V_n)^C (V_m)^D\right] \\
&\quad \frac{k_n^2}{2\left(k_n - k_m\right)^2} (V_m)^A (V_m)^C (V_m)^D \left[(V_m)^E (V_n)^F + (V_n)^E (V_m)^F\right] \\
&\quad \frac{k_n^2}{2\left(k_n - k_m\right)^2} (V_m)^A (V_m)^E (V_m)^F \left[(V_m)^C (V_n)^D + (V_n)^C (V_m)^D\right]
\end{aligned}
$$

(A.95)

The expressions given above allow the evaluation of all first-order and second-order derivatives of a_i and θ_i ($i = 1, 2, 3$) with respect to $\boldsymbol{\eta}$, $\mathbf{C}$ and $\boldsymbol{\mathcal{K}}$.

Approximation of the exponential Cauchy-Born rule: direct curvature approach

The approximation of the exponential Cauchy-Born rule via the direct curvature approach leads to the deformed bond vector $\mathbf{a}$ according to Equation (4.60). With reference to Equation (4.57), the tangent deformed bond vector $\mathbf{w}_i$ is further writeable as a linear combination with respect to the covariant base vectors $\mathbf{g}_\alpha$. This allows to state the components of the deformed bond vector $\mathbf{a}$ in the convected basis $\widetilde{\mathcal{C}} = \{\mathbf{g}_1, \mathbf{g}_2, \mathbf{n}\}$.

$$[\mathbf{a}_i]_{\widetilde{\mathcal{C}}} = \begin{bmatrix} w_i^1 \, \mathcal{S}\left(k_i w_i\right) \\ w_i^2 \, \mathcal{S}\left(k_i w_i\right) \\ \frac{k_i (w_i)^2}{2} \, \mathcal{S}^2\left(\frac{k_i w_i}{2}\right) \end{bmatrix} \tag{A.96}$$

As the basis $\widetilde{\mathcal{C}}$ is not orthonormal, the covariant components of the metric tensor are involved in the calculation of quantities that are based on the scalar product of vectors. Considering this fact, the length of the deformed bond vector a_i is given as:

$$a_i = \left[(a_i)^\alpha \, g_{\alpha\beta} \, (a_i)^\beta + (a_i)^3 \, (a_i)^3\right]^{1/2} \tag{A.97}$$

For a simpler notation, an extended metric tensor

$$g_{\mathfrak{ab}} = \begin{bmatrix} g_{11} & g_{12} & 0 \\ g_{21} & g_{22} & 0 \\ 0 & 0 & 1 \end{bmatrix} \tag{A.98}$$

is introduced, allowing to write the bond length a_i in a compact form.

$$a_i = \left[(a_i)^{\mathfrak{a}} \, g_{\mathfrak{ab}} \, (a_i)^{\mathfrak{b}}\right]^{1/2} \tag{A.99}$$

Consequently, $(a_i)^{\mathfrak{a}}$ denotes the $\mathfrak{a}$-th component of the observed vector in the convected basis $\widetilde{\mathcal{C}} = \{\mathbf{g}_1, \mathbf{g}_2, \mathbf{n}\}$ and summation on this index and the index $\mathfrak{b}$ in the range from 1 to 3 is implied. Moreover, as a reminder, $(a_i)^\alpha$ specifies the α-th component of the observed vector in the convected basis of the tangent space $\mathcal{C} = \{\mathbf{g}_1, \mathbf{g}_2\}$ and summation on this index and the index β, running from 1 to 2, is implied.

Using the scalar product, the deformed valence angle θ_i between two deformed lattice vectors $\mathbf{a}_j$ and $\mathbf{a}_k$ with $\{i, j, k\}$ being an even permutation of $\{1, 2, 3\}$ is calculated as:

$$\cos\left(\theta_i\right) = \frac{1}{a_j a_k}\left[(a_j)^\alpha \, g_{\alpha\beta} \, (a_k)^\beta + (a_j)^3 \, (a_k)^3\right] = \frac{(a_j)^{\mathfrak{a}} \, g_{\mathfrak{ab}} \, (a_k)^{\mathfrak{b}}}{a_j a_k} \tag{A.100}$$

$$\theta_i = \arccos\left[\frac{(a_j)^{\mathfrak{a}} \, g_{\mathfrak{ab}} \, (a_k)^{\mathfrak{b}}}{a_j a_k}\right] \tag{A.101}$$

In the calculation of the first-order and second-order derivatives of the bond length and the valence angles with respect to the inner displacements $\boldsymbol{\eta}$, the spatial metric tensor $\mathbf{g}$ and the spatial curvature tensor $\mathbf{k}$ these measures are symbolised by ( ) and [ ]. The related first-order and second-

order derivatives of the bond length a_i follow from Equation (A.99) as:

$$\frac{\partial a_i}{\partial\,(\,)} \;=\; \frac{1}{2a_i}\left[\frac{\partial\,(a_i)^{\mathfrak{a}}}{\partial\,(\,)}\,g_{\mathfrak{ab}}\,(a_i)^{\mathfrak{b}} + (a_i)^{\mathfrak{a}}\,g_{\mathfrak{ab}}\,\frac{\partial\,(a_i)^{\mathfrak{b}}}{\partial\,(\,)}\right] + \frac{1}{2a_i}\left[(a_i)^{\alpha}\,\frac{\partial g_{\alpha\beta}}{\partial\,(\,)}\,(a_i)^{\beta}\right] \tag{A.102}$$

$$\frac{\partial^2 a_i}{\partial\,(\,)\,\partial\,[\,]} \;=\; -\frac{1}{a_i}\frac{\partial a_i}{\partial\,(\,)}\otimes\frac{\partial a_i}{\partial\,[\,]}$$
$$+\frac{g_{\mathfrak{ab}}}{2a_i}\left[\frac{\partial^2\,(a_i)^{\mathfrak{a}}}{\partial\,(\,)\,\partial\,[\,]}\,(a_i)^{\mathfrak{b}} + (a_i)^{\mathfrak{a}}\,\frac{\partial^2\,(a_i)^{\mathfrak{b}}}{\partial\,(\,)\,\partial\,[\,]} + \frac{\partial\,(a_i)^{\mathfrak{a}}}{\partial\,(\,)}\otimes\frac{\partial\,(a_i)^{\mathfrak{b}}}{\partial\,[\,]} + \frac{\partial\,(a_i)^{\mathfrak{b}}}{\partial\,(\,)}\otimes\frac{\partial\,(a_i)^{\mathfrak{a}}}{\partial\,[\,]}\right]$$
$$+\frac{1}{2a_i}\left[\frac{\partial\,(a_i)^{\alpha}}{\partial\,(\,)}\otimes\frac{\partial g_{\alpha\beta}}{\partial\,[\,]}\,(a_i)^{\beta} + \frac{\partial g_{\alpha\beta}}{\partial\,(\,)}\otimes\frac{\partial\,(a_i)^{\alpha}}{\partial\,[\,]}\,(a_i)^{\beta}\right]$$
$$+\frac{1}{2a_i}\left[(a_i)^{\alpha}\,\frac{\partial\,(a_i)^{\beta}}{\partial\,(\,)}\otimes\frac{\partial g_{\alpha\beta}}{\partial\,[\,]} + (a_i)^{\alpha}\,\frac{\partial g_{\alpha\beta}}{\partial\,(\,)}\otimes\frac{\partial\,(a_i)^{\beta}}{\partial\,[\,]}\right] \tag{A.103}$$

The corresponding derivatives for the valence angle θ_i, resulting from Equation (A.100), are:

$$\frac{\partial\theta_i}{\partial\,(\,)} \;=\; -\frac{1}{\sin\,(\theta_i)}\frac{\partial\cos\,(\theta_i)}{\partial\,(\,)} \tag{A.104}$$

$$\frac{\partial^2\theta_i}{\partial\,(\,)\,\partial\,[\,]} \;=\; -\frac{1}{\sin\,(\theta_i)}\left[\cos\,(\theta_i)\,\frac{\partial\theta_i}{\partial\,(\,)}\otimes\frac{\partial\theta_i}{\partial\,[\,]} + \frac{\partial^2\cos\,(\theta_i)}{\partial\,(\,)\,\partial\,[\,]}\right] \tag{A.105}$$

Furthermore, the necessary derivatives of the cosine of the valence angle are given by:

$$\frac{\partial\cos\,(\theta_i)}{\partial\,(\,)} \;=\; -\frac{\cos\,(\theta_i)}{a_j a_k}\left[\frac{\partial a_j}{\partial\,(\,)}a_k + a_j\frac{\partial a_k}{\partial\,(\,)}\right]$$
$$+\frac{1}{a_j a_k}\left[g_{\mathfrak{ab}}\left(\frac{\partial\,(a_j)^{\mathfrak{a}}}{\partial\,(\,)}\,(a_k)^{\mathfrak{b}} + (a_j)^{\mathfrak{a}}\,\frac{\partial\,(a_k)^{\mathfrak{b}}}{\partial\,(\,)}\right) + (a_j)^{\alpha}\,\frac{\partial g_{\alpha\beta}}{\partial\,(\,)}\,(a_k)^{\beta}\right] \tag{A.106}$$

$$\frac{\partial^2\cos\,(\theta_i)}{\partial\,(\,)\,\partial\,[\,]} \;=\; \frac{\sin\,(\theta_i)}{a_j a_k}\left[\frac{\partial\theta_i}{\partial\,(\,)}\otimes\left(\frac{\partial a_j}{\partial\,[\,]}a_k + a_j\frac{\partial a_k}{\partial\,[\,]}\right) + \left(\frac{\partial a_j}{\partial\,(\,)}a_k + a_j\frac{\partial a_k}{\partial\,(\,)}\right)\otimes\frac{\partial\theta_i}{\partial\,[\,]}\right]$$
$$-\frac{\cos\theta_i}{a_j a_k}\left[\frac{\partial^2 a_j}{\partial\,(\,)\,\partial\,[\,]}a_k + \frac{\partial a_j}{\partial\,(\,)}\otimes\frac{\partial a_k}{\partial\,[\,]} + \frac{\partial a_k}{\partial\,(\,)}\otimes\frac{\partial a_j}{\partial\,[\,]} + a_j\frac{\partial^2 a_k}{\partial\,(\,)\,\partial\,[\,]}\right]$$
$$+\frac{g_{\mathfrak{ab}}}{a_j a_k}\left[\frac{\partial^2\,(a_j)^{\mathfrak{a}}}{\partial\,(\,)\,\partial\,[\,]}\,(a_k)^{\mathfrak{b}} + \frac{\partial\,(a_j)^{\mathfrak{a}}}{\partial\,(\,)}\otimes\frac{\partial\,(a_k)^{\mathfrak{b}}}{\partial\,[\,]} + \frac{\partial\,(a_k)^{\mathfrak{b}}}{\partial\,(\,)}\otimes\frac{\partial\,(a_j)^{\mathfrak{a}}}{\partial\,[\,]} + (a_j)^{\mathfrak{a}}\,\frac{\partial^2\,(a_k)^{\mathfrak{b}}}{\partial\,(\,)\,\partial\,[\,]}\right]$$
$$+\frac{1}{a_j a_k}\left[\frac{\partial\,(a_j)^{\alpha}}{\partial\,(\,)}\otimes\frac{\partial g_{\alpha\beta}}{\partial\,[\,]}\,(a_k)^{\beta} + \frac{\partial g_{\alpha\beta}}{\partial\,(\,)}\otimes\frac{\partial\,(a_j)^{\alpha}}{\partial\,[\,]}\,(a_k)^{\beta}\right]$$
$$+\frac{1}{a_j a_k}\left[(a_j)^{\alpha}\,\frac{\partial\,(a_k)^{\beta}}{\partial\,(\,)}\otimes\frac{\partial g_{\alpha\beta}}{\partial\,[\,]} + (a_j)^{\alpha}\,\frac{\partial g_{\alpha\beta}}{\partial\,(\,)}\otimes\frac{\partial\,(a_k)^{\beta}}{\partial\,[\,]}\right] \tag{A.107}$$

The evaluation of the expressions given above requires the first-order and second-order derivatives of the deformed bond vector components $(a_i)^{\mathfrak{a}}$ with respect to the inner displacements and the strain measures. These independent quantities are symbolised either by ( ) or [ ]. The first and the second component are related to the covariant base vectors and, therefore, they can be handled together. Introducing the abbreviation $\mathcal{S}_i = \mathcal{S}\,(k_i w_i)$, the components themselves and their derivatives are

given as:

$$(a_i)^\alpha = w_i^\alpha \mathcal{S}_i \tag{A.108}$$

$$\frac{\partial (a_i)^\alpha}{\partial ()} = \frac{\partial w_i^\alpha}{\partial ()} \mathcal{S}_i + w_i^\alpha \mathcal{S}_i' \left(\frac{\partial k_i}{\partial ()} w_i + k_i \frac{\partial w_i}{\partial ()} \right) \tag{A.109}$$

$$\begin{aligned}
\frac{\partial^2 (a_i)^\alpha}{\partial () \partial [\,]} = {} & \frac{\partial^2 w_i^\alpha}{\partial () \partial [\,]} \mathcal{S}_i + \frac{\partial w_i^\alpha}{\partial ()} \otimes \mathcal{S}_i' \left(\frac{\partial k_i}{\partial [\,]} w_i + k_i \frac{\partial w_i}{\partial [\,]} \right) + \mathcal{S}_i' \left(\frac{\partial k_i}{\partial ()} w_i + k_i \frac{\partial w_i}{\partial ()} \right) \otimes \frac{\partial w_i^\alpha}{\partial [\,]} \\
& + w_i^\alpha \mathcal{S}_i'' \left(\frac{\partial k_i}{\partial ()} w_i + k_i \frac{\partial w_i}{\partial ()} \right) \otimes \left(\frac{\partial k_i}{\partial [\,]} w_i + k_i \frac{\partial w_i}{\partial [\,]} \right) \\
& + w_i^\alpha \mathcal{S}_i' \left(\frac{\partial^2 k_i}{\partial () \partial [\,]} w_i + \frac{\partial k_i}{\partial ()} \otimes \frac{\partial w_i}{\partial [\,]} + \frac{\partial w_i}{\partial ()} \otimes \frac{\partial k_i}{\partial [\,]} + k_i \frac{\partial^2 w_i}{\partial () \partial [\,]} \right) \tag{A.110}
\end{aligned}$$

The necessary derivatives of the third component, which is coupled to the unit normal, use the short form $\mathcal{S}_{i/2} = \mathcal{S}\left(\frac{k_i w_i}{2} \right)$, and are specified as:

$$(a_i)^3 = \frac{k_i (w_i)^2}{2} \mathcal{S}_{i/2}^2 \tag{A.111}$$

$$\frac{\partial (a_i)^3}{\partial ()} = \left(\frac{\partial k_i}{\partial ()} \frac{w_i}{2} + k_i \frac{\partial w_i}{\partial ()} \right) w_i \mathcal{S}_{i/2}^2 + \frac{k_i (w_i)^2}{2} \mathcal{S}_{i/2} \mathcal{S}_{i/2}' \left(\frac{\partial k_i}{\partial ()} w_i + k_i \frac{\partial w_i}{\partial ()} \right) \tag{A.112}$$

$$\begin{aligned}
\frac{\partial^2 (a_i)^3}{\partial () \partial [\,]} = {} & w_i \mathcal{S}_{i/2}^2 \left[\frac{\partial^2 k_i}{\partial () \partial [\,]} \frac{w_i}{2} + \frac{\partial k_i}{\partial ()} \otimes \frac{\partial w_i}{\partial [\,]} + \frac{\partial w_i}{\partial ()} \otimes \frac{\partial k_i}{\partial [\,]} + k_i \frac{\partial^2 w_i}{\partial () \partial [\,]} \right] + k_i \mathcal{S}_{i/2}^2 \frac{\partial w_i}{\partial ()} \otimes \frac{\partial w_i}{\partial [\,]} \\
& + w_i \mathcal{S}_{i/2} \mathcal{S}_{i/2}' \left[\left(\frac{\partial k_i}{\partial ()} \frac{w_i}{2} + k_i \frac{\partial w_i}{\partial ()} \right) \otimes \left(\frac{\partial k_i}{\partial [\,]} w_i + k_i \frac{\partial w_i}{\partial [\,]} \right) \right] \\
& + w_i \mathcal{S}_{i/2} \mathcal{S}_{i/2}' \left[\left(\frac{\partial k_i}{\partial ()} w_i + k_i \frac{\partial w_i}{\partial ()} \right) \otimes \left(\frac{\partial k_i}{\partial [\,]} \frac{w_i}{2} + k_i \frac{\partial w_i}{\partial [\,]} \right) \right] \\
& + \frac{k_i (w_i)^2}{4} \left(\mathcal{S}_{i/2}' \mathcal{S}_{i/2}' + \mathcal{S}_{i/2} \mathcal{S}_{i/2}'' \right) \left(\frac{\partial k_i}{\partial ()} w_i + k_i \frac{\partial w_i}{\partial ()} \right) \otimes \left(\frac{\partial k_i}{\partial [\,]} w_i + k_i \frac{\partial w_i}{\partial [\,]} \right) \\
& + \frac{k_i (w_i)^2}{2} \mathcal{S}_{i/2} \mathcal{S}_{i/2}' \left(\frac{\partial^2 k_i}{\partial () \partial [\,]} w_i + \frac{\partial k_i}{\partial ()} \otimes \frac{\partial w_i}{\partial [\,]} + \frac{\partial w_i}{\partial ()} \otimes \frac{\partial k_i}{\partial [\,]} + k_i \frac{\partial^2 w_i}{\partial () \partial [\,]} \right) \tag{A.113}
\end{aligned}$$

The length w_i of the tangent deformed bond vector is analysed in the following. Using Equation (4.58), this length is given as:

$$w_i = \left(w_i^\alpha g_{\alpha\beta} w_i^\beta \right)^{1/2} \tag{A.114}$$

Then, the first-order and second-order derivatives are:

$$\frac{\partial w_i}{\partial ()} = \frac{1}{2w_i} \left[\frac{\partial w_i^\alpha}{\partial ()} g_{\alpha\beta} w_i^\beta + w_i^\alpha \frac{\partial g_{\alpha\beta}}{\partial ()} w_i^\beta + w_i^\alpha g_{\alpha\beta} \frac{\partial w_i^\beta}{\partial ()} \right] \tag{A.115}$$

$$\begin{aligned}
\frac{\partial^2 w_i}{\partial () \partial [\,]} = {} & -\frac{1}{w_i} \frac{\partial w_i}{\partial ()} \otimes \frac{\partial w_i}{\partial [\,]} + \frac{1}{2w_i} \left[g_{\alpha\beta} \frac{\partial w_i^\beta}{\partial ()} \otimes \frac{\partial w_i^\alpha}{\partial [\,]} + g_{\alpha\beta} \frac{\partial w_i^\alpha}{\partial ()} \otimes \frac{\partial w_i^\beta}{\partial [\,]} \right] \\
& + \frac{1}{2w_i} \left[\frac{\partial w_i^\alpha}{\partial ()} \otimes \frac{\partial g_{\alpha\beta}}{\partial [\,]} w_i^\beta + \frac{\partial g_{\alpha\beta}}{\partial ()} \otimes \frac{\partial w_i^\alpha}{\partial [\,]} w_i^\beta + w_i^\alpha \frac{\partial g_{\alpha\beta}}{\partial ()} \otimes \frac{\partial w_i^\beta}{\partial [\,]} + w_i^\alpha \frac{\partial w_i^\beta}{\partial ()} \otimes \frac{\partial g_{\alpha\beta}}{\partial [\,]} \right] \tag{A.116}
\end{aligned}$$

The normal curvatures k_i of the deformed surface, corresponding to the various tangent deformed bond vectors, is obtained using Equation (4.59).

$$k_i = \frac{w_i^\alpha k_{\alpha\beta} w_i^\beta}{w_i^\alpha g_{\alpha\beta} w_i^\beta} = \frac{w_i^\alpha k_{\alpha\beta} w_i^\beta}{(w_i)^2} \tag{A.117}$$

Based on this expression, the first-order and second-order derivatives are:

$$\frac{\partial k_i}{\partial\,(\,)} = \frac{1}{(w_i)^2}\left[\frac{\partial w_i^\alpha}{\partial\,(\,)}k_{\alpha\beta}w_i^\beta + w_i^\alpha\frac{\partial k_{\alpha\beta}}{\partial\,(\,)}w_i^\beta + w_i^\alpha k_{\alpha\beta}\frac{\partial w_i^\beta}{\partial\,(\,)}\right] - 2\frac{k_i}{w_i}\frac{\partial w_i}{\partial\,(\,)} \tag{A.118}$$

$$
\begin{aligned}
\frac{\partial^2 k_i}{\partial(\,)\partial[\,]} ={}& -\frac{2}{w_i}\left[\frac{\partial k_i}{\partial\,(\,)}\otimes\frac{\partial w_i}{\partial\,[\,]} + \frac{\partial w_i}{\partial\,(\,)}\otimes\frac{\partial k_i}{\partial\,[\,]}\right] - 2\frac{k_i}{w_i}\frac{\partial^2 w_i}{\partial(\,)\partial[\,]} - 2\frac{k_i}{(w_i)^2}\frac{\partial w_i}{\partial\,(\,)}\otimes\frac{\partial w_i}{\partial\,[\,]} \\
&+ \frac{1}{(w_i)^2}\left[\frac{\partial w_i^\alpha}{\partial\,(\,)}\otimes\frac{\partial k_{\alpha\beta}}{\partial\,[\,]}w_i^\beta + \frac{\partial k_{\alpha\beta}}{\partial\,(\,)}\otimes\frac{\partial w_i^\alpha}{\partial\,[\,]}w_i^\beta + w_i^\alpha\frac{\partial k_{\alpha\beta}}{\partial\,(\,)}\otimes\frac{\partial w_i^\beta}{\partial\,[\,]} + w_i^\alpha\frac{\partial w_i^\beta}{\partial\,(\,)}\otimes\frac{\partial k_{\alpha\beta}}{\partial\,[\,]}\right] \\
&+ \frac{1}{(w_i)^2}\left[k_{\alpha\beta}\frac{\partial w_i^\beta}{\partial\,(\,)}\otimes\frac{\partial w_i^\alpha}{\partial\,[\,]} + k_{\alpha\beta}\frac{\partial w_i^\alpha}{\partial\,(\,)}\otimes\frac{\partial w_i^\beta}{\partial\,[\,]}\right]
\end{aligned}
\tag{A.119}
$$

Finally, the various derivatives of w_i^α and $g_{\alpha\beta}$ as well as $k_{\alpha\beta}$ with respect to the inner displacements and the strain measures are essential.

Taking into account Equation (4.57) in combination with Equation (4.64), the components of the tangent deformed bond vector in the convected basis of the tangent space $\mathcal{C}$ are given as:

$$w_i^\alpha = \left(A_{0i}^A + \eta^A\right)G^\alpha{}_A \tag{A.120}$$

Therefrom, the only nonzero derivative is that with respect to the inner displacements.

$$\frac{\partial w_i^\alpha}{\partial\boldsymbol{\eta}} = G^\alpha{}_A \mathbf{E}^A = \mathbf{G}^\alpha \tag{A.121}$$

The derivatives of the covariant components of the spatial metric tensor and the spatial curvature tensor are only nonzero if they are derived by the corresponding specifying tensor.

$$\frac{\partial g_{\alpha\beta}}{\partial\mathbf{g}} = \mathbf{g}_\alpha \otimes \mathbf{g}_\beta \tag{A.122}$$

$$\frac{\partial k_{\alpha\beta}}{\partial\mathbf{k}} = \mathbf{g}_\alpha \otimes \mathbf{g}_\beta \tag{A.123}$$

With the help of the formulae given on top of that, all first-order and second-order derivatives of a_i and θ_i ($i = 1, 2, 3$) with respect to $\boldsymbol{\eta}$, $\mathbf{g}$ and $\mathbf{k}$ can be calculated.

A.2 First-order and second-order derivatives of the strain energy double density with respect to the distance between two distinct points of the continuum

This Appendix provides the first-order and second-order derivatives of the strain energy double density for modelling non-bonded interactions with respect to the distance between two distinct points of the continuum. These derivatives are essential for the specification of the global equilibrium for the mixed atomistic-continuum model. With reference to Subsection 4.5.4, the strain energy double density W_{nb} depends on the distance d between two distinct points of the continuum surface, which in turn is a function of the spatial position vectors of the involved points. The strain energy double density for an individual non-bonded interaction is given as:

$$W_{\mathrm{nb}} = V_{\mathrm{nb}}\left(d\right) \frac{2}{S_0} \frac{2}{S_0} \tag{A.124}$$

Thereof, the first-order and second-order derivatives with respect to the scalar distance d of two points on the deformed surface can be calculated in a straightforward manner.

$$\frac{\partial W_{\mathrm{nb}}}{\partial d} = V_{\mathrm{nb}}'\left(d\right) \frac{2}{S_0} \frac{2}{S_0} \tag{A.125}$$

$$\frac{\partial^2 W_{\mathrm{nb}}}{\partial d \partial d} = V_{\mathrm{nb}}''\left(d\right) \frac{2}{S_0} \frac{2}{S_0} \tag{A.126}$$

The first-order and second-order derivatives of the interatomic pair-potential V_{nb} for the non-bonded interactions are defined in Subsection 2.4.1 and, consequently, these terms can be applied for the evaluation of the expressions given above.

A.3 Variations of the strain measures and their increments

In this Appendix, the variations of the strain measures as well as their increments are specified for the continuous setting. Moreover, the related terms for the discrete setting are provided. These quantities are required for the specification of the global equilibrium that is defined in Section 4.6 for the continuous setting and in Subsection 4.8.2 for the discrete setting.

A.3.1 Continuous setting

The specification of the global equilibrium in Section 4.6 requires the variations of the appropriate strain measures as well as their increments. In addition, the Newton-Raphson procedure is in need of the increments of the variated strain measures as well. These important quantities are supplied within this section. Because the undeformed configuration is fixed, the virtual displacements solely influence the deformed configuration. As a consequence, the variations of the strain measures have to be expressed by the variations $\delta\mathbf{x}$ of the deformed configuration only. The same statement holds for the displacement increments so that the increments of the deformed configuration $\Delta\mathbf{x}$ are considered, exclusively. To call up, for the principal curvatures approach the strain measures are $\mathbf{C}$ and $\mathcal{K}$ whereas for the direct curvature approach the strain measures are $\mathbf{g}$ and $\mathbf{k}$. Using the fact that $\mathbf{C}$ is obtained as the pull-back of $\mathbf{g}$ and alike that the pull-back of $\mathbf{k}$ delivers $\mathcal{K}$, the derivation is started with the covariant base vectors. Recalling Equation (4.14), the variations of the convected basis vectors $\mathbf{g}_\alpha$ read:

$$\delta\mathbf{g}_\alpha = \frac{\partial \delta\mathbf{x}}{\partial \xi^\alpha} \qquad \alpha = 1, 2 \tag{A.127}$$

A Supplementary notes on the mixed atomistic-continuum model

The increments of the covariant base vectors are calculated similar to their variations and are, thus, given by:

$$\Delta \mathbf{g}_\alpha = \frac{\partial \Delta \mathbf{x}}{\partial \xi^\alpha} \qquad \alpha = 1, 2 \tag{A.128}$$

Combined with Equation (4.20), the variation of the covariant components $g_{\alpha\beta} = \mathbf{g}_\alpha \cdot \mathbf{g}_\beta$ of the spatial metric tensor follows as:

$$\delta g_{\alpha\beta} = \delta \mathbf{g}_\alpha \cdot \mathbf{g}_\beta + \mathbf{g}_\alpha \cdot \delta \mathbf{g}_\beta \tag{A.129}$$

Then, the variations of the right Cauchy-Green deformation tensor components C_{AB}, given according to Equation (4.25), are obtained as:

$$\delta C_{AB} = \delta g_{\alpha\beta} \frac{\partial \xi^\alpha}{\partial X^A} \frac{\partial \xi^\beta}{\partial X^B} \tag{A.130}$$

In the same fashion, the increments of the covariant components of the spatial metric tensor are:

$$\Delta g_{\alpha\beta} = \Delta \mathbf{g}_\alpha \cdot \mathbf{g}_\beta + \mathbf{g}_\alpha \cdot \Delta \mathbf{g}_\beta \tag{A.131}$$

Subsequently, the increments of the right Cauchy-Green deformation tensor components read:

$$\Delta C_{AB} = \Delta g_{\alpha\beta} \frac{\partial \xi^\alpha}{\partial X^A} \frac{\partial \xi^\beta}{\partial X^B} \tag{A.132}$$

The variation of the spatial curvature tensor, specifically of its covariant components $k_{\alpha\beta} = \mathbf{n} \cdot \mathbf{g}_{\alpha,\beta}$, requires the variations of the unit normal $\mathbf{n}$ and of the derived covariant base vectors $\mathbf{g}_{\alpha,\beta}$. The variation of the unit normal reads:

$$\delta \mathbf{n} = \frac{1}{\|\mathbf{g}_1 \times \mathbf{g}_2\|} \left[\delta \mathbf{g}_1 \times \mathbf{g}_2 + \mathbf{g}_1 \times \delta \mathbf{g}_2 - \delta \|\mathbf{g}_1 \times \mathbf{g}_2\| \mathbf{n} \right] \tag{A.133}$$

where

$$\delta \|\mathbf{g}_1 \times \mathbf{g}_2\| = \mathbf{n} \cdot \left[\delta \mathbf{g}_1 \times \mathbf{g}_2 + \mathbf{g}_1 \times \delta \mathbf{g}_2 \right] \tag{A.134}$$

The variations of the derived covariant base vectors $\mathbf{g}_{\alpha,\beta}$ are given by:

$$\delta \mathbf{g}_{\alpha,\beta} = \frac{\partial^2 \delta \mathbf{x}}{\partial \xi^\alpha \partial \xi^\beta} \tag{A.135}$$

Applying these expressions, the variations of the covariant components of the spatial curvature tensor follow as:

$$\delta k_{\alpha\beta} = \delta \mathbf{n} \cdot \mathbf{g}_{\alpha,\beta} + \mathbf{n} \cdot \delta \mathbf{g}_{\alpha,\beta} \tag{A.136}$$

Then, the variations of the pull-back of the spatial curvature tensor components, denoted as $\mathcal{K}_{AB}$, and given in Equation (4.26), are obtained as:

$$\delta \mathcal{K}_{AB} = \delta k_{\alpha\beta} \frac{\partial \xi^\alpha}{\partial X^A} \frac{\partial \xi^\beta}{\partial X^B} \tag{A.137}$$

Once more, an identical process delivers the appropriate increments

$$\Delta k_{\alpha\beta} = \Delta \mathbf{n} \cdot \mathbf{g}_{\alpha,\beta} + \mathbf{n} \cdot \Delta \mathbf{g}_{\alpha,\beta} \quad \text{with} \quad \Delta \mathbf{g}_{\alpha,\beta} = \frac{\partial^2 \Delta \mathbf{x}}{\partial \xi^\alpha \partial \xi^\beta} \tag{A.138}$$

of the spatial curvature tensor and, subsequently, the increments

$$\Delta\mathcal{K}_{AB} = \Delta k_{\alpha\beta}\frac{\partial\xi^{\alpha}}{\partial X^A}\frac{\partial\xi^{\beta}}{\partial X^B} \tag{A.139}$$

of its related pull-back. Herein, the increments of the unit normal are given by

$$\Delta\mathbf{n} = \frac{1}{\|\mathbf{g}_1\times\mathbf{g}_2\|}\left[\Delta\mathbf{g}_1\times\mathbf{g}_2 + \mathbf{g}_1\times\Delta\mathbf{g}_2 - \Delta\|\mathbf{g}_1\times\mathbf{g}_2\|\mathbf{n}\right] \tag{A.140}$$

where

$$\Delta\|\mathbf{g}_1\times\mathbf{g}_2\| = \mathbf{n}\cdot[\Delta\mathbf{g}_1\times\mathbf{g}_2 + \mathbf{g}_1\times\Delta\mathbf{g}_2] \tag{A.141}$$

In the next steps, the increments of the variated strain measures are calculated. Based on Equation (A.129), the increments of the variated covariant metric tensor components are:

$$\Delta\delta g_{\alpha\beta} = \delta\mathbf{g}_{\alpha}\cdot\Delta\mathbf{g}_{\beta} + \Delta\mathbf{g}_{\alpha}\cdot\delta\mathbf{g}_{\beta} \tag{A.142}$$

This allows to state the increments of the variated right Cauchy-Green deformation tensor components as:

$$\Delta\delta C_{AB} = \Delta\delta g_{\alpha\beta}\frac{\partial\xi^{\alpha}}{\partial X^A}\frac{\partial\xi^{\beta}}{\partial X^B} \tag{A.143}$$

The increments of the variated spatial curvature tensor components result from Equation (A.136).

$$\Delta\delta k_{\alpha\beta} = \Delta\delta\mathbf{n}\cdot\mathbf{g}_{\alpha,\beta} + \delta\mathbf{n}\cdot\Delta\mathbf{g}_{\alpha,\beta} + \Delta\mathbf{n}\cdot\delta\mathbf{g}_{\alpha,\beta} \tag{A.144}$$

The further pull-back delivers the increments of the variation in the undeformed configuration as:

$$\Delta\delta\mathcal{K}_{AB} = \Delta\delta k_{\alpha\beta}\frac{\partial\xi^{\alpha}}{\partial X^A}\frac{\partial\xi^{\beta}}{\partial X^B} \tag{A.145}$$

To complete this derivation, the increments of the variated unit normal are:

$$\begin{aligned}\Delta\delta\mathbf{n} = &\frac{1}{\|\mathbf{g}_1\times\mathbf{g}_2\|}\left[\delta\mathbf{g}_1\times\Delta\mathbf{g}_2 + \Delta\mathbf{g}_1\times\delta\mathbf{g}_2\right]\\ &-\frac{1}{\|\mathbf{g}_1\times\mathbf{g}_2\|}\left[\delta\|\mathbf{g}_1\times\mathbf{g}_2\|\Delta\mathbf{n} + \Delta\|\mathbf{g}_1\times\mathbf{g}_2\|\delta\mathbf{n} + \Delta\delta\|\mathbf{g}_1\times\mathbf{g}_2\|\mathbf{n}\right]\end{aligned} \tag{A.146}$$

where

$$\Delta\delta\|\mathbf{g}_1\times\mathbf{g}_2\| = \Delta\mathbf{n}\cdot[\delta\mathbf{g}_1\times\mathbf{g}_2 + \mathbf{g}_1\times\delta\mathbf{g}_2] + \mathbf{n}\cdot[\delta\mathbf{g}_1\times\Delta\mathbf{g}_2 + \Delta\mathbf{g}_1\times\delta\mathbf{g}_2] \tag{A.147}$$

To sum up, this part of the Appendix provides the necessary variations of the strain measures and their increments for the continuous setting. These quantities are important for the definition of the global equilibrium. The related terms for the discrete setup after discretisation via finite elements are given in the upcoming segment.

A.3.2 Discrete setting

The preparation of the element force vector and the element stiffness matrix due to bonded interactions in Subsection 4.8.2 requires the first-order and second-order derivatives of the strain measures with respect to the actual displacement vector components. These quantities are the analogies of the variations and increments as well as the incremental variations of the strain measures in the continuous setting as given in Subappendix A.3.1 immediately before that. In the specification of the essential derivatives, index notation is used and the conventions given in

Subsection 4.3.2 are used. According to Equation (4.113), the discrete form of the covariant base vectors on the deformed surface are given in component representation as:

$$(g_\alpha)^c = (N_K)_{,\alpha} (x_K)^c \tag{A.148}$$

In the course of this, summation on the local node index K is carried out. Then, the requested derivatives of the covariant base vectors with respect to the actual displacement vector components $(x_I)^a$ and $(x_J)^b$ follow directly as:

$$\frac{\partial (g_\alpha)^c}{\partial (x_I)^a} = (N_I)_{,\alpha} \, \delta_a^c \tag{A.149}$$

$$\frac{\partial^2 (g_\alpha)^c}{\partial (x_I)^a \partial (x_J)^b} = 0 \tag{A.150}$$

Using these terms and, additionally, recalling Equation (4.20) the derivatives of the covariant spatial metric tensor components $g_{\alpha\beta} = \mathbf{g}_\alpha \cdot \mathbf{g}_\beta = (g_\alpha)^c (g_\beta)^c$ are given by:

$$\frac{\partial g_{\alpha\beta}}{\partial (x_I)^a} = (N_I)_{,\alpha} (g_\beta)^a + (g_\alpha)^a (N_I)_{,\beta} \tag{A.151}$$

$$\frac{\partial^2 g_{\alpha\beta}}{\partial (x_I)^a \partial (x_J)^b} = \left[(N_I)_{,\alpha} (N_J)_{,\beta} + (N_J)_{,\alpha} (N_I)_{,\beta} \right] \delta_{ab} \tag{A.152}$$

Then, the corresponding derivatives of the right Cauchy-Green deformation tensor components C_{AB}, which is specified in Equation (4.25), are obtained via pull-back of the related spatial metric tensor terms. For this reason, the inverse of the discrete initial Jacobian tensor is necessary, which is obtained either from Equation (4.114) or directly from the component representation given in Equation (4.115).

$$\frac{\partial C_{AB}}{\partial (x_I)^a} = \frac{\partial g_{\alpha\beta}}{\partial (x_I)^a} (J^{-1})^\alpha{}_A (J^{-1})^\beta{}_B \tag{A.153}$$

$$\frac{\partial^2 C_{AB}}{\partial (x_I)^a \partial (x_J)^b} = \frac{\partial^2 g_{\alpha\beta}}{\partial (x_I)^a \partial (x_J)^b} (J^{-1})^\alpha{}_A (J^{-1})^\beta{}_B \tag{A.154}$$

For the curvature properties, the discrete form of the covariant base vector derivatives, given in Equation (4.117), is represented in components as:

$$(g_{\alpha,\beta})^c = (N_K)_{,\alpha\beta} (x_K)^c \tag{A.155}$$

with the local node number K acting as summation index. Then, the corresponding first-order and second-order derivatives with respect to the actual displacement vector components $(x_I)^a$ and $(x_J)^b$ are:

$$\frac{\partial (g_{\alpha,\beta})^c}{\partial (x_I)^a} = (N_I)_{,\alpha\beta} \, \delta_a^c \tag{A.156}$$

$$\frac{\partial^2 (g_{\alpha,\beta})^c}{\partial (x_I)^a \partial (x_J)^b} = 0 \tag{A.157}$$

The covariant spatial curvature tensor components $k_{\alpha\beta} = \mathbf{n} \cdot \mathbf{g}_{\alpha,\beta} = (n)^c (g_{\alpha,\beta})^c$ are defined with respect to Equation (4.21). Based on this definition, the essential derivatives are characterised by:

$$\frac{\partial k_{\alpha\beta}}{\partial (x_I)^a} = \frac{\partial (n)^c}{\partial (x_I)^a} (g_{\alpha,\beta})^c + (n)^a (N_I)_{,\alpha\beta} \tag{A.158}$$

$$\frac{\partial^2 k_{\alpha\beta}}{\partial (x_I)^a \partial (x_J)^b} = \frac{\partial^2 (n)^c}{\partial (x_I)^a \partial (x_J)^b} (g_{\alpha,\beta})^c + \frac{\partial (n)^b}{\partial (x_I)^a} (N_J)_{,\alpha\beta} + \frac{\partial (n)^a}{\partial (x_J)^b} (N_I)_{,\alpha\beta} \tag{A.159}$$

For their evaluation, the derivatives of the unit normal are needed. Following Equation (4.15), and considering the permutation tensor $\varepsilon^c{}_{de}$, the components of the unit normal vector are defined as:

$$(n)^c = \frac{\varepsilon^c{}_{de}\,(g_1)^d\,(g_2)^e}{\|\mathbf{g}_1 \times \mathbf{g}_2\|} \tag{A.160}$$

On the basis of this notation, the first-order and second-order derivatives of the unit normal vector components with respect to the actual displacement vector components $(x_I)^a$ and $(x_J)^b$ are:

$$\frac{\partial (n)^c}{\partial (x_I)^a} = \frac{1}{\|\mathbf{g}_1 \times \mathbf{g}_2\|} \left[\varepsilon^c{}_{de} \left((N_I)_{,1}\,\delta_a^d\,(g_2)^e + (g_1)^d\,(N_I)_{,2}\,\delta_a^e \right) - (n)^c\,\frac{\partial \|\mathbf{g}_1 \times \mathbf{g}_2\|}{\partial (x_I)^a} \right] \tag{A.161}$$

$$\begin{aligned}
\frac{\partial^2 (n)^c}{\partial (x_I)^a \partial (x_J)^b} = {}& \frac{1}{\|\mathbf{g}_1 \times \mathbf{g}_2\|} \left[\varepsilon^c{}_{de} \left((N_I)_{,1}\,\delta_a^d\,(N_J)_{,2}\,\delta_b^e + (N_J)_{,1}\,\delta_b^d\,(N_I)_{,2}\,\delta_a^e \right) \right. \\
& \left. - \frac{\partial (n)^c}{\partial (x_I)^a}\,\frac{\partial |\mathbf{g}_1 \times \mathbf{g}_2|}{\partial (x_J)^b} - \frac{\partial \|\mathbf{g}_1 \times \mathbf{g}_2\|}{\partial (x_I)^a}\,\frac{\partial (n)^c}{\partial (x_J)^b} - (n)^c\,\frac{\partial^2 \|\mathbf{g}_1 \times \mathbf{g}_2\|}{\partial (x_I)^a \partial (x_J)^b} \right]
\end{aligned}$$
$$\tag{A.162}$$

These expressions need the inner product norm of the cross product $\mathbf{g}_1 \times \mathbf{g}_2$, which can be calculated with the help of the permutation tensor as:

$$\|\mathbf{g}_1 \times \mathbf{g}_2\| = \left[\varepsilon^c{}_{de}\,(g_1)^d\,(g_2)^e\,\varepsilon^c{}_{fg}\,(g_1)^f\,(g_2)^g \right]^{1/2} \tag{A.163}$$

Therefrom, the first-order and second-order derivatives with respect to the actual displacement vector components $(x_I)^a$ and $(x_J)^b$ follow as:

$$\frac{\partial \|\mathbf{g}_1 \times \mathbf{g}_2\|}{\partial (x_I)^a} = \varepsilon^c{}_{de}\,(n)^c \left[(N_I)_{,1}\,\delta_a^d\,(g_2)^e + (g_1)^d\,(N_I)_{,2}\,\delta_a^e \right] \tag{A.164}$$

$$\begin{aligned}
\frac{\partial^2 \|\mathbf{g}_1 \times \mathbf{g}_\|\|}{\partial (x_I)^a \partial (x_J)^b} = {}& \varepsilon^c{}_{de} \left[(N_I)_{,1}\,\delta_a^d\,(g_2)^e + (g_1)^d\,(N_I)_{,2}\,\delta_a^e \right] \frac{\partial (n)^c}{\partial (x_J)^b} \\
& + \varepsilon^c{}_{de}\,(n)^c \left[(N_I)_{,1}\,\delta_a^d\,(N_J)_{,2}\,\delta_b^e + (N_J)_{,1}\,\delta_b^d\,(N_I)_{,2}\,\delta_a^e \right]
\end{aligned} \tag{A.165}$$

Herein, the definition of the unit normal vector components is reused to simplify the expressions. Therewith, the derivatives of the unit normal are fully specified and, furthermore, the derivatives of the covariant spatial curvature tensor are ascertainable. Subsequently, the related derivatives of the pull-back of the spatial curvature tensor are given in index notation as:

$$\frac{\partial \mathcal{K}_{AB}}{\partial (x_I)^a} = \frac{\partial k_{\alpha\beta}}{\partial (x_I)^a}\,\bigl(J^{-1}\bigr)^\alpha{}_A\,\bigl(J^{-1}\bigr)^\beta{}_B \tag{A.166}$$

$$\frac{\partial^2 \mathcal{K}_{AB}}{\partial (x_I)^a \partial (x_J)^b} = \frac{\partial^2 k_{\alpha\beta}}{\partial (x_I)^a \partial (x_J)^b}\,\bigl(J^{-1}\bigr)^\alpha{}_A\,\bigl(J^{-1}\bigr)^\beta{}_B \tag{A.167}$$

Again, the inverse of the discrete initial Jacobian tensor is necessary for the pull-back operation. This tensor is given explicitly in Equation (4.114) and in its component representation in Equation (4.115). With that, all first-order and second-order derivatives of the strain measures with respect to the components of the actual displacement vector are declared. This enables the evaluation of the element force vector and the element stiffness matrix resulting from bonded interactions. After this, the global properties are well defined and the finite element equations can be set up.

A.4 Shape functions for subdivision finite elements

In this Appendix, explicit expressions for the finite element shape functions are specified. These shape functions are essential for the treatment of the mixed atomistic-continuum model in a discrete setting by means of the finite element method. For this purpose, the parametrisation of regular subdivision surfaces on the basis of triangular and quadrilateral patches is discussed. Thereof, the triangular and quadrilateral finite elements and the associated shape functions are defined.

A.4.1 Triangular subdivision finite element

For a regular triangular patch as illustrated in Figure A.1, the subdivision scheme of Loop [33] leads to quartic box-splines for the central triangle, which is denoted as the finite element. This allows
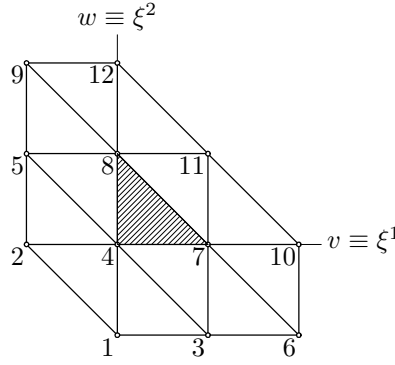

Figure A.1: The regular triangular patch with the parametrised central triangular finite element and the twelve defining nodes in their local numbering.

to define the triangular surface within the central face in terms of shape functions, which makes this type of element applicable for the finite element method. Resulting from the structure of the triangular finite element patch, there are 12 shape functions, one for each node. With reference to Stam [47], the shape functions are given in barycentric coordinates u, v, w. These coordinates have to fulfil $0 \leq u, v, w \leq 1$ and $u + v + w = 1$ so that they remain within the central 4-7-8 unit triangle. Then, the polynomial shape functions of maximum order four are given as:

$$N_1 = \frac{1}{12} \left(u^4 + 2\,u^3\,v \right)$$

$$N_2 = \frac{1}{12} \left(u^4 + 2\,u^3\,w \right)$$

$$N_3 = \frac{1}{12} \left(u^4 + 2\,u^3\,w + 6\,u^3\,v + 6\,u^2\,v\,w + 12\,u^2\,v^2 + 6\,u\,v^2\,w + 6\,u\,v^3 + 2\,v^3\,w + v^4 \right)$$

$$N_4 = \frac{1}{12} \left(6\,u^4 + 24\,u^3\,w + 24\,u^2\,w^2 + 8\,u\,w^3 + w^4 + 24\,u^3\,v + 60\,u^2\,v\,w + 36\,u\,v\,w^2 \right.$$
$$\left. + 6\,v\,w^3 + 24\,u^2\,v^2 + 36\,u\,v^2\,w + 12\,v^2\,w^2 + 8\,u\,v^3 + 6\,v^3\,w + v^4 \right)$$

$$N_5 = \frac{1}{12} \left(u^4 + 6\,u^3\,w + 12\,u^2\,w^2 + 6\,u\,w^3 + w^4 + 2\,u^3\,v + 6\,u^2\,v\,w + 6\,u\,v\,w^2 + 2\,v\,w^3 \right)$$

$$N_6 = \frac{1}{12} \left(2\,u\,v^3 + v^4 \right)$$

$$N_7 = \frac{1}{12} \left(u^4 + 6\,u^3\,w + 12\,u^2\,w^2 + 6\,u\,w^3 + w^4 + 8\,u^3\,v + 36\,u^2\,v\,w + 36\,u\,v\,w^2 \right.$$
$$\left. + 8\,v\,w^3 + 24\,u^2\,v^2 + 60\,u\,v^2\,w + 24\,v^2\,w^2 + 24\,u\,v^3 + 24\,v^3\,w + 6\,v^4 \right)$$

$$N_8 = \frac{1}{12} \left(u^4 + 8\,u^3\,w + 24\,u^2\,w^2 + 24\,u\,w^3 + 6\,w^4 + 6\,u^3\,v + 36\,u^2\,v\,w + 60\,u\,v\,w^2 \right.$$
$$\left. + 24\,v\,w^3 + 12\,u^2\,v^2 + 36\,u\,v^2\,w + 24\,v^2\,w^2 + 6\,u\,v^3 + 8\,v^3\,w + v^4 \right)$$

$$N_9 = \frac{1}{12} \left(2\,u\,w^3 + w^4 \right)$$

$$N_{10} = \frac{1}{12} \left(2\,v^3\,w + v^4 \right)$$

$$N_{11} = \frac{1}{12} \left(2\,u\,w^3 + w^4 + 6\,u\,v\,w^2 + 6\,v\,w^3 + 6\,u\,v^2\,w + 12\,v^2\,w^2 + 2\,u\,v^3 + 6\,v^3\,w + v^4 \right)$$

$$N_{12} = \frac{1}{12} \left(w^4 + 2\,v\,w^3 \right) \tag{A.168}$$

For the finite element method, the barycentric coordinates (v, w) are further renamed as local curvilinear coordinates (ξ^1, ξ^2). This allows to state the shape function corresponding to the local node I and evaluated at the referential coordinates (ξ^1, ξ^2) in a compact form as $N_I\left(\xi^1, \xi^2\right)$. Finally, this is the notation that makes the triangular patch suitable for the finite element method.

A.4.2 Quadrilateral subdivision finite element

In the case of a regular quadrilateral patch, as illustrated in Figure A.2, so-called tensor product B-spline surfaces are the result of a proper subdivision process. When using the scheme of Catmull
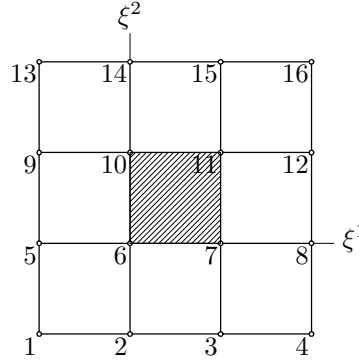

Figure A.2: The regular quadrilateral patch with the parametrised central quadrilateral finite element and the sixteen defining nodes in their local numbering.

and Clark [13], the process of subdivision is based on quadrilaterals. According to Stam [48], the parametrisation of the subdivision surface leads to a bi-cubic B-spline surface for the central quad. Similar to the triangular patch, the central quad is now denoted as finite element. The bi-cubic B-spline surface shape functions are constructed from cubic B-spline curves via tensor products. In a first step, the corresponding cubic B-spline basis functions for a curve with four control nodes are given by:

$$\widetilde{N}_1 = \frac{1}{6} \left(1 - 3\,\xi + 3\,\xi^2 - \xi^3 \right)$$

$$\widetilde{N}_2 = \frac{1}{6} \left(4 - 6\,\xi^2 + 3\,\xi^3 \right)$$

$$\widetilde{N}_3 = \frac{1}{6} \left(1 + 3\,\xi + 3\,\xi^2 - 3\,\xi^3 \right)$$

$$\widetilde{N}_4 = \frac{1}{6}\xi^3 \tag{A.169}$$

This parametrisation is valid for the part of the curve between the two interior nodes 2 and 3 with $0 \leq \xi \leq 1$. On the basis of this one dimensional description, the bi-cubic B-spline surface for the central quad in Figure A.2 can be set up. In doing so, the two local curvilinear coordinates (ξ^1, ξ^2) with the constraints $0 \leq \xi^1, \xi^2 \leq 1$ are introduced so that the central 6-7-10-11 quad is not trespassed. Now, in each of these directions, the above stated cubic B-spline basis functions are employed. For the regular patch, this is possible because there are four nodes in each direction. As a consequence, in total sixteen nodes define the quadrilateral finite element patch. For each of these nodes, a related shape function is uniquely defined by the product of two appropriate one dimensional cubic B-spline basis functions given in Equation (A.169). Performing this task, the demanded sixteen shape functions, considering the numbering of the nodes given in Figure A.2, are obtained as:

$$N_{J+4(K-1)} = \widetilde{N}_J \left(\xi^1 \right) \widetilde{N}_K \left(\xi^2 \right) \qquad \text{with} \qquad J, K = 1, \ldots, 4 \qquad (A.170)$$

The index $J + 4\,(K - 1) = 1, \ldots, 16$ runs over all nodes in the patch and is therefore directly assignable to a local node indexation with I. With this notation, the expression $N_I \left(\xi^1, \xi^2 \right)$ denotes the shape function corresponding to the local node I, which is evaluated at the referential coordinates (ξ^1, ξ^2). The existence of this local parametrisation for the central quadrilateral enables its possibility to serve as finite element.

Bibliography

[1] M. P. Allen and D. J. Tildesley. *Computer Simulation of Liquids*. Oxford University Press, Oxford, UK, 2009.

[2] M. Arroyo. *Finite Crystal Elasticity for Curved Single Layer Lattices: Applications to Carbon Nanotubes*. PhD thesis, Department of Mechanical Engineering, Northwestern University, Evanston, Illinois, 2003.

[3] M. Arroyo and T. Belytschko. An atomistic-based finite deformation membrane for single layer crystalline films. *Journal of the Mechanics and Physics of Solids*, 50(9):1941–1977, 2002.

[4] M. Arroyo and T. Belytschko. Finite crystal elasticity of carbon nanotubes based on the exponential Cauchy-Born rule. *Physical Review B*, 69(11):115415, 2004.

[5] M. Arroyo and T. Belytschko. Finite element methods for the non-linear mechanics of crystalline sheets and nanotubes. *International Journal for Numerical Methods in Engineering*, 59(3):419–456, 2004.

[6] M. Arroyo and T. Belytschko. Continuum Mechanics Modeling and Simulation of Carbon Nanotubes. *Meccanica*, 40(4):455–469, 2005.

[7] K. J. Bathe. *Finite Element Procedures*. Prentice-Hall, Upper Saddle River, NJ, 2 edition, 1996.

[8] Z. P. Bažant and L. Cedolin. *Stability of Structures*. Oxford University Press, Oxford, UK, 1991.

[9] J. Bonet and R. D. Wood. *Nonlinear Continuum Mechanics for Finite Element Analysis*. Cambridge University Press, Cambridge, UK, 2 edition, 2008.

[10] M. Born and K. Huang. *Dynamical Theory of Crystal Lattices*. Oxford University Press, Oxford, UK, 1954.

[11] D. W. Brenner. Empirical potential for hydrocarbons for use in simulating the chemical vapor deposition of diamond films. *Physical Review B*, 42(15):9458–9471, 1990.

[12] G. Cao and X. Chen. Buckling of single-walled carbon nanotubes upon bending: Molecular dynamics simulations and finite element method. *Physical Review B*, 73(15):155435, 2006.

[13] E. Catmull and J. Clark. Recursively generated B-spline surfaces on arbitrary topological meshes. *Computer-Aided Design*, 10(6):350–355, 1978.

[14] K. Chandraseker, S. Mukherjee, and Y. X. Mukherjee. Modifications to the Cauchy-Born rule: Applications in the deformation of single-walled carbon nanotubes. *International Journal of Solids and Structures*, 43(22-23):7128–7144, 2006.

[15] W. H. Chen, H. C. Cheng, and Y. C. Hsu. Mechanical Properties of Carbon Nanotubes Using Molecular Dynamics Simulations with the Inlayer van der Waals Interactions. *CMES - Computer Modeling in Engineering and Sciences*, 20(2):123–145, 2007.

[16] H. C. Cheng, Y. L. Liu, Y. C. Hsu, and W. H. Chen. Atomistic-continuum modeling for mechanical properties of single-walled carbon nanotubes. *International Journal of Solids and Structures*, 46(7-8):1695–1704, 2009.

[17] F. Cirak and M. Ortiz. Fully C^1-conforming subdivision elements for finite deformation thin-shell analysis. *International Journal for Numerical Methods in Engineering*, 51(7):813–833, 2001.

[18] F. Cirak, M. Ortiz, and P. Schröder. Subdivision surfaces: a new paradigm for thin-shell finite-element analysis. *International Journal for Numerical Methods in Engineering*, 47(12):2039–2072, 2000.

[19] C. S. G. Cousins. Inner elasticity. *Journal of Physics C: Solid State Physics*, 11(24):4867–4879, 1978.

[20] M. P. do Carmo. *Differential Geometry of Curves and Surfaces*. Prentice-Hall, Upper Saddle River, NJ, 1976.

[21] M.S. Dresselhaus, G. Dresselhaus, and R. Saito. Physics of carbon nanotubes. *Carbon*, 33(7):883–891, 1995.

[22] L. A. Girifalco, M. Hodak, and R. S. Lee. Carbon nanotubes, buckyballs, ropes, and a universal graphitic potential. *Physical Review B*, 62(19):13104–13110, 2000.

[23] X. Guo, A.Y.T. Leung, X.Q. He, H. Jiang, and Y. Huang. Bending buckling of single-walled carbon nanotubes by atomic-scale finite element. *Composites Part B: Engineering*, 39(1):202–208, 2008.

[24] X. Guo, J. B. Wang, and H. W. Zhang. Mechanical properties of single-walled carbon nanotubes based on higher order Cauchy-Born rule. *International Journal of Solids and Structures*, 43(5):1276–1290, 2006.

[25] H. D. Hibbitt, B. I. Karlsson, and E. P. Sorensen. *ABAQUS Theory Manual, Version 5.8*. Hibbitt, Karlsson & Sorensen Inc., Pawtucket, RI, 1998.

[26] S. Iijima, C. Brabec, A. Maiti, and J. Bernholc. Structural flexibility of carbon nanotubes. *The Journal of Chemical Physics*, 104(5):2089–2092, 1996.

[27] A. R. Leach. *Molecular modelling: principles and applications*. Prentice-Hall, Harlow, UK, 2 edition, 2002.

[28] M. J. Leamy, P. W. Chung, and R. Namburu. On an Exact Mapping and a Higher Order Born Rule for Use in Analyzing Graphene Carbon Nanotubes. In *ARL-TR-3117*, Army Research Laboratory: Aberdeen Proving Ground, MD, 2003.

[29] A. Y. T. Leung, X. Guo, X. Q. He, H. Jiang, and Y. Huang. Postbuckling of carbon nanotubes by atomic-scale finite element. *Journal of Applied Physics*, 99(12):124308, 2006.

[30] B. Liu, Y. Huang, H. Jiang, S. Qu, and K. C. Hwang. The atomic-scale finite element method. *Computer Methods in Applied Mechanics and Engineering*, 193(17-20):1849–1864, 2004.

[31] B. Liu, H. Jiang, Y. Huang, S. Qu, M. F. Yu, and K. C. Hwang. Atomic-scale finite element method in multiscale computation with applications to carbon nanotubes. *Physical Review B*, 72(3):035435, 2005.

[32] W. K. Liu, E. G. Karpov, S. Zhang, and H. S. Park. An introduction to computational nanomechanics and materials. *Computer Methods in Applied Mechanics and Engineering*, 193(17-20):1529–1578, 2004.

[33] C. T. Loop. Smooth Subdivision Surfaces Based on Triangles. Master's thesis, Department of Mathematics, University of Utah, Salt Lake City, Utah, 1987.

[34] J. E. Marsden and T. J. R. Hughes. *Mathematical Foundations of Elasticity*. Prentice-Hall, Englewood Cliffs, NJ, 1983.

[35] J. W. Martin. Many-body forces in solids and the Brugger elastic constants. II. Inner elastic constants. *Journal of Physics C: Solid State Physics*, 8(18):2858–2868, 1975.

[36] K. Mylvaganam, T. Vodenitcharova, and L. Zhang. The bending-kinking analysis of a single-walled carbon nanotube – a combined molecular dynamics and continuum mechanics technique. *Journal of Materials Science*, 41(11):3341–3347, 2006.

[37] L. Nasdala and G. Ernst. Development of a 4-node finite element for the computation of nano-structured materials. *Computational Materials Science*, 33(4):443–458, 2005.

[38] M. J. O'Connell, editor. *Carbon nanotubes: properties and applications.* Taylor & Francis, Boca Raton, FL, 2006.

[39] A. Pantano, M. C. Boyce, and D. M. Parks. Mechanics of Axial Compression of Single and Multi-Wall Carbon Nanotubes. *Journal of Engineering Materials and Technology*, 126(3):279–284, 2004.

[40] A. Pantano, D. M. Parks, and M. C. Boyce. Mechanics of deformation of single- and multi-wall carbon nanotubes. *Journal of the Mechanics and Physics of Solids*, 52(4):789–821, 2004.

[41] D. Qian, G. J. Wagner, W. K. Liu, M. F. Yu, and R. S. Ruoff. Mechanics of carbon nanotubes. *Applied Mechanics Reviews*, 55(6):495–533, 2002.

[42] A. K. Rappé and C. J. Casewit. *Molecular Mechanics across Chemistry.* University Science Books, Sausalito, CA, 1997.

[43] E. Riks. Buckling. In E. Stein, R. de Borst, and T. J. R. Hughes, editors, *Encyclopedia of Computational Mechanics: Volume 2 Solids and Structures*, chapter 4, pages 139–167. John Wiley & Sons: Chichester, UK, 2004.

[44] C. Q. Ru. Effective bending stiffness of carbon nanotubes. *Physical Review B*, 62(15):9973–9976, 2000.

[45] A. Sears and R. C. Batra. Buckling of multiwalled carbon nanotubes under axial compression. *Physical Review B*, 73(8):085410, 2006.

[46] H. Shima. Buckling of Carbon Nanotubes: A State of the Art Review. *Materials*, 5(1):47–84, 2012.

[47] J. Stam. Evaluation Of Loop Subdivision Surfaces. In *SIGGRAPH '98 CD-ROM Proceedings*, New York, NY, USA, 1998. ACM.

[48] J. Stam. Exact Evaluation Of Catmull-Clark Subdivision Surfaces At Arbitrary Parameter Values. In *SIGGRAPH '98 Proceedings*, pages 395–404, New York, NY, USA, 1998. ACM.

[49] Y. Sun and K. M. Liew. The buckling of single-walled carbon nanotubes upon bending: The higher order gradient continuum and mesh-free method. *Computer Methods in Applied Mechanics and Engineering*, 197(33-40):3001–3013, 2008.

[50] Y. Sun and K. M. Liew. Mesh-free simulation of single-walled carbon nanotubes using higher order Cauchy-Born rule. *Computational Materials Science*, 42(3):444–452, 2008.

[51] R. Sunyk and P. Steinmann. On higher gradients in continuum-atomistic modelling. *International Journal of Solids and Structures*, 40(24):6877–6896, 2003.

[52] E. B. Tadmor, R. Phillips, and M. Ortiz. Mixed Atomistic and Continuum Models of Deformation in Solids. *Langmuir*, 12(19):4529–4534, 1996.

[53] E. B. Tadmor, G. S. Smith, N. Bernstein, and E. Kaxiras. Mixed finite element and atomistic formulation for complex crystals. *Physical Review B*, 59(1):235–245, 1999.

[54] J. Tersoff. New empirical approach for the structure and energy of covalent systems. *Physical Review B*, 37(12):6991–7000, 1988.

[55] T. von Kármán and H. S. Tsien. The Buckling of Thin Cylindrical Shells under Axial Compression. *Journal of the Aeronautical Sciences*, 8(8):303–312, 1941.

[56] J. Wackerfuß. Molecular mechanics in the context of the finite element method. *International Journal for Numerical Methods in Engineering*, 77(7):969–997, 2009.

[57] W. Wagner and P. Wriggers. A simple method for the calculation of postcritical branches. *Engineering Computations*, 5(2):103–109, 1988.

[58] C. M. Wang, Y. Y. Zhang, Y. Xiang, and J. N. Reddy. Recent Studies on Buckling of Carbon Nanotubes. *Applied Mechanics Reviews*, 63(3):030804, 2010.

[59] C. Y. Wang, Y. Y. Zhang, C. M. Wang, and V. B. C. Tan. Buckling of Carbon Nanotubes: A Literature Survey. *Journal of Nanoscience and Nanotechnology*, 7(12):4221–4247, 2007.

[60] J. C. Wohlever and T. J. Healey. A group theoretic approach to the global bifurcation analysis of an axially compressed cylindrical shell. *Computer Methods in Applied Mechanics and Engineering*, 122(3-4):315–349, 1995.

[61] P. Wriggers. *Nichtlineare Finite-Elemente-Methoden*. Springer, Berlin, 2001.

[62] B. I. Yakobson, C. J. Brabec, and J. Bernholc. Nanomechanics of Carbon Tubes: Instabilities beyond Linear Response. *Physical Review Letters*, 76(14):2511–2514, 1996.

[63] L. Zhang. *Stability Analysis Of Atomic Structures*. PhD thesis, University of Iowa, Iowa City, Iowa, 2006.

[64] O. C. Zienkiewicz and R. L. Taylor. *The Finite Element Method, Volume 1: Basic Formulation and Linear Problems*. McGraw-Hill, London, UK, 4 edition, 1989.

[65] O. C. Zienkiewicz and R. L. Taylor. *The Finite Element Method, Volume 2: Solid and Fluid Mechanics - Dynamics and Non-linearity*. McGraw-Hill, London, UK, 4 edition, 1991.